departamento
de
comunicaciones

# ANÁLISIS Y ESTIMACIÓN DE PARÁMETROS FÍSICOS DE VEGETACIÓN MEDIANTE POLARIMETRÍA RADAR

## Analysis and Estimation of Biophysical Parameters of Vegetation by Radar Polarimetry

Juan Manuel López Sánchez

Director: Dr. Mariano Baquero Escudero

A Yolanda

# Acknowledgments

This thesis is the result of a work carried out since July 1996. Since then, I have been in contact with many people. In these few lines, I would like to acknowledge their help, support and friendship.

The formalization of the thesis work can be divided into two periods. The first corresponds to the research accomplished at the Departamento de Comunicaciones of the Universidad Politécnica de Valencia (UPV), Valencia, Spain, from July 1996 to January 1998. I started in 1996 with a *Tercer Ciclo* grant from the UPV, and in 1997 I enjoyed a predoctoral grant from the Spanish Ministry of Education and Science (MEC) under the program of Formation of Research Personnel (FPI). During the second period, from February 1998, I joined the Joint Research Centre (JRC) of the European Commission in Ispra, Italy, with a predoctoral grant supported by the European Commission. My acknowledgment goes to these institutions, which have contributed importantly with financial support.

I am very grateful to Joaquim Fortuny. His encouragement and assistance, both on technical and personal aspects, and a number of discussions about many topics, have contributed significantly to the development of this thesis and, more importantly, to the growth of a sincere friendship.

The invaluable support of Mariano Baquero, supervisor of this thesis at the UPV, is sincerelly and gratefully acknowledged. I also would like to thank Miguel Ferrando for his support and advice for my engagement with the FPI grant, as well as his flexibility when I decided to move to JRC.

During my stage at JRC, I worked at the Unit of Technology for Detection and Positioning; Anti-personnel Mines, a part of the Space Applications Institute (SAI). Thanks are due to Alois J. Sieber, the unit head, for his encouraging interest on this topic, despite the global enrollment of the unit in other issues. I also extend my thanks to all the staff of the European Microwave Signature Laboratory (EMSL), headed by Giuseppe Nesti, whose experimental data constitute the basis of most of the research presented in this thesis. Their professionalism and care in preparing the experiments and carrying out the measurements is highly appreciated. I also would like to thank Giovanni Nico for his pleasant company at the office we shared. His enjoyable attitude and disinterested help by proofreading most of the thesis are also acknowledged. Special thanks go to Steve Lewis and Brian Hosgood for carefully proofreading the final version of the text.

The main topic of this thesis is radar polarimetry. The starting point of my dedication to this argument was a three-day course delivered by Shane R. Cloude at JRC in October 1997. His clear, rigorous and thorough explanations, not exempt from enthusiasm, involved me in this issue. Later on, some collaborations with him have produced important results which in turn form the skeleton of the thesis. Therefore, I owe him a debt of gratitude for all

that his assistance has meant to me.

I also would like to extend my acknowledgement to all people and organizations forming part of the TMR European Network on Radar Polarimetry. I really appreciate the opportunity I had of sharing my findings and discussing my results with them. Special mention is deserved by Lluís Sagués, from the Universitat Politècnica de Catalunya (UPC), who has worked together with me in some parts of this thesis. His comments and discussions helped me to overcome some difficulties and to interpret many results. I think that our collaboration has been very productive for both of us.

Once again, I would like to recognize the support from my parents. I hope to correspond with enough love to their sacrifice during all these years.

Finally, I am specially indebted to Yolanda, whose love, unconditional support, and patience, allowed me to endure our separation for such a long time.

# Contents

# List of Tables

# List of Figures

# Introducción

Con el desarrollo industrial y el rápido crecimiento de la población mundial, se ha mostrado evidente la necesidad tanto de controlar como de usar eficientemente los recursos naturales de la Tierra, así como de monitorizar los cambios climáticos que están teniendo lugar. Uno de los elementos determinantes de dichos cambios climáticos a escala global, a la vez que afectado por el desarrollo industrial y la expansión de la civilización, es la cubierta vegetal de la superficie terrestre. La cantidad total de masa vegetal se conoce como biomasa, y constituye un índice de gran interés en estos estudios.

Para poder monitorizar de forma global la biomasa terrestre, o bien algún parámetro asociado (volumen de madera aprovechable para la construcción, altura de las plantas, área de la base de los árboles, etc.), se han venido implementando sistemas de teledetección con variadas tecnologías. Los sistemas radar han sido los más ampliamente usados gracias a su independencia del sol como fuente de iluminación y a su capacidad para operar bajo cualquier situación climática. Además, la información proporcionada por los sensores de microondas es complementaria respecto a la obtenida con instrumentos que trabajan en otras bandas, como infrarrojos u ópticos.

La configuración que mejor se adapta a estas aplicaciones es el radar de apertura sintética (SAR), que se emplea para generar mapas de reflectividad de la superficie terrestre. En los últimos años se están realizando muchas campañas de medidas dedicadas a vegetación con radares aerotransportados o desde satélite. El objetivo de dichas campañas es múltiple: obtención de mapas de zonas forestales y cultivos, clasificación de diferentes especies, estimación de parámetros para medir la biomasa, monitorización del crecimiento de cosechas, etc. Sea cual sea la aplicación final, el estudio de los datos proporcionados por un SAR es muy complicado debido a la complejidad del proceso de interacción entre las ondas electromagnéticas y la vegetación.

En las últimas décadas se ha realizado un gran esfuerzo en el desarrollo de modelos de dispersión electromagnética para cubiertas vegetales, así como en la construcción de algoritmos para estimar parámetros físicos de las plantas a partir de medidas hechas con radar. Sin embargo, la aplicación de estas técnicas SAR de teledetección de bosques, cosechas y otras

cubiertas vegetales ha tenido un éxito bastante limitado hasta la fecha. La razón principal es la falta de suficientes conocimiento y comprensión de los mecanismos de interacción que se producen entre las ondas electromagnéticas y los elementos que constituyen la vegetación.

A todo esto hay que añadir que las medidas en condiciones naturales son muy complejas. Las dificultades que se encuentran pueden clasificarse en tres tipos. En primer lugar, es necesario medir *in situ* las magnitudes físicas que se consideren relevantes para la comparación posterior (comúnmente conocidas como *ground truth*). En segundo lugar, la realización de medidas con sistemas radar requiere un control y calibración precisos del equipamiento a utilizar, tareas no siempre fáciles debido a imprecisiones en las trayectorias descritas por el sensor, problemas de derivas de los equipos, etc. Finalmente, efectos tales como variaciones de las condiciones climáticas, presencia de interferencias de RF, cambios no previstos de las condiciones del suelo, etc. pueden influenciar notablemente las medidas. Por todo ello los datos experimentales adquiridos en estas condiciones pueden conducir a interpretaciones erróneas y, por lo tanto, a conclusiones equivocadas acerca de la escena de interés. En cambio, si las medidas se llevan a cabo en una cámara anecoica en condiciones perfectamente controladas, se puede realizar un análisis completo y preciso de muestras aisladas sin la influencia de todas estas potenciales fuentes de error. Además, es posible seleccionar de modo flexible la banda de frecuencia y los ángulos de incidencia que interesen para cada experimento, así como ecualizar con gran precisión los datos, incluso si son polarimétricos. Como consecuencia, la interpretación de los resultados es más simple y menos condicionada por efectos indeseados.

Existe una razón adicional para realizar medidas de vegetación con radares en cámaras anecoicas. Desde el punto de vista metodológico, el desarrollo de modelos está generalmente admitido como un medio eficiente de complementar los experimentos. Al fin y al cabo, no es realista tratar de realizar experimentos cubriendo todos los tipos de vegetación y condiciones posibles, así que se deben desarrollar modelos para complementarlos. Para crear los modelos, sus fundamentos físicos deben ser comprendidos totalmente, y las relaciones entre las variables del modelo y los valores de salida deben estar bien cuantificadas. En el caso concreto que nos ocupa, se podría proceder paso a paso midiendo en laboratorio las respuestas de los componentes elementales de los árboles, luego árboles enteros y, finalmente, grupos de plantas o árboles. Por último, cuando se llevaran a cabo medidas en condiciones naturales, la influencia del ambiente y del sistema podría ser identificada por comparación con los resultados previos del laboratorio.

En este contexto, el *European Microwave Signature Laboratory* (EMSL) del *Space Applications Institute* (SAI), perteneciente al *Joint Research Centre* (JRC) de la Comisión Europea, en Ispra, Italia, es un laboratorio con características únicas para tales experimentos. El personal del EMSL ha venido colaborando con grupos de trabajo punteros dedicados a la teledetección con sensores activos de microondas con el fin de poner en común conocimientos y tratar de identificar aquellos aspectos que necesitan una validación experimental en condiciones controladas. La tarea del EMSL es no sólo proveer a la comunidad científica datos de gran calidad obtenidos para una amplia variedad de muestras, sino también implementar los métodos o técnicas que han sido propuestos más recientemente y que requieren una comprobación experimental antes de proseguir con su estudio o antes de adaptar instru-

mentación y equipos de sensores operativos a estas técnicas. El trabajo presentado en esta tesis ha sido desarrollado dentro de este marco global.

Antes de proseguir, es importante aclarar en este punto el objetivo de la tesis. Hasta la fecha, la mayoría de investigaciones acerca de la dispersión electromagnética producida por la vegetación se han concentrado en el llamado *problema directo*, es decir, en el modelado de la vegetación para estimar o anticipar qué valores se obtendrán luego al medir con un radar. La construcción de estos modelos, analíticos y/o numéricos, puede considerarse bastante evolucionada. Sin embargo, la aplicación de dichos modelos al *problema inverso* (esto es, a la estimación de parámetros físicos de la escena usando las medidas radar como valores de entrada) es muy limitada. Una de las principales causas de esta limitación es la falta de verdadero significado físico, en relación a la morfología o estructura natural de la vegetación, de las magnitudes empleadas hasta ahora. Tal como se explica en los próximos capítulos, la forma en que la polarización de los campos dispersados depende de la arquitectura de las plantas es una característica fundamental que debe ser explotada para afrontar el problema inverso con garantías de éxito. De forma escueta, el objetivo global de esta tesis es mostrar la contribución que la medida de las características de polarización de la señal radar (una técnica conocida como polarimetría radar) puede ofrecer en la solución de problemas inversos existentes en teledetección de vegetación.

La polarimetría radar ya ha demostrado su utilidad en varias aplicaciones *cualitativas*, tales como clasificación, mejora del contraste en imágenes, etc. Su aplicación a problemas inversos o de estimación ha atraído mucha atención últimamente, y varias investigaciones realizadas recientemente han mostrado su potencial. Sin embargo, aunque la teoría matemática de la polarimetría es muy robusta, la comunidad científica no está plenamente convencida de sus características únicas ni de la posibilidad real de implementarla de forma práctica. Por lo tanto, la meta final de esta tesis es probar la contribución fundamental que la polarimetría puede tener en teledetección *cuantitativa* de vegetación. De acuerdo con el espíritu del EMSL, se pondrá especial énfasis en los resultados experimentales obtenidos en laboratorio.

Una vez se ha enunciado el objetivo global de la tesis, las metas concretas y las contribuciones originales de la misma se describen a continuación. Tal como indica el título, y procediendo de manera normal en investigación, el trabajo ha sido dividido en dos etapas sucesivas: un análisis previo para caracterizar las muestras y una consiguiente prueba de diferentes técnicas de estimación aplicadas a dichas muestras. La etapa de análisis corresponde al examen de un conjunto de medidas realizadas en el EMSL usando muestras vegetales. Este examen será presentado de forma descriptiva y trata de mostrar cómo son vistos por el radar los árboles o las plantas. Para ello, los datos adquiridos serán tratados mediante técnicas de descomposición polarimétrica. Estas técnicas de descomposición permiten, bajo ciertas condiciones, identificar los mecanismos de dispersión presentes dentro del volumen ocupado por las muestras. Los experimentos se efectuarán con tres configuraciones diferentes, que proporcionan tres tipos de resultados con información complementaria:

1. Gráficas en el dominio de la frecuencia: se calculan a partir de datos de dispersión puros y muestran los mecanismos de dispersión dominantes en la planta considerada

como conjunto. Se analizará cómo varían los resultados con la banda de frecuencias y la geometría de la medida (ángulo de incidencia). Se establecerá una generalización a medidas de campo en condiciones naturales.

2. Gráficas en el dominio del tiempo: se obtienen a partir de la variación de la reflectividad con la coordenada de *slant range* o distancia a la antena. Estos resultados deberán ilustrar la equivalencia entre la vegetación y un volumen multicapa, incluyendo la posición y espesor de cada capa y su comportamiento polarimétrico. Además, se definirá y medirá un coeficiente de extinción diferencial entre polarizaciones. Este coeficiente es muy importante en algunos algoritmos de estimación, como la técnica para encontrar la altura de la vegetación mediante interferometría polarimétrica que se presenta más adelante.

3. Imágenes bi- y tridimiensionales: imágenes polarimétricas de alta resolución obtenidas mediante SAR inverso (ISAR). Estas imágenes permiten la identificación de diferentes partes de la muestra en la estructura tridimensional, y sus respectivas contribuciones polarimétricas también pueden obtenerse mediante técnicas de descomposicíon.

Estos experimentos constituyen un paso previo necesario para entender cómo funciona la polarimetría cuando se aplica a la vegetación y por qué los métodos que se presentan más adelante están bien fundados. Por sí mismos estos experimentos también son importantes para explicar la interacción entre el campo incidente y la vegetación, así como la diferente respuesta de distintas partes de las plantas. Éste es el primer trabajo aparecido en la literatura donde las citadas técnicas de descomposición se han aplicado a datos de laboratorio.

La segunda parte de la investigación descrita en esta tesis consiste en la validación experimental de dos algoritmos de resolución de problemas inversos. El primero ha sido diseñado para estimar la forma y la orientación de las partículas elementales que componen la estructura de la vegetación en ciertos casos. Este algoritmo es una contribución original de esta tesis, aunque fue formulado e implementado en colaboración con Dr. S. R. Cloude. La segunda técnica que se ha probado es la estimación de la altura de la vegatación mediante interferometría SAR polarimétrica. Este método revolucionario está basado en la formación de varios interferogramas de la misma escena, cada uno de ellos asociado a un mecanismo de dispersión distinto. La teoría básica necesaria para la generalización de la interferometría SAR al caso polarimétrico fue formulada originalmente por Dr. S. R. Cloude y Dr. K. P. Papathanassiou. En esta tesis, el proceso a seguir en la estimación se explica detalladamente. Además, los resultados presentados aquí son la primera comparación con datos de *ground truth* que ha aparecido en la literatura.

Finalmente, se presentará otra contribución original de esta tesis. Consiste en la formulación, implementación y validación de un nuevo método eficiente para reconstruir imágenes radar tridimensionales. Este algoritmo se ha desarrollado para generar imágenes de alta resolución de objetos complejos y está diseñado especialmente para el modo de funcionamiento y geometría del EMSL.

El material de la tesis está organizado como sigue. En el capítulo 2 se presenta un

repaso bibliográfico acerca de los temas tratados en el resto del texto. Se ha prestado especial atención a los puntos donde esta tesis puede suponer una contribución significativa. Después, en el capítulo 3 se define la formulación que se necesitará en las siguientes partes de la tesis. Toda la teoría polarimétrica ha sido ya publicada en otras referencias, pero aquellos aspectos directamente relacionados con la tesis han sido reescritos en este capítulo para hacer la tesis autocontenida. Los tres capítulos siguientes forman el núcleo de la tesis. En primer lugar, en el capítulo 4 se describe las características y modo de funcionamiento del EMSL, las muestras vegetales que se emplearán en las medidas, y el análisis de los resultados experimentales obtenidos mediante el uso de técnicas de descomposición polarimétrica. Más adelante, el algoritmo de inversión dedicado a la forma y orientación de los componentes elementales de las plantas se describe en el capítulo 5, donde también se muestran resultados experimentales. Algunas fórmulas auxiliares y resultados intermedios necesarios para el desarrollo de este método se recogen en el apéndice B. En tercer lugar, el método de inversión que trata la estimación de la altura de cubiertas vegetales mediante la combinación de interferometría y polarimetría se ha validado experimentalmente en el capítulo 6. En dicho capítulo se repasa la formulación del método y se presentan resultados comparados con *ground truth*. El capítulo 7 tiene un carácter diferente al resto de la tesis, puesto que no está relacionado directamente con la polarimetría. En él se ilustra un nuevo algoritmo de reconstrucción de imágenes SAR que ha sido desarrollado por el autor de esta tesis, y que se ha empleado para calcular las imágenes tridimensionales empleadas en el capítulo 4. Ha sido incluído en la tesis porque supone una contribución original, y porque fue desarrollado con el mismo propósito que el resto de la tesis. Este capítulo está complementado por el material recogido en los apéndices C y D. En ellos se describe la formulación correspondiente a la extensión del algoritmo a geometrías cilíndrica y esférica, respectivamente, además de importantes detalles de la implementación eficiente de dicha extensión. Para terminar, las conclusiones de la tesis aparecen en el capítulo 8, donde también se sugieren varias líneas futuras de investigación como continuación al trabajo presentado aquí. Después de las conclusiones se ha incluído una lista con las publicaciones en revistas y congresos internacionales que se han ido generando durante el desarrollo de la presente tesis. El apéndice A muestra un par de tablas con abreviaciones empleadas en la tesis y con la nomenclatura de las bandas de frecuencia.

CHAPTER 1

# Introduction

THE industrial development and the rapid growth of the world population have revealed an increasing necessity for control and efficient management of the earth's natural resources, in addition to a continuous monitoring of the environmental and climate changes that are taking place. One of the major determinants of the weather conditions at global scale, which in turn is affected by the modern civilization expansion, is the vegetation cover on the earth's surface. The main index of interest of this cover is the biomass, or total quantity of vegetation mass on the earth's surface.

The remote monitoring of biomass, or related parameters (timber volume, plants height, basal area, etc.), has been performed by means of remote sensing systems with various technologies. Due to their operation capability in all-weather conditions and their independence of the sun as a source of illumination, radar systems are the most widely used ones. Moreover, the information provided by microwave sensors is complementary to that obtained by instruments working in other spectral regions, such as visible and infrared.

The radar configuration specially adapted to this application is the synthetic aperture radar (SAR), which is extensively employed for obtaining reflectivity maps of the earth's surface. In recent years an increasing number of measurement campaigns dedicated to vegetation has been carried out from SAR's mounted in air- and spaceborne platforms. The objectives of these campaigns are multiple: forests and crop mapping, terrain classification into different vegetation kinds, monitoring of crop growth, retrieval of parameters for estimating biomass, and so on. Whatever the final application is, the analysis of SAR data is complicated because the interaction between electromagnetic waves and vegetation is a very complex process.

Over the past decades, much effort has been devoted to the development of scattering models of vegetation and to the construction of algorithms for estimation of biophysical parameters by means of radar measurements. However, the application of SAR systems to remote sensing of forestry, crops and other vegetation covers has shown limited success so far. The main reason is the lack of sufficient knowledge and understanding of the interaction mechanisms between the incident electromagnetic waves and the scatterers inside the

vegetation volume.

In addition, measurements of vegetation cover under natural conditions are complex, and three kinds of difficulties are usually encountered. First, one has to define and measure the relevant biophysical parameters (i.e., ground truth data); second, the deployment of the required instrumentation associated with outdoor radar measurements is complicated, including calibration procedures, working constraints of the platform in which the sensor is mounted, etc; and third, effects such as varying weather conditions, presence of RF interfering signals, unknown variations of the local topography and soil conditions may heavily influence the measurement. As a result, experimental data acquired under these conditions may not be interpreted properly and consequently may lead to wrong conclusions concerning the vegetation cover under study. Alternatively, when running the measurements in an anechoic chamber under laboratory conditions, all relevant measurement parameters can be fully controlled and a complete and accurate analysis of an isolated sample can be carried out. We can also freely select the frequency range and incidence angles of interest, and the radar backscatter can be accurately equalized by applying a single reference fully polarimetric calibration. Thus, leading to a simpler interpretation of the results.

There is an additional reason for carrying out radar measurements on vegetation in laboratory conditions. From the methodological point of view, it is acknowledged that modeling must complement the experimental approaches for the sake of efficiency. In other words, it is not realistic attempting to cover with experiments all the wide variety of vegetation types and environment conditions, so vegetation models must be developed. For doing that, the physical foundations of the models should be fully understood, and the relationships between input and output values accurately quantified. Therefore, proceeding step by step, it is important to measure under laboratory conditions the responses of elementary tree components, single trees and plants, and groups of them. Finally, trees in natural conditions should be measured, and the influence of the environment could be identified by comparison with previous laboratory results.

In this context, the European Microwave Signature Laboratory (EMSL) of the Space Applications Institute (SAI) at the Joint Research Centre of the European Commission (JRC), Ispra, Italy, is an unique facility for such experiments. The EMSL team has collaborated with outstanding research groups worldwide in the identification of those aspects that require an experimental validation in controlled conditions. The task of the EMSL is not only to provide high-quality data from a variety of targets, but to implement state-of-the-art methods and techniques that have been proposed and need to be tested. These tests constitute an important previous step before the application of any technique to conventional air- or spaceborne systems, and also before further enhancements can be developed. They are also useful for anticipating requirements and ideal working parameters in the design of future systems. The work presented in this thesis is embodied within this general framework.

A remark must be stated at this point in order to clarify the scope of the present thesis. To date, most research concerning the scattering from vegetation has been concentrated on the *direct problem*, i.e. the modeling of vegetation for estimating its response to an illuminating radar signal. The construction of analytical and/or numerical models of vegetation from

the electromagnetic point of view has already reached maturity. However, the applicability of these models to solve the *inverse problem* (i.e. the estimation of physical parameters of the target by using radar measurements as inputs) is very limited. One of the main causes of this failure is the lack of physical meaning (in relation to the natural morphology and structure of vegetation) of the observables used so far. As will be explained in next chapters, the polarization dependence of the scattered fields on the vegetation architecture is a key feature that must be exploited to face the inverse problem with guarantees of success. In summary, the global objective of this thesis is to show the contribution that the measurement of the polarization characteristics of the radar signal (a general technique known as radar polarimetry) can provide for the solution of inverse problems regarding vegetation remote sensing.

Radar polarimetry has already shown its usefulness in terrain classification, image contrast enhancement, and other *qualitative* applications. Moreover, its application to inverse problems has attracted a great deal of attention lately, and some recent researches have illustrated its potentials. Nevertheless, although the mathematical foundations of polarimetry are very robust, the scientific community is not fully convinced of its uniqueness and practical implementation in real situations. Therefore, the final aim of the present thesis is to prove the important contribution of polarimetry in *quantitative* remote sensing of vegetation. In accordance with the spirit of the EMSL, the focus will be placed on experimental results.

Once the global objective of the present thesis has been stated, the specific goals and original contributions are described in the following. Proceeding in the usual manner in research, and as the title indicates, the work has been divided into two sequential stages: a previous analysis or inspection, and an ensuing test of estimation techniques. The analysis stage corresponds to the study of a set of measurements carried out in the EMSL on vegetation samples. This study will be presented in a descriptive way, and tries to show how the plants or trees are seen by the radar. For doing this, decomposition theories will be applied to full polarimetric data. These decomposition methods allow, under certain conditions, identificaton of the scattering mechanisms that are present in the targets volume. The experiments will be performed for three configurations, thus resulting in three kinds of data that will provide complementary information:

1. Frequency domain plots: computed from pure scatterometric data, yield the dominant scattering mechanisms of the target as a whole. The dependence on the frequency band and measurement geometry (incidence angles) will be analyzed, and a generalization to field measurements under natural conditions will be established.

2. Time domain profiles: calculated by reconstructing reflectivity functions versus the slant-range coordinate. They should illustrate the equivalence between vegetation and a multilayer volume, including the position and depth of each layer and its scattering behavior. Moreover, a differential extinction coefficient between polarizations will be defined and measured by using this technique. This coefficient is of prime importance for some inverse algorithms, like the estimation of vegetation height by polarimetric SAR interferometry that will be presented later.

3. Two- and three-dimensional images: high-resolution polarimetric reflectivity images

obtained by means of inverse SAR (ISAR) scanning geometries. These images will enable the identification of different parts within the target three-dimensional structure, and their respective polarimetric contributions will be derived by decomposition techniques as well.

These experiments constitute a necessary previous step for understanding how polarimetry works for vegetation, and why the inversion methods presented later are well founded. By itself, this step is also important for gaining an insight on the interaction between waves and vegetation and on the different responses from different parts of the plants. This is the first work appeared in the literature where such decomposition techniques have been applied to laboratory data.

The second stage of the work presented in this thesis consists in the experimental validation of two algorithms for inverse problems. The first algorithm will be applied to estimating the shape and the orientation of elementary particles into which a vegetation volume can be decomposed under certain conditions. This algorithm is an original contribution of this thesis, though it was formulated and developed in collaboration with Dr. S. R. Cloude. The second technique to be tested is the retrieval of vegetation height by means of polarimetric SAR interferometry. This revolutionary technique is based on the formation of various interferograms of the same scene, each of them associated with a different scattering mechanism. The basic theory about the generalization of SAR interferometry to the polarimetric case was originally formulated by Dr. S. R. Cloude and Dr. K. P. Papathanassiou. In this thesis, the estimation procedure will be thoroughly explained, and it will be validated for the first time with ground truth data.

Finally, there is an additional original contribution of this thesis. It is the formulation, implementation and validation of a new and efficient algorithm for three-dimensional radar imaging. This algorithm will be developed in order to obtain high-resolution radar images of complex volume targets, and will be specially suited for the geometry and operating modes of the EMSL.

The material of the thesis is organized as follows. Chapter 2 presents a bibliographical review about the topics that will be addressed in the text. Special attention is payed on the points where this thesis can contribute significantly. The formulation that will be needed in the rest of the thesis is defined in Chapter 3. All the polarimetric theory has been published already in the literature, but the issues directly related with the thesis are rewritten in this chapter for the sake of completeness. The next three chapters comprise the nucleus of the thesis. Firstly, Chapter 4 describes the operating mode and characteristics of the EMSL, the vegetation targets employed in the laboratory measurements, and the analysis of the experimental results obtained by polarimetric decomposition techniques. Secondly, the inversion algorithm for estimating the shape and orientation of the basic particles into which vegetation can be decomposed is presented and tested in Chapter 5. Some auxiliary formulas and results used in the derivation of this inversion method are described in Appendix B. In third place, an inversion method for retrieving the height of vegetation covers by using polarimetry in combination with interferometry is experimentally validated in Chapter 6. This

chapter reviews the formulation of the method and describes laboratory results compared with ground truth. Chapter 7 has a different character from the rest of the thesis, since it is not directly related to polarimetry. This chapter describes a new imaging algorithm for SAR that has been developed by the present author, and that has been used for computing the three-dimensional images presented in Chapter 4. It has been included in the thesis because it is an original contribution and was developed with the same final purpose of the rest of the thesis. Appendices C and D present details of the formulation needed to extend this imaging algorithm to cylindrical and spherical scanning geometries, and also gives particulars about the implementation of this extension. Finally, the conclusions of the thesis are shown in Chapter 8, where some future fields of research are also suggested as a continuation of the work presented here. A list with the publications in journals and conference proceedings that have been written during the development of this thesis is presented after the conclusions. Appendix A consists of two tables with band designations and some abbreviations employed in the text.

# State of the Art

THE aim of this chapter is to present a bibliographical review of the approaches employed so far for analyzing the microwave scattering by vegetation and for solving problems related to the estimation of vegetation physical parameters. The focus is also placed on the historical development of radar polarimetry for remote sensing applications, and on the role played by laboratory experiments on vegetation radar studies. Therefore, the goal of this chapter is not to perform a comprehensive survey of the history and progress of radar remote sensing of the earth, but to focus on the topics directly related with this thesis. The interested reader can find an excellent review about microwave remote sensing of the earth in [1]-[3], where there is material concerning history, mathematical models, applications, hardware, etc.

This chapter has been divided into several sections for helping the reader in the identification of the different subjects that are considered later in the text. Firstly, a brief historical review concerning radar polarimetry is presented in Section 2.1. A specific topic of radar polarimetry, called target decomposition theory, is dealt with in Section 2.2. It has been treated apart from basic polarimetry in order to concentrate on these methods, which really constitute the foundations of the application of polarimetry to inverse remote sensing. Then, Section 2.3 describes an important number of tests performed on vegetation by means of radar measurements in indoor facilities and outdoor controlled environments. The objective of this section, besides completeness, is to justify the use of laboratory experiments for the validation of remote sensing techniques, and, more importantly, to show the originality of the laboratory study carried out in the present thesis. Then, known approaches to the solution of inverse problems about vegetation are shown in Section 2.4. Moreover, this section focuses on techniques, based on SAR data, for retrieving the height of vegetation covers. Finally, a global overview of radar imaging algorithms is outlined in Section 2.5, where the necessity of the new algorithm presented in Chapter 7 is demonstrated.

## 2.1 Radar Polarimetry

Some comprehensive reviews of the history of radar polarimetry can be found elsewhere in the literature [4]-[7]. However, it is worthwhile giving in a few lines some bibliographical references where one can find details about basic radar polarimetry, from the early discoveries to recent developments.

The foundations of polarimetry must be searched for in the nature. Polarization effects are apparent in nature, and there are also many historical examples of the practical utilization of polarization properties of materials. Regarding its application to radar, the early stages began with the development of radar technologies and, to define a date, with the progress that accompanied the World War II. The first work on specific radar polarimetry is attributed to Sinclair [8], after whom the scattering matrix is named. It is known that the information provided by a fully polarimetric radar can be arranged in matrix form. In this way, a single data is a $2 \times 2$ complex scattering matrix (simply named *scattering matrix* or *Sinclair matrix*) whose entries are the measured reflectivities for the four combinations of transmitted-received polarizations in an orthogonal basis. Note that all the matrix definitions and related formulation are explained in Chapter 3. The scattering matrix is somewhat equivalent to the Jones matrix [9], that has been defined for optical problems to characterize transformations of light polarization (see [10, 11]).

Later, an important pioneering work was done by Kennaugh [12], who defined the concept of optimal polarization for a target in the monostatic case, and whose ideas were the basis of further advances throughout the fifties and sixties. From that period it is important to note the works by Rumsey [13] on the study of the transmission between elliptically polarized antennas by making use of the impedance concept that appears in transmission lines; Deschamps [14, 15] on the geometrical representation of polarization on the Poincaré sphere[1]; Kales [16] on the polarization efficiency concept; and Bohnert [17] on experimental issues. There were also some advances in practical applications about the information provided by the scattering matrices. For example, Graves [18] showed that the scattering matrix can be reduced to diagonal form by sub-group transformations, and this eigenanalysis was further employed by Bickel [19]-[21] to define some quantities that entirely specify the scattered return from a body. By using the Poincaré sphere, Copeland [22] demonstrated how to classify a target according to its polarization transforming properties, whereas Lowenschuss [23] postulated that it is possible to distinguish between objects of similar shape by looking at polarization responses.

The next important milestone in radar polarimetry was the work conducted by Huynen [4] on target decomposition theory. His contribution constituted the first attempt of generalization of decomposition techniques and renewed the interest of the remote sensing community on radar polarimetry. The principles of target decomposition theory and a bibliographical review to date are detailed in next section.

---

[1]Note that Poincaré showed that all polarization states can be represented on the Riemann sphere, but this original idea made the following literature to rename the sphere as Poincaré sphere instead of Riemann's one.

More recently, Ioannidis [24] reported a method to use polarization to discriminate between radar targets and background clutter. The importance of polarization in various inverse problems at different frequency bands, and with many applications, was theoretically shown by Boerner *et al.* [25]. Two reviews about polarization diversity in radar were also presented in [26, 27].

The understanding in the variation of the scattering coefficients with polarization increased with the introduction by van Zyl *et al.* [28] of the concept of wave synthesis and a new way to display the polarization dependence of the radar cross section, called polarization signatures. With those ideas, the polarization characteristics of a scene can be synthesized and studied at any possible polarization by only measuring at two orthogonal polarizations. These studies, mainly based on two-dimensional plots, were extensively employed in successive years for analyzing the scattering mechanisms present in natural scenes.

Apart from target decomposition, there have been more recent notable developments in aspects regarding radar polarimetry. Some important workshops focused on polarimetry have been celebrated in last years, where the discussions and contributions from many authors have provided an important advance in this technique (see [29]-[32]). Moreover, two useful books have been published, illustrating the early applications of radar polarimetry to remote sensing of the earth's cover [33, 34], and including theoretical modeling of natural targets, operational aspects of polarimetric SAR's and examples with real data. Finally, it is important to cite contributions from some authors to calibration issues: Wiesbeck [35], Freeman [36]-[38], van Zyl [39], and Sarabandi [40]-[43].

## 2.2   Decomposition Theory

The main objective in radar remote sensing is to extract physical information about any natural target by observing the microwave scattering. Natural targets, like vegetation, are generally random media with surface and volume structures. The interactions of waves with scatterers in a random medium is a complex process that depends on: 1) geometrical attributes of the constituent particles, such as size, shape, and orientation distributions, 2) dielectric properties of the particles, and 3) particle arrangement or target architecture. All three factors are usually grouped in a single term called *dielectric geometry*. Although the physical parameters to be retrieved are usually a few gross indicators, such as vertical height, density or biomass, the scattering observations are sensitive to a much larger number of target attributes. As a result, instead of only obtaining the parameters of interest, all the fine characteristics must be extracted or taken into account. This implies that a large number of radar measurements are needed and, more importantly, that those observations must provide independent information in order to facilitate the inversion procedure.

The ways to increase the number of independent radar observations have evolved with the advances in radar technology. Currently there are three standard approaches for achieving this objective with SAR data: multifrequency, multipolarization and interferometry. For

example, the application of these approaches to the estimation of vegetation height is compared in Section 2.4. In general, the inversion studies that consider observations at different frequency bands (multifrequency) are mainly based on empirical rules and, consequently, are strongly dependent on the site under study and are not easily extrapolated to different scenarios. The same can be stated for the early methods that made use of multipolarization data or SAR interferograms. Those early techniques were based on parameters such as differences or ratios between HH and VV power responses, comparisons between co-polarized and cross-polarized backscatter returns, and the like. However, when fully polarimetric SAR data are acquired, a great step forward can be done by using the polarimetric information in a rigorous way.

As outlined before, the information provided by a fully polarimetric radar can be arranged in matrix form, so a scattering matrix is the smallest information unity. Since the scene often exhibits a natural variability in the scattering properties, an averaging is needed for a correct interpretation of the results. This averaging can be performed in a coherent or incoherent mode. The coherent mode yields an average scattering matrix, whereas the incoherent one results in a Stokes or covariance matrix. Note again that all the formulation is detailed in Chapter 3. At this point, there are two aspects to be highlighted. Firstly, since vegetation has a strongly anisotropic physical structure, it produces changes in the polarization of the scattered fields. These changes depend on the physical attributes outlined above. In second place, there exists a robust and complete mathematical theory for characterizing polarization through the cited matrices and, more importantly, for relating different scattering behaviors to different physical components of vegetation. These ideas form the core of the Target Decomposition (TD) theory. In summary, the aim of TD is to decompose or express such an average matrix into a sum of independent matrices representing independent elements, and to associate a physical mechanism with each element. This decomposition leads to an easier interpretation of the scattering processes and to a simplified approach in the extraction of biophysical parameters of the scene.

The first documented example of such a decomposition appeared in [44], where Chandrasekhar proposed the decomposition of the scattering by a cloud of small anisotropic particles into the sum of a conventional Rayleigh scattering term plus a randomly polarized noise term (due to the particle anisotropy). The generalization of the TD approaches to other scattering problems was addressed later by Huynen [4]. Since then, there has been a great interest in the formulation of TD theorems for establishing a unified scheme of analysis and a complete mathematical description of the problem in order to avoid ambiguities and incoherences between alternative approaches. In this context, Cloude and Pottier [45] published a review which, in the opinion of the present author, is an indispensable reference for understanding the potential and mathematical rigor of these techniques. That review not only classifies the works published to date, but also presents a unified framework using eigenvector analysis, thus providing a rigorous comparison between them. In addition, some forms of the proposed decompositions are applied to the interpretation of important types of backscattering from natural targets.

Following the indications of [45], TD theories can be classified according to the kind of matrix that is effectively decomposed as a sum of matrices, and also to the type of analysis

carried out with the averaged matrices. There are three main groups of TD theories:

- Coherent decomposition theory: a coherently averaged scattering matrix is decomposed as a sum of elementary matrices.

- Huynen type decompositions: a single scattering matrix (plus other secondary terms) is extracted from the Mueller matrix, which is incoherently averaged by definition.

- Eigenvector decomposition of the covariance or coherency matrix (incoherently averaged by definition, too): the eigenanalysis enables the extraction of a set of basis vectors with statistical independence and orthogonality.

There have been many cases of the three classes in the literature, and some hybrid approaches have also been proposed. The main example of the first class, i.e. coherent decomposition, was formulated by Krogager [6, 46, 47]. He postulated the separation of a coherently averaged scattering matrix into a weighted sum of the scattering matrices of a sphere, a diplane and an helix. Note that, as shown in [45], this particular selection of elementary targets entails that the single components of the decomposition are not orthogonal and that the decomposition is not basis invariant. Besides these drawbacks, the key issue of the averaging must be pointed out. The scattered fields from a set of particles, or elementary targets, inside a resolution cell or pixel are added coherently when received by the radar. Hence, the measured signal is the result of the interference between all these fields, producing scintillations and fadings. This phenomenon is known as coherent *speckle*, and must be accounted for when dealing with data from a coherent radar (the physical origin of speckle is described in [48]). To solve this problem, which can be treated as a multiplicative noise, there are a number of techniques available (see for instance [49] for a review on speckle filtering techniques, and [50, 51] for speckle in the specific polarimetric case), but they generally involve an incoherent averaging to arrive at the second order statistics which are needed to represent this type of noise. In conclusion, the TD theories based on coherent averaging of the scattering matrix are exposed to problems due to speckle, so they are not appropriate when applied to radar remote sensing of natural random targets like vegetation. Nonetheless, they are still suitable when the scene is dominated by a single scattering element, or a few of them, and a radar with high resolution is employed (see [6]).

The other two classes of TD theories are based on matrices resulting from an incoherent averaging, thus avoiding the effect of coherent speckle. Huynen type decompositions usually works with the Mueller matrix, whereas the eigenvector decompositions use covariance or coherency matrices. As will be explained in next chapter, there is a direct relation between all three matrices. Therefore, the key difference between these two types of TD is not the matrix to be manipulated (they are equivalent), but the way in that the decomposition is faced. Huynen type theories (for example [44, 4]) attempt the extraction of a single scattering matrix from the averaged data, and the remainder is assigned to a distributed target or a "noise" contribution, but not to other single scattering component. Instead, the goal of the eigenvectors-based TD analyses is to represent the averaged data as a summation of single

scattering mechanisms. The selection of these single scattering mechanisms is based on statistical independence between them. At first sight, the TD based on eigenvector analyses has two fundamental advantages: 1) the eigenvalue problem is basis invariant, and 2) the solution of the problem leads to a diagonalization of the coherency matrix, thus yielding statistical independence between the set of scattering processes.

The development of the last class of TD theories can be considered quite recent, since it started about the middle 1980s. The starting point was a new formalism presented in [52] for describing depolarizing systems. This new formalism consisted in a vectorization of the scattering matrix into a so-called target vector and, depending on the basis of the vectorization, a corresponding coherency matrix (see more details in Chapter 3). This is also the first example where an eigenvector decomposition of the coherency matrix was shown. Although the physical interpretation of this theory was clear since the beginning, its application to remote sensing still took some years. In the meantime, the complete algebraic description of this formalism was rigorously formulated, based on group theory [53, 54], and the TD based on the coherency matrix was demonstrated to be unique [55].

The application of this theory to remote sensing has produced an increasing number of publications and works that deal with this decomposition in rather different ways. Some examples are cited in the following. In [56] the decomposition was tested with a theoretical case of randomly oriented cylinders as a function of their shape ratio, and some multifrequency polarimetric radar measurements from the ocean, a clear cut and a forested area were analyzed to find the dominant scattering mechanisms. The concept of polarization entropy for describing the randomness of the scattering process, that was already briefly introduced in [52], was revisited in [57] and applied to two situations: 1) the theoretical problem of multiple scattering from a cloud of particles in the backscattering direction, as treated by vector radiative transfer [58], and 2) numerical data from rough surfaces. Reference [57] also establishes the interpretation of the parameters that appear when diagonalizing the coherency matrix as a central topic for the applicability of this TD scheme to inverse problems in remote sensing.

The physical interpretation of the coherency or covariance matrix had also been addressed by a particular case of a Huynen type decomposition which was proposed by Freeman [59, 60, 61]. This decomposition, based on the assumption of highly random scenes, separated the covariance matrix into three scattering processes: two single scattering mechanisms (for slightly rough surfaces and dihedral scattering respectively), and a random scattering process with no single scattering matrix representation. It was demonstrated in [45] that it is not applicable to a wide range of scattering problems. However, when applied to some observations of mature forests it has been quite useful for discrimination and classification purposes.

Turning back to the interpretation of the different parameters that appear when the eigenvector decomposition is performed, besides entropy, two new parameters with a physical meaning were defined later in [62]: an angle related to the type of scattering mechanism (alpha), and an orientation angle of a canonical target that represents the scattering mechanism (beta). Moreover, [62] presents a classification scheme for polarimetric SAR images

based on the combination of entropy and alpha. These concepts will be further described in Chapter 3. An additional parameter, called anisotropy, was proposed in [63] in order to form, together with entropy and alpha, a useful feature vector (set of parameters) for training of neural networks used in image classification. In a similar way, reference [64] presents a classification procedure based on the eigenvalue spectrum measured at different frequency bands. The main advantage of polarimetry for constructing classification schemes is that no a priori knowledge about the scene is required because the observables have an intrinsic physical meaning. This fact makes polarimetric data ideal for unsupervised classification, as firstly attempted by van Zyl [65].

The application of radar polarimetry to inverse problems in remote sensing is still in its infancy, and many issues that have not been completely solved so far by traditional techniques are now incorporating the polarimetric analysis into their formulations. A first example is a recently developed method for remotely measuring topography and terrain azimuthal slopes by the sole use of polarimetric images [66]. This original idea is currently being extended to the estimation of the slope in the ground-range direction as well [63]. The remote extraction of vegetation attributes, like the shape and orientation distribution of the elementary components (i.e., leaves and small branches), is a new example of the contribution of polarimetry in inverse problems (see Chapter 5). Another case where polarimetry has drastically improved the performance of other SAR techniques is its application to interferometry. The selection of an appropriate pair of scattering mechanisms to form the interferogram between two polarimetric images enables the optimization of the interferometric coherence [67, 68, 69]. In addition, the optimization algorithm has been used for retrieving the height of vegetation covers, as will be cited in Section 2.4. The experimental validation of this estimation technique constitutes one of the objectives of the present thesis (see Chapter 6).

## 2.3   Laboratory Measurements on Vegetation

The first detailed laboratory radar measurement from a vegetation sample was presented in [70]. The experiment was performed on a solitary fir tree by means of a high-resolution pulsed coherent radar working at X band. The main aim of the experiment was to identify the scattering centers of the tree. The results indicated that the green outside branches were the major sources of scattering at this band, and a significant difference in cross-section and attenuation was found between the green and the dry branches, being higher for the green ones, as expected. Other quantitative conclusions were obtained, but it is important to note that the data were based on single measurements, and they were not averaged over an ensemble of statistical data. The success of this early experiment entailed a great campaign of radar measurements on vegetation in laboratory or controlled-environment conditions. Successive investigations have shown that both attenuation and backscattering are strongly dependent on the sample structure, including the size, shape and orientation of the components (trunk, branches and leaves). These studies in controlled environments have been traditionally aimed to two different vegetation covers: crops and trees. Next, some of those experiments are

explained focusing on: analysis methods, characteristics of the radar (frequency band and polarization), and main conclusions of each one.

The study of crops was originally designed for searching relations between microwave backscattering and physical parameters of the crop. The latter were usually employed in models for inferring the yields. A relation between the leaf area index (LAI) and the backscattering coefficient ($\sigma_0$) was found in [71] for crops of corn, sorghum and wheat. The LAI determines the solar radiation intercepted by the plants in an active way, so it is of prime importance for estimating the yields. The microwave backscattering was measured at different frequencies (8 to 36 GHz), and the green leaves were shown to determine the major contribution to the total backscattering when the plants were mature. Instead, during the early stage of growth the soil backscattering was also high, so it was difficult to separate both contributions if no information about the stage of growth was available. The difficulties of determining the physical properties of crops by means of backscattering coefficients were also shown in [72]. That study presented results from crops of soybean, corn and wheat, obtained with passive and active microwave sensors at C band. The main findings were the different attenuations for different corn types, or even for the same type but with different plant densities, and the importance of knowing the look direction relative to the row direction (i.e. the observation geometry). Reference [73] presented an interesting study on the sources of scattering of corn and milo crops at X band. The experiments were conducted with a high-resolution radar for VV polarization, and two incidence angles were selected: $0°$ (vertical) and $30°$. In order to identify the sources of scattering and quantify the attenuation of each component of the plants, a defoliation scheme was performed, and profiles of the RCS were plotted as a function of height before and after the successive defoliations. By doing that, it was found that the top leaves of a corn plant are almost isotropic scatterers and constitute the strongest sources of backscattering for full-grown corns. For the milo plants, the main finding was that their head usually suffers of wind displacements, thus producing fadings in backscattering. For both species, the attenuation of each layer was successfully measured by looking at the relative level of the ground reflection peaks. Those studies were extended in [74] following two lines: 1) a greater coverage of wavelength, incidence and polarization, and 2) measurements of the phase difference between HH and VV. The experiments were performed with mature corn fields at L, C and X band, with a defoliation procedure, too. The main conclusions were the differences in attenuation between HH and VV due to the maize vertical stalks, and its dependence on the frequency band. It was also demonstrated that for X band the coherent interaction between elements must be taken into account in the interpretation of measurements.

In the case of trees, the vast variety of species with different morphologies has produced an even higher number of experiments. An ingenious approach to laboratory measurements on trees was presented in [75]. In this work, an L band microwave scatterometer was employed for characterizing the backscattering from coniferous trees (a spruce tree and a Weymouth pine) and deciduous trees (a walnut tree). This research is somewhat complementary to [70], that was performed at X band instead of L band, but also includes an ensemble averaging to account for the statistical variability of vegetation. The backscattering analyses of these trees gave the following conclusions: 1) the dominant scattering centers

at L band for coniferous trees are the outside green branches coated with needles, regardless of the polarization, 2) the attenuation in coniferous trees is greater for horizontal polarization than for vertical polarization at L band, 3) for the deciduous case, deeper tree components (such as branches, twigs, and nodes where the branches connect to the trunk) show a higher RCS at L band than the leaf crowns of the trees, and 4) these leaves of the tree's crown only cause some attenuation, but their contribution to the backscattering is negligible. On the other hand, a polarization dependence study was also carried out, leading to important results. The experimental procedure consisted of like-polarization measurements as a function of the polarization angle, from $0°$ (vertical) to $90°$ (horizontal). The look direction was always horizontal, and the experiments were repeated for two cases: illuminating the tree with the trunk in the line of sight, and illuminating the tree avoiding the face of the trunk. The curves of backscattering versus the polarization angle showed clear differences between tree types, some trees exhibited peaks at certain polarizations depending on the orientation of the branches, and asymmetries arose in correspondence to their morphology. Therefore, this research supported the hypothesis that, at L band, a radar can work as a shape filter. However, at the same time, it demonstrated that the classical polarization combinations (HH,VV and HV powers) are insufficient to successfully characterize vegetation because it is a very complex medium.

Other experiments on trees and forest components are described in the following. In [76], the same fine-resolution scatterometer used in [73] was employed for identifying the major scattering sources in a few kinds of trees and shrubs at X band. This work was concentrated in the branches, that were illuminated obliquely to avoid the response of the trunk. For pine trees, the needles were confirmed to cause the strongest backscatter and attenuation, whereas the cones only contribute slightly to backscatter. For the rest of trees, the leaves were also the main contributors to backscattering, and only when they are not present, the fruits affect the total backscatter if they are packed in clusters. It was also shown that thick stems scatter more than the thin ones, due to their size and water content. Moreover, the authors noted that some particular elements of the tree structure occasionally exhibit a high radar response if their size is comparable to the wavelength. Later, an additional work was published on the same data but with a different objective [77]: the extraction of the volume backscatter coefficient and the volume extinction coefficient. The work presented in [76] for X band, was repeated for C band in [78]. It was shown that petioles and stems are much more important than leaves for depolarization at C band, and that the scattering at this band cannot be assumed to be simply due to leaf scattering, since the shape, size, moisture content and relative location of branches play an important role. Another related experiment was described in [79, 80], where small Japanese conifers were grouped in extended targets and measured at S, C and X band. In this case, independent samples were obtained by rotating the target, and the experiments were repeated after defoliation. The authors analyzed: 1) differences between HH and VV, 2) levels of the like backscatters of the three conifers, and 3) depolarization. They showed that at S and C band the RCS changed little at all polarizations with and without leaves, so the backscatter originated from branches and trunks even when the leaves were present. Moreover, the presence of needle-like leaves in Japanese conifers introduced a substantial amount of depolarization only at X band. Another interesting research was conducted in [81] at C band on a peach orchard. That study attempted the characteri-

zation of the canopy with slant range profiles, showing different extinction coefficients for different polarizations.

An additional step forward was accomplished in [82] by introducing an artificial target for determining the response of trees to some important parameters. Clearly, the physical model cannot be taken as a direct analog of the field vegetation, though it resembled the field forest structure in some important aspects. Rather, they used the model to improve the understanding of the contribution of individual structural elements to microwave backscatter. The measurements were performed at C band with a multi-polarization radar. The physical parameters that showed the highest influence upon the radar signal were: forest leaf and branch surface area, total tree biomass, and water content. In fact, the surface area of leaves plays a greater role than leaf mass "per se". Although stems represented the largest biomass contribution, dry branches had considerable effect in the backscattering, probably due to their dispersed arrangement. A similar approach was used later in [83] with an small artificial target that was measured at C and X band. In this second case, two properties of tree backscatter were investigated: azimuthal variation and polarization dependence, both with and without leaves for simulating the tree in summer and winter. The authors found that the signal faded with an exponential distribution when rotating in azimuth, and no angular trend was apparent. They also concluded that the radar backscatter was always a strong function of the polarization angle of the transmitted signal with respect to the orientation of branches and leaves at C band, but not at X band when leaves were present.

In the 1980s examples of scatterometric measurements from well defined areas also exist, but carried out from aeroplanes [84, 85] and helicopters [86]. In [84], vertical profiles of attenuation and backscattering were retrieved from forest stands at L, C and X band. The attenuation at X band was measured by placing corner reflectors on the ground below the forest canopies. It was shown that the attenuation is determined by the canopy architecture and observation geometry. However, it was found that the attenuation from crowns in both deciduous and coniferous trees was high. At L and C band, and incidence angles close to the vertical, most of the backscatter comes from the ground, so vegetation is more transparent at these wavelengths. A similar study was performed in [87] at L band, showing that a very dense and compact pine canopy is a nearly isotropic medium. Special mention is required of [85], where L band polarimetric SAR data were analyzed by looking at the phase difference between HH and VV polarizations. The mean of this phase difference was found to be zero for bare soil and short agricultural vegetation, but corn fields exhibited a dependence on the incidence angle. This dependence was justified and successfully modeled as the combination of propagation delay, direct scatter by the soil surface and specular bistatic reflection by the stalks. Hence, phase information showed to be useful in image interpretation and classification, a role previously reserved to the modulus of the backscattering coefficients.

As explained above, the development of physically justified theoretical models of vegetation is a main goal of these laboratory experiments. An important feature of the models is the characterization of every individual component of the vegetation architecture: leaves, branches, stems, trunks, etc. Therefore, many experiments have been conducted for measuring the individual responses of those single scatterers. One of the first examples was [88, 89], where a leaf was measured at X band and a mathematical model was developed for estimat-

ing its RCS, including the effects of the curvature of the leaf. Another early example was presented in [90], where measurements at X band with circularly polarized signals were carried out on a leaf and a branch. Those measurements helped to validate the equivalent models of the targets: a small disk for the leaf, and a finite dielectric cylinder for the branch. Another detailed example of this type of measurement was presented in [91, 92]. X band experiments were undertaken on elementary components of cylindrical shape, and were combined with simulations. The measured scatterers were bare twigs and needles, and leafy twigs from different coniferous species. Bare twigs with electrically small radii exhibited anisotropy in the attenuation (differences between polarizations), and a linear relation between the attenuation and the water content was demonstrated. On the other hand, the polarization behaviors of attenuation due to leafy twigs are correlated to the general orientation distribution of the needles.

Two other interesting laboratory tests have been published more recently. In the first [93], some groups of small balsam fir trees with different selected densities were analyzed at C band. An absorber layer was positioned under the trees for avoiding soil background effects in the results. Again, it was found that the main contribution to backscattering at this band comes from the branches, whereas the effect of the needles is negligible. This result was shown to be independent of the canopy density and the signal polarization. The second recent example [94] was performed at X band on conifers. There, the main scatterers were identified by means of range profiles of the RCS along the horizontal direction in the HH and VV polarizations, and also their contribution to the final RCS was quantified. It was found that the main scatterers are the leafy branches, and the difference between VV and HH is significant only in the upper portion of the tree, due to the simpler structure of the tree in this part. Moreover, the angular trends of both VV and HH are different, and it was demonstrated that these depend on the branch orientation distributions, i.e. the tree architecture. Moreover, the penetration depth at X band was quantified, always being very low: between 50 cm and 1 m.

With the progress in radar technologies and imaging algorithms, a new method of analysis of laboratory measurements on vegetation has been developed in recent dates. It consists of high resolution radar images of the vegetation samples in two and three dimensions. Two examples are described here. The first one [95] was carried out at X band on small, almost defoliated deciduous trees. High resolution 2-D images were computed by using a planar synthetic aperture, and covering the target with two sheets of polystyrene in a "sandwich" configuration. The main conclusions were: 1) those branches (or portions of them) that are dead do not appear in the images due to their low reflectivity, 2) some multiple reflections between adjacent branches were present, 3) all the leaf clusters are well seen in the images for all polarizations, and 4) some parts of the trees do not appear in the cross-polar images although they have similar orientations to those others that do appear (this fact was not justified in the paper). The second example of imaging results was carried out in the European Signature Microwave Laboratory, and constitutes one of the starting points of the analysis presented in Section 4.4. The experiment consisted of high resolution 3-D images of a big fir tree [96]. The frequency bandwidth was 1 to 5.5 GHz, thus covering L to C band and ensuring a large amount of penetration into the tree. In agreement with previous

experiments, it was shown that the main scatterers are the leafy branches and the difference between VV and HH is significant only in the upper portion of the tree (produced by the simpler structure of the tree in this part). The rest of the tree is viewed equally for HH, VV and HV polarizations due to the randomness.

From all those experimental approaches to vegetation analysis in laboratory conditions, one can conclude that many different techniques have been proposed for characterizing the response of vegetation to microwaves, but two main drawbacks are evident: 1) most of the experiments have been performed only in some part of the microwave spectrum, not allowing a direct comparison between different bands, 2) with respect to polarization responses, all the experiments carried out so far have made use of power responses at each polarization combination (HH, VV and HV), but a joint analysis of the full polarimetric information is missing. These are main short falls that the present thesis tries to fill in. Chapter 4 will present the first results in the literature obtained with decomposition techniques in laboratory conditions, thus accounting for full polarimetric information. In addition, a complete analysis is carried out at all microwave bands (L, S, C and X), with a free selection of the incidence angle and resolution. As stated in the Introduction, decomposition theory is applied to three types of data that were obtained with different techniques that have already been used by other authors: 1) scatterometric data, 2) one-dimension profiles, and 3) high-resolution radar images in two and three dimensions. As expected, some of the findings already stated in previous research will be confirmed by this study, but various new contributions are also illustrated. To take two examples, the propagation or attenuation properties between any orthogonal polarizations (differential extinction coefficients), and the spatial maps with the scattering behavior of every part of the plants.

## 2.4   Approaches to Inverse Problems on Vegetation

The retrieval of biophysical parameters from SAR data is a topic with more than thirty years of history. A short, but clear and well-oriented, review of the goals already achieved and the remaining challenges in this subject can be found in [97]. In the case of vegetation, there have been developments in direct and inverse problems since 1970. The direct problem consists of modeling of the scattering of vegetation by means of numerical or theoretical methods. These methods employ some knowledge about the physical attributes of the vegetation target for predicting the magnitude of the scattering when an incident field is present. In this way, the model must know two kinds of inputs for computing the scattering output: 1) physical features of the plants (shape, dimensions and orientations distribution of the particles, density of plants, soil moisture, etc.), and 2) characteristics of the incident signal (frequency, incidence angle, etc). The inverse problem is just the retrieval or estimation of physical parameters of interest by using radar measurements as inputs. Therefore, most inverse algorithms are based on a previously developed model for the vegetation cover under study.

Making a bibliographical review of all the electromagnetic models for vegetation that

have appeared in the literature could be an almost endless task, but some helpful indications are stated in the following. There are two general kinds of approach in the construction of vegetation models, namely incoherent and coherent. Incoherent approaches are based on radiative transfer theory [98], and are the most widely used ones. To give a known example, the most popular canopy model, MIMICS [99], is based on this theory. Radiative transfer can accurately predict the second moments of the radar backscatter statistics when the medium consists of sparse scatterers that are small compared to the field correlation length within the random medium. Unfortunately, this approach has two important shortcomings: 1) no information about the absolute phase of the scattered field can be extracted and, consequently, it is useless when an interferometric analysis is attempted; and 2) this theory does not account for the coherent effects that may exist between different scatterers. The second drawback is determinant when working with trees and other types of vegetation since, as it has been experimentally demonstrated in Section 2.3, both backscattering and attenuation are significantly influenced by the morphology of the plants.

Some vegetation models based on coherent approaches have been developed in the last decades. They can be grouped into two global types. The models of the first type consider the structure of vegetation from a statistical point of view. Therefore, although taking into account the coherent behavior of the interaction between scatterers, they only provide the second moments of the scattered fields, thus losing the information about the absolute phase. Several remarkable examples of this type of models are [100]-[102]. In [100], the distorted Born approximation is used to find the mean field illuminating each scatterer, and the backscattered fields are added coherently. A two-scale cylinder cluster is used for a branching model to characterize soybean plants in [101]. In a similar way, a coherent model for cultural grass canopies was described in [102]. On the other hand, the second type of coherent approaches deals with the exact structure of a vegetation sample (a tree or a plant) in order to provide the backscattered field with no statistical description. A good example of this practice was presented in [103], where a tree structure was constructed by a direct survey of its architecture: lengths of trunk, branches and leaves, with their positions and orientation angles. More recently, a sophisticated coherent scattering model based on fractal-generated trees has been successfully used for modeling a deciduous forest stand [104].

The next part of this section is dedicated to describing methods used so far in inverse problems on vegetation. As stated above, the construction of accurate models for describing the scattering from vegetation is a complex process that depends on many parameters. Therefore, if these models are intended to be applied in the construction of inverse techniques, they must be simplified to models with as few input parameters as possible, so that the inversion becomes tractable. This simplification is usually carried out by fitting polynomials or simple curves to plots that relate output data (experimentally measured or provided by simulations with a model) to the parameters of interest (physical attributes). Once this simplification is achieved, the inverse problem must be solved by an optimization technique that yields the combination of values of the physical attributes that best fit to the input data. Depending on the complexity of the data and the selected model, and on the dimension of the parameter space (the number of them), the optimization is more or less easy to perform.

Recent examples exist in the literature that face the solution of inverse problems on

vegetation with many free parameters. A relevant example is presented in [105, 106], where neural networks are used in the inversion process. That study examines two cases: first, a neural network is trained by using data produced by a direct model (MIMICS) and then solves the inverse problem as usual; second, the neural network is trained without any model, thus only using experimental data. Results were obtained for the estimation of trunk density, average trunk diameter and average trunk height, in aspen and loblolly pine stands. Input parameters were backscattering coefficients (VV, HH and HV) at L and C bands. This method is computationally intensive, and its success is limited by the extent (in the experiment-trained case) and fidelity (in the model-trained case) of the training data. The neural network has great flexibility and can provide good results, but, in most cases, is used essentially as a black box. This means that there is no way currently known to discern the underlying physical processes that give rise to a determined network behavior. Alternatively, an iterative gradient-based search routine was used in [107]. In this new case the behavior of the algorithm is derived from the physical scattering mechanisms existing within the system, and it is also possible to monitor the decision path taken by the algorithm, thus giving a control over the reliability of the achievable results. Nevertheless, its applicability is limited to systems with small dimensionality and, due to its model dependence, its success is subject to the fidelity of the direct model. Finally, a promising new approach has been formulated in [108], based on genetic algorithms for the solution of the inversion system. This method has been successfully tested on the simultaneous inversion of tree height, trunk diameter, tree density, branching angle, soil moisture and vegetation moisture over a test stand of red pine forests. The input parameters were the backscattering coefficients at one polarization for C band from two different incidence angles, and the interferometric phase centers obtained at these angles at C band.

Leaving apart these complicated methods which attempt the solution of inverse problems with some output parameters, there have been many examples in the literature of inversion algorithms specifically devoted to the extraction of a single parameter of interest. The particular case of the retrieval of vegetation height and biomass is historically reviewed in the next paragraphs. These parameters have been chosen because they are very correlated in general. They also exhibit clear relationships with other parameters of interest (such as timber volume, bassal area, etc.). A lot of effort has been devoted to their retrieval in the scientific community since the early 1990s. Biomass is related to the height of the trees or plants by means of allometric equations and growth models. Another important application of the vegetation height estimation is the remote monitoring of crops at large scale, such as rice and corn, that are fundamental for the world economy and food resources.

In the case of short agricultural vegetation, some promising results have been obtained by only using the backscattering coefficient ($\sigma_0$) at a single frequency band. For example, ERS-1 C band SAR data were successfully used in [109, 110] for monitoring the growth of rice crops, where a simple model was used for relating $\sigma_0$ to the growth stage of the crops. Other more sophisticated forward models have been developed to consider some additional features that are important in these vegetation layers, like the coherent scattering effects due to the row structure in agricultural fields and the non-randomness of the stems arrangement [102, 111].

When dealing with forest canopies, there are new aspects that must be addressed. For example it has been shown in [112]-[115] that the radar backscatter intensity increase approximately regularly with increasing biomass until it saturates at a biomass level that depends on the radar frequency. At low frequencies the penetration into the vegetation is high and, as a result, the sensitivity to biomass changes presents a high dynamic range without saturation. In fact, recent results at VHF have provided better results than those achieved with a conventional SAR at microwave frequencies [116]. It has been also observed that cross-polarized backscatter intensities give better sensitivities than the co-polarized ones.

The common point of all those studies is that the inversion procedure is performed by using $\sigma_0$ as input. As explained in [117], this parameter has an essential drawback: at short wavelengths the penetration is limited and therefore the inversion techniques lose sensitivity, and at long wavelengths the penetration is high but there are three main aspects that make it ambiguous: 1) the sensitivity of $\sigma_0$ depends on the relative level of the ground backscatter compared to the canopy backscatter, 2) the size of the branches is comparable to the wavelength and the consequent interactions (and possible resonances) make the relation between biomass and $\sigma_0$ non-regular, and 3) there is interaction between the canopy scatterers and the ground, thus producing a final signal too complex to be analyzed by only employing simple relations.

As is already clear at this point, the interaction of electromagnetic fields with vegetation targets is a complex process. As a result, any inverse algorithm for estimating one, or more, physical parameters should be provided with many independent and meaningful inputs. To achieve this, frequency and/or polarization diversity and interferometry are usually employed. The use of frequency diversity in this application is limited by the saturation described above. On the other hand, if the frequencies are not very separated, frequency diversity is equivalent to interferometry. For instance, in [118] a theoretical study for the estimation of vegetation height makes use of the equivalence between a $\Delta k$–radar (frequency diversity) and interferometry. This study is based on the properties of the frequency correlation function [119], which has also been successfully applied to the estimation of height of grass layers in a controlled environment [120].

Some approaches for retrieving biomass and canopy height based on SAR interferometry (InSAR) have been applied recently. The interferometric applications originate from two observables that interferometry gives as outputs: coherence and interferometric effective phase center. It is known that the interferometric coherence decreases with increasing volume scattering and with temporal changes [121]. Therefore, the coherence can be used to identify zones covered by forests. It has been used in [122, 123] for classification purposes together with the backscatter intensity because the interferometric information is in most cases independent of the intensity information. The interferometric coherence has also been related to crop heights in [124] by means of linear relations, which can be useful in monitoring applications. Moreover, the effective phase centers obtained by SAR interferometry have been used in [125, 126] for inverting the height of forest canopies. In order to do that, the interferometric information must be combined with a precise available DEM, or alternatively two interferograms at different frequencies should be combined (for example at C and P band, since the latter penetrates more the canopy). The main advantage of interferome-

try is that the results depend mainly on the geometry of the target (i.e. on the morphology, structural components and dimensions).

Another interesting example of a combination of interferometric information (phase center and coherence) with backscattered power in order to invert characteristics of a layer of vegetation and the underlying topography was presented in [127]. This paper makes a thorough analysis of the sensitivity of the proposed observables on the parameters of the scene and on the radar characteristics. Derivations are based on a simplified scattering model, but it is enough to demonstrate the performance of this approach.

As outlined above, the first inversion methods based on InSAR estimated the canopy height by comparing the interferometric phase centers in presence of vegetation with a previously known DEM of the area. Thus, the inverted height depends on the availability of a precise DEM of the area of interest. An efficient way to circumvent this problem is the use of polarimetry. Polarimetry enables the generation of simultaneous intereferograms of the same scene by selecting various scattering mechanisms. If those scattering mechanisms are associated with different layers that constitute the vegetation volume, the relative height difference between them should be closely related to the height of the plants. A more detailed justification of this approach and the first examples appeared in the literature are described in Chapter 6. At the time this part of the thesis was originally written, the first results of this technique that had been successfully compared with ground truth data were those presented in this thesis.

## 2.5   SAR Imaging Algorithms

The practical problem motivating this part of the thesis is the formation of near-field 3-D ISAR images of vegetation samples in the EMSL. The final objective, as explained in the Introduction, is to identify the scattering centers within the sample volume and to quantify their polarimetric contribution by means of decomposition techniques. Therefore, it is important to develop an efficient 3-D ISAR algorithm adapted to the EMSL measurement set-up.

SAR is a well developed technique for producing high resolution images [128]-[130]. There is a wide variety of imaging algorithms that have been used to reconstruct reflectivity images of a scene by using SAR techniques. A 2-D reflectivity image can be formed by synthesizing an 1-D aperture with a wide-band radar. Accordingly, a 3-D reflectivity image is formed by synthesizing a 2-D aperture. As an example, typical geometries of the 2-D apertures that can be synthesized in an anechoic chamber are planar, spherical and cylindrical. More precisely, 3-D ISAR images can be obtained by coherently processing the backscattered fields as a function of the frequency and two rotation angles about axes which are mutually orthogonal.

When the radar is within the far-field zone of the target, the illuminating wavefront can be considered to be plane and, hence, the processing reduces to an interpolation plus

a 3-D inverse discrete Fourier transform (DFT) [131]. However, if the radar is located in the near-field region, the planar wavefront assumption is not longer valid, and the fast, and straightforward, Fourier processing cannot be used in the image reconstruction. Unfortunately, the latter is the situation at the EMSL. Near-field ISAR imaging of large objects by a direct Fourier inversion yields images which are increasingly unfocused at points which are more distant from the center of rotation [128], or even images with scattering points misplaced from their true position.

Attending to the working principle of the existing radar imaging algorithms, a general classification is the following [129]:

**Polar Format Algorithm, PFA** : This algorithm, also known as *Range-Doppler*, was the first one to be developed and originates from optical signal processing. It is based on the polar nature of the frequency domain backscatter data, works with motion compensation to a point and as such needs to be used under the far field condition, requires an interpolation prior to the Fourier transform, and compensates only partially the range curvature. Both the 2-D and 3-D versions of this algorithm are of easy implementation and have been used extensively.

**Range Migration Algorithm, RMA** : This algorithm originates from seismic engineering and Geophysics, and is known in its 2-D version as $\omega - k$ algorithm [132]. It works with motion compensation to a line, requires an one-dimensional (1-D) interpolation (known as Stolt interpolation [133]) and compensates completely the curvature of the wavefront. In the radar remote sensing domain it has only been used in its 2-D version. This thesis presents the first attempt known to the author to formulate its 3-D version using a 2-D planar synthetic aperture. The RMA was firstly introduced to focus 2-D SAR data acquired from a spaceborne platform in the strip map mode. Later it was adapted to be used in the spotlight mode [134]-[136]. Results showing that the RMA can also focus 2-D SAR data acquired in an anechoic chamber using the strip map mode are reported in [137]. Both the 2-D and 3-D versions of the RMA basically require a 1-D interpolator and Fast Fourier Transform (FFT) codes. As a result, their implementation on a massively parallel supercomputer becomes fairly straightforward [138].

**Chirp Scaling Algorithm, CSA** : It has the unique characteristic of not requiring any interpolation [139]. It works with motion compensation to a line and corrects approximately the range curvature. It is widely used to focus 2-D space- and air-borne SAR data sets.

All three types of SAR imaging algorithms are quite efficient because their implementation is mostly based on FFT's, thus speeding up the computation time. Nevertheless, their applicability to near-field ISAR configurations is limited by the correction of the wavefront curvature, that is accounted for in a exact manner only by the RMA. Consequently,

selecting the RMA for approaching the construction of an efficient near-field 3-D ISAR algorithm seems the best option[2].

Examples of 2-D and 3-D ISAR algorithms that implement the near field correction are presented in [140]-[143]. The principle of these algorithms is different from the conventional algorithms cited so far. These algorithms are based on an 1-D azimuth convolution between a near-field focusing function and the frequency domain backscatter data, which precisely accounts for the wavefront curvature and the free space propagation losses. This azimuth convolution is efficiently implemented by using FFT's techniques. However, to get the complex radar reflectivity of a voxel in a 3-D image, two more integrations over the frequency and the incidence angle in elevation are required. These integrations cannot be implemented with FFT's and therefore the algorithm becomes very demanding from the computational viewpoint.

This thesis will present a 3-D version of the RMA algorithm. Firstly, the 2-D synthetic aperture is assumed to be planar and within the near-field zone of the target. As an input, the algorithm requires frequency domain backscatter data which can be acquired using a stepped frequency radar. Thus, resolution in the vertical and horizontal cross-range directions are given by the dimensions of the synthetic aperture, whereas resolution in ground-range is provided by the synthesized frequency bandwidth. The frequency domain data is preferred because the RMA algorithm works in the frequency wavenumber domain. Note that the focusing of time domain data sets acquired with a pulsed system would become straightforward by simply applying a Fourier transform. Secondly, an extension of the algorithm to cylindrical and spherical scanning geometries (the usual ones at EMSL) will be formulated and implemented by means of spectral translations to reduce the problem to the planar-aperture case.

Finally, note that the measurements are supposed to be fully controlled and therefore factors such as irregular sample spacing, platform position errors and mitigation of RFI have not been investigated.

---

[2]Note that the PFA cannot be used when the backscatter data are acquired on a planar aperture

# Theory of Radar Polarimetry

T HE purpose of this chapter is the definition of the basic concepts that will be used throughout the thesis. All the definitions and formulae present in this chapter can be found spread in many bibliographical references, so it seems necessary to group them here to make the text self-contained. Furthermore, due to the use of different conventions in the literature, there are sometimes confusions that can be avoided by clearly stating all the definitions in the first part of the text.

This chapter is organized in three sections. Section 3.1 presents the basic formulation of electromagnetic problems and the polarization description of a wave. Then, the matrix formulation of the polarization characteristics of a target is detailed in Section 3.2, where all the conventionally used matrices are defined, and the relationships between them are stated. Finally, the target decomposition theory is explained in Section 3.3. As it was justified in Chapter 2, this section will be mainly devoted to the eigenvector decomposition of the coherency matrix. All details of this decomposition are explained, since it is of prime importance for understanding the rest of the thesis.

## 3.1 Wave Polarization

### 3.1.1 Maxwell's Equations

The fundamental laws that govern all aspects of electromagnetism, including wave generation, propagation and interaction with matter, are Maxwell's equations. At any point in time $t$ and position $\mathbf{r}$, which is a vector defined with respect a specified coordinate system, Maxwell's equations establish the relations that the electric and magnetic fields, $\mathbf{E}(\mathbf{r}, t)$ and $\mathbf{H}(\mathbf{r}, t)$, and the magnetic flux density and electric displacement, $\mathbf{B}(\mathbf{r}, t)$ and $\mathbf{D}(\mathbf{r}, t)$, must

satisfy:

$$\nabla \times \mathbf{E}(\mathbf{r}, t) = -\frac{\partial \mathbf{B}(\mathbf{r}, t)}{\partial t} \tag{3.1}$$

$$\nabla \times \mathbf{H}(\mathbf{r}, t) = \mathbf{J}(\mathbf{r}, t) + \frac{\partial \mathbf{D}(\mathbf{r}, t)}{\partial t} \tag{3.2}$$

$$\nabla \cdot \mathbf{D}(\mathbf{r}, t) = \rho(\mathbf{r}, t) \tag{3.3}$$

$$\nabla \cdot \mathbf{B}(\mathbf{r}, t) = 0 \,, \tag{3.4}$$

where $\mathbf{J}(\mathbf{r}, t)$ and $\rho(\mathbf{r}, t)$ are the current and charge densities associated with free charges at the point and time under consideration[1].

Maxwell's equations are complemented by the law of conservation of charge

$$\nabla \cdot \mathbf{J}(\mathbf{r}, t) + \frac{\partial \rho(\mathbf{r}, t)}{\partial t} = 0, \tag{3.5}$$

and a set of constitutive relations with physical characteristics of the medium:

$$\mathbf{D}(\mathbf{r}, t) = \epsilon' \mathbf{E}(\mathbf{r}, t) \tag{3.6}$$

$$\mathbf{B}(\mathbf{r}, t) = \mu \mathbf{H}(\mathbf{r}, t) \tag{3.7}$$

$$\mathbf{J}(\mathbf{r}, t) = \sigma \mathbf{E}(\mathbf{r}, t) \tag{3.8}$$

where $\epsilon'$, $\mu$ and $\sigma$ are the permittivity, permeability and conductivity of the medium, respectively. A non dispersive medium has been assumed for simplicity.

In the following, we will assume an harmonic time dependence of the form $e^{j\omega t}$ for all fields. Then, for convenience, the electric field can be obtained at a specific time and at specific point in space by means of the following expression:

$$\mathbf{E}(\mathbf{r}, t) = \Re\left(\mathbf{E}(\mathbf{r})e^{j\omega t}\right), \tag{3.9}$$

where $\mathbf{E}(\mathbf{r})$ is a function of $\mathbf{r}$ only, and $\Re$ denotes the real part of the complex argument. The angular frequency has been denoted by $\omega$ which relates to the frequency by $\omega = 2\pi f$.

Substitution of the harmonic time dependence and the constitutive relations in Maxwell's equations yields:

$$\nabla \times \mathbf{E}(\mathbf{r}, t) = -j\omega\mu \mathbf{H}(\mathbf{r}, t) \tag{3.10}$$

$$\nabla \cdot \mathbf{E}(\mathbf{r}, t) = \rho(\mathbf{r}, t)/\epsilon' \tag{3.11}$$

$$\nabla \times \mathbf{H}(\mathbf{r}, t) = (\sigma + j\omega\epsilon') \mathbf{E}(\mathbf{r}, t) \tag{3.12}$$

$$\nabla \cdot \mathbf{H}(\mathbf{r}, t) = 0. \tag{3.13}$$

It is often convenient to write (3.12) in the form

$$\nabla \times \mathbf{H}(\mathbf{r}, t) = j\omega\epsilon_r\epsilon_0 \mathbf{E}(\mathbf{r}, t), \tag{3.14}$$

---

[1]The notation convention is: *bold letters* for vectors (i.e. $\mathbf{v}$) and *uppercase letters between brackets* for matrices (i.e. $[M]$).

where

$$\epsilon_r = \frac{\epsilon'}{\epsilon_0} - j\frac{\sigma}{\omega\epsilon_0} = \epsilon'_r + j\epsilon''_r \tag{3.15}$$

is the complex relative dielectric constant of the medium ($\epsilon'_r$ and $\epsilon''_r$ are real numbers), and $\epsilon_0$ is the permittivity of free space.

### 3.1.2 Solution of the Wave Equation

In a source-free, isotropic, lossless homogeneous medium, Maxwell's equations can be combined to obtain the *wave equation*, which dictates the form of the electric field:

$$\nabla^2 \mathbf{E}(\mathbf{r}, t) + k^2 \mathbf{E}(\mathbf{r}, t) = 0 \tag{3.16}$$

where

$$k = \omega\sqrt{\mu\epsilon'} = \omega/c \tag{3.17}$$

is the wave number, and $c$ is the velocity of electromagnetic propagation.

A general solution that satisifies (3.16) is the following:

$$\mathbf{E}(\mathbf{r}) = \mathbf{E}\, e^{-j\mathbf{k}\cdot\mathbf{r}} = \mathbf{E}\, e^{-jk\hat{\mathbf{k}}\cdot\mathbf{r}}, \tag{3.18}$$

which is a plane wave propagating in the direction of $\mathbf{k}$. The magnitude of $\mathbf{k}$ is the wave number $k$, so the direction of propagation is completely defined by the unit vector $\hat{\mathbf{k}} = \mathbf{k}/k$.

The magnetic field is provided by (3.10), and has a similar solution:

$$\mathbf{H}(\mathbf{r}) = \mathbf{H}\, e^{-jk\hat{\mathbf{k}}\cdot\mathbf{r}}, \tag{3.19}$$

with

$$\mathbf{H} = \frac{1}{\eta}\,\hat{\mathbf{k}} \times \mathbf{E}, \tag{3.20}$$

where $\eta = \sqrt{\mu/\epsilon'}$ is the intrinsic impedance of the medium.

At this stage, it is time to translate the solutions of the wave equation into words. The physical meaning of (3.18–3.20) is that the electric and magnetic fields, at a specified time, at any point of the space $\mathbf{r}$, are two perpendicular vectors, $\mathbf{E}$ and $\mathbf{H}$, that lie on a plane normal to the direction of propagation. This plane is called *isophase plane*. If the direction of propagation does not change in the space, and the amplitude of the fields does not attenuate with the propagation, then this solution of the wave equation is named a *plane wave*, and represents a fundamental solution to Maxwell's equations.

In practical situations, however, the antennas cannot create pure plane waves, and also the scattering by objects is not a plane wave. In this case, the wave amplitude decreases with the distance from the antenna, and the *isophase* surfaces are spherical. Anyway, in the far-field region, which is of interest for us in remote sensing, the radius of curvature of the isophase spheres is so large that on a local scale the isophase surfaces can be considered plane for all practical purposes. Therefore, the wave is said to be a *spherical TEM wave*, because both electric and magnetic fields are transverse to the direction of propagation, as in the plane wave case. The only difference with respect to a plane wave is the attenuation with distance, but it is not related with the analysis of the wave polarization. Therefore, in the following, the fields will correspond to those of a spherical TEM wave or a plane wave, without distinction.

Note that, since both electric and magnetic field vectors are mutually orthogonal, the description of the wave can be carried out by only looking at one of them. Hereafter, only the electric field will be considered. Although the time variable $t$ had been omitted in (3.18–3.19) for simplicity, it is important to note that the amplitude and orientation of the electric vector $\mathbf{E}$ depends on the time. Indeed, the *polarization* of the wave is a concept used for describing the shape and locus of the tip of the vector $\mathbf{E}$ as a function of time, for a specific point is space. This vector, as shown before, always lies on a plane orthogonal to the direction of propagation.

### 3.1.3  Polarization Description

In order to describe the polarization of a wave, a coordinate system must be established. In the following, a generic spherical coordinate system is described. It has been widely used in remote sensing because the earth's surface can be represented by the $x$–$y$ plane, and the incident or scattered direction of a wave can be described by the spherical angles $\theta$ and $\phi$. A plane wave traveling in the direction $\hat{\mathbf{k}}$ has an electric field vector $\mathbf{E}$ that can be characterized in terms of two orthogonal components: *horizontal polarization* $E_h\hat{\mathbf{h}}$ and *vertical polarization* $E_v\hat{\mathbf{v}}$. It can be conveniently done by defining the coordinate system $(\hat{\mathbf{k}}, \hat{\mathbf{v}}, \hat{\mathbf{h}})$ in coincidence with the standard spherical coordinate system $(\hat{\mathbf{r}}, \hat{\boldsymbol{\theta}}, \hat{\boldsymbol{\phi}})$. This is depicted in Fig. 3.1.

Thus, the electric field is:

$$\mathbf{E}(\mathbf{r}) = \left( E_v\hat{\mathbf{v}} + E_h\hat{\mathbf{h}} \right) e^{-jk\hat{\mathbf{k}}\cdot\mathbf{r}}, \tag{3.21}$$

where, according to Fig. 3.1,

$$\hat{\mathbf{h}} = \frac{\hat{\mathbf{z}} \times \hat{\mathbf{k}}}{|\hat{\mathbf{z}} \times \hat{\mathbf{k}}|} \tag{3.22}$$

$$\hat{\mathbf{v}} = \hat{\mathbf{h}} \times \hat{\mathbf{k}}. \tag{3.23}$$
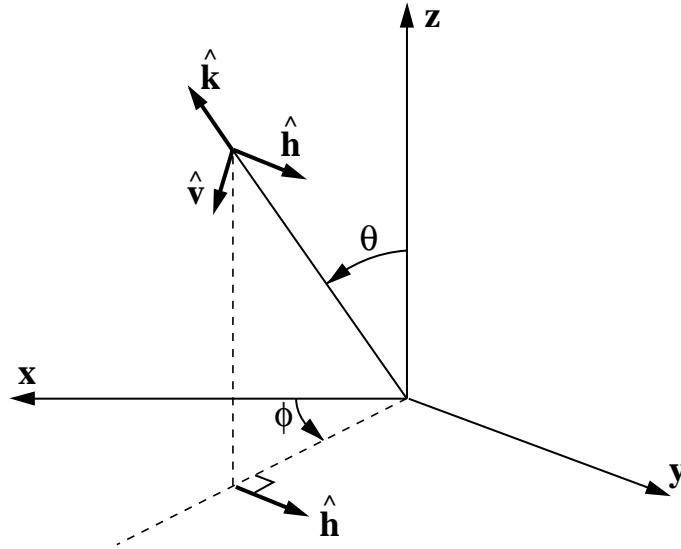
**Fig. 3.1.** Spherical coordinate system for a plane wave

These vectors can be also defined in terms of the spherical angles:

$$\hat{\mathbf{k}} = \sin\theta\cos\phi\,\hat{\mathbf{x}} + \sin\theta\sin\phi\,\hat{\mathbf{y}} + \cos\theta\,\hat{\mathbf{z}} \tag{3.24}$$

$$\hat{\mathbf{h}} = -\sin\phi\,\hat{\mathbf{x}} + \cos\phi\,\hat{\mathbf{y}} \tag{3.25}$$

$$\hat{\mathbf{v}} = \cos\theta\cos\phi\,\hat{\mathbf{x}} + \cos\theta\sin\phi\,\hat{\mathbf{y}} - \sin\theta\,\hat{\mathbf{z}}. \tag{3.26}$$

### 3.1.3.1  Polarization Ellipse

Without loss of generality, let us suppose the propagation direction $\hat{\mathbf{k}}$ and the position vector $\mathbf{r}$ to be parallel as depicted in Fig. 3.1. As a result, the scalar product $\mathbf{k} \cdot \mathbf{r}$ simplifies to $kr$, and the position of the wave is simply dictated by the scalar variable $r$.

If the coordinates on the isophase plane are defined in terms of the two orthogonal vectors $\hat{\mathbf{v}}$ and $\hat{\mathbf{h}}$, then the loci of the vector $\mathbf{E}$ on the $v$–$h$ plane[2] are:

$$\mathbf{E}(r) = E_v(r)\hat{\mathbf{v}} + E_h(r)\hat{\mathbf{h}}. \tag{3.27}$$

For studying the polarization of the wave it is important to explicitly show the phase dependence with the radial coordinate:

$$E_v(r) = A_v e^{-jkr} = a_v e^{j\phi_v} e^{-jkr} \tag{3.28}$$

$$E_h(r) = A_h e^{-jkr} = a_h e^{j\phi_h} e^{-jkr}, \tag{3.29}$$

---

[2]Note that the plane is denoted $v$–$h$ (not $h$–$v$) following the criterion employed in the definition of $\hat{\mathbf{v}}$ and $\hat{\mathbf{h}}$, i.e. the coordinates $(\hat{\mathbf{k}}, \hat{\mathbf{v}}, \hat{\mathbf{h}})$ form a right-handed system.

where $A_v$ and $A_h$ are the amplitudes of $E_v(r)$ and $E_h(r)$, respectively, which can be further decomposed into modulus ($a_v$ and $a_h$) and phase ($\phi_v$ and $\phi_h$). The instantaneous value of the field is calculated as:

$$E_v(r, t) = \Re\left(E_v(r)e^{j\omega t}\right) = a_v \cos(\omega t - kr + \phi_v) \tag{3.30}$$

$$E_h(r, t) = \Re\left(E_h(r)e^{j\omega t}\right) = a_h \cos(\omega t - kr + \phi_h). \tag{3.31}$$

Let us consider the nature of the curve described by the end point of the electric vector at a certain point in space. This curve is contained on the $v$–$h$ plane, and can be obtained by eliminating the dependence on $(\omega t - kr)$ [10, pp. 24–27], yielding:

$$\left(\frac{E_v(r, t)}{a_v}\right)^2 + \left(\frac{E_h(r, t)}{a_h}\right)^2 - \left(\frac{2E_v(r, t)E_h(r, t)}{a_v a_h}\right)\cos\Delta\phi = \sin^2\Delta\phi \tag{3.32}$$

wherein

$$\Delta\phi = \phi_h - \phi_v. \tag{3.33}$$

The formula in (3.32) is the equation of an ellipse. The ellipse is inscribed into a rectangle whose sides are parallel to the coordinate axes and whose lengths are $2a_v$ and $2a_h$, as shown in Fig. 3.2. The ellipse touches the sides at the points $(\pm a_v, \pm a_h \cos\Delta\phi)$ and $(\pm a_v \cos\Delta\phi, \pm a_h)$.

In general, the axes of the ellipse are not in the $\hat{\mathbf{h}}$ and $\hat{\mathbf{v}}$ directions. Let $\hat{\boldsymbol{\xi}}$ and $\hat{\boldsymbol{\eta}}$ be a new set of axes along the main axes of the ellipse, and let $\psi$ be the angle between $\hat{\mathbf{v}}$ and the direction of the major axis $\hat{\boldsymbol{\xi}}$. Therefore, the components $E_\xi$ and $E_\eta$ are related to $E_v$ and $E_h$ by:

$$E_\xi = E_v \cos\psi + E_h \sin\psi \tag{3.34}$$

$$E_\eta = -E_v \sin\psi + E_h \cos\psi. \tag{3.35}$$

According to the length of the axes, $a$ and $b$ with $a \geqslant b$, a new equation of the ellipse is:

$$E_\xi = a \cos(\omega t - kr + \phi_0) \tag{3.36}$$

$$E_\eta = \mp b \sin(\omega t - kr + \phi_0), \tag{3.37}$$

where the sign ambiguity is explained below.

Starting from the former equations, some trigonometric and algebraic derivations permit the solution of all the geometrical relations between the parameters shown in Fig. 3.2 (see [10, pp. 24–27] for details). That ellipse corresponds to the most general case of polarization, so every polarization state can be described by means of a set of a few geometrical
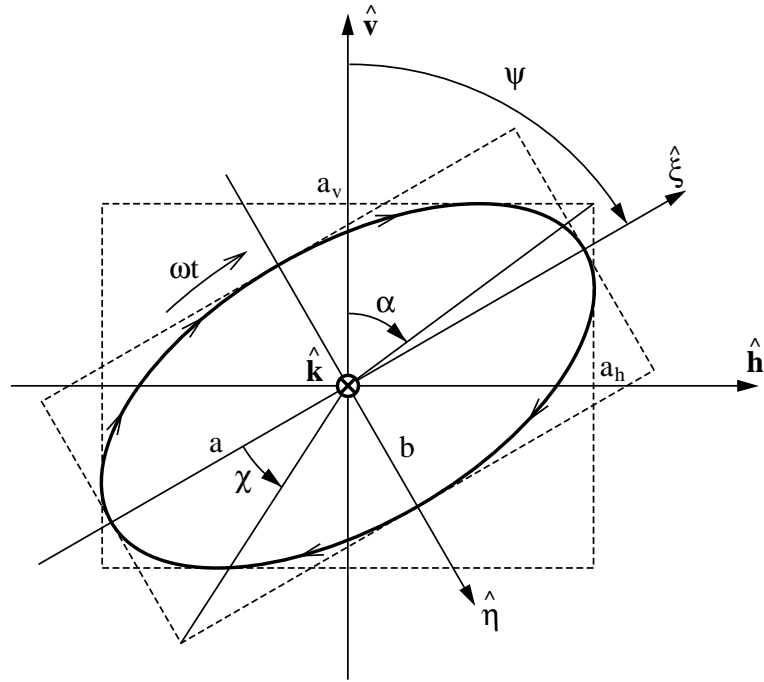
**Fig. 3.2.** Polarization ellipse in the $v$–$h$ plane and geometrical parameters. The rotation corresponds to a right-handed polarization

values. The most important concepts are summarized here. If $a_v$, $a_h$ and the phase difference $\Delta\phi$ are given, referred to an arbitrary set of axes, and if $\alpha$ denotes an angle such that

$$\tan\alpha = \frac{a_h}{a_v}, \qquad 0 \leqslant \alpha \leqslant \pi/2, \tag{3.38}$$

then the principal semiaxes $a$ and $b$ of the ellipse, the *orientation angle* $\psi$ which the major axis makes with $\hat{\mathbf{v}}$, and the *ellipticity angle* $\chi$ which specifies the ratio of the ellipse axes, are specified by the following formulae:

$$a^2 + b^2 = a_v^2 + a_h^2 \tag{3.39}$$

$$\tan 2\psi = \tan 2\alpha \,\cos\Delta\phi, \qquad 0 \leqslant \psi < \pi \tag{3.40}$$

$$\sin 2\chi = \sin 2\alpha \,\sin\Delta\phi \tag{3.41}$$

$$\tan\chi = \pm b/a, \qquad -\pi/4 < \chi \leqslant \pi/4. \tag{3.42}$$

The sign of $\chi$ distinguishes the two possible senses in which the end point of the electric vector may describe the ellipse. It is a matter of definition whether a sense of rotation of the electric vector is referred to as *right-handed* or *left-handed*. In this thesis, the IEEE definition has been employed, which states that a wave has a *right-handed* (*left-handed*) polarization if its electric field vector has a clockwise (counterclockwise) sense of rotation when it is viewed along the axis of propagation. Note that the rotation must be viewed from the "rear" of the wave in the direction of propagation. This last point is the reason why the ellipse displayed in Fig. 3.2 has been drawn from that point of view, i.e. the wave is traveling

into the page, so that the rotation is examined from an observation point looking into the page and perpendicular to it (see [144, pp. 154–168]). Some bibliographical references have been found where, although the criterion coincides with that stated here, the figures used for describing the polarization ellipse are drawn from the opposite sense, thus making it difficult to understand the rotation criterion ([33, pp. 7],[6, pp. 9]). Finally, and as a result of the defined criterion, note that the ellipticity angle $\chi$ is negative for right-handed polarization, and positive for left-handed polarization.

### 3.1.3.2  Typical Polarization States

Attending to the defining parameters of the polarization ellipse, some important particular cases of polarization states can be recognized. The first special type is the reduction of the ellipse to a straight line. It occurs when

$$\Delta\phi = \phi_h - \phi_v = m\pi, \qquad m = 0, \pm 1, \pm 2, \ldots \tag{3.43}$$

leading to

$$\frac{E_h}{E_v} = (-1)^m \frac{a_h}{a_v}. \tag{3.44}$$

In this case the field is said to present *linear polarization*. The ellipticity angle $\chi$ is zero, and the orientation angle $\psi$ coincides with $\alpha$ whose tangent is given by (3.44). In the $v$–$h$ basis, $\psi = 0$ corresponds to *vertical polarization*, and $\psi = \pi/2$ to *horizontal polarization*.

Another special case is that of a wave with *circular polarization*, the ellipse then degenerating to a circle. A necessary condition for this is that the circumscribed rectangle becomes a square:

$$a_v = a_h = a. \tag{3.45}$$

In addition, one of the components must be zero when the other has an extreme value; thus:

$$\Delta\phi = \phi_h - \phi_v = m\pi/2, \qquad m = \pm 1, \pm 3, \pm 5, \ldots \tag{3.46}$$

When the wave has a right-handed circular polarization (RHC), $\sin\Delta\phi < 0$, so that

$$\Delta\phi = -\frac{\pi}{2} + 2m\pi, \qquad m = 0, \pm 1, \pm 2, \ldots \tag{3.47}$$

$$E_v = a\cos(\omega t - kr + \phi_v) \tag{3.48}$$

$$E_h = a\cos(\omega t - kr + \phi_v - \pi/2) = a\sin(\omega t - kr + \phi_v). \tag{3.49}$$

Instead, for a left-handed circular polarization (LHC), $\sin \Delta\phi > 0$, so that

$$\Delta\phi = \frac{\pi}{2} + 2m\pi, \qquad m = 0, \pm 1, \pm 2, \ldots \tag{3.50}$$

$$E_v = a\cos(\omega t - kr + \phi_v) \tag{3.51}$$

$$E_h = a\cos(\omega t - kr + \phi_v + \pi/2) = -a\sin(\omega t - kr + \phi_v). \tag{3.52}$$

The rest of cases, i.e. when $a_v \neq a_h$ or $\sin \Delta\phi \neq 0$, correspond to a so-called *elliptical polarization*.

### 3.1.3.3 Stokes Vector

So far we have seen that the polarization state of a plane wave can be characterized by two sets of three parameters: $(a_v, a_h, \Delta\phi)$, or alternatively $(\psi, \chi, a_v^2 + a_h^2)$. A different representation of the polarization of plane waves, that has been widely used in optics and radar, is the Stokes vector $\mathbf{g}$:

$$\mathbf{g} = \begin{bmatrix} I \\ Q \\ U \\ V \end{bmatrix} = \begin{bmatrix} |E_v|^2 + |E_h|^2 \\ |E_v|^2 - |E_h|^2 \\ 2\Re(E_v E_h^*) \\ -2\Im(E_v E_h^*) \end{bmatrix} \tag{3.53}$$

where the asterisk denotes the complex conjugate operation, and $\Re$ and $\Im$ stand for the real and imaginary part, respectively.

A particular characteristic of these parameters is that all are real and have the same physical dimensions. The parameter $I$ is proportional to the total intensity to the wave, $Q$ is the difference of the intensities in both polarizations, while $U$ and $V$ contain the phase information.

Although the Stokes vector has four components, only three of them are independent, because they must satisfy[3]

$$I^2 = Q^2 + U^2 + V^2. \tag{3.54}$$

The relationship between the Stokes parameters and the other sets of parameters is:

$$\mathbf{g} = \begin{bmatrix} I \\ Q \\ U \\ V \end{bmatrix} = \begin{bmatrix} a_v^2 + a_h^2 \\ a_v^2 - a_h^2 \\ 2a_v a_h \cos\Delta\phi \\ 2a_v a_h \sin\Delta\phi \end{bmatrix} = I \begin{bmatrix} 1 \\ \cos 2\psi \cos 2\chi \\ \sin 2\psi \cos 2\chi \\ \sin 2\chi \end{bmatrix} \tag{3.55}$$

---

[3]The identity in (3.54) only holds for completely polarized waves. See Section 3.3 for explanation.
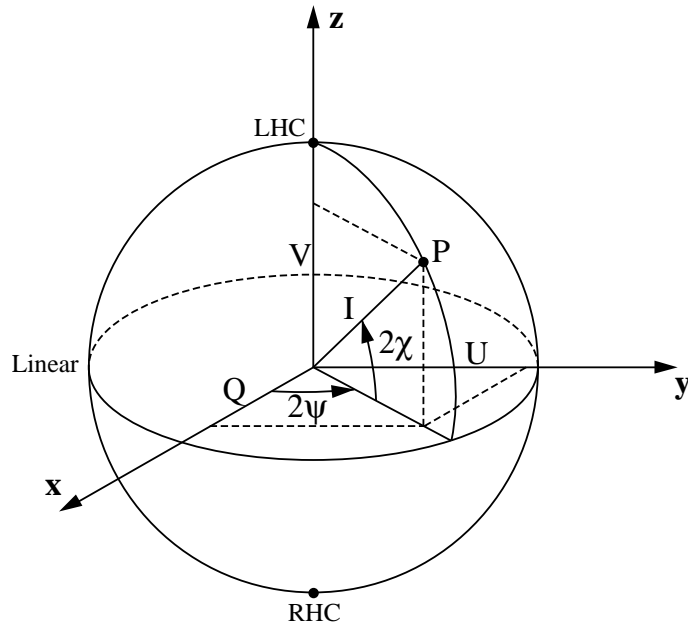
**Fig. 3.3.** Poincaré sphere with Stokes parameters as Cartesian coordinates

The relationship in (3.55) indicates that the state of polarization of a plane wave can be geometrically represented by regarding $(Q, U, V)$ as the Cartesian coordinates of a point $P$. In fact, there is an unique mapping of every polarization state $P$ on the surface of a sphere of radius $I$. The angles $2\chi$ and $2\psi$ define the latitude and longitude of the point $P$, and the sphere is usually called a Poincaré sphere (Fig. 3.3). Attending to the ranges of the different parameters, the upper hemisphere, corresponding to $\chi > 0$, displays left-handed polarizations, whereas the lower hemisphere, corresponding to $\chi < 0$, displays right-handed polarizations. The north pole of the sphere represents left circular polarization, the south pole represents right circular polarization, and all the linear polarizations are in the equatorial plane.

There is another definition of the Stokes parameters, which has been widely used for convenience in solving radiative transfer problems. This new definition is known as *modified Stokes vector*, and separates the intensities for vertical and horizontal polarization:

$$\mathbf{g}_m = \begin{bmatrix} I_v \\ I_h \\ U \\ V \end{bmatrix} = \begin{bmatrix} |E_v|^2 \\ |E_h|^2 \\ 2\Re(E_v E_h^*) \\ -2\Im(E_v E_h^*) \end{bmatrix} = \begin{bmatrix} \frac{1}{2}(I+Q) \\ \frac{1}{2}(I-Q) \\ U \\ V \end{bmatrix} = I \begin{bmatrix} \frac{1}{2}(1 + \cos 2\psi \cos 2\chi) \\ \frac{1}{2}(1 - \cos 2\psi \cos 2\chi) \\ \sin 2\psi \cos 2\chi \\ \sin 2\chi \end{bmatrix}. \quad (3.56)$$

Both vectors are related by

$$\mathbf{g} = \begin{bmatrix} 1 & 1 & 0 & 0 \\ 1 & -1 & 0 & 0 \\ 0 & 0 & 1 & 0 \\ 0 & 0 & 0 & 1 \end{bmatrix} \mathbf{g}_m \quad \text{and} \quad \mathbf{g}_m = \begin{bmatrix} \frac{1}{2} & \frac{1}{2} & 0 & 0 \\ \frac{1}{2} & -\frac{1}{2} & 0 & 0 \\ 0 & 0 & 1 & 0 \\ 0 & 0 & 0 & 1 \end{bmatrix} \mathbf{g}. \quad (3.57)$$

## 3.2   Polarization Scattering Matrices

So far we have seen how to characterize the polarization of a wave by means of the polarization ellipse, the Stokes vector, or other sets of parameters. When dealing with the scattering produced by an object of interest, we will have to relate the polarization characteristics of two waves: a wave generated by the radar for illuminating the target (incident field), and a wave scattered by the target and then received by the radar receiving antenna (scattered field). The polarization parameters of both waves can be arranged as a vector, thus enabling the construction of matrices for formulating the relation between the polarizations of the incident and scattered fields. As a result, the polarization behavior of the target is assigned to a matrix. This section presents the different matrices that are commonly used for describing the polarization characteristics of single targets.

### 3.2.1   Scattering Matrix

#### 3.2.1.1   Definition

Let us consider an object illuminated by an electromagnetic plane wave with incident electric field

$$\mathbf{E}^i = E_v^i \hat{\mathbf{v}}_i + E_h^i \hat{\mathbf{h}}_i, \tag{3.58}$$

wherein the phase factor has been suppressed for convenience, $\hat{\mathbf{v}}_i$ and $\hat{\mathbf{h}}_i$ have been arbitrarily defined according to Section 3.1.3, and the incident direction is denoted as $\hat{\mathbf{k}}_i$.

The incident wave excites currents in the object, which in turn reradiate a field. The reradiated field is known as scattered field, and the object is denoted as a *scatterer*. In the far-field zone of the scatterer, the scattered wave is an outgoing spherical TEM wave, which can be locally considered as a plane wave over the area occupied by the receiving antenna. If a new coordinate system, $\hat{\mathbf{v}}_s$–$\hat{\mathbf{h}}_s$, is defined for describing the polarization of the scattered wave along the direction $\hat{\mathbf{k}}_s$, the transverse components of the scattered field $\mathbf{E}^s$ are:

$$\mathbf{E}^s = E_v^s \hat{\mathbf{v}}_s + E_h^s \hat{\mathbf{h}}_s. \tag{3.59}$$

For the polarization description of the scatterer it will be useful to adopt the following matrix notation for the electric fields in (3.58) and (3.59):

$$\mathbf{E}^i = \begin{bmatrix} E_v^i \\ E_h^i \end{bmatrix} \qquad \mathbf{E}^s = \begin{bmatrix} E_v^s \\ E_h^s \end{bmatrix}. \tag{3.60}$$

By using this matrix notation, the components of $\mathbf{E}^i$ and $\mathbf{E}^s$ are related by a complex $2 \times 2$ matrix in the following manner:

$$\begin{bmatrix} E_v^s \\ E_h^s \end{bmatrix} = \frac{e^{-jkr}}{r} \begin{bmatrix} S_{vv} & S_{vh} \\ S_{hv} & S_{hh} \end{bmatrix} \begin{bmatrix} E_v^i \\ E_h^i \end{bmatrix}, \tag{3.61}$$

or more succinctly,

$$\mathbf{E}^s = \frac{e^{-jkr}}{r}[S]\mathbf{E}^i, \tag{3.62}$$

where $r$ is the distance between the scatterer and the antenna, and $k$ is the wave number of the illuminating field. The $r^{-1}$ coefficient represents the attenuation between the scatterer and the antenna, which is produced by the spherical nature of the wave. On the other hand, the phase factor represents the delay due to the travel of the wave from the scatterer to the antenna. Examples exist in the literature where different coefficients have been used in the definition of $[S]$. The one used in (3.62) has been chosen for simplicity.

The $[S]$ matrix is called the *scattering matrix* (see Chapter 2 and bibliography therein). The elements of the scattering matrix are known as the complex scattering amplitudes. Equation (3.62) also indicates how the scattering amplitudes may be measured. For example, $S_{vv}$ is the complex ratio of the electric field of the vertically polarized parts of the scattered wave and the incident wave; thus to measure $S_{vv}$, a vertically polarized wave is transmitted, and both amplitude and phase of the vertically polarized part of the scattered wave are measured. The other elements of the scattering matrix can be measured in a similar manner by choosing the appropriate combination of transmit and receive polarizations and measuring both amplitude and phase of the desired component of the scattered field. Hence, this matrix provides the scattered field by the scatterer in the far-field region in a given observation direction ($\hat{\mathbf{k}}_s$) as a response to a plane wave incident in the direction $\hat{\mathbf{k}}_i$. So, the incidence and scattering directions must be specified. In addition, the definition of the polarization bases ($\hat{\mathbf{v}},\hat{\mathbf{h}}$) for both incident and scattered waves has to be provided. In order to do that, two classical conventions are explained in the following.

### 3.2.1.2 Coordinate System Conventions

The scattering description of objects is usually represented in two major coordinate systems: the *forward scattering alignment* (FSA) convention and the *backward scattering alignment* (BSA) convention. All coordinate systems are defined in terms of a global coordinate system centered inside the scatterer. They are defined in the following.

**Forward Scattering Alignment (FSA) Convention**   The FSA convention is commonly used in problems with bistatic geometries or with multiple scattering. The reason is that the directions of the vertical and horizontal unit vectors are always defined with respect to the direction of the wave propagation. Thus, this convention is also known as *wave coordinates*. The coordinate system ($\hat{\mathbf{k}},\hat{\mathbf{v}},\hat{\mathbf{h}}$) coincides with the standard spherical coordinate system ($\hat{\mathbf{r}}, \hat{\boldsymbol{\theta}}, \hat{\boldsymbol{\phi}}$), as illustrated in Fig. 3.4.
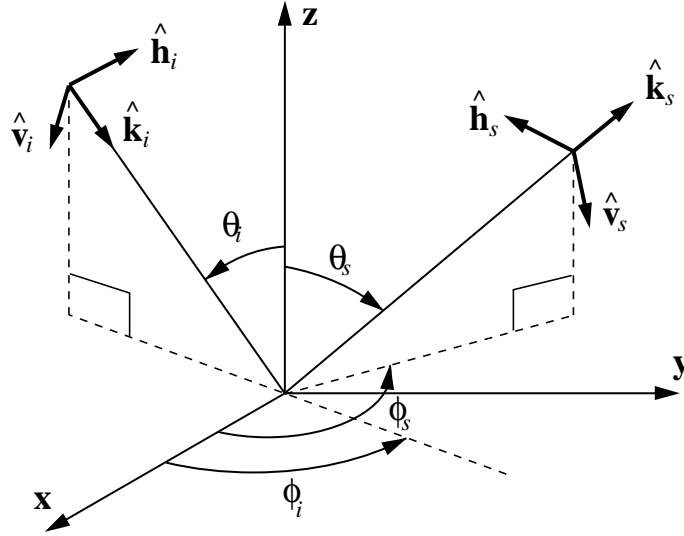
**Fig. 3.4.** Forward scattering alignment (FSA) convention: coordinate system and scattering geometry

In terms of the elevation $\theta$ and azimuth $\phi$ angles, the unit vectors are:

$$\hat{\mathbf{k}}_i = \sin\theta_i \cos\phi_i \, \hat{\mathbf{x}} + \sin\theta_i \sin\phi_i \, \hat{\mathbf{y}} - \cos\theta_i \, \hat{\mathbf{z}} \tag{3.63}$$

$$\hat{\mathbf{h}}_i = \frac{\hat{\mathbf{z}} \times \hat{\mathbf{k}}_i}{|\hat{\mathbf{z}} \times \hat{\mathbf{k}}_i|} = -\sin\phi_i \, \hat{\mathbf{x}} + \cos\phi_i \, \hat{\mathbf{y}} \tag{3.64}$$

$$\hat{\mathbf{v}}_i = \hat{\mathbf{h}}_i \times \hat{\mathbf{k}}_i = -\cos\theta_i \cos\phi_i \, \hat{\mathbf{x}} - \cos\theta_i \sin\phi_i \, \hat{\mathbf{y}} - \sin\theta_i \, \hat{\mathbf{z}}, \tag{3.65}$$

for the incident field, and:

$$\hat{\mathbf{k}}_s = \sin\theta_s \cos\phi_s \, \hat{\mathbf{x}} + \sin\theta_s \sin\phi_s \, \hat{\mathbf{y}} + \cos\theta_s \, \hat{\mathbf{z}} \tag{3.66}$$

$$\hat{\mathbf{h}}_s = \frac{\hat{\mathbf{z}} \times \hat{\mathbf{k}}_s}{|\hat{\mathbf{z}} \times \hat{\mathbf{k}}_s|} = -\sin\phi_s \, \hat{\mathbf{x}} + \cos\phi_s \, \hat{\mathbf{y}} \tag{3.67}$$

$$\hat{\mathbf{v}}_s = \hat{\mathbf{h}}_s \times \hat{\mathbf{k}}_s = \cos\theta_s \cos\phi_s \, \hat{\mathbf{x}} + \cos\theta_s \sin\phi_s \, \hat{\mathbf{y}} - \sin\theta_s \, \hat{\mathbf{z}}, \tag{3.68}$$

for the scattered field.

For forward scattering, the angles are $\theta_s = \pi - \theta_i$ and $\phi_s = \phi_i$, so all three unit vectors coincide. In contrast, for backscattering the angles are $\theta_s = \theta_i$ and $\phi_s = \pi + \phi_i$ for doing $\hat{\mathbf{k}}_s = -\hat{\mathbf{k}}_i$. Therefore, $\hat{\mathbf{v}}_s = \hat{\mathbf{v}}_i$ and $\hat{\mathbf{h}}_s = -\hat{\mathbf{h}}_i$.

**Backward Scattering Alignment (BSA) Convention** The BSA convention is more commonly used in communications and radar because the unit vectors are defined with respect to the antenna polarization. The antenna is equally characterized in transmission and reception, so the unit vectors of the incident and the scattered wave, when defined according to the BSA, are identical in the backscattering case. The BSA convention is also known as *antenna coordinates*.
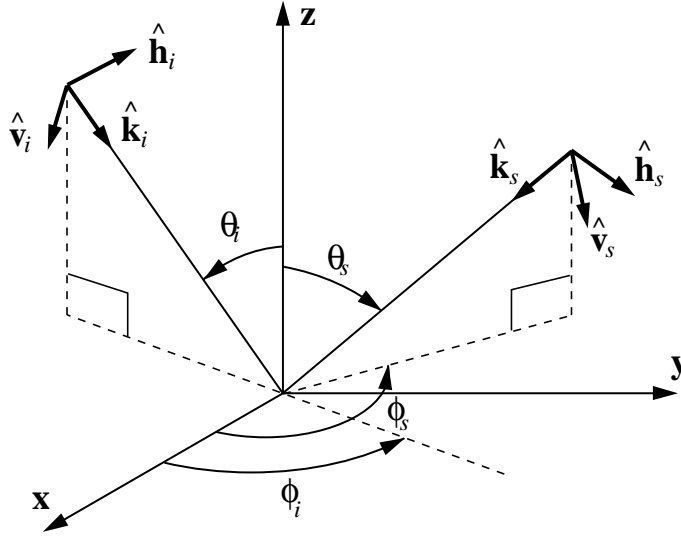
**Fig. 3.5.** Backward scattering alignment (BSA) convention: coordinate system and scattering geometry

In terms of the elevation and azimuth angles (see Fig. 3.5) the unit vectors are:

$$\hat{\mathbf{k}}_i = \sin\theta_i \cos\phi_i \,\hat{\mathbf{x}} + \sin\theta_i \sin\phi_i \,\hat{\mathbf{y}} - \cos\theta_i \,\hat{\mathbf{z}} \tag{3.69}$$

$$\hat{\mathbf{h}}_i = \frac{\hat{\mathbf{z}} \times \hat{\mathbf{k}}_i}{|\hat{\mathbf{z}} \times \hat{\mathbf{k}}_i|} = -\sin\phi_i \,\hat{\mathbf{x}} + \cos\phi_i \,\hat{\mathbf{y}} \tag{3.70}$$

$$\hat{\mathbf{v}}_i = \hat{\mathbf{h}}_i \times \hat{\mathbf{k}}_i = -\cos\theta_i \cos\phi_i \,\hat{\mathbf{x}} - \cos\theta_i \sin\phi_i \,\hat{\mathbf{y}} - \sin\theta_i \,\hat{\mathbf{z}}, \tag{3.71}$$

for the incident field (which coincide with the FSA case), and:

$$\hat{\mathbf{k}}_s = -\sin\theta_s \cos\phi_s \,\hat{\mathbf{x}} - \sin\theta_s \sin\phi_s \,\hat{\mathbf{y}} - \cos\theta_s \,\hat{\mathbf{z}} \tag{3.72}$$

$$\hat{\mathbf{h}}_s = \frac{\hat{\mathbf{z}} \times \hat{\mathbf{k}}_s}{|\hat{\mathbf{z}} \times \hat{\mathbf{k}}_s|} = \sin\phi_s \,\hat{\mathbf{x}} - \cos\phi_s \,\hat{\mathbf{y}} \tag{3.73}$$

$$\hat{\mathbf{v}}_s = \hat{\mathbf{h}}_s \times \hat{\mathbf{k}}_s = \cos\theta_s \cos\phi_s \,\hat{\mathbf{x}} + \cos\theta_s \sin\phi_s \,\hat{\mathbf{y}} - \sin\theta_s \,\hat{\mathbf{z}}, \tag{3.74}$$

for the scattered field.

As outlined above, in the backscattering direction the two coordinate systems are coincident:

$$\hat{\mathbf{k}}_i = \hat{\mathbf{k}}_s \qquad \hat{\mathbf{h}}_i = \hat{\mathbf{h}}_s \qquad \hat{\mathbf{v}}_i = \hat{\mathbf{v}}_s. \tag{3.75}$$

**Relation Between Scattering Matrices Expressed in FSA and BSA Conventions**
By comparing the expressions of the unit vectors for the FSA and BSA local coordinate systems, the relations between the incident and scattered field vectors are:

$$\mathbf{E}^i_{FSA} = \mathbf{E}^i_{BSA} \tag{3.76}$$

$$\mathbf{E}^s_{FSA} = \begin{bmatrix} 1 & 0 \\ 0 & -1 \end{bmatrix} \mathbf{E}^s_{BSA}. \tag{3.77}$$

This means that the scattering matrices are different for those two conventions. The relation between the scattering matrices obtained by using the FSA and the BSA conventions is easily derived by substituting (3.76) and (3.77) in (3.62), yielding:

$$[S]_{FSA} = \begin{bmatrix} 1 & 0 \\ 0 & -1 \end{bmatrix} [S]_{BSA} \tag{3.78}$$

The relation in (3.78) means that both matrices result in the same by simply changing the sign of the second row.

In the practical case of backscattering, the general property of *reciprocity* for electromagnetic fields leads to the following property:

$$S_{hv} = -S_{vh} \tag{3.79}$$

if the FSA convention is used, and

$$S_{hv} = S_{vh} \tag{3.80}$$

if the BSA convention is used. Therefore, in backscattering, the effect of the reciprocity relation on the scattering matrix is that it becomes symmetric when the BSA convention is used, and antisymmetric in the FSA case. Fig. 3.6 shows the coordinate systems of the FSA and BSA conventions in the backscattering case. A possible parameterization of the scattering matrices for a reciprocal target in both cases is:

$$[S]_{FSA} = \begin{bmatrix} a & b \\ -b & d \end{bmatrix} \qquad [S]_{BSA} = \begin{bmatrix} a & b \\ b & e \end{bmatrix}, \tag{3.81}$$

wherein $e = -d$.

It is usual to neglect the absolute phase coefficient, that appears before the scattering matrix, in radar measurements because the power received is independent of this. Note that in a general bistatic or nonreciprocal case the number of independent parameters that fully characterize a scattering matrix is seven (four amplitudes and three phases) if the absolute phase term is ignored. On the other hand, when reciprocity holds and we examine the monostatic case there are only five independent parameters in the scattering matrix.

### 3.2.1.3 Target Vector for Backscatter Problems

With the aim of extracting physical information from the polarization description of a scatterer, a new formalism can be developed. It consists of the construction of the so-called
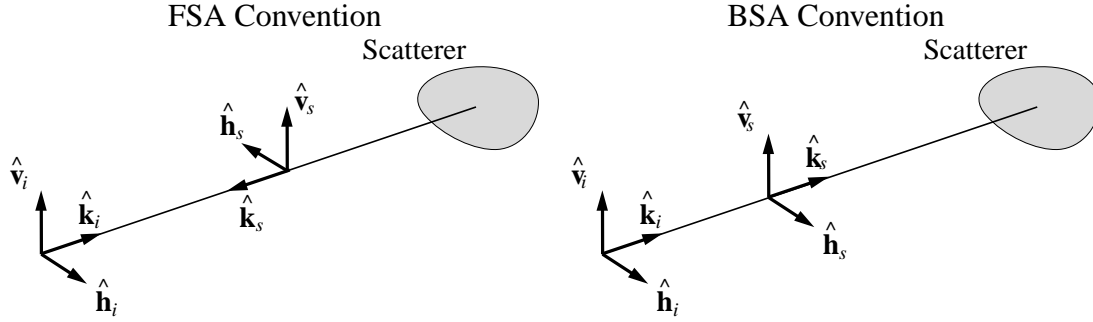
**Fig. 3.6.** Backscattering geometry with FSA and BSA conventions

*target vector* of a scatterer, which is simply a vectorization of the scattering matrix. In mathematical form, it can be formally written as:

$$\mathbf{k} = V([S]) = \frac{1}{2} \operatorname{Trace}([S]\Psi), \qquad (3.82)$$

where $V(\cdot)$ is the vectorization operator, $\operatorname{Trace}(\cdot)$ is the sum of the diagonal elements of the argument, and $\Psi$ is a set of $2 \times 2$ complex basis matrices which are orthonormal under an hermitian inner product [52]. The vector $\mathbf{k}$ has four entries which are complex numbers[4].

There exist several basis sets that can be readily applied to this formulation. Two examples often used are: $\Psi_L$, which corresponds to a straightforward ordering of the elements of $[S]$, and $\Psi_P$, which makes use of the Pauli spin matrices $[\sigma_i]$ usually applied in quantum mechanics. Their explicit expressions are:

$$\Psi_L : 2 \left\{ \begin{bmatrix} 1 & 0 \\ 0 & 0 \end{bmatrix}, \begin{bmatrix} 0 & 0 \\ 1 & 0 \end{bmatrix}, \begin{bmatrix} 0 & 1 \\ 0 & 0 \end{bmatrix}, \begin{bmatrix} 0 & 0 \\ 0 & 1 \end{bmatrix} \right\}, \qquad (3.83)$$

and

$$\Psi_P : \sqrt{2} \left\{ [\sigma_i] \right\}, \qquad i = 0, 1, 2, 3 \qquad (3.84)$$

wherein

$$[\sigma_0] = \begin{bmatrix} 1 & 0 \\ 0 & 1 \end{bmatrix}, \quad [\sigma_1] = \begin{bmatrix} 1 & 0 \\ 0 & -1 \end{bmatrix}, \quad [\sigma_2] = \begin{bmatrix} 0 & 1 \\ 1 & 0 \end{bmatrix}, \quad [\sigma_3] = \begin{bmatrix} 0 & -j \\ j & 0 \end{bmatrix}. \qquad (3.85)$$

Note that the premultiplying factors appear from the requirement to keep the total power scattered by the target invariant, namely $\operatorname{Trace}([S][S]^{*T})$.

In this thesis, the Pauli basis will be used in most cases. This choice is founded on two properties of the Pauli basis representation. In first place, any scattering matrix can be decomposed in terms of the Pauli matrices as follows:

$$[S] = \begin{bmatrix} a+b & c-jd \\ c+jd & a-b \end{bmatrix} = a[\sigma_0] + b[\sigma_1] + c[\sigma_2] + d[\sigma_3], \qquad (3.86)$$

---

[4]Do not confuse the target vector $\mathbf{k}$ with the direction of propagation of the wave

where $a$, $b$, $c$ and $d$ are complex coefficients. This original decomposition can be verbally expressed as: TARGET = Iso-Surface + Iso-Dihedral + $45°$ Iso-Dihedral + Iso-Crosspolarizer.

Therefore, the decomposition in terms of Pauli matrices has a substantial physical meaning because each of them represents an important scattering mechanism in radar imagery. In second place, this decomposition has the additional advantage that the scattering mechanisms are orthogonal. This means that their separation is possible even in the case of second order statitics, where noise and depolarization effects can be introduced. These ideas will be extended in next sections in the interpretation of the target decomposition based on the coherency matrix (see Section 3.3).

Finally, the explicit formulation of the target vectors, in terms of the entries of $[S]$, yields:

$$\mathbf{k}_L = \begin{bmatrix} S_{vv} \\ S_{vh} \\ S_{hv} \\ S_{hh} \end{bmatrix} \qquad \mathbf{k}_P = \frac{1}{\sqrt{2}} \begin{bmatrix} S_{vv} + S_{hh} \\ S_{vv} - S_{hh} \\ S_{vh} + S_{hv} \\ j(S_{vh} - S_{hv}) \end{bmatrix}. \tag{3.87}$$

In the general case of backscattering and a reciprocal target, one of the entries of the target vector is redundant, and new three-component vectors are usually defined. For example:

$$\mathbf{k}_{3L} = \begin{bmatrix} S_{vv} \\ \sqrt{2}S_{vh} \\ S_{hh} \end{bmatrix} \qquad \mathbf{k}_{3P} = \frac{1}{\sqrt{2}} \begin{bmatrix} S_{vv} + S_{hh} \\ S_{vv} - S_{hh} \\ 2S_{vh} \end{bmatrix}. \tag{3.88}$$

## 3.2.2 Coherency and Covariance Matrices

With the vectorization explained in Section 3.2.1.3, it is possible to generate a matrix from the outer product of a target vector and its conjugate transpose (adjoint vector). If the target vector is defined using the Pauli matrices basis, the resulting matrix is called the *coherency matrix*, $[T]$; whereas if $\Psi_L$ is used, the new matrix is known as the *covariance matrix*, $[C]$. Then, following this definition, these matrices are:

$$[T] = \mathbf{k}_P \cdot \mathbf{k}_P^{*T} = [T]^{*T} \tag{3.89}$$

$$[C] = \mathbf{k}_L \cdot \mathbf{k}_L^{*T} = [C]^{*T} \tag{3.90}$$

Both matrices are related by the transformation:

$$[C] = [A]^{*T}[T][A] \tag{3.91}$$

wherein

$$[A] = \frac{1}{\sqrt{2}} \begin{bmatrix} 1 & 0 & 0 & 1 \\ 1 & 0 & 0 & -1 \\ 0 & 1 & 1 & 0 \\ 0 & j & -j & 0 \end{bmatrix}. \tag{3.92}$$

These matrices share some interesting properties: both are hermitian positive semidefinite and have the same eigenvalues (because the transformation in (3.92) has unitary similarity). The eigenvectors of $[T]$ and $[C]$ form orthonormal sets of vectors that can be used as a suitable basis for the vectorization operation detailed previously.

For future use, it is useful at this point to present a parameterization of the coherency matrix, that reads:

$$[T] = \begin{bmatrix} A_0 + A & C - jD & H + jG & I - jJ \\ C + jD & B_0 + B & E + jF & K - jL \\ H - jG & E - jF & B_0 - B & M + jN \\ I + jJ & K + jL & M - jN & A_0 - A \end{bmatrix}. \tag{3.93}$$

The important case of backscattering from a reciprocal target is expressed in the following for the coherency matrix. Two cases are distinguished, depending on the polarization convention. Note that the scattering matrices for both conventions are displayed in (3.81).

In case of FSA, the target vector results:

$$\mathbf{k}_P = \frac{1}{\sqrt{2}} \begin{bmatrix} a + d \\ a - d \\ 0 \\ 2jb \end{bmatrix}, \tag{3.94}$$

and the coherency matrix is:

$$[T]_{FSA} = \begin{bmatrix} A_0 + A & C - jD & 0 & I - jJ \\ C + jD & B_0 + B & 0 & K - jL \\ 0 & 0 & 0 & 0 \\ I + jJ & K + jL & 0 & A_0 - A \end{bmatrix} \tag{3.95}$$

Since there are only 9 nonzero elements, a reduced $3 \times 3$ coherency matrix can be defined as:

$$[T_3]_{FSA} = \begin{bmatrix} A_0 + A & C - jD & I - jJ \\ C + jD & B_0 + B & K - jL \\ I + jJ & K + jL & A_0 - A \end{bmatrix}. \tag{3.96}$$

In contrast, when the BSA convention is used, the target vector is:

$$\mathbf{k}_P = \frac{1}{\sqrt{2}} \begin{bmatrix} a+e \\ a-e \\ 2b \\ 0 \end{bmatrix}, \tag{3.97}$$

and the coherency matrix yields:

$$[T]_{BSA} = \begin{bmatrix} A_0 + A & C - jD & H + jG & 0 \\ C + jD & B_0 + B & E + jF & 0 \\ H - jG & E - jF & B_0 - B & 0 \\ 0 & 0 & 0 & 0 \end{bmatrix}. \tag{3.98}$$

Again, a reduced $3 \times 3$ coherency matrix can be defined as:

$$[T_3]_{BSA} = \begin{bmatrix} A_0 + A & C - jD & H + jG \\ C + jD & B_0 + B & E + jF \\ H - jG & E - jF & B_0 - B \end{bmatrix}. \tag{3.99}$$

As stated before, the parameterization in (3.93) and successive equations will be useful in next section for stating a relationship between the coherency and covariance matrices and other important matrices. At this point, however, it is necessary to present an explicit expression of $[T]$ and $[C]$ for the backscattering case, with reciprocity, and by means of the BSA convention. This specific situation is in turn the most common in radar polarimetry and, hence, will always be used in this thesis when dealing with target decomposition applications. By substituting the reduced target vectors defined in (3.88) into the definitions of both coherency and covariance matrices (3.89–3.90), the new simplified matrices are:

$$[T_3]_{BSA} = \frac{1}{2} \begin{bmatrix} |S_{vv} + S_{hh}|^2 & (S_{vv} + S_{hh})(S_{vv} - S_{hh})^* & 2(S_{vv} + S_{hh})S_{vh}^* \\ (S_{vv} - S_{hh})(S_{vv} + S_{hh})^* & |S_{vv} - S_{hh}|^2 & 2(S_{vv} - S_{hh})S_{vh}^* \\ 2S_{vh}(S_{vv} + S_{hh})^* & 2S_{vh}(S_{vv} - S_{hh})^* & 4|S_{vh}|^2 \end{bmatrix} \tag{3.100}$$

$$[C_3]_{BSA} = \begin{bmatrix} |S_{vv}|^2 & \sqrt{2}S_{vv}S_{vh}^* & S_{vv}S_{hh}^* \\ \sqrt{2}S_{vh}S_{vv}^* & 2|S_{vh}|^2 & \sqrt{2}S_{vh}S_{hh}^* \\ S_{hh}S_{vv}^* & \sqrt{2}S_{hh}S_{vh}^* & |S_{hh}|^2 \end{bmatrix}, \tag{3.101}$$

and are related by the following matrix products:

$$[C_3]_{BSA} = \frac{1}{2} [A_3]^T [T_3]_{BSA} [A_3] \qquad [T_3]_{BSA} = \frac{1}{2} [A_3] [C_3]_{BSA} [A_3]^T, \tag{3.102}$$

where

$$[A_3] = \begin{bmatrix} 1 & 0 & 1 \\ 1 & 0 & -1 \\ 0 & \sqrt{2} & 0 \end{bmatrix} \qquad [A_3]^T = \begin{bmatrix} 1 & 1 & 0 \\ 0 & 0 & \sqrt{2} \\ 1 & -1 & 0 \end{bmatrix}. \tag{3.103}$$

### 3.2.3 Mueller and Kennaugh Matrices

In the previous sections we have seen that the scattering matrix characterizes a scatterer, from the polarization point of view, by providing a relationship between the incident and scattered field vectors. In an analogous way, a matrix could be defined for relating the Stokes vector of the incident and scattered fields. This new matrix is known as *Mueller matrix*, and is defined in the following.

The Mueller matrix, $[M]$, relates the Stokes vector of the incident and the scattered field, i.e.:

$$\mathbf{g}^s = \frac{1}{r^2}[M]\mathbf{g}^i. \tag{3.104}$$

The Mueller matrix is a $4 \times 4$ real matrix, that can be expressed in terms of the elements of the coherency matrix according to the parameterization in (3.93). For a general case, the Mueller matrix has the form:

$$[M] = \begin{bmatrix} A_0 + B_0 & C + N & H + L & F + I \\ C - N & A + B & E + J & G + K \\ H - L & E - J & A - B & D + M \\ I - F & K - G & M - D & A_0 - B_0 \end{bmatrix}. \tag{3.105}$$

If the backscatter case with reciprocity is examined, the resulting Mueller matrices for both polarization conventions are:

$$[M]_{FSA} = \begin{bmatrix} A_0 + B_0 & C & L & I \\ C & A + B_0 & J & K \\ -L & -J & A - B_0 & D \\ I & K & -D & A_0 - B_0 \end{bmatrix} \tag{3.106}$$

and

$$[M]_{BSA} = \begin{bmatrix} A_0 + B_0 & C & H & F \\ C & A_0 + B & E & G \\ H & E & A_0 - B & D \\ -F & -G & -D & A_0 - B_0 \end{bmatrix}. \tag{3.107}$$

At this stage it is important to point out a convention usually employed in the radar community. It is known that, for optimal reception, the antenna must be matched to the incoming wave. This is equivalent to saying that the incident field to the antenna (i.e. the scattered vector $\mathbf{E}^s$) and the antenna polarization must be matched. The matching optimization is formally achieved by conjugating the received scattered field. As a result, the polarization ellipses of the antenna and the field are identical, but travel in opposite directions with respect to the antenna reference. This scheme is depicted in Fig. 3.7, where vector
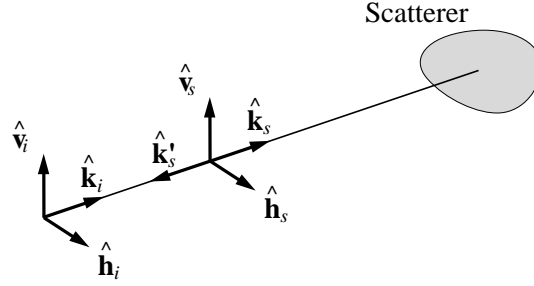
**Fig. 3.7.** Backscattering geometry with the BSA convention and matching transformation

$\hat{\mathbf{k}}'_s = -\hat{\mathbf{k}}_s$ denotes the new propagation direction accordingly. Of course, for that processing to make sense, the BSA convention must be used when defining the polarizations. The final consequence of this conjugation is that the $\mathbf{E}^s$ vector changes its handedness with respect to the original BSA. Therefore, the ellipticity angle $\chi$ has the opposite sign and, as a result, the last element of the Stokes vector of the scattered field changes its sign too. Finally, if this criterion is accounted for in (3.107), the sign of the last row of the Mueller matrix is changed.

Since this matching step is commonly used in radar polarimetry, the resulting matrix (with opposite sign in the last row) must be differentiated to avoid confusion with the original Mueller matrix, as it was encouraged in [145]. The new matrix is therefore usually known as the *Kennaugh matrix* $[K]$, and in the backscattering case with reciprocity yields:

$$[K] = \begin{bmatrix} A_0 + B_0 & C & H & F \\ C & A_0 + B & E & G \\ H & E & A_0 - B & D \\ F & G & D & B_0 - A_0 \end{bmatrix}. \tag{3.108}$$

Thus, the Kennaugh matrix is symmetric under the BSA convention, whereas the Mueller matrices (both under FSA and BSA conventions) are not symmetric.

As already explained, the Mueller matrix and the Kennaugh matrix do not differ so much: only the elements of one row have opposite signs. This well-known similarity has led to many researchers mistaking one matrix for the other. The key point to avoid any confusion is the origin of their definition, since the two matrices correspond to two distinct operations: the Mueller matrix relates the scattered field to the incident field by using the Stokes formalism, whereas the Kennaugh matrix provides the received power, given the receiving antenna polarization characteristics.

In this thesis, the use of Mueller and Kennaugh matrices will be very scarce because the polarimetric information will usually be treated by means of the coherency matrix. However, it seemed important to clarify their definitions in order to ease a possible comparison between results obtained with the coherency matrix and those from the Mueller or Kennaugh matrices.

A last remark must be stated about both matrices. It is also possible to define a

relation between the Stokes vectors of the incident and scattered field by using the Kennaugh matrix, in a similar way to (3.104). The new relation is:

$$\mathbf{g}_K^s = \frac{1}{r^2}[K]\mathbf{g}^i,\tag{3.109}$$

where the scattered Stokes vector is modified (as denoted by the subscript) with respect to the original one, having reversed the sign of the fourth element.

## 3.3  Target Decomposition Theory

As explained in Section 2.2, the central point of this thesis is the extraction of physical information about the target by means of an analysis of the polarization matrices that describe the target. This analysis is known as *target decomposition* (TD) and is formally presented in this Section.

Firstly, the matrices previously defined are extended to the the case of scattering by natural random targets, which is the group where, among others, vegetation is included. Then, the TD theory based on eigenvalue analysis of the coherency matrix is fully developed.

### 3.3.1  Scattering by Random Media. Partial Polarization

In Section 3.2 the description of the polarization characteristics of a scatterer has been carried out by using several matrices, and the relation between all these matrices has also been shown. The common point of all the polarization descriptors (matrices) presented so far is that all of them have been defined by considering the polarization of the wave to behave in a deterministic manner, i.e. the wave is monochromatic, and $\omega$, $a_v$, $a_h$ and $\Delta\phi$ are deterministic or constant. Such a wave is said to be *completely polarized*. However, although the wave transmitted by a radar can be considered completely polarized in most cases, the field scattered by any natural scatterer is seldom completely polarized when observed as a function of time or spatial position. This "loss" of polarization is due to the randomness of the illuminated scene, unavoidable noise, etc. The extreme case is that of a wave whose polarization state changes in a totally random way, so that it is equally probable to find any possible polarization state from a single observation. Such a wave is known as *unpolarized*. The common situation is between the two extremes, and the wave is said to be *partially polarized*.

Historically, one of the most widely used polarization descriptors of a wave is based on the Stokes vector. For radar scattering from a natural scene, the electric field components are random variables, and averaging must be performed to express the polarimetric information of the wave. In the case of the Stokes vector, the averaging is incoherent, since the

elements of such a vector are defined as intensities. The Stokes vector of a partially polarized wave is defined as:

$$\langle \mathbf{g} \rangle = \begin{bmatrix} \langle I \rangle \\ \langle Q \rangle \\ \langle U \rangle \\ \langle V \rangle \end{bmatrix} = \begin{bmatrix} \langle |E_v|^2 \rangle + \langle |E_h|^2 \rangle \\ \langle |E_v|^2 \rangle - \langle |E_h|^2 \rangle \\ \langle 2\Re(E_v E_h^*) \rangle \\ -\langle 2\Im(E_v E_h^*) \rangle \end{bmatrix} = \begin{bmatrix} \langle a_v^2 \rangle + \langle a_h^2 \rangle \\ \langle a_v^2 \rangle - \langle a_h^2 \rangle \\ \langle 2a_v a_h \cos \Delta\phi \rangle \\ \langle 2a_v a_h \sin \Delta\phi \rangle \end{bmatrix}, \tag{3.110}$$

where $\langle \cdot \rangle$ denotes the ensemble averaging over the available samples. For example:

$$\langle I \rangle = \frac{1}{N} \sum_{n=1}^{N} I_n \tag{3.111}$$

wherein $I_n$ is the total intensity measured in the $n$th individual measurement.

For an unpolarized wave, $\langle a_v^2 \rangle = \langle a_h^2 \rangle$ and $E_v$ and $E_h$ are uncorrelated, thus leading to an averaged Stokes vector with only one nonzero element, $I$, since $Q = U = V = 0$. For a partially polarized case, the equality in (3.54) becomes:

$$I^2 \geqslant Q^2 + U^2 + V^2, \tag{3.112}$$

and the *degree of polarization* of a wave is defined as:

$$m = \frac{\text{Polarized power}}{\text{Total power}} = \frac{\sqrt{Q^2 + U^2 + V^2}}{I}, \qquad 0 \leqslant m \leqslant 1. \tag{3.113}$$

In the same way as the polarization of a wave can be described with the average Stokes vector, the polarization characteristics of a scatterer can be represented by an average matrix. The averaging can be performed in two alternative ways: coherently and incoherently. Coherent averaging is suitable to be applied, by definition, to the scattering matrix, whereas the incoherent averaging is appropriate for the other matrix descriptors defined in last section (Mueller, Kennaugh, coherency and covariance matrices). The average matrices can be computed by averaging every element of them. So the definition of the average matrices is the same as previous section but adding the average operation $\langle \cdot \rangle$ at each element. To avoid confusion, it is usual to denote the averaged matrix as $\langle [T] \rangle$ instead of $[T]$ as before.

Note that, after averaging, the relationship between the incoherently averaged matrices ($\langle [M] \rangle, \langle [K] \rangle, \langle [T] \rangle, \langle [C] \rangle$) and a single scattering matrix $[S]$ is no longer an unique correspondence, except in the trivial case of the averaging of proportional scattering matrices. The necessary conditions for that unique correspondence have been formulated in several ways (see for example [146]), but the simpler one was presented in [45], where only the *rank* of the coherency matrix must be examined. An incoherently averaged matrix (of any kind of those defined before) has such an equivalent matrix $[S]$ only if the matrix $\langle [T] \rangle$ has rank equal to one. This loss of equivalence increases the number of independent parameters that are necessary to fully characterize the polarization information. The averaged matrices are represented by sixteen independent values in the bistatic case and nine independent parameters in the monostatic reciprocal situation. This can be easily checked in the parameterization presented in last section.

Whether to use incoherent or coherent averaging, what kind of matrix is better to be analyzed, and what type of analysis or decomposition to perform are subjects that have attracted a lot of attention over the last decades in radar polarimetry. Following the final objective of TD theories, i.e. to decompose or express such an average matrix into a sum of matrices representing independent elements with associated physical mechanisms, there have been different approaches in the literature. All of them have already been reviewed and compared in Chapter 2. It was concluded that the coherent decompositions based on the scattering matrix suffer problems with coherent speckle noise, basis invariance and lack of basis orthogonality. On the other hand, the so-called Huynen type decompositions attempt the extraction of a single scattering matrix from an incoherently averaged matrix, and the remainder is assigned to a distributed target or a "noise" contribution, but this separation into single scattering plus noise is not appropriate for many natural targets. Finally, in contrast, the goal of the eigenvector-based TD analyses is to represent the averaged data as a summation of single scattering mechanisms, and this separation is well founded in the underlying mathematical properties of any eigenvalue approach: 1) the eigenvalue problem is basis invariant, and 2) the solution of the problem leads to a diagonalization of the coherency matrix, thus yielding statistical independence between the set of scattering processes.

In summary, the TD approach based on the eigenvector decomposition of the coherency matrix has been extensively used throughout this thesis. It has been chosen as the basic tool for the analysis of polarimetric data from vegetation and for the construction of inverse algorithms for retrieval of physical parameters. The next section is devoted to an explanation of all the details of this approach.

## 3.3.2 Eigenvector Decomposition of the Coherency Matrix

Let us assume that we have a measured coherency matrix, obtained after an ensemble averaging, $\langle [T] \rangle$, and defined according to (3.89) and (3.100), from a scene with reciprocity and in the backscatter direction:

$$\langle [T] \rangle = \langle \mathbf{k}_{3P} \cdot \mathbf{k}_{3P}^{*T} \rangle. \tag{3.114}$$

Then, the eigenvector-based decomposition states that the coherency matrix can be written in the form:

$$\langle [T] \rangle = [U_3][\Sigma][U_3]^{-1}, \tag{3.115}$$

where

$$[\Sigma] = \begin{bmatrix} \lambda_1 & 0 & 0 \\ 0 & \lambda_2 & 0 \\ 0 & 0 & \lambda_3 \end{bmatrix} \tag{3.116}$$

is a $3 \times 3$ diagonal matrix with nonnegative real elements, $\lambda_1 \geqslant \lambda_2 \geqslant \lambda_3 \geqslant 0$, which are the eigenvalues of the coherency matrix; and

$$[U_3] = [\mathbf{e}_1 \, \mathbf{e}_2 \, \mathbf{e}_3] = \begin{bmatrix} \cos\alpha_1 & \cos\alpha_2 & \cos\alpha_3 \\ \sin\alpha_1 \cos\beta_1 e^{j\delta_1} & \sin\alpha_2 \cos\beta_2 e^{j\delta_2} & \sin\alpha_3 \cos\beta_3 e^{j\delta_3} \\ \sin\alpha_1 \sin\beta_1 e^{j\gamma_1} & \sin\alpha_2 \sin\beta_2 e^{j\gamma_2} & \sin\alpha_3 \sin\beta_3 e^{j\gamma_3} \end{bmatrix} \quad (3.117)$$

is a $3 \times 3$ matrix whose columns are the eigenvectors of the coherency matrix: $\mathbf{e}_1$, $\mathbf{e}_2$ and $\mathbf{e}_3$. The parameterization of the matrix $[U_3]$ will be explained in next section.

Equivalently, we can express the coherency matrix as a linear combination of the outer products of the eigenvectors. The weights of this linear combination are the eigenvalues:

$$\langle [T] \rangle = \sum_{i=1}^{3} \lambda_i \, \mathbf{e}_i \mathbf{e}_i^{*T}. \quad (3.118)$$

By simply comparing (3.118) with (3.114), it is evident that the eigenvectors are physically equivalent to scattering mechanisms, since they are targets vectors which can be obtained from a vectorization of a scattering matrix. Therefore, the interpretation of (3.118) is that the coherency matrix can be decomposed as a weighted sum of three scattering mechanisms. This decomposition has the intrinsic characteristics of every eigenvalue decomposition, namely:

1. The decomposition is basis invariant, i.e. the same result is obtained for any basis that can be employed in the polarization definition.

2. The three scattering mechanisms are statistically independent.

3. The eigenvalues are the weights of the decomposition, so they indicate which scattering mechanisms are the dominant ones, and quantify in what proportion they dominate.

The expressions presented so far provide a general framework, since only reciprocity was assumed. The next subsections are dedicated to show the particular form of the decomposition when the scene exhibits symmetries, and to provide a physical interpretation of the parameterization of the matrix $[U_3]$.

## 3.3.2.1 Symmetries

Let us consider a medium that contains many identical particles or scatterers with different orientations in space. If a certain assumption about the distribution of orientations is made, it is possible to find simplifications in the polarization scattering matrices. This would be also the case if there are particles that can be regarded as mirror images of others also present in
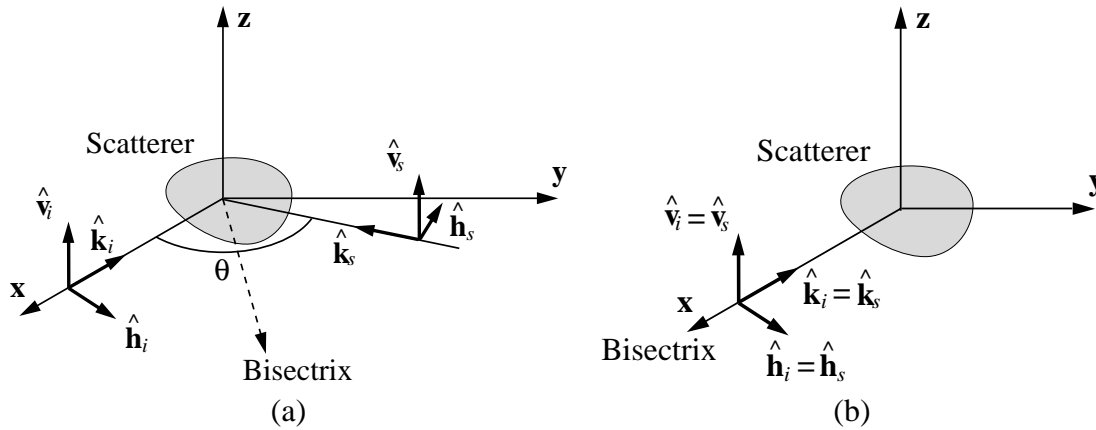
**Fig. 3.8.** General geometry of the scattering by an arbitrary particle (a), and particular case of backscattering (b).

the scene. Finally, an equivalent situation is that of particles exhibiting a plane of symmetry: they are their own mirror images.

The idea of the analysis presented here is the following. If the scattering matrix of a particle in a particular position and for a particular direction is known, then the scattering matrix of the same particle, or its mirror image, in certain symmetrical positions is also known. This holds for the scattering matrix, but also for the rest of the matrices usually employed in polarimetry, thus also for the coherency matrix. These ideas were firstly formulated in [11, pp. 46–59] for any arbitrary geometry by using the FSA convention. Here, the results are rewritten for the BSA convention. Moreover, they are explained in more detail for backscattering problems from reciprocal targets.

The general geometry of the scattering by an arbitrary particle is illustrated in Fig. 3.8a, where, for convenience and without loss of generality, the direction of incidence has been selected as the negative **x** axis. The directions of incidence and scattering form a plane known as the *scattering plane*, which in Fig. 3.8a coincides with the $x$–$y$ plane. The line in the backscattering plane that bisects the angle $\theta$ between the incident and the scattered directions is called the *bisectrix*. Accordingly, the plane through the bisectrix and perpendicular to the plane of scattering is known as *bisectrix plane*. There are three basic operations that yield scattering matrices directly related to the original one:

1. Rotation of $180°$ about the bisectrix.

2. Mirroring with respect to the plane of scattering.

3. Mirroring with respect to the bisectrix plane.

Any two of these three transformations, in succession, give the third one. In the case of backscattering, the incidence and scattering directions are parallel, so the bisectrix coin-
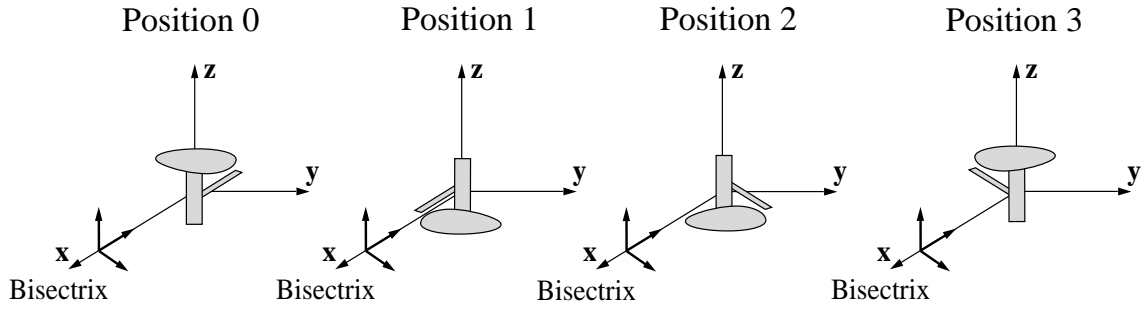
**Fig. 3.9.** Four related positions of an arbitrary particle. 0: Original, 1: Rotated $180°$ about the bisectrix, 2: Mirrored with respect to the plane of scattering, and 3: Mirrored with respect to the bisectrix plane

cides with both $\hat{\mathbf{k}}_i$ and $\hat{\mathbf{k}}_s$ (this direction is commonly known as the *line of sight*). As a result, the scattering plane and, consequently, the bisectrix plane become ill defined. However, by looking at this case as the limit of the previous general arrangement when $\theta \to 0$, the scattering plane can still be identified as the $x$–$y$ plane, and the bisectrix plane should be the $x - z$ plane. This new set-up is depicted in Fig. 3.8b.

The four positions (original plus rotated and mirrored) of the particle are shown in Fig. 3.9 for the backscattering case. The shape of the scatterer has been selected to clarify the following mirror and rotation operations. The scattering matrix of the original situation, denoted as $[S_0]$, and the resulting scattering matrices for the other three configurations, all according to the BSA convention, yield:

$$[S_0] = \begin{bmatrix} a & b \\ b & d \end{bmatrix} \quad [S_1] = \begin{bmatrix} a & b \\ b & d \end{bmatrix} \quad [S_2] = \begin{bmatrix} a & -b \\ -b & d \end{bmatrix} \quad [S_3] = \begin{bmatrix} a & -b \\ -b & d \end{bmatrix} \tag{3.119}$$

The proof of the relationships to the original scattering matrix is not detailed here. However, it is easy to see that $[S_1]$ comes from reciprocity relationships, while $[S_2]$ is only due to a change in one coordinate. Finally, $[S_3]$ can be demonstrated as the successive applications of the two other transformations. Note that from (3.119) we see that there are only two possible forms of the scattering matrix, both symmetric.

In the following, three assumptions will be done according to the distribution of particles among these positions. These assumptions lead to some important cases in remote sensing of natural targets.

**Reflection Symmetry** The first case is that of a distributed target that has one plane of symmetry containing the line of sight. This means that for every particle ($A$) at one side of the plane, there is a mirrored or image particle ($A'$) at the other side. This property is named *reflection symmetry*. If we construct the target vectors (based on Pauli matrices) of

both particles, they result in:

$$\mathbf{k}_A = \begin{bmatrix} a_1 \\ a_2 \\ a_3 \end{bmatrix} \qquad \mathbf{k}_{A'} = \begin{bmatrix} a_1 \\ a_2 \\ -a_3 \end{bmatrix}. \tag{3.120}$$

Then, after integration of the contributions of all the particles in the distributed target, we can compose the coherency matrix as the sum of the coherency matrix from both symmetrical components:

$$\langle [T] \rangle = \langle [T]_A \rangle + \langle [T]_{A'} \rangle = \begin{bmatrix} x & x & x \\ x & x & x \\ x & x & x \end{bmatrix} + \begin{bmatrix} x & x & -x \\ x & x & -x \\ -x & -x & x \end{bmatrix} = \begin{bmatrix} x & x & 0 \\ x & x & 0 \\ 0 & 0 & x \end{bmatrix}, \tag{3.121}$$

wherein the symbol $x$ denotes a general nonzero element of the coherency matrix.

The identity in (3.121) shows that if the scatterer has reflection symmetry about a plane, then the coherency matrix will have this general form with only five nonzero elements. The interpretation of the zero terms is that the crosspolar scattering is uncorrelated with the copolar terms.

Since the coherency matrix shown in (3.121) has a simpler form than that of the general case, the particular expressions of the eigenvector decomposition for this specific case will be written here. It is easy to derive the new expression for the unitary matrix $[U_3]$ in (3.117) [56, 45]:

$$[U_3] = \begin{bmatrix} e^{j\phi}\cos\alpha & e^{j\delta}\sin\alpha & 0 \\ -e^{-j\delta}\sin\alpha & e^{-j\phi}\cos\alpha & 0 \\ 0 & 0 & 1 \end{bmatrix}, \tag{3.122}$$

and substituting it in (3.115) yields[5]:

$$\langle [T] \rangle = \begin{bmatrix} \lambda_1\cos^2\alpha + \lambda_2\sin^2\alpha & \cos\alpha\sin\alpha(\lambda_2 - \lambda_1)e^{-j(\delta+\phi)} & 0 \\ \cos\alpha\sin\alpha(\lambda_2 - \lambda_1)e^{-j(\delta+\phi)} & \lambda_2\cos^2\alpha + \lambda_1\sin^2\alpha & 0 \\ 0 & 0 & \lambda_3 \end{bmatrix}. \tag{3.123}$$

Therefore, the coherency matrix of a target with reflection symmetry is fully characterized by five parameters. From (3.123) these five parameters are: $\lambda_1$, $\lambda_2$, $\lambda_3$, $\alpha$ and $(\delta + \phi)$. This fact was firstly stated in [147] by using the covariance matrix $[C]$.

**Rotation Symmetry** The second special case is that of a medium with *rotation symmetry*, i.e. the coherency matrix is invariant when the target (or alternatively the antenna) is rotated about the line of sight. This condition is examined in the following.

---

[5]This parameterization will be further explained in the next section

Let $[U_3^R(\theta)]$ be an unitary matrix that allows the computation of the coherency matrix when the target is rotated by an angle $\theta$ about the line of sight. The matrix $[U_3^R(\theta)]$ is known as *rotation matrix*, and the expression for the rotated coherency matrix is:

$$\langle[T(\theta)]\rangle = [U_3^R(\theta)]\,\langle[T]\rangle\,[U_3^R(\theta)]^{-1}, \tag{3.124}$$

where

$$[U_3^R(\theta)] = \begin{bmatrix} 1 & 0 & 0 \\ 0 & \cos 2\theta & \sin 2\theta \\ 0 & -\sin 2\theta & \cos 2\theta \end{bmatrix} \qquad [U_3^R(\theta)]^{-1} = \begin{bmatrix} 1 & 0 & 0 \\ 0 & \cos 2\theta & -\sin 2\theta \\ 0 & \sin 2\theta & \cos 2\theta \end{bmatrix}. \tag{3.125}$$

We have seen in previous sections that the coherency matrix is composed by the ensemble averaging of outer products of target vectors. Since these target vectors will always remain in a subspace of all possible target vectors, there will always be other targets vectors $\mathbf{k}_N$ such that,

$$\langle[T]\rangle\mathbf{k}_N = 0, \tag{3.126}$$

so the vectors $\mathbf{k}_N$ define the null space of the coherency matrix [45]. If the target is rotationally invariant, then:

$$\langle[T(\theta)]\rangle\mathbf{k}_N = 0, \tag{3.127}$$

i.e. the null space should be unchanged under the transformation of (3.124). By substituting (3.127) into (3.124), the requirement for invariance under rotations is equivalent to find the eigenvectors of the rotation matrix:

$$\left([U_3^R(\theta)]^{-1} - \lambda[I_3]\right)\mathbf{k}_N = 0, \tag{3.128}$$

where $[I_3]$ is the $3 \times 3$ identity matrix.

The solution of (3.128) yields three eigenvectors,

$$\mathbf{k}_N^1 = \begin{bmatrix} 1 \\ 0 \\ 0 \end{bmatrix}, \qquad \mathbf{k}_N^2 = \frac{1}{\sqrt{2}}\begin{bmatrix} 0 \\ 1 \\ j \end{bmatrix}, \qquad \mathbf{k}_N^3 = \frac{1}{\sqrt{2}}\begin{bmatrix} 0 \\ 1 \\ -j \end{bmatrix}, \tag{3.129}$$

that are invariant under rotations about the line of sight. This fact implies that if the coherency matrix of a scene is to be rotationally invariant, then it must be constructed from a linear combination of the outer products of this eigenvectors, as in (3.118):

$$\langle[T]\rangle = \sum_{i=1}^{3} \lambda_i\,\mathbf{k}_N^i\mathbf{k}_N^{i*T} = \begin{bmatrix} \lambda_1 & 0 & 0 \\ 0 & (\lambda_2 + \lambda_3)/2 & j(\lambda_2 - \lambda_3)/2 \\ 0 & -j(\lambda_2 - \lambda_3)/2 & (\lambda_2 + \lambda_3)/2 \end{bmatrix}. \tag{3.130}$$

In this case, hence, there are also five nonzero coefficients in the coherency matrix, but the coherency matrix is fully characterized by only using three parameters. This reduction in the number of independent factors, with respect to the reflection symmetry case, was expected because the rotation symmetry is more restrictive.

**Full Azimuthal Symmetry**    Finally, let us assume that the medium exhibits not only reflection symmetry about a special plane, but also rotation symmetry, that is to say, all planes that contain the line of sight are valid as reflection planes. This property is called *full azimuthal symmetry*. If a coherency matrix is expected to represent a target with such a symmetry, it must satisfy simultaneously the conditions of reflection and rotation symmetry.

Both conditions can be expressed as follows. We know that the target is rotation invariant, so it has a coherency matrix like the one in (3.130). At the same time, according to the explanation of the reflection symmetry, the total coherency matrix is the sum of the coherency matrices of the mirrored parts. Then, we can decompose the coherency matrix of a target with full azimuthal symmetry as:

$$\langle[T]\rangle = \begin{bmatrix} \lambda_1 & 0 & 0 \\ 0 & (\lambda_2+\lambda_3)/2 & j(\lambda_2-\lambda_3)/2 \\ 0 & -j(\lambda_2-\lambda_3)/2 & (\lambda_2+\lambda_3)/2 \end{bmatrix} + \begin{bmatrix} \lambda_1 & 0 & 0 \\ 0 & (\lambda_2+\lambda_3)/2 & -j(\lambda_2-\lambda_3)/2 \\ 0 & j(\lambda_2-\lambda_3)/2 & (\lambda_2+\lambda_3)/2 \end{bmatrix}$$

$$= \begin{bmatrix} 2\lambda_1 & 0 & 0 \\ 0 & (\lambda_2+\lambda_3) & 0 \\ 0 & 0 & (\lambda_2+\lambda_3) \end{bmatrix}. \tag{3.131}$$

Therefore, the resulting coherency matrix of a target with full azimuthal symmetry is a diagonal matrix, with only two different parameters. It is equivalent to saying that the Pauli matrices are the eigenvectors, and that there are two equal eigenvalues.

### 3.3.2.2   Parameterization of the Eigenvector Decomposition

Having formulated the eigenvector decomposition of the coherency matrix, the underlying physical meaning of the resulting parameters is studied in this section from the point of view of the extraction of information about the target.

**Definitions**    We have previously demonstrated in (3.118) that an average coherency matrix, obtained in a monostatic measurement with reciprocity from a natural random target, can be expressed as a linear combination of the outer products of three eigenvectors. In other words, this means that the coherency matrix can be decomposed into a sum of three independent scattering mechanisms, since each eigenvector corresponds to a scattering matrix and they are statistically independent from the properties of every eigenvalue decomposition (the coherency matrix becomes diagonal). The weights of the linear combination are, not surprisingly, the eigenvalues, which yield the relative contribution of each component, $\lambda_1 \geqslant \lambda_2 \geqslant \lambda_3 \geqslant 0$.

These eigenvalues can be combined to form a single scalar quantity that is a measure of the polarimetric disorder or randomness of the system. This scalar, firstly introduced

in [52, 57], is known as *entropy* and is defined for backscatter as:

$$H = -\sum_{i=1}^{3} p_i \log_3 p_i, \tag{3.132}$$

where

$$p_i = \frac{\lambda_i}{\sum_{i=1}^{3} \lambda_i} \tag{3.133}$$

are the probabilities of each eigenvalue (in the von Neumann sense), and the entropy is defined in the range $0 \leqslant H \leqslant 1$. Note also that $\sum_{i=1}^{3} p_i = 1$.

At one extreme of (3.132) we find the case of a nondepolarizing system and consequently the coherency matrix has a single scattering matrix equivalent descriptor. For this case, $\langle [T] \rangle$ has only one nonzero eigenvalue and the entropy is zero. At the other extreme we find a perfect depolarizer with $H = 1$. This means that the target depolarizes all the incident wave states, regardless of their polarization. For that case, we have degenerate eigenvalues[6] and, as a result, any basis set can be used to represent the system or target. Such cases represent complete polarimetric disorder. Their corresponding Mueller and coherency matrices take the form:

$$\langle [M] \rangle = \begin{bmatrix} x & 0 & 0 & 0 \\ 0 & 0 & 0 & 0 \\ 0 & 0 & 0 & 0 \\ 0 & 0 & 0 & 0 \end{bmatrix} \qquad \langle [T] \rangle = \begin{bmatrix} x & 0 & 0 \\ 0 & x & 0 \\ 0 & 0 & x \end{bmatrix}. \tag{3.134}$$

Both extremes represent somewhat ideal behaviors, so we can expect in practice systems to lie between them, thus being able to observe important information on the entropy and eigenvectors about the target characteristics, correlations, etc.

Turning back to (3.117), we also adopted a parameterization of the eigenvector of the form:

$$\mathbf{e} = \begin{bmatrix} \cos\alpha \\ \sin\alpha\cos\beta e^{j\delta} \\ \sin\alpha\sin\beta e^{j\gamma} \end{bmatrix}. \tag{3.135}$$

In (3.135) the absolute phase of the eigenvector has been canceled, so it is fully characterized by four parameters: $\alpha$, $\beta$, $\delta$ and $\gamma$. This eigenvector is equivalent to a scattering matrix (or scattering mechanism), with power normalized to one. In fact, we have seen that any scattering matrix can be characterized by five parameters, so the missing one is the power, which is proportional to the square root of the eigenvalue $\sqrt{\lambda}$.

Before going into the interpretation of the individual parameters, let us take a look at the probabilistic interpretation of the scattering processes. We can model the target as a three

---

[6]Two or more eigenvalues are said to be degenerate when they are equal

symbol Bernoulli process, i.e. the target is represented by three $[S]$ matrices, the eigenvectors in (3.117), which occur with probabilities $p_i$. In this way, for example, the parameter $\alpha$ is associated with a random sequence like:

$$\alpha(n) = \alpha_1 \, \alpha_3 \, \alpha_1 \, \alpha_1 \, \alpha_2 \, \alpha_3 \, \alpha_1 \, \alpha_2 \, \ldots \tag{3.136}$$

and the best estimate of the parameter is given by the mean of this sequence. This mean is evaluated as:

$$\overline{\alpha} = \sum_{i=1}^{3} p_i \alpha_i = p_1 \alpha_1 + p_2 \alpha_2 + p_3 \alpha_3. \tag{3.137}$$

If this type of mean is extracted for all parameters we can establish a dominant mechanism or scattering matrix, namely

$$\overline{\mathbf{e}} = \begin{bmatrix} \cos \overline{\alpha} \\ \sin \overline{\alpha} \cos \overline{\beta} e^{j\overline{\delta}} \\ \sin \overline{\alpha} \sin \overline{\beta} e^{j\overline{\gamma}} \end{bmatrix}, \tag{3.138}$$

wherein

$$\overline{\alpha} = p_1 \alpha_1 + p_2 \alpha_2 + p_3 \alpha_3 \tag{3.139}$$
$$\overline{\beta} = p_1 \beta_1 + p_2 \beta_2 + p_3 \beta_3 \tag{3.140}$$
$$\overline{\delta} = p_1 \delta_1 + p_2 \delta_2 + p_3 \delta_3 \tag{3.141}$$
$$\overline{\gamma} = p_1 \gamma_1 + p_2 \gamma_2 + p_3 \gamma_3. \tag{3.142}$$

The following step is the physical interpretation of the parameters used in the expression of the eigenvectors. In principle, $\delta$ and $\gamma$ are phase terms without a straightforward interpretation, however we will see that the other two values have a clear physical meaning, thus leading to a useful interpretation of the scattering mechanisms present in the target. It is evident from (3.135) that both $\alpha$ and $\beta$ can be considered as angles. All possible target vectors can be mapped into $(\alpha, \beta)$ pairs (discarding the phase terms) by using the following effective range of validity for both angles:

$$0 \leqslant \alpha \leqslant 90° \qquad 0 \leqslant \beta \leqslant 180° \tag{3.143}$$

A first inspection of the $\alpha$ dependence of the eigenvector entries yields some typical features. For example, if $\alpha = 0$ the only nonzero element of the eigenvector is the first one, so $S_{vv} = S_{hh}$ and $S_{hv} = 0$. This is the common behavior of the scattering by a sphere, or a surface normal to the incidence direction. If we go to the other extreme, $\alpha = 90°$, the only zero element is the first, so $S_{vv} = -S_{hh}$. This negative correlation is typical of a dihedral or an helix. Another important case is $\alpha = 45°$, which corresponds to a dipole-like scattering, since the scattered wave is always linearly polarized.
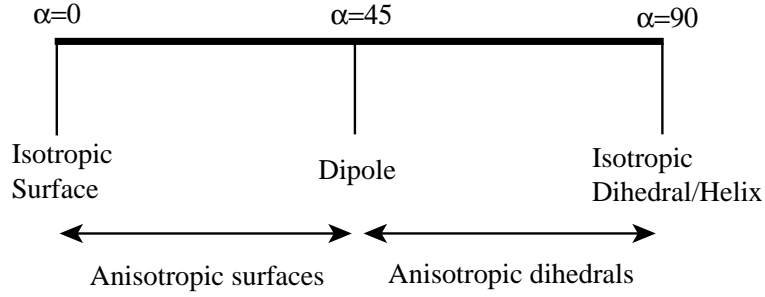
**Fig. 3.10.** Schematic representation of the range of the $\alpha$ parameter

In order to clarify these ideas, and to include the effect of the $\beta$ angle, it is useful to decompose the eigenvector as the product of three matrices as:

$$\mathbf{e} = \begin{bmatrix} 1 & 0 & 0 \\ 0 & e^{j\delta} & 0 \\ 0 & 0 & e^{j\gamma} \end{bmatrix} \begin{bmatrix} 1 & 0 & 0 \\ 0 & \cos\beta & -\sin\beta \\ 0 & \sin\beta & \cos\beta \end{bmatrix} \begin{bmatrix} \cos\alpha & -\sin\alpha & 0 \\ \sin\alpha & \cos\alpha & 0 \\ 0 & 0 & 1 \end{bmatrix} \begin{bmatrix} 1 \\ 0 \\ 0 \end{bmatrix}, \qquad (3.144)$$

where the second and third matrices are typical rotation operators, and the first one only accounts for the phases.

More generally, the following *Point Target Reduction Theorem* can be established: Any polarimetric backscattering mechanism obeying reciprocity can be reduced to the identity $[1, 0, 0]^T$ by a series of three matrix transformations, as shown in (3.145). Note that, the absolute phase has been included in (3.145) for generality.

$$\mathbf{e} = \begin{bmatrix} 1 \\ 0 \\ 0 \end{bmatrix} = \begin{bmatrix} \cos\alpha & \sin\alpha & 0 \\ -\sin\alpha & \cos\alpha & 0 \\ 0 & 0 & 1 \end{bmatrix} \begin{bmatrix} 1 & 0 & 0 \\ 0 & \cos\beta & \sin\beta \\ 0 & -\sin\beta & \cos\beta \end{bmatrix} \begin{bmatrix} e^{-j\phi} & 0 & 0 \\ 0 & e^{-j\delta} & 0 \\ 0 & 0 & e^{-j\gamma} \end{bmatrix} \mathbf{k} \quad (3.145)$$

As we have outlined above, although $\alpha$ seems to be a rotation angle, it can be identified as the target scattering type. This interpretation is illustrated in Fig. 3.10, where the terms "isotropic" and "anisotropic" refer to the amplitude differences between vertical and horizontal polarizations (isotropic means that both are equal, while anisotropic means that they are different). On the other hand, the angle $\beta$ is a true rotation angle and gives the orientation of the target which corresponds to the scattering mechanism described by $\alpha$. For the sake of completeness, Table 3.1 shows the values of the four parameters for some canonical targets with known scattering behavior, namely: sphere, dipole, dihedral and helix. For those canonical scatterers whose orientation is not trivial, the angle $\beta$ is proportional to the orientation. For example, for a dipole or a dihedral that are positioned forming an angle $\theta$ with respect to $\hat{\mathbf{v}}$, the angle $\beta$ is twice this angle: $\beta = 2\theta$. Details about the scattering matrices for many canonical targets can be consulted elsewhere [6, pp. 69–77],[33, pp. 33–44].

**Roll-Invariant Parameters**    We have already seen that the coherency of a random target can be decomposed by following an eigenanalysis, and that some parameters related to the randomness of the process and the scattering mechanisms that are present in the scene can be retrieved from the coherency matrix. An important question arises at this point: Are these retrieved parameters dependent on the relative orientation of the antenna with respect to the target? If this were the situation, the scattering mechanisms that we extract would depend on that orientation, thus not being reliable. For example, think about a target whose dominant scattering mechanism is dipole-like, but when it is rotated about the line of sight it becomes a surface-like or a dihedral scattering mechanism. Evidently, this is an undesirable situation, because we want to know what scattering mechanism is in the scene regardless of its particular orientation with respect to the radar.

In the following we will analyze which of the parameters obtained from the eigenvector decomposition are independent of the orientation of the target about the line of sight. These parameters will be called *roll-invariant*. This analysis can be readily performed by using again the unitary rotation matrix $[U_3^R(\theta)]$ presented in the symmetries study of Section 3.3.2.1. In this way, the coherency matrix of a target rotated by angle $\theta$ about the line of sight is:

$$\langle [T(\theta)] \rangle = [U_3^R(\theta)] \, \langle [T] \rangle \, [U_3^R(\theta)]^{-1}. \tag{3.146}$$

If we substitute the eigenvalue decomposition of the original coherency matrix (3.115) into (3.146), it yields:

$$\langle [T(\theta)] \rangle = [U_3^R(\theta)] \, \langle [T] \rangle \, [U_3^R(\theta)]^{-1} = [U_3^R(\theta)][U_3][\Sigma][U_3]^{-1}[U_3^R(\theta)]^{-1}. \tag{3.147}$$

We can define a new decomposition matrix $[U_3(\theta)] = [U_3^R(\theta)][U_3]$ in order to write

**Table 3.1.** Examples of parameters values for canonical scatterers

|  | $\alpha$ | $\beta$ | $\delta, \gamma$ | $[S]$ |
|---|---|---|---|---|
| Sphere | $0°$ | Arbitrary | Arbitrary | $a \begin{bmatrix} 1 & 0 \\ 0 & 1 \end{bmatrix}$ |
| Dipole at $\theta$ | $45°$ | $2\theta$ | $\delta = \gamma$ | $a \begin{bmatrix} 1 + \cos\beta & \sin\beta \\ \sin\beta & 1 - \cos\beta \end{bmatrix}$ |
| Dihedral at $\theta$ | $90°$ | $2\theta$ | $\delta = \gamma$ | $a \begin{bmatrix} \cos\beta & \sin\beta \\ \sin\beta & -\cos\beta \end{bmatrix}$ |
| Helix | $90°$ | $\pm 45°$ | $\gamma - \delta = 90°$ | $a \begin{bmatrix} 1 & \pm j \\ \pm j & -1 \end{bmatrix}$ |

the last equation as the typical eigenvector decomposition:

$$\langle [T(\theta)] \rangle = [U_3(\theta)][\Sigma][U_3(\theta)]^{-1}, \tag{3.148}$$

where, after some algebraic manipulations, the new matrix is:

$$[U_3(\theta)] = \begin{bmatrix} \cos\alpha_1 & \cos\alpha_2 & \cos\alpha_3 \\ \sin\alpha_1\cos\beta_1' e^{j\delta_1'} & \sin\alpha_2\cos\beta_2' e^{j\delta_2'} & \sin\alpha_3\cos\beta_3' e^{j\delta_3'} \\ \sin\alpha_1\sin\beta_1' e^{j\gamma_1'} & \sin\alpha_2\sin\beta_2' e^{j\gamma_2'} & \sin\alpha_3\sin\beta_3' e^{j\gamma_3'} \end{bmatrix}. \tag{3.149}$$

The inspection of (3.148) and (3.149) gives the following conclusions. Firstly, the eigenvalues are the same as before, so any parameter derived directly from them is roll-invariant. For example, the entropy and probabilities previously defined, and other two parameters widely used, namely: *total power* and *anisotropy*. The total power, $W$, is the trace or sum of the eigenvalues, and represents the total power scattered by the target and collected by an orthogonally polarized antenna pair. The anisotropy, $A$, is a second parameter defined from the ratio between eigenvalues and complements the target entropy. So the expressions of these two additional parameters are:

$$W = \lambda_1 + \lambda_2 + \lambda_3 \qquad A = \frac{\lambda_2 - \lambda_3}{\lambda_2 + \lambda_3} \tag{3.150}$$

In second place, and very importantly, equation (3.149) says that the three scattering mechanisms $\alpha_i$ are the same as before the rotation. Hence, the dominant scattering mechanism $\overline{\alpha}$ is also roll-invariant. This fact is of prime importance when we observe a scene with a radar and want to retrieve the present scattering mechanisms, since we do not have to take care about the orientation of the targets about the line of sight in order to know their behavior.

**Symmetries**   In the previous definitions we have considered the general case of a random target without any symmetry, so we need the three eigenvalues and eigenvectors for defining a "mean" or dominant scattering mechanism. However, when some of the symmetries studied in Section 3.3.2.1 are present, the parameterization of the coherency matrix becomes simpler.

For example, if the scene only exhibits reflection symmetry, the parameterization of the coherency matrix is that shown in (3.123), with the eigenvectors formulated in (3.122). In this case there is no dependence on the orientation angle $\beta$ due to the reflection symmetry. The three eigenvectors can be interpreted, by assuming zero phases for simplicity, as the scattering mechanisms of a dihedral ($S_{vv}$ and $S_{hh}$ with opposite signs), a surface ($S_{vv}$ and $S_{hh}$ with the same sign) and a target that always scatters a cross-polarized signal.

In addition, if a full rotation symmetry about the line of sight is examined, the result in (3.131) states that the coherency matrix is already diagonal. Consequently, the Pauli

matrices are the corresponding eigenvectors. These Pauli matrices, at the same time, correspond to the scattering matrices of a sphere, a dihedral and an helix. Furthermore, it is easy to apply the Bernoulli averaging of the three scattering mechanisms for computing $\overline{\alpha}$, since the $\alpha$ angle of the first eigenvector is zero and the other two (which are the same) is $90°$. If the coherency is rewritten from (3.131) as:

$$\langle [T] \rangle = \begin{bmatrix} \lambda_1 & 0 & 0 \\ 0 & \lambda_2 & 0 \\ 0 & 0 & \lambda_2 \end{bmatrix}, \tag{3.151}$$

then

$$\overline{\alpha} = 0 \cdot \frac{\lambda_1}{\lambda_1 + 2\lambda_2} + 90° \cdot \frac{2\lambda_2}{\lambda_1 + 2\lambda_2} = 90° \cdot \frac{2\lambda_2}{\lambda_1 + 2\lambda_2}. \tag{3.152}$$

This result will used later in this thesis for analyzing the behavior of a random cloud of scattering particles.

**Application: Classification on the $H-\alpha$ Plane**    Although the dominant target vector presented in (3.138) has four parameters, we have seen in the above analysis that for natural random media problems the main component for identifying the scattering behavior of the target is the so-called dominant scattering mechanism $\overline{\alpha}$. This angle has a useful range of $90°$ whose interpretation has already been presented, and is roll-invariant as previously demonstrated. Moreover, if one wants to quantify not only the scattering mechanism, but also the randomness of the scattering process, the target entropy $H$ is an appropriate parameter. Following these ideas, a classification scheme for polarimetric SAR was first postulated in [148] and later firmly described in [62].

The classification procedure is based on the location of the pairs $(H, \overline{\alpha})$ on a 2-D plane. All random scattering mechanisms can be represented in this 2-D space. However, the averaging inherent in this model implies that as the entropy increases the range of $\overline{\alpha}$ is reduced. As a result, not all regions of the $H-\alpha$ plane are equally populated. When $H = 1$ there is only one possible value for $\overline{\alpha}$, which is $60°$. This reflects our increasing inability to distinguish between scattering mechanisms as the underlying disorder or entropy increases. On the other hand, at $H = 0$, the full range of possible $\overline{\alpha}$ values is accessible.

We can quantify the bounds for such a feasible region of $(H, \overline{\alpha})$ loci on the plane by invoking symmetry arguments. When we do this, we find that for each value of entropy $H$ the parameter $\overline{\alpha}$ lies between two curves. The feasible region is shown in Fig. 3.11, where the curves are identified as I and II. Physically these curves represent bounds on the maximum and minimum observable $\overline{\alpha}$ values as a function of entropy. These curves are determined by the $(H, \overline{\alpha})$ variation for a coherency matrix with degenerate minor eigenvalues. Equations (3.153–3.154) give the canonical form of the coherency matrices for these bounding curves, and (3.155–3.158) their corresponding $H$ and $\overline{\alpha}$ values. Curve I represents the important case of full azimuthal symmetry already studied in (3.131), and the border of the $\overline{\alpha}$
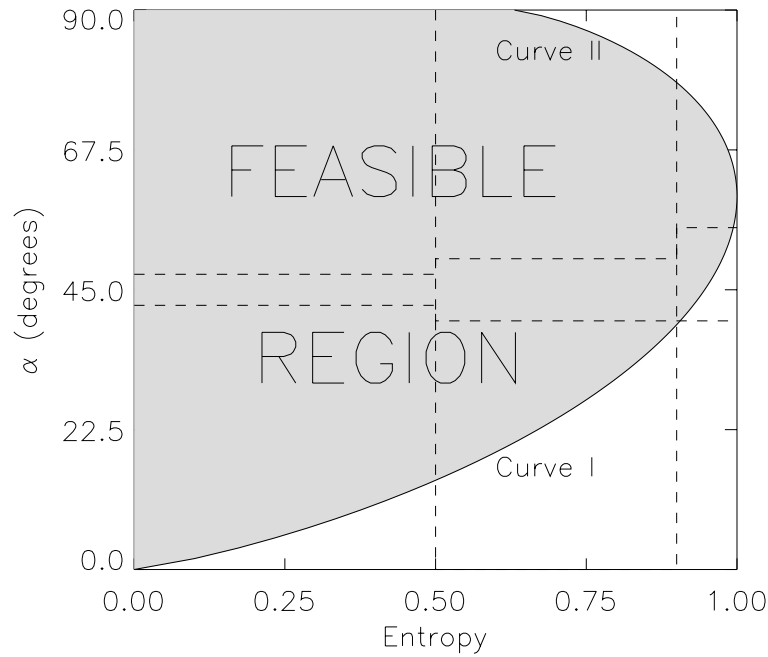
**Fig. 3.11.** $H-\alpha$ Plane for classification purposes

values follows from a minimization of $\overline{\alpha}$ with increasing entropy. The minimum value is obtained by adding isotropic noise (the parameter $m$ in $[T]_I$) to the subspace orthogonal to the $\alpha = 0$ scattering mechanism. Curve II follows from a maximization of $\alpha$ with increasing entropy. In this case two regions must be identified. The first is for low values of $m$ when we can fill up the $\alpha = 0$ subspace with noise and $\overline{\alpha}_{max}$ stays at $90°$. However, eventually (for $m > 0.5$) this subspace is filled and the noise starts to spill into the whole space.

$$[T]_I = \begin{bmatrix} 1 & 0 & 0 \\ 0 & m & 0 \\ 0 & 0 & m \end{bmatrix} \quad 0 \leqslant m \leqslant 1 \tag{3.153}$$

$$[T]_{II} = \begin{cases} \begin{bmatrix} 0 & 0 & 0 \\ 0 & 1 & 0 \\ 0 & 0 & 2m \end{bmatrix} & 0 \leqslant m \leqslant 0.5 \\ \\ \begin{bmatrix} 2m-1 & 0 & 0 \\ 0 & 1 & 0 \\ 0 & 0 & 1 \end{bmatrix} & 0.5 \leqslant m \leqslant 1 \end{cases} \tag{3.154}$$

$$H_I(m) = \frac{-1}{1+2m} \log_3 \left( \frac{m^{2m}}{(1+2m)^{2m+1}} \right) \tag{3.155}$$

$$H_{II}(m) = \begin{cases} \frac{-1}{1+2m} \log_3 \left( \frac{m^{2m}}{(1+2m)^{2m+1}} \right) \\[2ex] \frac{-1}{1+2m} \log_3 \left( \frac{(2m-1)^{2m-1}}{(1+2m)^{2m+1}} \right) \end{cases} \tag{3.156}$$

$$\alpha_I(m) = \frac{m\pi}{1+2m} \tag{3.157}$$

$$\alpha_{II}(m) = \begin{cases} \frac{\pi}{2} \\[2ex] \frac{\pi}{1+2m} \end{cases} \tag{3.158}$$

In this thesis, frequent use will be made of this plane to analyze many measurements. It will be shown that every experimental result lies inside the feasible region. Moreover, the inversion algorithm presented in Chapter 5 is also based on this plane. Finally, note that Fig. 3.11 also contains some dashed lines which correspond to the nine zones into which the plane was decomposed in [62] for classification purposes. They are included here only for completeness.

# Polarimetric Decomposition Techniques: Analysis of Indoor Measurements of Vegetation

THIS chapter is devoted to the description of results that can be obtained by analyzing the scattering from vegetation with the use of the target decomposition (TD) theory explained in Chapter 3. The same polarimetric analysis has been carried out for various measurement configurations and signal domains in a complementary way. It will be shown that all types of results provide important information about the morphology and physical structure of the sample under study.

The chapter is organized as follows. Section 4.1 describes the characteristics of the measurement system (the EMSL) and the vegetation samples that have been used throughout this thesis. Then the TD method based on the eigenanalysis of the coherency matrix is applied to measurements from those samples by following three different procedures.

The first, shown in Section 4.2, consists in the construction of the target vectors $\mathbf{k}$ with the values of the frequency domain backscatter data as a function of frequency, incidence angle and polarization. As explained below, this is known as scatterometric mode. After selecting a fixed elevation incidence angle, the ensemble averaging is computed with all the azimuth angles and frequencies within the working band. As a result, a single coherency matrix is obtained and a $H - \overline{\alpha}$ pair is derived for each elevation incidence angle and frequency band. Obviously, with the frequency domain data, we can study the response of the whole target as a function of incidence angle and frequency. However, we cannot identify the elements of the sample originating the scattering mechanisms.

The next step is described in Section 4.3 and applies the proposed decomposition scheme in the time domain. In this domain, though with some limitations, we can give an indication of the origin and location of the scattering mechanisms previously estimated in the frequency domain. The time domain decomposition scheme starts with the computation of one-dimension reflectivity profiles along the slant range direction for each polarization

and every elevation and azimuth angle. Then, for a fixed incidence angle, a target vector $\mathbf{k}$ is constructed at every range bin by employing the complex values of the images. With these target vectors a position dependent coherency matrix $\langle [T] \rangle$ is computed by averaging over the measured azimuth angles. Finally, the decomposition previously explained will provide us an estimate for the parameters $\overline{\alpha}$ and $H$ as a function of the position. Therefore, we will be able to identify the dominant scattering mechanism associated with each position in slant range, besides its randomness. Furthermore, since we can also obtain information of the power reflected by the target as a function of the position, we will identify which parts originate the $H - \overline{\alpha}$ values obtained in the frequency domain. As a result, the time domain processing yields in most cases a vertical distribution of scattering characteristics which can be identified with a multilayer structure. This morphology is usually employed in scattering models for vegetation.

Finally, Section 4.4 illustrates the application of this technique to 2-D and 3-D images of the vegetation samples. In this way, the polarimetric contribution of every part of the target volume can be fully characterized. These results are important for understanding how the global scattering from vegetation is formed by a superposition of many different contributions, and how the TD theory can help to identify them.

# 4.1    Description of the Vegetation Samples and the EMSL

All measurements presented in this thesis have been performed at the anechoic chamber of the European Microwave Signature Laboratory (EMSL), an unique indoor facility operating at the Joint Research Centre of the European Commission in Ispra, Italy, since 1993. A first technical description of the EMSL was presented in [149], and the initial experimental results, together with many operational details, were reported later in [150, 151]. The interested reader can find a considerable number of specifications in those references, but a brief illustration about the EMSL is also reported in the following for the sake of completeness.

The experimental set-up for all measurements on vegetation is shown in Fig. 4.1, and a photograph of the global arrangement of the chamber with a target inside is presented in Fig. 4.2. The overall structure is formed by the conjunction of a hemispherical and a cylindrical part, both with radius 10 m. In the gap between the two parts, a circular rail is mounted on which two sleds carrying the antennas can move independently. The sleds with the antennas cover a range of $\pm 115°$ around the zenith. On the inner surface of the hemisphere there exist about 80 fixing points for additional sensors. Currently, 37 of these locations host fixed receiving antennas, integrated in the microwave measurement system.

The object under test is transported inside the chamber through a large door (5 m wide and 8 m high) by means of a target positioner moving on a linear rail. This target support allows precise linear and rotational positioning of the object inside the chamber before and during the measurements. The linear movement can cover a span of 5 m, while the rotation is possible in the full circular range (360°).
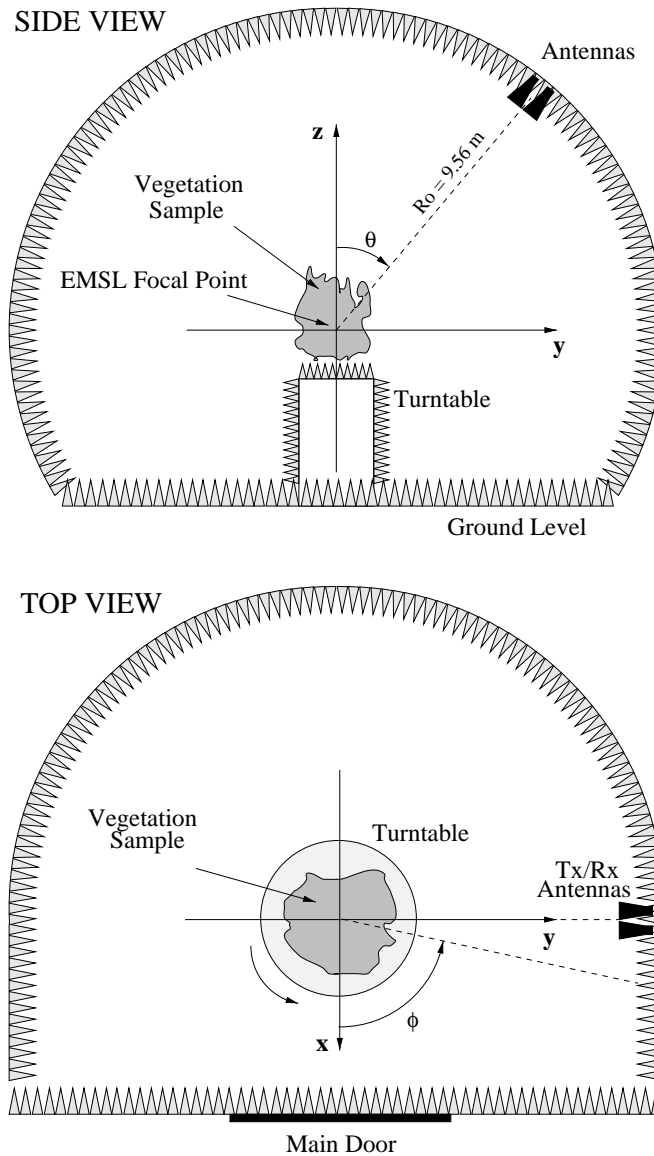
**Fig. 4.1.** Measurement set-up of the experiments with vegetation samples

The measurement system is based on a network analyzer and operates in stepped-frequency mode. The acquired data in frequency domain are empty room subtracted and gated in the time domain to isolate the response of the target under test from the residual antenna coupling and eventual spurious reflections in the chamber. Then, for monostatic case, a single reference, fully polarimetric calibration [35] is applied by using a metallic sphere or a disc as reference object and a dihedral in two orientations as auxiliary target, both placed at the focal point of the chamber[1]. The calibration accuracy of the measurement system is better than 0.5 dB in power and $5°$ in phase at 0 dBsm. The sensitivity depends on the number of measurements averaged for a single frequency point and on the time gate span.

---

[1]A polarimetric calibration procedure for the most general bistatic configuration is not yet available. Several partial solutions have been proposed but are still subject of ongoing research

For example, with an averaging factor of 128, equivalent to an integration time of 0.025 s, and a time gate span of 10 ns, a system noise floor ranging from -55 dBsm at 2 GHz to -40 dBsm at 15 GHz has been measured. Note that the working frequency currently available at the EMSL ranges from 300 MHz to 26 GHz, but the upper limit employed in the experiments presented in the text is 10 GHz because it is enough to cover the main microwave bands used so far in remote sensing from vegetation, i.e. L, S, C and X band[2].

Two different antenna systems were used in the experiments, both consisting of two dual polarized horn antennas. A system with large antennas was used in the low frequency range (0.3–4.3 GHz), while another with small antennas covered a wider range (1–10 GHz). Both systems have a large beamwidth for illuminating the entire sample under test. The distance between the antenna apertures and the focal point of the chamber is always 9.56 m. The measured cross-pol isolation is better than 30 dB in the region occupied by the target. The backscattered fields of the target are actually measured in a quasi-monostatic mode, since the transmitting and receiving antennas are spaced about $1°$ in elevation.

The laboratory configuration has been designed to permit both monostatic and bistatic measurements with almost any desirable combination of incidence and scattering angles. In addition, the target under test can be moved perpendicularly to the line of sight of the antenna or rotated around the vertical axis. This freedom in the scanning geometry is usually employed for two general measurements configurations: scatterometric and imaging mode. In the scatterometric mode the spatial resolution is determined by the antenna footprint. The variation of the measurement parameters can be used either to characterize the response of the whole object (e.g. the dependence of the radar cross section on frequency and incidence angle), or to obtain independent samples for non-deterministic objects (e.g. azimuth rotation of a rough surface or a vegetation sample). In fact, this thesis has made use of this mode with both goals. In the latter case, the number of samples is fixed by the minimum angular step to provide statistical independence between samples, which in turn depends on the target size in terms of the wavelength.

In the imaging mode, angular and frequency diversity are used to reconstruct a reflectivity image or spatial distribution of the target scattering properties. The images can be one-, two-, or three-dimensional, depending on the number of parameters that have been combined. For example, the inverse SAR (ISAR) configuration allows the generation of 2-D images by rotating the object in azimuth and using a non-zero frequency bandwidth, and 3-D images can be formed by adding a scan of the elevation incidence angle. If the target is displaced with the linear positioner, images can be formed with the well-known *strip map* SAR mode [129]. Note that for producing radar images, the step in the scanning (along angle rotation, linear displacement and frequency sweep) must be small, and normally the range in the azimuth rotation is not complete (usually $10°$ to $20°$). Therefore, if data obtained from imaging mode measurements are used to provide independent samples for non-deterministic objects, as proceeding from scatterometric mode measurements, the number of independent samples by rotating in azimuth is low for that purpose. So, if required, an additional fre-

---

[2]Some slightly different conventions for the limits of each band have appeared in the literature. For clarity, the convention used in this thesis is detailed in Table A.1 on page 180
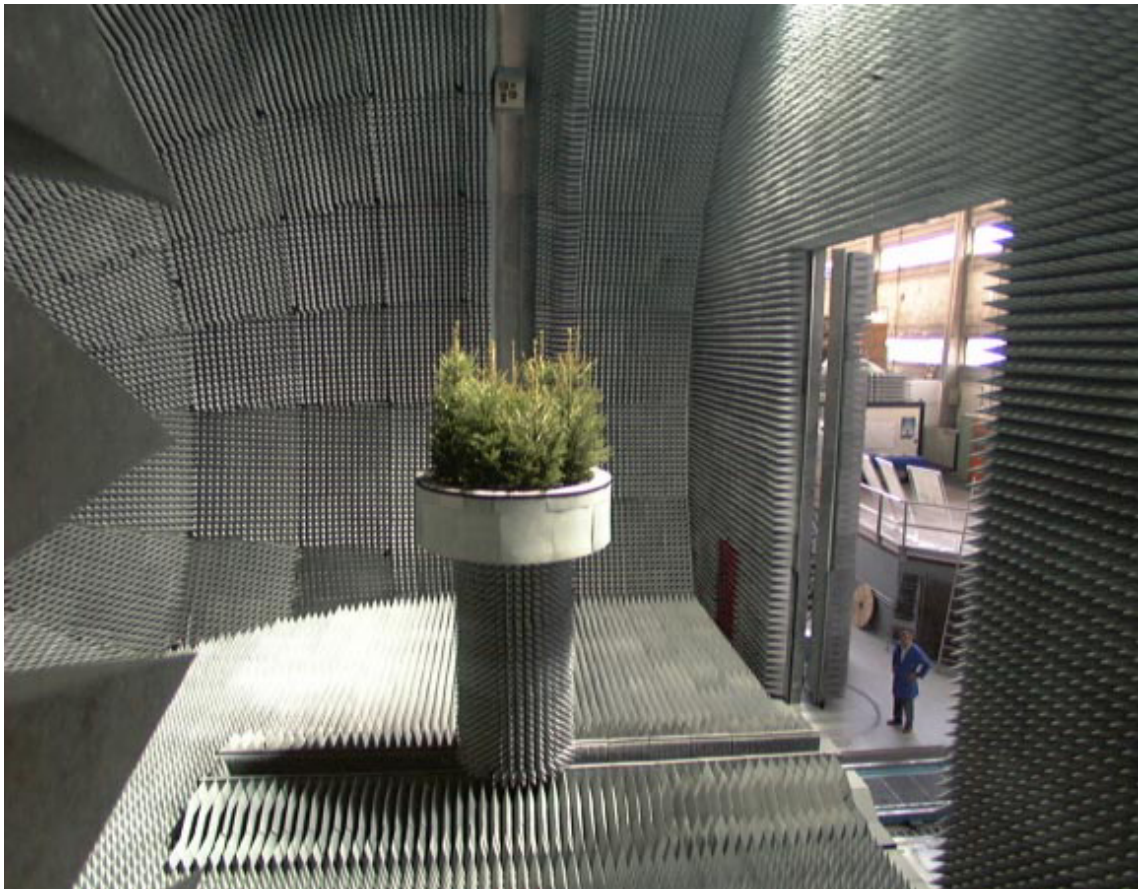
**Fig. 4.2.** Photograph of the interior of the EMSL



Maize A              Maize B                      Maize C

**Fig. 4.3.** Photographs of the maize samples

quency averaging must be applied to reduce the variability of the results.

In both modes, if a scan in elevation angle is performed with a small step, it is also possible to apply interferometric techniques, as will be shown in Chapter 6.
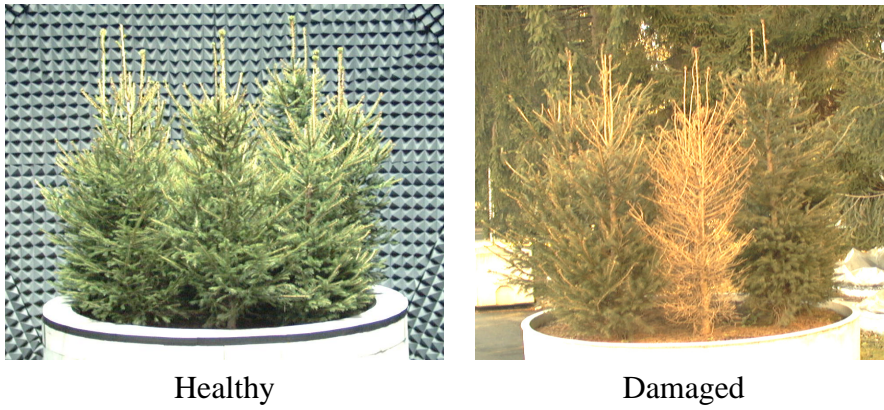
Healthy                    Damaged

**Fig. 4.4.** Photographs of the cluster of small fir trees: healthy and damaged
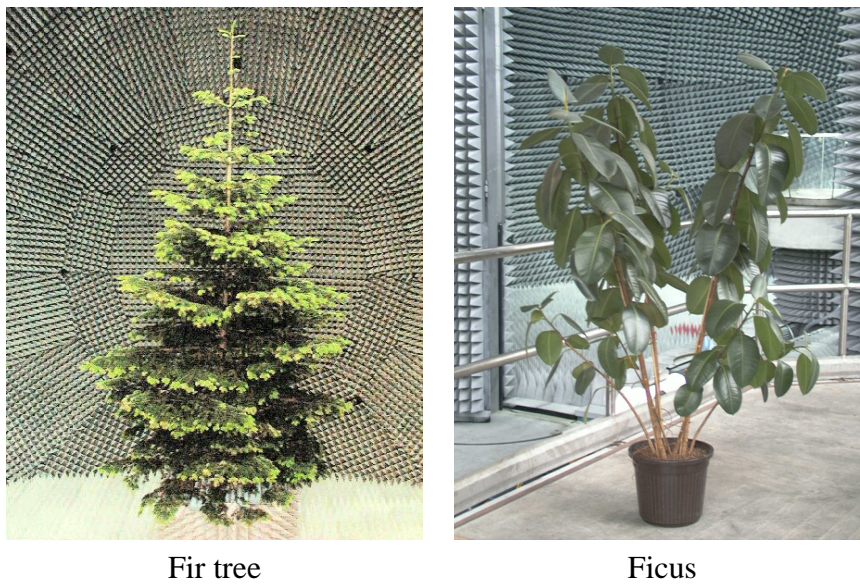


Fir tree                    Ficus

**Fig. 4.5.** Photographs of the fir tree and the ficus plant



**Fig. 4.6.** Photograph the sample of rice

A physical description of the vegetation samples used in the present thesis is detailed in the following (see photographs on Figs. 4.3–4.6):

**Maize**  Three samples of maize at different growth stages:

> **Maize A**  Stand of 4×4 mature plants about 1.7 m high, uniformly planted in a square container of side length 1 m. The plants show a vertical bare trunk with diameter about 2 cm. They only bear leaves in the upper half of the stems. The leaves are about 50–70 cm long and 5–7 cm wide, and are bent and randomly oriented.

> **Maize B**  Stand of 6×6 mature plants about 1.3 m high, uniformly planted in a square container of side length 1 m. The structure of trunks and leaves is the same as sample A.

> **Maize C**  Stand of 6×6 young plants about 1.8 m high, uniformly planted in a square container of side length 2 m. The plants show a green vertical fresh trunk with diameter about 4 cm. The stems carry wide leaves from a height of 40 cm up to the top. The leaves are about 30–40 cm long and 7–8 cm wide, and are oriented at around $45°$ with respect to the trunk.

**Cluster of small fir trees**  Stand of 9 small fir trees about 1.8 m high, regularly planted in a round container with diameter 2.4 m. The trees are very close together. The structure of each tree is cone-shaped, with no branches in the upper 20 cm. The branches bear 2–3 cm needles showing a brush-like distribution. After one year, three trees occupying the center of the target died because of the excessive proximity among trees. Some measurements were also performed on this target which is hereafter called *damaged* in contrast to the *healthy* original situation.

**Fir tree**  A balsam fir tree about 5 m high and 2.5 m wide, which was about 21 years old. The tree presents quasi-horizontal branches bearing 2–3 cm needles in a brush-like distribution, with branches constituting large horizontal planar surfaces at different levels in height. The top of the tree conforms to a young tree of its same species.

**Ficus**  A ficus tree about 2.5 m high and 1 m wide. This tree exhibits 10 to 25 cm long pointed leaves and many-twigged slender branches. The leaves can be viewed as folded elliptical discs.

**Rice**  Stand of 9×9 rice plants of about 0.6 m high, uniformly distributed in a square container with side length 1 m. Each plant presents a cluster of green stems or long leaves that originates directly from the ground. In the upper half of the sample, these stems are notably bent and oriented in a random fashion. The leaves are about 2 cm wide. The soil was flooded to replicate the natural conditions of rice crops.

An illumination level (about 1000 lux) sufficient for maintaining plants in normal physiological conditions is guaranteed by some lamps mounted in the chamber. The illumination level can be modulated (e.g. to simulate the night-day transitions) by switching the lamps on or off. The air inside the chamber can be exchanged depending on the requested

environmental conditions. Moreover, in order to have stable measurement conditions, prior to and during the experiments the plants are watered regularly.

Note that not all experiment configurations were repeated for all samples. Therefore, the characteristics and measurement parameters of each particular experiment will be stated in the text.

## 4.2    Frequency Domain Results

In this part of the analysis we are interested mainly in the dependence of the scattering behavior of the vegetation samples on two important measurement parameters: frequency and incidence angle. If we consider the trees or plants as heterogeneous clouds of anisotropic scattering particles then, as the wavelength changes, we should become sensitive to different shaped structures within the cloud. Moreover, when the measurement geometry changes the radar backscatter from different parts can dominate or become negligible in the total volume response. To investigate this, the coherency matrix has been calculated as a function of frequency and elevation angle by averaging over all azimuth angles. Then, the target entropy $H$ and mean scattering mechanism $\overline{\alpha}$ have been plotted in pairs on the $H - \alpha$ plane. These loci illustrate the scattering behavior of the whole target and also the influence of the measurement frequency and incidence angle. This procedure is not shown in this thesis applied to all vegetation samples, for the sake of economy. Nevertheless, a complete set of measurements and a deep discussion of the results are described in the following, thus demonstrating the potential of this analysis tool.

The first results were computed for frequency spans of 1 GHz centered at L, S, C and X bands: 0.5–1.5, 2.4–3.4, 4.5–5.5 and 7.8–8.8 GHz respectively. The elevation incidence angles ranged from $0°$ (i.e., from the top of the sample) to $60°$ with a step of $10°$.

To begin with, Fig. 4.7 shows the frequency domain results for the three samples of maize at S, C and X band. The $H - \overline{\alpha}$ pairs are positioned on the plane, where we have also displayed the border of the feasible region (dashed line) and the zones (solid line) used in the classification scheme presented in [62]. As shown in the photographs of Fig. 4.3, the three samples have different structures besides their density and height. These morphological differences are successfully resolved by plotting the loci resulting from the decomposition scheme on the $H - \alpha$ plane. Two common trends can be observed at all three frequency bands: 1) the loci cover a wide range along the border of the feasible region, 2) they present a clear dependence upon the incidence angle. As the angle increases, the dominant scattering mechanism goes from surface ($\alpha$ close to $0°$) to dipole like ($\alpha$ close to $45°$), and the entropy reaches its maximum for every $\alpha$. At this stage of the analysis, this fact can be justified as follows: from steep angles the ground is more visible, thus the scattering mechanism should be more surface like; on the other hand, as the incidence angle becomes more gentle, the radar sees the maize sample as a distribution of vertical cylinders which must show a scattering mechanism closer to dipole like. Note that, for all vegetation samples, the same
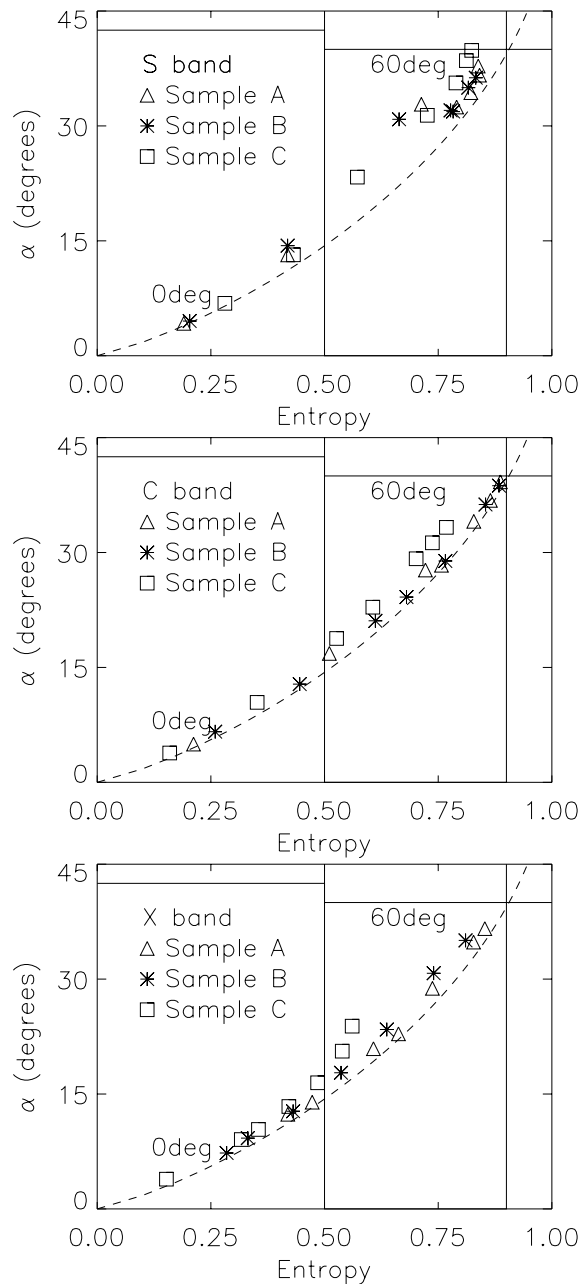
**Fig. 4.7.** $H - \overline{\alpha}$ as a function of incidence angle at S, C and X band for the three maize samples. Incidence angles = $0° - 60°$

general trend with the incidence angle has been observed: the loci go roughly from the bottom-left corner towards the top-right corner on the $H - \alpha$ plane. Since there are not cases with swapped positions, the only loci to be labeled are the first (0 deg) and the last (60 deg). The reader can easily follow this path and identify the loci for every angle by simply counting from the first to the last.

With regard to the contribution of polarimetry, the maize targets, when considered

as a whole, are so random that the information provided by polarimetry is limited. In fact, when the loci lie along the lower curve of the feasible region, the measurements can be fully characterized by two parameters: total power ($\lambda_1 + \lambda_2 + \lambda_3$) and depolarization $m$. As was explained in Chapter 3, the points of the lower curve of the feasible region correspond to a coherency matrix with the form:

$$\langle[T]\rangle = \begin{bmatrix} 1 & 0 & 0 \\ 0 & m & 0 \\ 0 & 0 & m \end{bmatrix} \tag{4.1}$$

where $m$ fixes the location on the $H-\alpha$ plane. It also means that the polarimetric parameters can be obtained by using only $\langle|S_{hv}|\rangle$ and $\langle|S_{hh}|\rangle = \langle|S_{vv}|\rangle$.
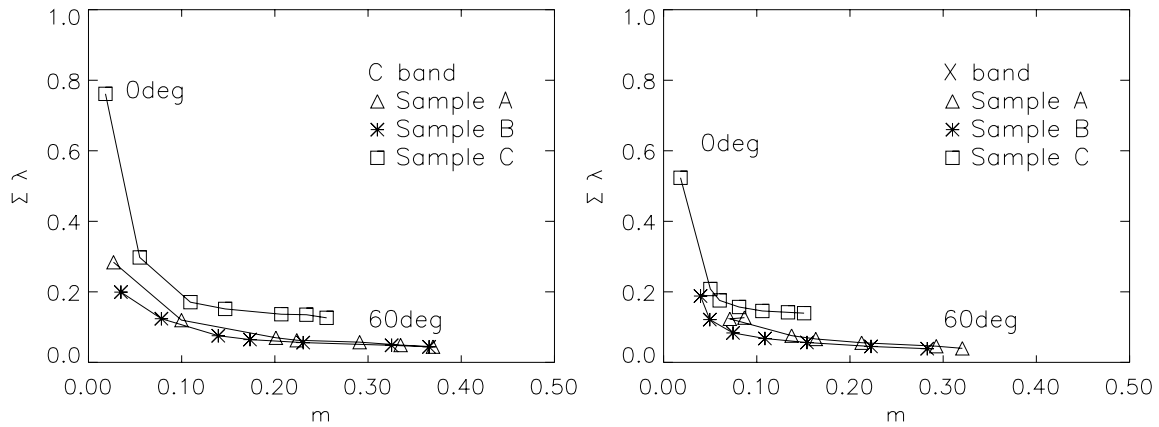


**Fig. 4.8.** Total power ($\sum \lambda$) vs $m$ as a function of incidence angle at C and X band for the three maize samples. Incidence angles $= 0° - 60°$

We have plotted the curves of $\sum \lambda$ vs $m$ as a function of the incidence angle for the three maize samples at C and X band in Fig. 4.8. At S band the loci actually lie off the lower banding and therefore they are not shown here. From the curves at C and X band, it is evident that sample C can be easily separated from the others by looking at the total power at any incidence angle. With respect to samples A and B, it is possible to distinguish them at a single incidence angle, but the global trend is quite similar. Note that the samples with mature plants (A and B) could be modeled as a two-layer structure above the ground: a top layer with a random distribution of wide long bent leaves, and a bottom layer with thin trunks without leaves. In contrast, the young plants of sample C have wider green trunks with an almost regular distribution of wide leaves (not bent) from the bottom to the top of the plant, thus matching better a model with a single layer. In Fig. 4.7 the loci of the samples for a fixed incidence angle change significantly as the frequency increases from S to X band. At higher frequencies, the penetration depth is more limited and the backscatter associated with the top layer of the plant should be the dominating scattering mechanism. In the next section, this is further supported by the decomposition results in the time domain.

Fig. 4.9 displays the loci on the $H-\alpha$ plane for the group of small fir trees at the four
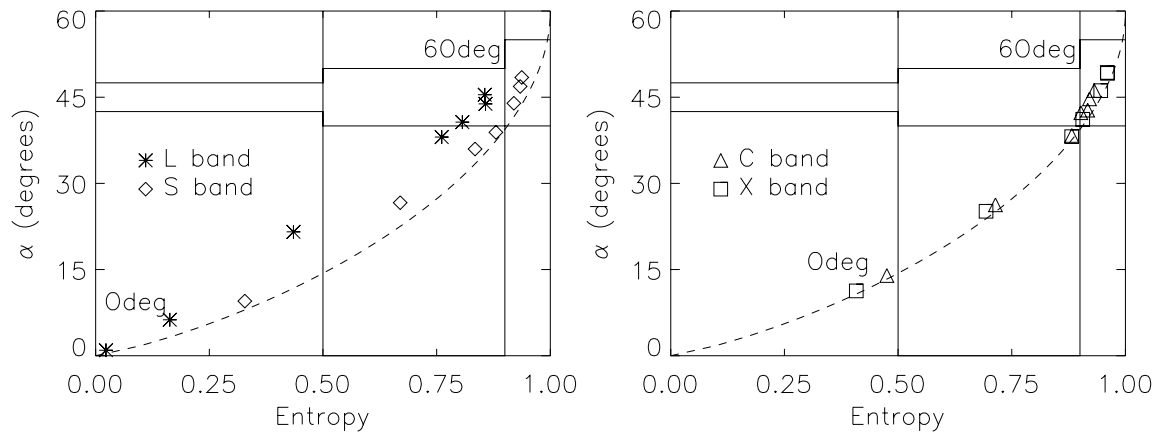
**Fig. 4.9.** $H - \overline{\alpha}$ as a function of incidence angle at L, S, C and X band for the group of small fir trees. Incidence angles $= 0° - 60°$
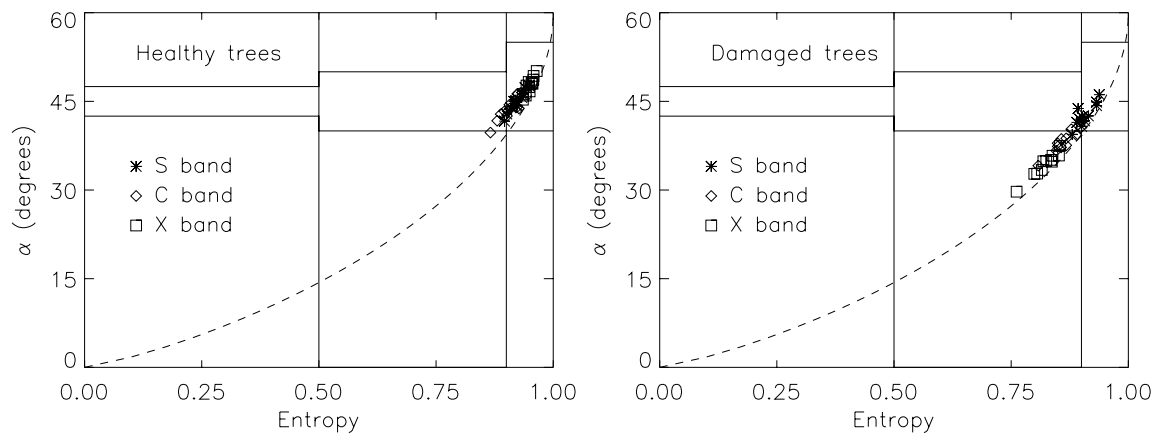


**Fig. 4.10.** $H - \overline{\alpha}$ at S, C and X band for the group of small fir trees in two states: healthy (left) and damaged (right). Incidence angles $= 30° - 50°$

frequency bands. As before, an evident dependence on the measurement geometry can be observed. For angles gentler than $20°$ the loci remain in a narrow region with high entropy and $\overline{\alpha}$ close to $45°$. This is evidence that the green needles of the trees, which are the main scattering centers, show a dipole like response. However, for lower angles the loci separate from this area showing a wide spread. This may be due to the presence of the ground, which is more visible from steep angles. It is also important to note the difference between the sample with fir trees and the maize samples, which demonstrates the sensitivity of this method to changes in the morphology of the target.

As was outlined above, the sample with a cluster of small fir trees suffered damage due to the proximity between trees, and three of them died. Fig. 4.10 presents a comparison at S, C and X band of the $H - \overline{\alpha}$ loci for both states (healthy and damaged) in measurements performed for incidence angles from $30°$ to $50°$. Although at low frequencies the loci occupy similar positions on the plane, when it increases they go to lower $\alpha$ and $H$ values in the
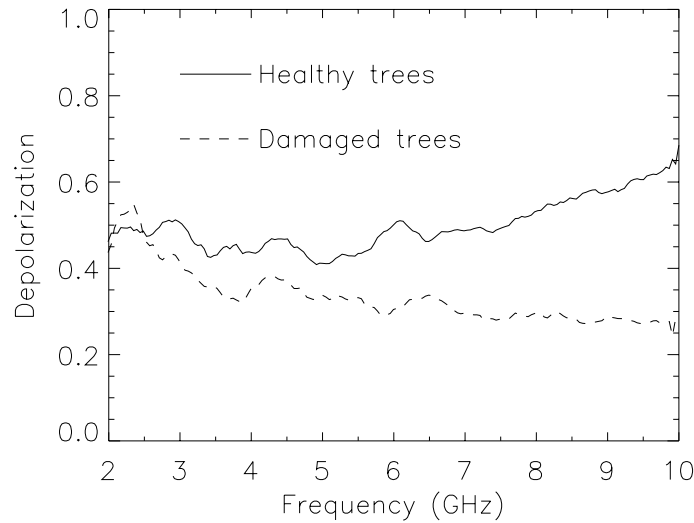
**Fig. 4.11.** Depolarization vs frequency for the group of small fir trees in two states: healthy and damaged. Incidence angle $= 50°$

damaged case. This change in the scattering behavior is due to the death of some trees. The dead trees become dry, so the green needles that were the main scattering centers at high frequency in the healthy state do not scatter any more. As a result, the scattering response is only equivalent at low frequency, because in that case the main scatterers are still the branches and trunks.

This phenomenon has been studied in more detail by plotting the depolarization factor $m$ as a function of frequency for both samples in Fig. 4.11. This figure illustrates the previous comments. The change in the trend of the depolarization is evident when frequency increases. For the healthy sample the green needles become more and more important as main scatterers, thus producing a high depolarization. On the other hand, the lack of green needles in three of the nine trees has the opposite effect. This trend would be even more evident if all the trees had died.

Fig. 4.12 shows a comparison between the group of small fir trees and the single fir tree from another measurement that was carried out within the angular range $\theta_i = 39° − 51°$ at S and C band. The fir tree also presents loci close to the $\alpha = 45°$ region, corresponding to the dipole like scattering from their leaves and branches. The spread for the group of trees is smaller than that of the single fir tree. Moreover, in contrast to the big tree, the loci of the group of trees at both bands fall in the same region. These differences may be due to the differing tree architecture. The small trees present shorter branches and the trunk is thinner than that of the big one. In addition, the top of the big tree conforms to a young tree. This fact could explain the similar results at higher frequencies.

In order to highlight the discrimination capabilities of the representation of the $H − \overline{\alpha}$ loci on a plane, a final result is shown in this section. It corresponds to two ISAR measurements from the fir tree and the ficus. For consistency, the result corresponds to the frequency
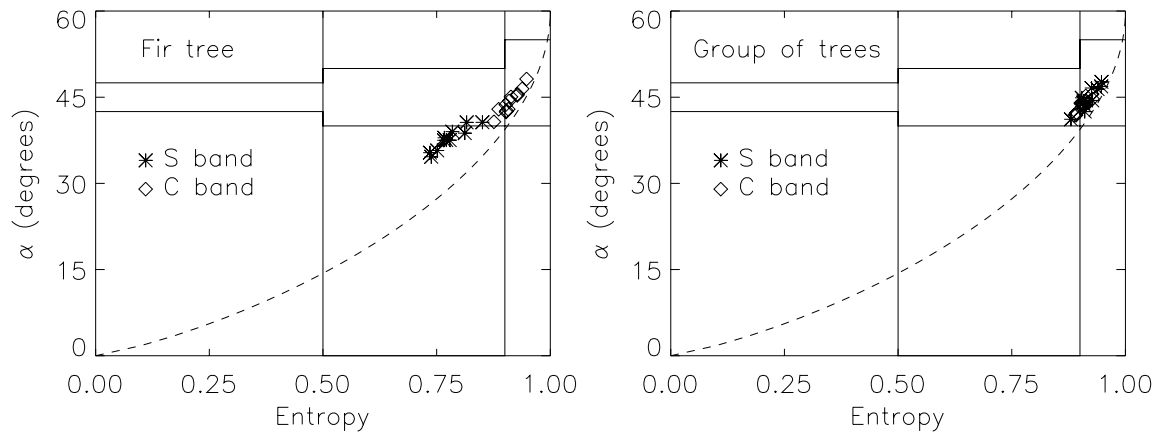
**Fig. 4.12.** $H - \overline{\alpha}$ as a function of incidence angle at S and C band for the fir tree and the group of small fir trees. Incidence angles $= 39° - 51°$
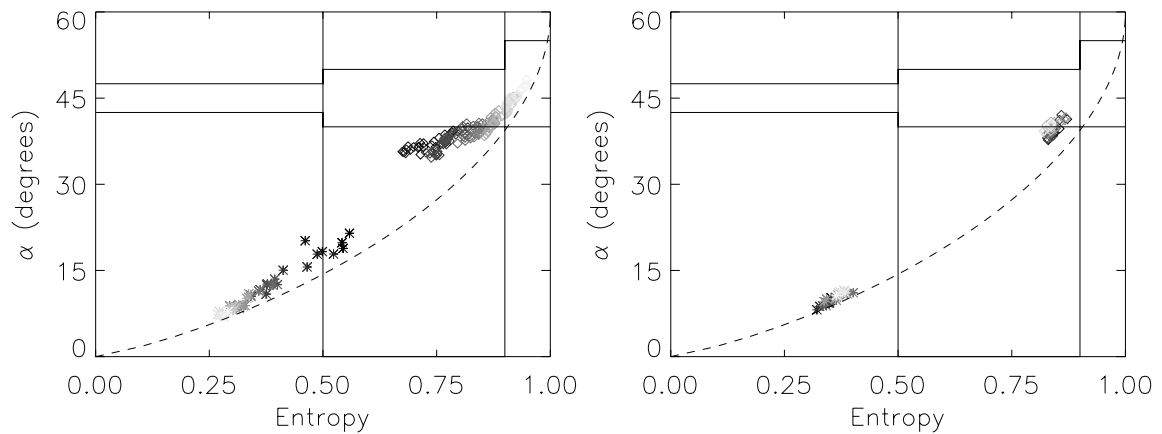


**Fig. 4.13.** Comparison of $H - \overline{\alpha}$ as a function of frequency (left) and incidence elevation angle (right) for the fir tree (diamonds) and the ficus (stars). Frequencies $= 2 - 5.5$ GHz, Incidence angles $= 39° - 51°$

band and angular span that intersect the measurements from both trees: $2 - 5.5$ GHz and $39° - 51°$. The average coherency matrices were calculated firstly as a function of frequency by averaging over all azimuth and elevation angles. Then, a second group of coherency matrices was obtained as a function of the incidence elevation angle by averaging over all azimuth angles and frequencies. Using the $\langle[T]\rangle$ matrices so computed we then calculated the $H - \overline{\alpha}$ values. Figure 4.13 shows the results obtained, plotted as points on the $H - \alpha$ plane. The varying parameters (frequency and incidence angle, respectively) are represented by the gray scale of the points, going from the black (lowest value) to the white (highest value). It is obvious that the loci of the $H - \overline{\alpha}$ points are different for these trees. Moreover, the trends as frequency increases are clearly opposite. Entropy and $\overline{\alpha}$ increase with frequency for the fir tree, while they decrease for the ficus. The result as a function of the incidence angle could be employed in classification techniques, since the points corresponding to the same tree are very close together but are well separated between tree types.

# 4.3 Time Domain Results

The frequency domain results have shown that the dominant scattering mechanism is an observable sensitive to the physical structure of the sample and, consequently, to biophysical parameters such as height, leaf density and shape, and so on. In order to develop a reliable inversion technique (like polarimetric interferometry for the retrieval of vegetation height [69]), we need to study the origin of the estimated scattering mechanisms. Alternatively to the frequency domain results which provide the response of the sample as a whole, the same decomposition scheme has been applied in the time domain. The objective is to identify the position (range bin $r$) in which every scattering mechanism is located.

The time domain decomposition scheme starts with the computation of complex reflectivity profiles along the slant range direction for each polarization and every elevation and azimuth angle. These profiles are obtained by applying a Fourier transform to the collected data in the frequency range of interest, resulting in time domain signals. The time variable is directly related with the slant range. Then, for a fixed incidence angle, a target vector **k** is constructed at every range bin by employing the complex values of the images (called $[R]$ for clarity), instead of the $[S]$ entries, as in (3.88). With these target vectors, a position dependent coherency matrix $\langle [T] \rangle$ is computed by averaging over the measured azimuth angles. This averaging can be applied because the sample is always at the same range from the antennas. Finally, the decomposition previously explained gives us an estimate of the parameters (for instance, $\overline{\alpha}$ and $H$) as a function of position. Therefore, we can identify the dominant scattering mechanism associated with each position in slant range. Furthermore, since we can also obtain information of the power reflected by the target as a function of position, we can quantify the strength of the contribution of each part to the $H - \overline{\alpha}$ values obtained in the frequency domain.

As we did in the frequency domain, we can observe the results as a function of incidence angle and frequency band. Note that we only have resolution in the slant-range direction, and therefore contributions in the cross-range direction are integrated at each range bin. Here we are interested in justifying the frequency domain results and hence we will use the same frequency ranges: bandwidths of 1 GHz centered at each frequency band. The corresponding resolution in slant range is about 15 cm. Note also that no windowing has been applied in the study.

In order to better illustrate the analysis, the following parameters have been plotted as a function of $r$:

- Probabilities of occurrence of each eigenvalue: $p_i$

- Scattering mechanism of each eigenvector: $\alpha_i$

- Mean scattering mechanism: $\overline{\alpha}$

- Entropy: $H$

- Total reflectivity power[3]:

$$\text{Power} = \frac{1}{2}\left(|R_{hh} + R_{vv}|^2 + |R_{hh} - R_{vv}|^2 + 4|R_{hv}|^2\right)$$
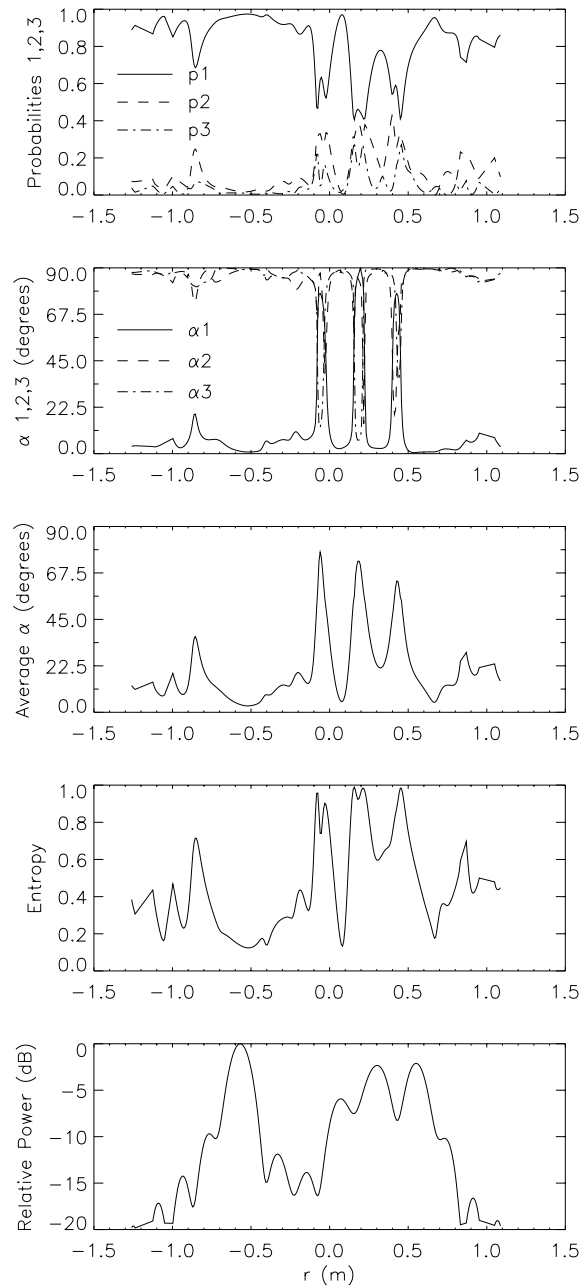


**Fig. 4.14.** Analysis parameters in time domain at X band for the maize sample A. Incidence angle = 0°

---

[3]The power has been normalized to its maximum value, because the absolute power is of no interest for locating the origin or position of the estimated scattering mechanisms

Fig. 4.14 presents the decomposition results for the maize sample A at X band and vertical incidence (incidence angle equal to zero). The relative power plot shows clearly the ground reflection peak ($r \simeq -0.5$ m), revealing that there is high penetration even at X band for this incidence. There is also an area of strong reflectivity within the window $0.1 < r < 0.8$, that seems to originate from the wide leaves of the sample. On the other hand, from the plots of the probabilities of occurrence of each eigenvalue, we see that the area near the ground is dominated by a surface-like scattering mechanism ($\alpha$ close to zero with probability close to one), whereas in the top part of the sample no single scattering mechanism is dominant (some double bounce reflections with $\alpha$ close to $90°$ are present). It has been observed that by integrating $\overline{\alpha}$ weighted by its relative power over the entire time domain, the resulting $\overline{\alpha}$ value is roughly that estimated from the frequency domain data. So, the results in both domains seem to be consistent. This holds for all the samples considered in this study.

In Fig. 4.7, we saw that the response from both samples of mature maize were almost identical at S and C band for every incidence angle. However, at X band, the $H - \overline{\alpha}$ pairs did not coincide at any incidence angle. The time domain results for sample B at X band are shown in Fig. 4.15. Since the plants of sample B are smaller (about 1.3 m high instead of 1.7 m), they have a shallower layer with leaves and, consequently, the high reflectivity window associated with this layer is narrower. This is also the cause of the low $\overline{\alpha}$ retrieved for the whole sample in the frequency domain. In addition to the differing heights, the second sample exhibits a higher density of plants. However, this does not seem to justify the differences in Fig. 4.7 because the relative power at the leaf layer with respect to the ground reflection is the same. We can conclude that the average $\overline{\alpha}$ value at X band is a function of the plant height *for these two samples* and, consequently, it might be used in the future for inverting the height of maize crops. This is also the case for entropy, since both $\overline{\alpha}$ and entropy lie at the border of the feasible region on the $H - \alpha$ plane. The fact that $\overline{\alpha}$ and $H$ depend on the height of the samples only at X band is due to the larger penetration at lower microwave frequencies, for which the layer of leaves (that dictates the height of the plants) is almost transparent, thus not changing the total response. In any case, the usefulness of these parameters to construct an inversion algorithm has not been accurately analyzed yet in terms of biophysical parameters.

Fig. 4.16 depicts the parameters of the maize sample C at X band and incidence angle equal to $0°$. The power reflected from the leaf layer, relative to the ground reflection, is much lower than that of the mature samples because of the lower density and wider spread of leaves along the entire trunk. This wider spread is also evident in the more uniform reflected power from all the leaves present at the trunk ($0 < r < 1.4$). The final average $\overline{\alpha}$ is lower than that of the mature samples (i.e., A and B) although the plants are taller. This may be due to the lower density of leaves in the top layer, that produces a scattering mechanism always close to zero since there are less double bounce contributions (see the picture of the probabilities of each eigenvalue). Therefore, the use of the final $\overline{\alpha}$ or entropy for estimating the heights of maize plants is conditioned (among other aspects) by the growth state or age of the plants.

The following result has been computed for the maize sample A to study the dependence on the incidence angle. Fig. 4.17 presents the relative power and the $\overline{\alpha}$ plots for four
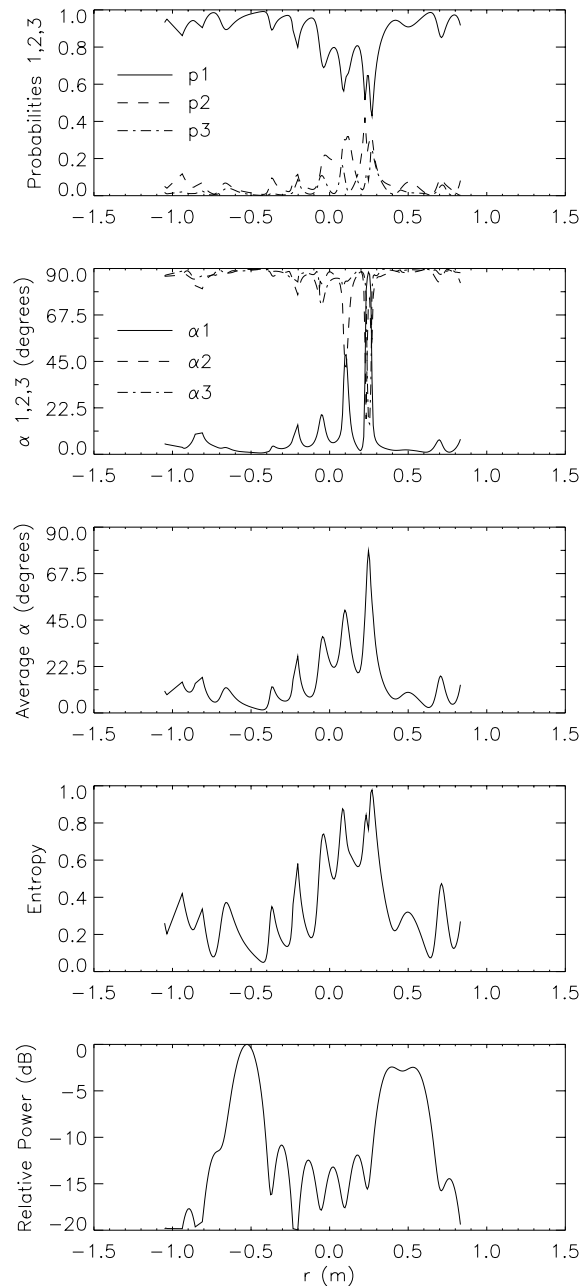
**Fig. 4.15.** Analysis parameters in time domain at X band for the maize sample B. Incidence angle $= 0°$

incidence angles: $0°$, $20°$, $40°$ and $60°$, respectively. The reflected power is very sensitive to the incidence angle. As expected, the peak that appears around $r = -0.5$ m for $0°$, corresponding to the ground reflection, becomes lower and lower as the incidence angle increases, while the plots of $\overline{\alpha}$ become uniformly distributed. This phenomenon is due to the integration in the direction normal to the slant range. These results can be extrapolated to the other mature maize sample (maize B).

Fig. 4.18 shows the results for the maize sample C at X band for the same incidence
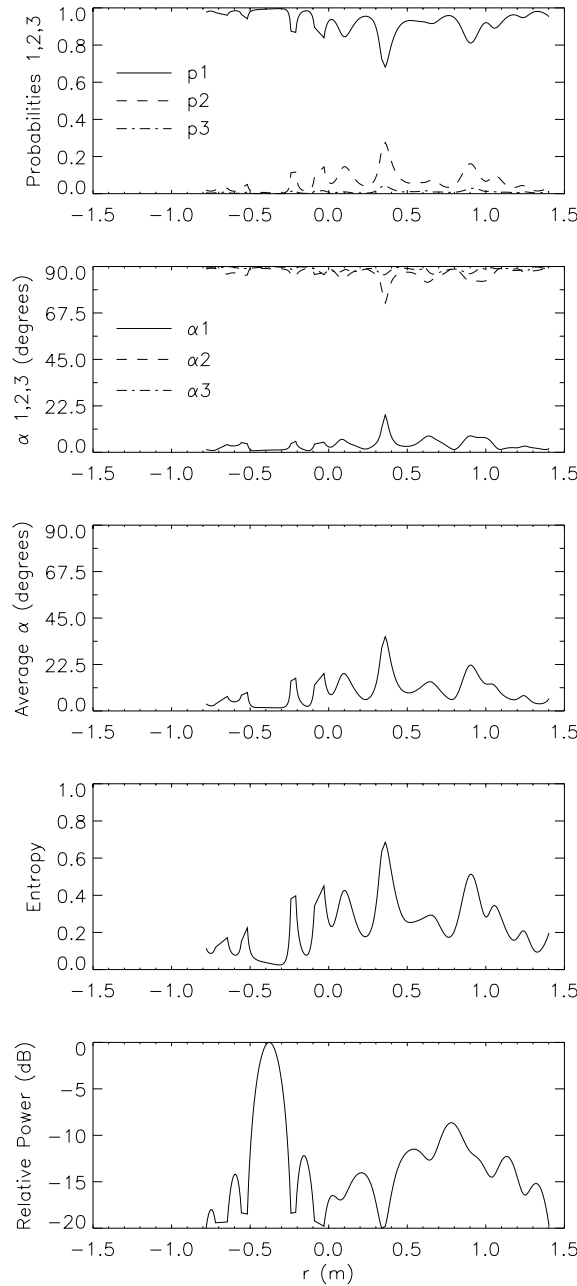
**Fig. 4.16.** Analysis parameters in time domain at X band for the maize sample C. Incidence angle = 0°

angles. We see that the average $\overline{\alpha}$ is even more uniform than that of the mature samples, because of its more homogeneous structure.

An additional comment can be stated according to Figs. 4.17 and 4.18. It is known that when a wave propagates through a random medium, if the medium has some kind of orientation, then the effective propagation velocity for two different polarizations becomes
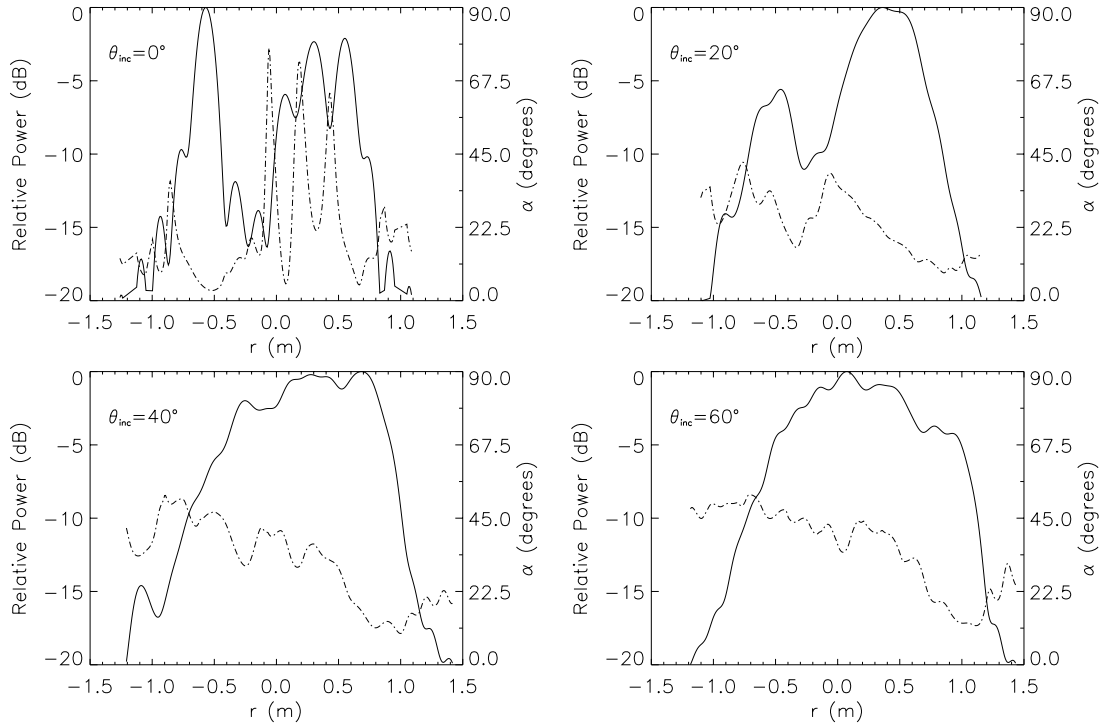
**Fig. 4.17.** Relative power (—) and average alpha $(-\cdot-)$ in time domain at X band for the maize sample A. Incidence angles = 0°, 20°, 40°, 60°

different. The propagation matrix is expressed as,

$$[\rho] = \begin{bmatrix} e^{j\gamma_h z'} & 0 \\ 0 & e^{j\gamma_v z'} \end{bmatrix} \quad \text{with} \quad \gamma_h, \gamma_v \in C, \tag{4.2}$$

where $z' = z/\cos\theta$ denotes a variable indicating the position into the layer (equivalent to the slant range variable $r$ used in the time-domain plots), and $h, v$ are supposed to be the eigenstates. The real parts of $\gamma_h$ and $\gamma_v$ correspond to the phase change, and the imaginary parts represent any attenuation along the path. If a wave propagates through such a medium and $\Im(\gamma_h) < \Im(\gamma_v)$, the extinction coefficients are different. Therefore, $\overline{\alpha}$ should start at 0° at the top of the layer and should tend towards 45°, whether or not this value will be reached depends upon the depth of the random layer. This fact matches the trend in $\overline{\alpha}$ observed in Figs. 4.17 and 4.18 mainly for incidences of 40° and 60°, where $\overline{\alpha}$ grows as the slant range coordinate penetrates into the vegetation sample. We also can define a *mean differential extinction coefficient*, $\gamma_h/\gamma_v$, that is directly related to the slope of $\overline{\alpha}$ with $r$, namely $d\overline{\alpha}/dr$. Observing Figs. 4.17 and 4.18 at incidence angles of 40° and 60°, it is evident that these vegetation samples match this random medium model, being the average slopes of both samples at these incidences about 17 degrees/m in sample A and 12 degrees/m in sample C. It means that sample A has a higher differential extinction coefficient than sample C and, hence, it must be accounted for in future applications of polarimetric interferometry for locating the phase centers within the volume of these maize samples.
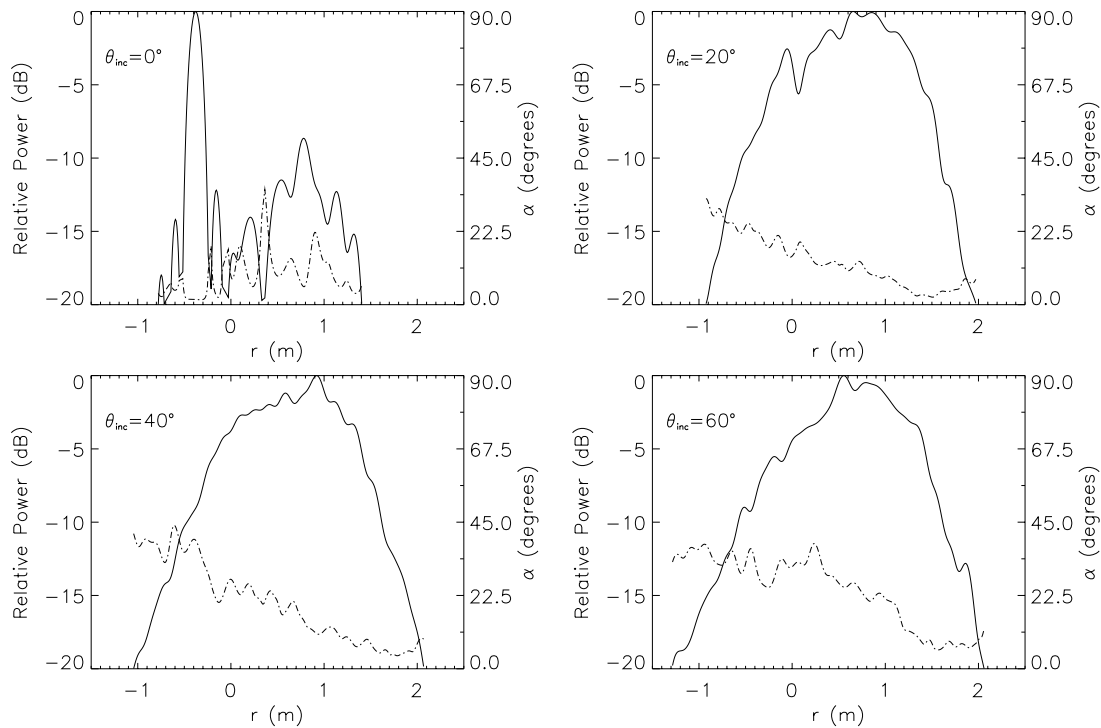
**Fig. 4.18.** Relative power (—) and average alpha $(- \cdot -)$ in time domain at X band for the maize sample C. Incidence angles $= 0°, 20°, 40°, 60°$

Fig. 4.19 shows the time domain results for the cluster of small fir trees with an incidence angle of $10°$ for all frequency bands. The structure of this target is quite homogeneous and, consequently, its response is uniform as well. We see that there are no differences between the results at C and X band. We can clearly identify two parts in the power plot: one peak corresponding to the ground reflection, and a second smooth plate that fits the volume of the vegetation sample. At S band, the penetration is higher and therefore the relative power associated with the vegetation volume becomes much lower. As a result, the global entropy decreases drastically. This is even more evident at L band, where the penetration is so strong that the ground reflection is dominant. This fact justifies that in Fig. 4.9 only for angles higher than $20°$ the average $\overline{\alpha}$ at L band is similar to those in the other bands.

There is another interesting aspect to note here. One of the scattering models more widely used for studying a canopy, due to its simplicity, is composed of one layer of random particles over a half-space that corresponds to the ground. This is basically the model presented in [69] for studying the properties of a technique for inverting the canopy height. According to this model, the randomness of the scattering as a function of depth into the vegetation should ideally be high at the canopy layer and low at the bottom of the canopy. Since the entropy is a parameter directly related to the randomness in the scattering, it also should be high at the canopy layer and low at the ground. Fig. 4.19 presents this behavior of entropy as a function of the slant range, being obvious at C and X band.
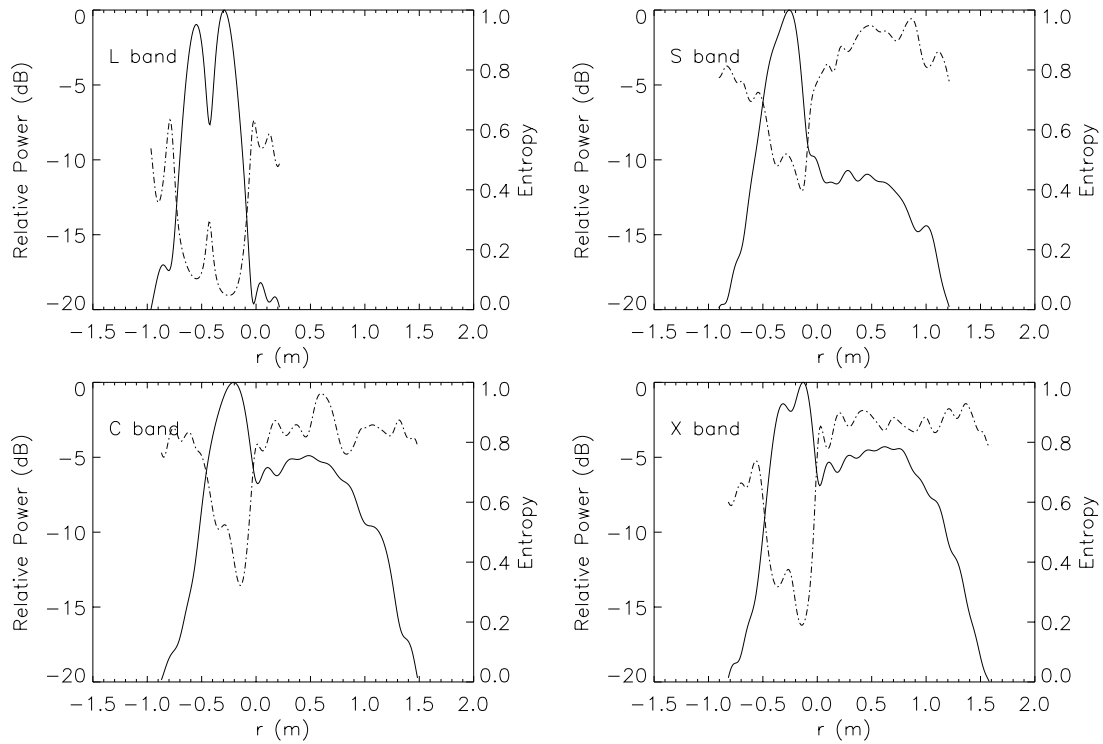
**Fig. 4.19.** Relative power (—) and entropy (− · −) in time domain for the cluster of small fir trees with incidence angle of $10°$. Frequency bands: L, S, C and X
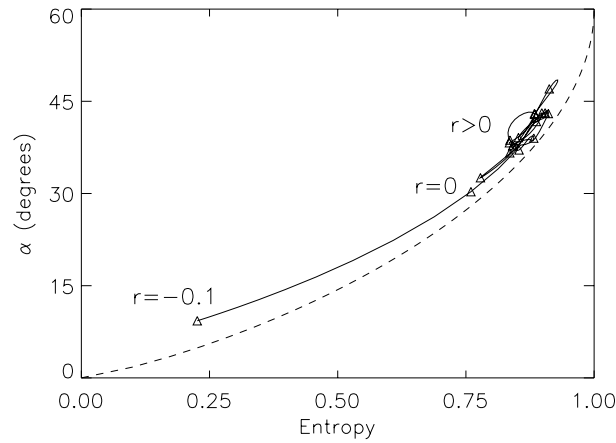


**Fig. 4.20.** $H − \overline{\alpha}$ as a function of range at X band for the group of small fir trees. Incidence angle $= 10°$. $−0.1 \leq r \leq 1.5$

In Fig. 4.20 the loci of $H − \overline{\alpha}$ are plotted as a function of range for the group of small fir trees at X band and incidence angle of $10°$. The slant range variable goes from $r = −0.1$ m to $r = 1.5$ m. It is evident that the distribution of loci matches the expectations. Again, this fact is very important for the success of polarimetric interferometry.

## 4.4   Imaging Results

By making use of the potential of the EMSL measurement system, some ISAR imaging experiments have been carried out on vegetation samples. The final results of these experiments are 2-D and 3-D complex reflectivity images with fine resolutions in all directions. Consequently, the major scatterers and their position within the sample volume can be identified. Moreover, since the measurements are fully polarimetric, the images at different polarizations (HH, HV and VV) have been combined for applying the TD theories presented in Chapter 3. Therefore, this procedure accomplishes a step forward with respect to the 1-D time domain results described in the previous section, because the identification of the polarimetric characteristics of the target can be now performed along all directions.

The 3-D ISAR experimental set-up consists of the acquisition of the radar backscatter from the target by using a large bandwidth, and introducing an azimuth rotation of the target with small steps and a scanning in the elevation angle by changing the position of the antennas. Once the data have been acquired following this procedure, a focusing algorithm is applied to create the reflectivity images. In this thesis, results obtained with two accurate algorithms will be shown. Both algorithms take into account the exact curvature of the wavefront produced by the near-field configuration of the EMSL. The first algorithm was presented in [143] and is based on an azimuth convolution between the data and a near-field focusing function. The second method, based on range migration techniques, was developed as part of this thesis and is described in Chapter 7. Since the final images from both methods are indistinguishable, and we are not interested in the computation efficiency at this moment, it will not be specified which method was used for computing every image in this section. The main parameters of the ISAR experiments, and the approximate resolutions in all directions, are reported in Table 4.1.

In order to facilitate the interpretation of the results, the application of this analysis technique is illustrated by performing the eigenvector-based TD on 2-D images corresponding to slices through the complete 3-D images. The ensemble averaging of the coherency matrix is applied in the spatial domain by using a moving window. In general, a window with a low number of pixels is chosen for reducing the potential degradation in resolution.

The first example of this method is shown in Fig. 4.21. The target is the fir tree, and its corresponding reflectivity images for all three polarizations were already published in [96]. As was observed in that paper, the differences in polarization are more evident in the top part of the tree, in which there are almost no branches and the trunk is providing the main contribution to the backscattering. Consequently, the top part of the trunk is more visible in the VV image. On the other hand, in the middle and bottom part of the tree, the architecture is more complex and the differences in polarization are smaller. The backscattered power in HV is comparable to that in HH and VV, which indicates that the main scattering centers are associated with the green, outer branches coated with needles which are randomly oriented in the tree volume.

Fig. 4.21 constitutes a further analysis than that made by comparison between polar-

**Table 4.1.** Measurements parameters and resolutions of the ISAR imaging results

| Sample | Frequency (GHz) | | Azimuth (deg) | | Elevation (deg) | |
| --- | --- | --- | --- | --- | --- | --- |
| | Min | Max | Min | Max | Min | Max |
| Fir tree | 1.0 | 5.5 | -12.0 | 12.0 | 28.0 | 52.0 |
| Ficus | 2.0 | 6.0 | -12.0 | 12.0 | 45.0 | 75.0 |
| Cluster Small Trees (Healthy) | 2.0 | 6.0 | -6.0 | 6.0 | 39.0 | 51.0 |
| Cluster Small Trees (Damaged) | 2.0 | 6.0 | -7.5 | 7.5 | 37.5 | 52.5 |
| Rice | 1.5 | 9.5 | -10.0 | 10.0 | 30.0 | 50.0 |

| Sample | Approx. Resolution (cm) | | |
| --- | --- | --- | --- |
| | Ground-range | Vertical X-range | Horizontal X-range |
| Fir tree | 6 | 6 | 15 |
| Ficus | 6 | 6 | 9 |
| Cluster Small Trees (Healthy) | 6 | 6 | 22 |
| Cluster Small Trees (Damaged) | 6 | 6 | 20 |
| Rice | 5 | 5 | 12 |

ization responses. Fig. 4.21 shows the spatial distribution of the dominant scattering mechanism $\overline{\alpha}$ and the target entropy $H$ corresponding to slices taken at zero ground-range and zero cross-range. It is evident that most values on the $\overline{\alpha}$ map are close to $45°$, which reflects the contribution of the needle-shaped leaves and branches at different frequency scales. Moreover, we can observe some areas with $\overline{\alpha}$ close to zero on the outer part of the branches. This indicates a surface-like behavior with no interaction with other tree parts, and corresponds to some planar structures formed by branches and leaves arrangements. On the other hand, there are some small spots near the trunk with values close to $90°$, which are due to double bounce reflections between the trunk and the branches. These conclusions obtained from $\overline{\alpha}$ maps are possible thanks to the roll-invariant properties of this parameter, thus giving the same response although the constituent particles could be rotated around the line of sight.

The inspection of the entropy maps in Fig. 4.21 reveals that at the working frequencies (1 to 5.5 GHz) the entropy is seldom maximum, and usually remains in the interval $0 \leqslant H \leqslant 0.7$. In the slice at zero ground-range (on the left) there are many areas with low entropy. These are due to two different behaviors. Firstly, parts of the tree exist with a dominant scattering mechanism and low randomness. The low randomness is produced by simple structures with a size comparable to the resolution cell or high reflectivity, so they prevail over other scattering mechanisms. Secondly, when $\overline{\alpha}$ is low, the maximum entropy is also low, as dictated by the feasible region on the $H - \alpha$ plane. Both cases can be distinguished by observing the entropy and $\overline{\alpha}$ maps at the same time.
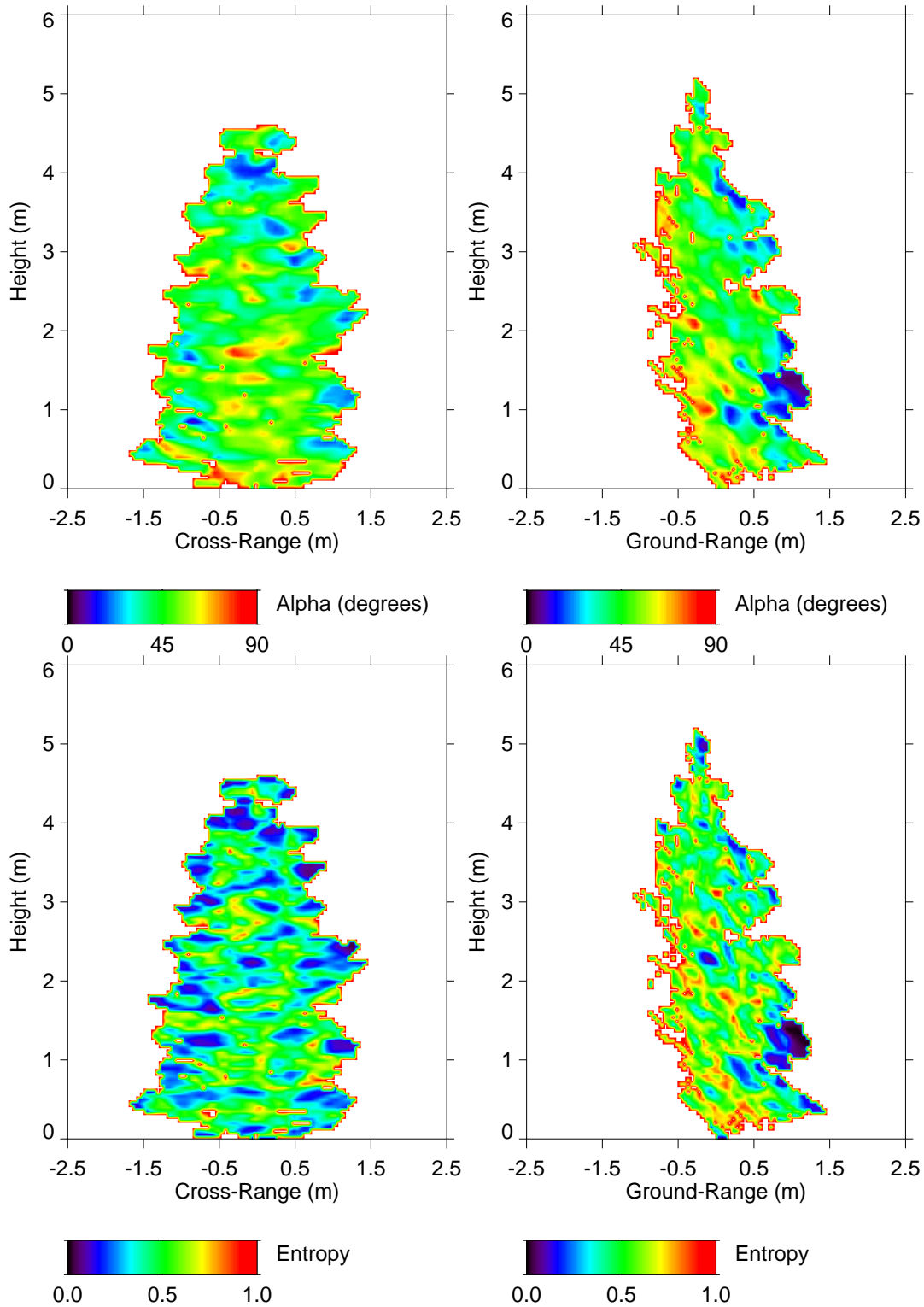
**Fig. 4.21.** Alpha and entropy values in the vertical slices at zero ground-range (left) and zero cross-range (right) out of the 3-D radar image of the fir tree

The ficus is more heterogeneous and, as a result, the reflectivity images can be described as a distribution of well-defined spots corresponding to leaves and branches. The spatial distribution of $\overline{\alpha}$ and entropy values is presented in Fig. 4.22. There is a cluster of leaves in the near-range area that produces a clear surface-like response. This response may originate from leaves which are oriented normally to the line of sight, thus pointing to the antenna. The other parts of the image show a dipole-like behavior that may be due to the scattering produced by the cylindrical branches on which no leaves are pointing to the antennas. For this target the entropy is very low everywhere, as can be expected for a sample with its physical characteristics, i.e. it is a plant with big and regular components (leaves and branches) in contrast with the fir tree.

Fig. 4.23 shows a comparison between the $\overline{\alpha}$ values for the cluster of small fir trees in healthy and damaged status. It is interesting to see that the central tree (a dead one) has drastically changed its scattering behavior, thus justifying the differences studied in Section 4.2.

The last example corresponds to images of the rice sample. The first, shown in Fig. 4.24, is a vertical slice at zero ground-range, whereas Fig. 4.25 displays two horizontal slices at two different heights (0 cm and 30 cm). The rice sample is quite small and, as a result, it is difficult to distinguish details inside the target volume. However, in the horizontal slice at 0 cm there are some evident spots with $\overline{\alpha}$ close to $90°$ which are produced by the double bounce between the cluster of stems of each plant and the wet ground. At 30 cm the target does not present those spots any more, but only areas with low and medium $\overline{\alpha}$ values which are created by the long leaves that constitute the structure of the plants.
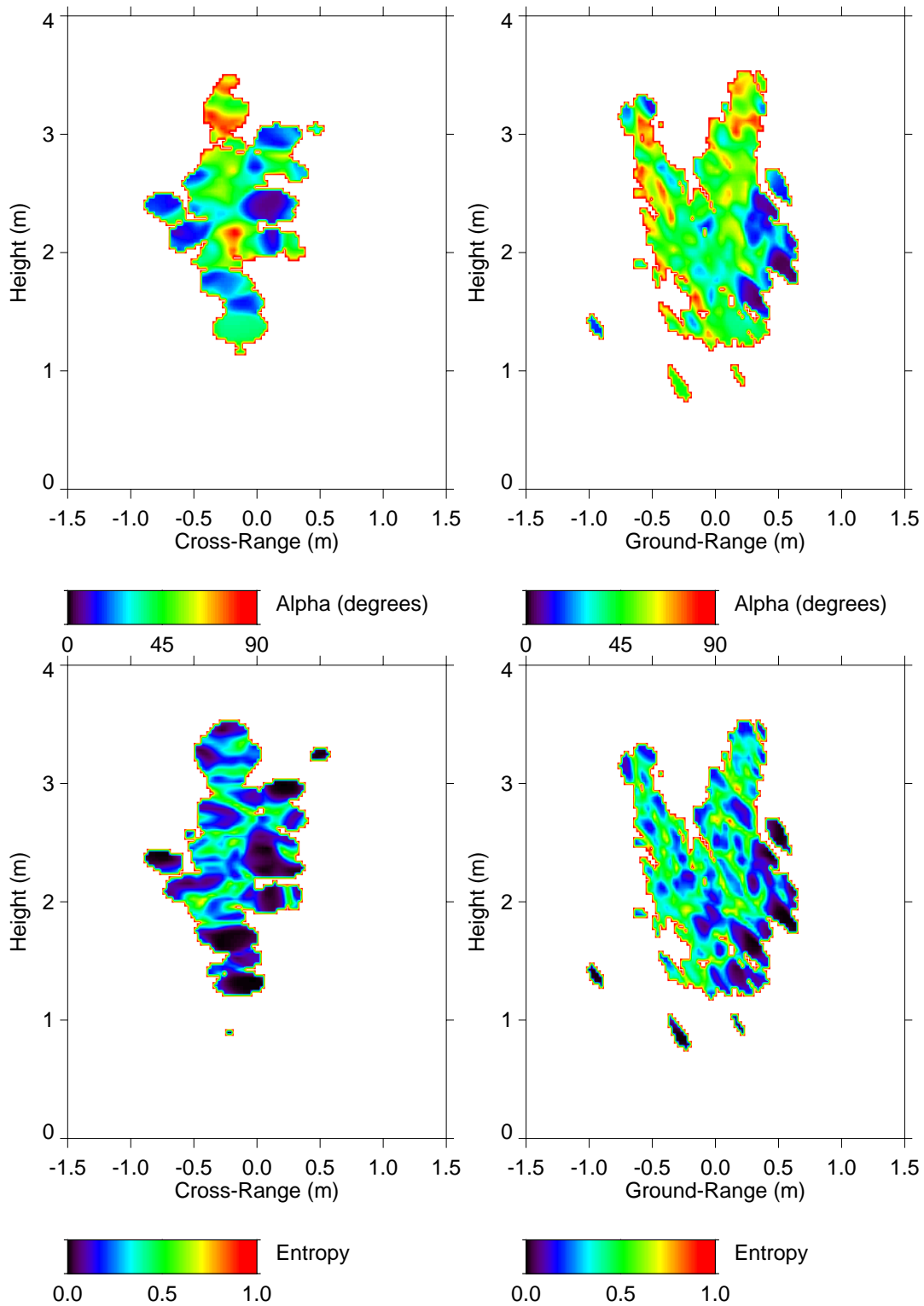
**Fig. 4.22.** Alpha and entropy values in the vertical slices at zero ground-range (left) and zero cross-range (right) out of the 3-D radar image of the ficus
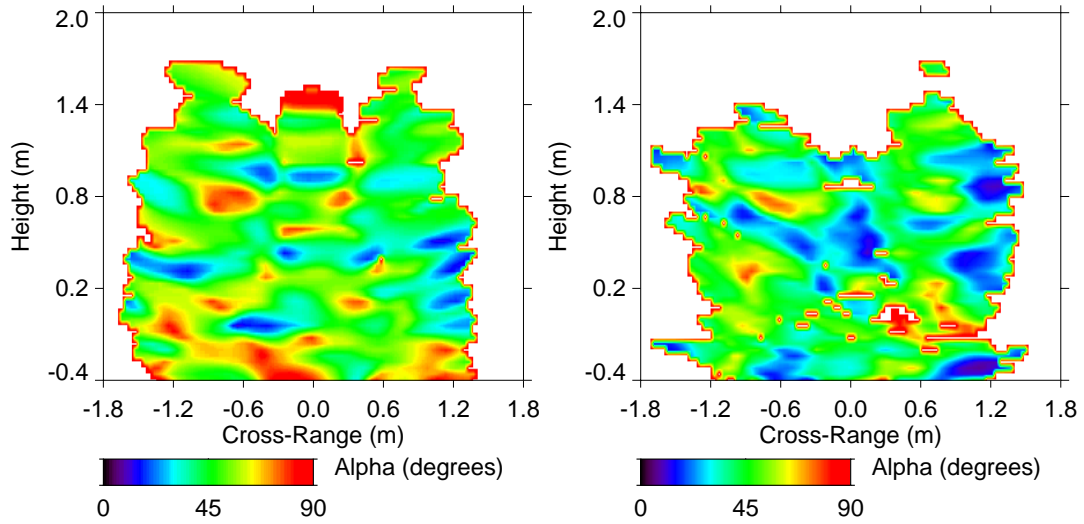
**Fig. 4.23.** Alpha values in the vertical slices at zero ground-range out of the 3-D radar image of the cluster of small fir trees: healthy (left) and damaged (right)
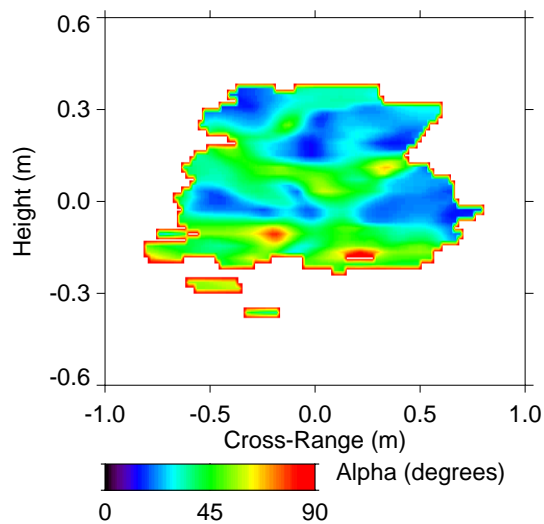


**Fig. 4.24.** Alpha values in the vertical slice at zero ground-range out of the 3-D radar image of the rice sample
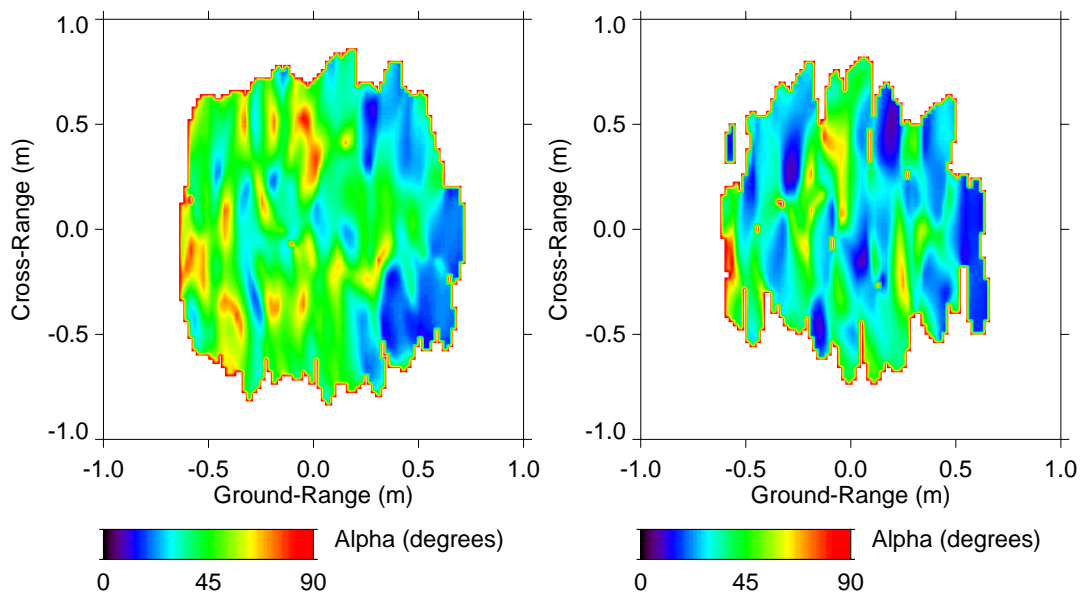
**Fig. 4.25.** Alpha values in horizontal slices at heights of 0 cm (left) and 30 cm (right) out of the 3-D radar image of the rice sample

## 4.5   Conclusions

The target decomposition theory presented in Chapter 3 has been applied to indoor polarimetric radar measurements at L, S, C and X band from different vegetation samples. The analysis has been performed in some complementary ways by computing the outputs of the decomposition theory from data in different domains. Firstly, the application of this technique to frequency domain backscatter data leads to a distribution of points on the $H - \alpha$ plane that are related to the dominant scattering mechanisms of the whole target and depend on the frequency band and the incidence angle. For all samples the dominant scattering mechanism at steep angles is close to surface type due to the reflection from the ground. The exact dependence on the frequency band and incidence angle depends on the physical structure of the target in an obvious way. In most cases the entropy was so high that the polarimetric information of the frequency domain data is limited, and the targets can be analyzed only in terms of reflected power and depolarization.

The frequency domain results have been justified by transforming the measured data into the time domain and thus identifying the position of the parts of the sample that contribute to the scattering mechanisms. The time domain decomposition helps to understand the scattering processes present in the samples and their dependence on the frequency and incidence angle, leading to some interesting findings. For example, at X band the penetration into the maize samples is quite high and, at the same time, there is a strong response from the leaves. Moreover, maize samples with young and mature plants have shown a different scattering behavior as the wave penetrates into the sample, and a differential extinction coefficient between orthogonal polarizations has been estimated in both cases. Concerning the measurements of the cluster of small fir trees, the high dependence on the working band observed in the frequency domain results has been associated with the varying penetration depth observed in the time domain results. Plots of entropy and average alpha as a function of range also confirm that this target can be simply modeled as a random volume over a half-space interface (the ground). The multi-layer vertical distribution of scattering mechanisms inside the vegetation volume has been demonstrated, so this work validates experimentally the foundations of polarimetric interferometry.

Finally, some 3-D reflectivity images obtained by ISAR experiments have been employed, together with the TD technique, for identifying the position and characteristics of the scattering mechanisms present in the target volume. These results have demonstrated the complex nature of the interaction of the electromagnetic waves and the vegetation structure, and the different types of scattering mechanisms have been successfully located inside the samples.

# An Inversion Algorithm for Vegetation

THIS chapter shows how the target decomposition scheme presented in Chapter 3 may be used for solving inverse problems on vegetation remote sensing. A simple algorithm is developed for a random cloud of particles that models an homogeneous vegetation layer. In the method presented here, the target entropy $H$ and the dominant scattering mechanism $\overline{\alpha}$ are used as inputs for the inversion procedure. In order to establish the relationship between these parameters and the physical attributes of the vegetation layer, a three-parameter model for backscatter from a random cloud of small anisotropic particles is formulated. The three parameters to be inverted are the particle shape ratio, the mean orientation angle of the cloud and the width of the distribution of orientation angles.

The chapter is organized as follows. Firstly, Section 5.1 presents a scattering model for a cloud of anisotropic particles. This model provides the relation between the parameters of the cloud (particle shape and orientation distribution) and the polarimetric observables of the TD theory used in this thesis ($H$ and $\overline{\alpha}$). Then, the inversion procedure is shown in Section 5.2, where there are also some examples of its application to experimental data. Finally, some conclusions are stated in Section 5.3.

## 5.1 Particle Scattering Model

The scattering from a cloud of anisotropic particles is considered in the following. The solution of this problem is detailed in Appendix B, and only the basic formulas have been repeated here for the sake of clarity. A schematic representation of a particle is shown in Fig. 5.1. We assume that only single scattering is significant and that each particle in the cloud acts independently of its neighbors. Each particle has a scattering matrix in its characteristic coordinate system of the form:

$$[S] = \begin{bmatrix} a & c \\ c & d \end{bmatrix} \quad \text{with} \quad a, d, c \in \mathbb{C}, \tag{5.1}$$
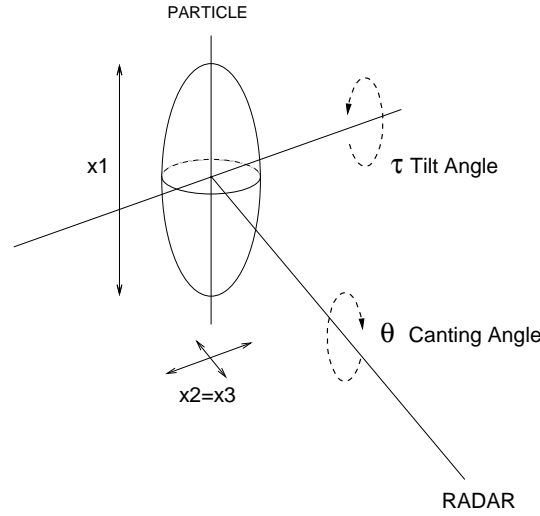
**Fig. 5.1.** Particle dimensions and rotating angles. The particle is shown at orientation $\theta = 0, \tau = 90°$

where $a$, $c$ and $d$ are complex scattering amplitudes:

$$a = \rho_1 \cos^2 \theta \sin^2 \tau + \rho_2 \sin^2 \theta + \rho_3 \cos^2 \theta \cos^2 \tau \tag{5.2}$$

$$d = \rho_1 \sin^2 \theta \sin^2 \tau + \rho_2 \cos^2 \theta + \rho_3 \sin^2 \theta \cos^2 \tau \tag{5.3}$$

$$c = (\rho_1 \sin^2 \tau - \rho_2 + \rho_3 \cos^2 \tau) \cos \theta \sin \theta. \tag{5.4}$$

They are defined in terms of the particle polarizabilities $\rho_1$, $\rho_2$ and $\rho_3$, canting angle $\theta$ and tilt angle $\tau$, according to the following expressions:

$$\rho_i = \frac{V}{4\pi \left( L_i + \frac{1}{\epsilon_r - 1} \right)} \tag{5.5}$$

$$L_1 + L_2 + L_3 = 1 \tag{5.6}$$

$$L_1 : L_2 : L_3 = \frac{1}{x_1} : \frac{1}{x_2} : \frac{1}{x_3}, \tag{5.7}$$

where $V$ is the particle volume and $x_i$ are the particle dimensions. Of particular importance is the anisotropy $A$ defined as the ratio of eigenvalues of $[S]$ and expressed in terms of the particle shape and material composition as

$$A = \frac{L_1(\epsilon_r - 1) + 1}{L_2(\epsilon_r - 1) + 1}. \tag{5.8}$$

As is explained in Appendix B, assuming spheroidal shapes so that $x_2 = x_3$, we can express the particle anisotropy $A$ directly in terms of the particle shape ratio $m = x_2/x_1$ as

$$A = \frac{m\epsilon_r + 2}{m + \epsilon_r + 1}$$

$$0 \leqslant m < \infty \quad \begin{cases} m < 1 & \text{Prolate spheroids} \\ m > 1 & \text{Oblate spheroids} \end{cases} \tag{5.9}$$

From this we see that if the dielectric constant is small ($\epsilon_r \simeq 1$) then the particle shape makes little difference to $A$ and polarimetry is of limited applicability. However, if $\epsilon_r$ is large (as it is for many vegetation remote sensing problems in the microwave spectrum) then $A$ becomes strongly dependent on the shape ratio of the particle. In this case polarimetry becomes useful and we can hope to invert the $[S]$ matrix data to obtain an estimate of particle shape.

Before getting into the whole problem with more degrees of freedom, let us study a simpler case. We now assume a generic particle with no tilt angle variation and initially oriented as in Fig. 5.1, i.e. with $\tau = 90°$ and $\theta = 0°$. In this particular situation its scattering matrix is:

$$[S] = \begin{bmatrix} a & 0 \\ 0 & d \end{bmatrix}. \tag{5.10}$$

Such a single particle has a coherency matrix of the form:

$$[T] = \begin{bmatrix} \epsilon & \mu & 0 \\ \mu^* & \nu & 0 \\ 0 & 0 & 0 \end{bmatrix}, \tag{5.11}$$

wherein

$$\begin{aligned} \epsilon &= \frac{1}{2}|a+d|^2 \\ \mu &= \frac{1}{2}(a+d)(a^*-d^*) \\ \nu &= \frac{1}{2}|a-d|^2. \end{aligned} \tag{5.12}$$

We can now generate the effect of rotation about the line of sight on the coherency matrix by pre- and post-multiplying by rotation matrices. This notation was already presented in Chapter 3 for studying the effect of symmetries on the coherency matrix. The coherency matrix of a single particle rotated by an angle $\theta$ is:

$$\begin{aligned} [T(\theta)] &= \begin{bmatrix} 1 & 0 & 0 \\ 0 & \cos 2\theta & \sin 2\theta \\ 0 & -\sin 2\theta & \cos 2\theta \end{bmatrix} [T] \begin{bmatrix} 1 & 0 & 0 \\ 0 & \cos 2\theta & -\sin 2\theta \\ 0 & \sin 2\theta & \cos 2\theta \end{bmatrix} \\ &= \begin{bmatrix} \epsilon & \mu \cos 2\theta & \mu \sin 2\theta \\ \mu^* \cos 2\theta & \nu \cos^2 2\theta & \nu \sin 2\theta \cos 2\theta \\ \mu^* \sin 2\theta & \nu \sin 2\theta \cos 2\theta & \nu \sin^2 2\theta \end{bmatrix}. \end{aligned} \tag{5.13}$$

If we assume a uniform distribution with mean $\theta = (\theta_1 + \theta_2)/2$ and width $\Delta\theta = \theta_2 - \theta_1$ for the orientation angle, as shown in Fig. 5.2, the analytic form of the coherency

$$P(\theta) = \begin{cases} \frac{1}{\theta_2 - \theta_1} & \theta_1 \leq \theta \leq \theta_2 \\ 0 & \text{otherwise} \end{cases}$$
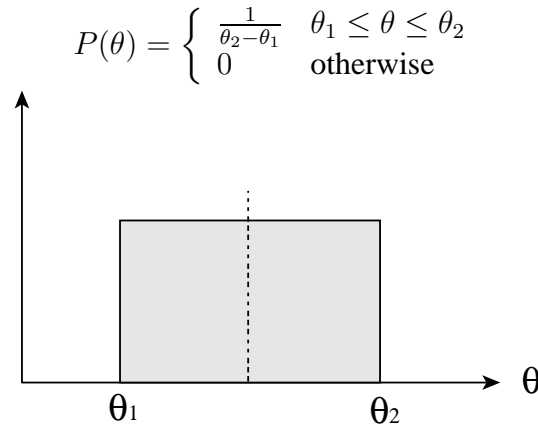


**Fig. 5.2.** Uniform distribution of particle canting angles

matrix yields [62]:

$$\langle [T] \rangle = \frac{1}{2\Delta\theta} \begin{bmatrix} \epsilon 2\Delta\theta & \mu[\sin 2\theta]_{\theta_1}^{\theta_2} & \mu[\cos 2\theta]_{\theta_1}^{\theta_2} \\ \mu^*[\sin 2\theta]_{\theta_1}^{\theta_2} & \nu[\theta + \frac{1}{4}\sin 4\theta]_{\theta_1}^{\theta_2} & \frac{1}{4}\nu[\cos 4\theta]_{\theta_1}^{\theta_2} \\ \mu^*[\cos 2\theta]_{\theta_1}^{\theta_2} & \frac{1}{4}\nu[\cos 4\theta]_{\theta_1}^{\theta_2} & \nu[\theta - \frac{1}{4}\sin 4\theta]_{\theta_1}^{\theta_2} \end{bmatrix}. \tag{5.14}$$

We see that the structure in this matrix depends on the sum and differences of the particle scattering coefficients, as well as on the distribution of orientation angles. Note that this is a more general model than that widely used in the radar literature [59], which normally supposes a uniform distribution over $\pi$ radians. In this model we can now include the case of aligned particles. Since natural vegetation may often be expected to have correlated orientation of leaves and scatterers, such an extension is important for attempting quantitative remote sensing inversion.

In the fully random case, the extreme values are $\theta_1 = 0$ and $\theta_2 = 180°$, and $\langle [T] \rangle$ has the diagonal form shown in (5.15) (compare with $[T_I]$ in (3.153)). The eigenvalues of $\langle [T] \rangle$ are then just its diagonal elements and from these we can calculate the $H - \overline{\alpha}$ values for a random cloud.

$$\langle [T] \rangle = \frac{1}{2} \begin{bmatrix} 2\epsilon & 0 & 0 \\ 0 & \nu & 0 \\ 0 & 0 & \nu \end{bmatrix} \tag{5.15}$$

If we now turn back to the particles with ellipsoid shape, by changing the anisotropy $A$ (defined in 5.9) it is possible to analyze a variety of shape aspects. For $A = 1$ we have either spheres or low dielectric material, for $A < 1$ we have prolate particles (needles) and for $A > 1$ oblate particles (disks). Fig. 5.3 shows how the $H$ and $\overline{\alpha}$ values vary as a function of $A$. Note the following points:
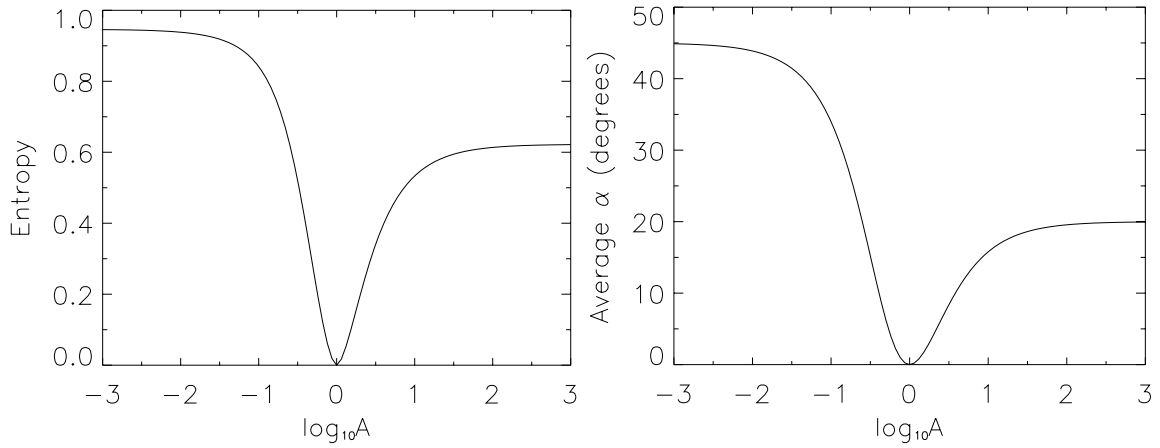
**Fig. 5.3.** Entropy and $\overline{\alpha}$ values for a random cloud of particles versus anisotropy $A$
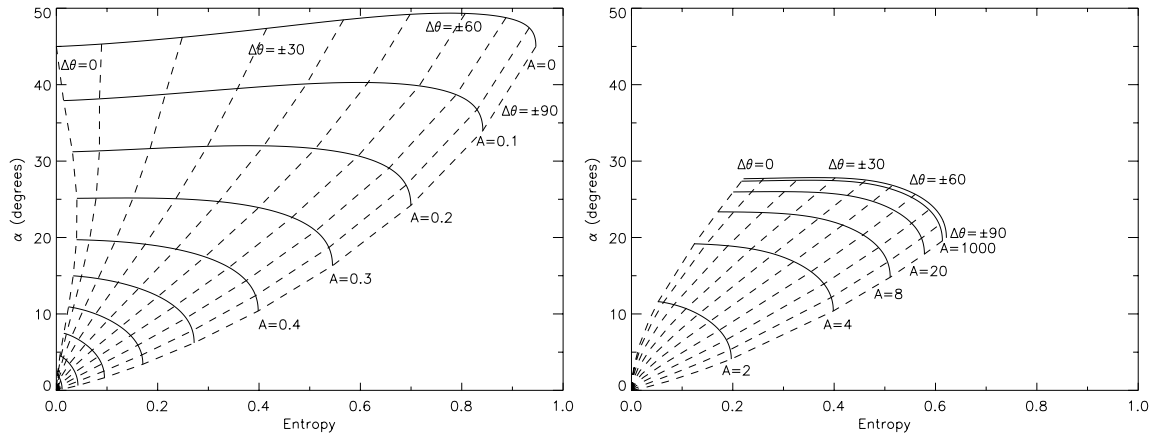


**Fig. 5.4.** Loci of $H - \overline{\alpha}$ values for fixed shape and varying orientation distribution

- For $A = 1$ the entropy is zero and $\overline{\alpha}$ is zero. The particles are spherical, so the orientation does not change their aspect

- Prolate particles yield a higher limiting entropy ($H = 0.95$) than oblate particles ($H = 0.62$)

- There is ambiguity as to the oblate/prolate shape of the particle for $H < 0.62$.

- If we plot the $H - \overline{\alpha}$ values in a plane then they all lie along curve I in Fig. 3.11.

It follows from the last point that we can consider curve I in Fig. 3.11 to be the locus of $H - \overline{\alpha}$ values for a truly random distribution but varying shape. This will be important when we come to try and invert data to obtain estimates of the orientation distribution.

The next stage of analysis is to examine the case where the particle shape is fixed but the cloud has a varying distribution of angles. The corresponding coherency matrix (derived

in Appendix B) has only five non-zero entries which are:

$$t_{11} = \frac{2}{15}(2 + 6A + 7A^2) \tag{5.16}$$

$$t_{12} = t_{21} = \frac{(2 + A - 3A^2)\sin 2\Theta}{15\Theta} \tag{5.17}$$

$$t_{22} = \frac{(A - 1)^2(4\Theta + \sin 4\Theta)}{30\Theta} \tag{5.18}$$

$$t_{33} = \frac{(A - 1)^2(4\Theta - \sin 4\Theta)}{30\Theta}. \tag{5.19}$$

Fig. 5.4 shows the $H - \overline{\alpha}$ loci for this case, where we now further assume that the tilt angle is uniformly distributed over $\pi$ radians. Here we can see that when $A = 0$ (i.e. dipoles) the locus is approximately a straight line at constant $\overline{\alpha}$ value ($45°$ as expected). Hence as the randomness of the distribution increases it effects mainly the entropy $H$. In the limiting situation of random distribution we obtain a point on curve I at $H = 0.95$ as expected from Fig. 5.3.

As $A$ increases so the loci remain of the same general form, i.e. lines parallel to the $H$ axis. In the limit $A = 1$ and the locus is just a point at the origin of $H - \alpha$ space. If $A$ is further increased ($A > 1$), the loci turn back to points with increasing $H$ and $\overline{\alpha}$. We conclude from this that the position of an $H - \overline{\alpha}$ data point obtained from an estimate of $\langle [T] \rangle$ for the scattering cloud can be used to infer information about both particle shape and orientation distribution. Note that there is still the ambiguity between oblate and prolate particles but only for $H$ values below 0.62. This means that in Fig. 5.4 the loci below $H = 0.62$ are bi-valued in $A$. For each locus there is a value of $A > 1$ and a value $A < 1$.

The final stage of this analysis is to consider the extraction of the mean orientation angle $\theta$. When the entropy is zero then $\theta$ may be estimated directly from the $[S]$ matrix data, as it was explained in Chapter 3. However, as the entropy increases so the estimate becomes biased by the averaging inherent in the definition of $\overline{\beta}$. To investigate the effect of increasing entropy we show in Fig. 5.5 the error between $\overline{\beta}$ and the true mean value $2\theta$. We see that the error is a function of particle anisotropy $A$. For strongly anisotropic particles the error can be significant.

If for example we have no *a priori* idea about the shape of the particles, then Fig. 5.5 gives an indication of the error in mean orientation angle with entropy. However, if we can obtain an estimate of particle shape then we can select the appropriate characteristic in Fig. 5.5 to compensate for the entropy bias and hence obtain an improved estimate of the mean canting angle.

To illustrate the extraction of mean orientation angle we consider the following examples. We consider a cloud of particles with shape anisotropy $A = 0.1$. In the first instance such a cloud is oriented at a mean angle of $40°$ with a spread of $\pm 40°$. The normalized
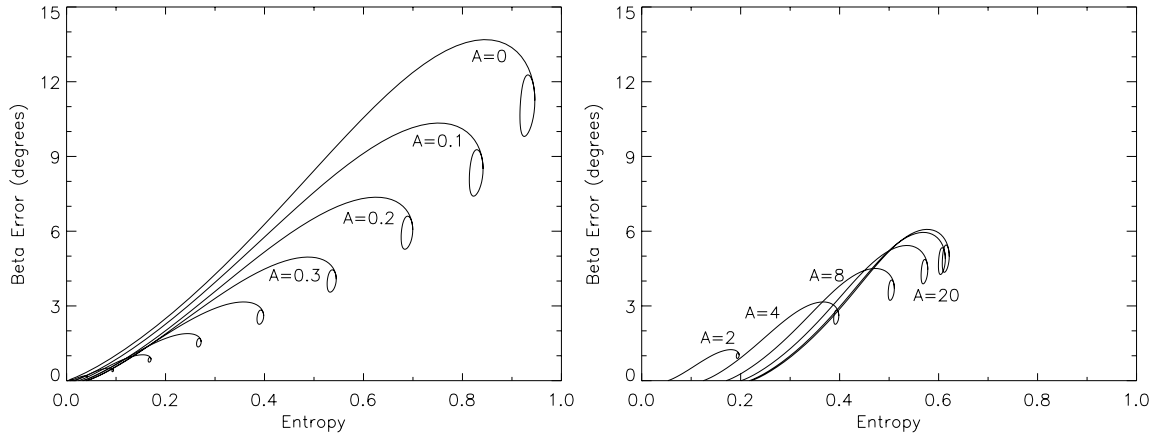
**Fig. 5.5.** Error in $\overline{\beta}$ angle estimate with increasing entropy and for varying particle shapes

coherency matrix for this case is:

$$\langle[T]\rangle = \begin{bmatrix} 1.000 & -0.100 & -0.568 \\ -0.100 & 0.2962 & 0.014 \\ -0.568 & 0.014 & 0.3732 \end{bmatrix}. \tag{5.20}$$

This matrix can be expressed in terms of its eigenvalues and eigenvectors and then estimates obtained for $H$, $\overline{\alpha}$ and $\overline{\beta}$. The entropy is $H = 0.5$ and the $\overline{\beta}$ estimate is $64°$ so that the mean orientation is estimated at $32°$. From Fig. 5.5 and using $A = 0.1$ we see that the expected bias error is around $8°$ which can be used to correct this estimate.

If we consider the same particle cloud but now with a mean inclination of only $10°$, the coherency matrix yields:

$$\langle[T]\rangle = \begin{bmatrix} 1.000 & -0.542 & -0.198 \\ -0.542 & 0.366 & 0.026 \\ -0.198 & 0.026 & 0.303 \end{bmatrix}. \tag{5.21}$$

The entropy is again $H = 0.5$ but this time the estimate of $\overline{\beta}$ is $4°$ corresponding to a mean inclination of $2°$. Again the corresponding bias is $8°$ which can be corrected through knowledge of $A$.

As an alternative to employing the mean $\overline{\beta}$, we also considered estimating the mean cloud orientation as $\beta_1$, i.e. the orientation of the maximum eigenvector of $\langle[T]\rangle$. For cloud simulations, this showed less bias than the Bernoulli mean and so does not require the above correction. Future studies will address the probem of the best orientation estimator. However, for the vegetation data considered in this thesis, the entropy is high and the orientation has a wide distribution (as later shown in Fig. 5.7). Moreover, the extensive azimuth averaging that has been used destroys the physical meaning of this angle in the estimates. Hence the mean orientation is not well defined and we have ignored it in the experimental analysis.

# 5.2   Inversion Algorithm and Experimental Results

From the average coherency matrix $\langle [T] \rangle$ we can obtain estimates of three main parameters: the entropy $H$ from the eigenvalues, the average scattering mechanism $\overline{\alpha}$ and the mean orientation angle $\overline{\beta}$ both from the eigenvectors. It is of interest to see if we can use these estimates to obtain the three physical parameters of the particles cloud, namely the mean particle anisotropy $A$, the mean orientation angle $\theta$ and the width of the orientation distribution $\Theta$.

Using the model of Section 5.1 we have an analytic nonlinear mapping from the physical parameters into the observables. Formally we may write

$$\Omega = \left[ \begin{array}{c} H \\ \overline{\alpha} \\ \overline{\beta} \end{array} \right] \qquad \Gamma = \left[ \begin{array}{c} A \\ \theta \\ \Theta \end{array} \right] \qquad \Omega = F(\Gamma), \tag{5.22}$$

where the function $F$ is given by the definitions of $H$, $\overline{\alpha}$ and $\overline{\beta}$ from the coherency matrix. If we denote the measured estimate of $\Omega$ as $\overline{\Omega}$ then the inversion procedure can be formally stated as

$$\overline{\Gamma} = F^{-1}(\overline{\Omega}) \quad \text{with} \quad F^{-1} \equiv \min_{\Gamma} \text{norm}(\overline{\Omega} - F(\Gamma)). \tag{5.23}$$

In practical terms the inversion proceeds in the following manner:

1. From an $H - \overline{\alpha}$ point obtain an estimate of the two parameters $A$ and $\Theta$ as in Fig. 5.4

2. Use the estimated $A$ value and $H$ to obtain a corrected $\overline{\beta}$ value

3. From the new $\overline{\beta}$ obtain an estimate of $\theta$

The most difficult stage is the first, where a two-parameter optimization must be employed. A straightforward simplex numerical optimization method can be readily used, as it requires no gradient information and is easy to implement. It is also possible to write the expressions for $H$ and $\overline{\alpha}$ as a function of $A$ and $\Theta$, which correspond to the parametric plots in Fig. 5.4. Hence, a simple search-and-refinement estimation of the nearest $A$ and $\Theta$ is performed iteratively.

The application of this inversion method to experimental data obtained from some vegetation samples is shown in the next figures. Since the method makes the assumption that the vegetation target is homogeneous, the inversion algorithm has been tested with frequency domain data. In this way, as it was explained in Chapter 4, the radar backscatter characterizes the sample as a whole. Attention is payed to the dependence of the results on frequency. Therefore an estimation of $A$ and $\Theta$ is obtained for each frequency in the working band.

Figs. 5.6 and 5.7 show the comparison of results between the fir tree and the ficus. The experimental data correspond to a measurement averaged in azimuth and with a small
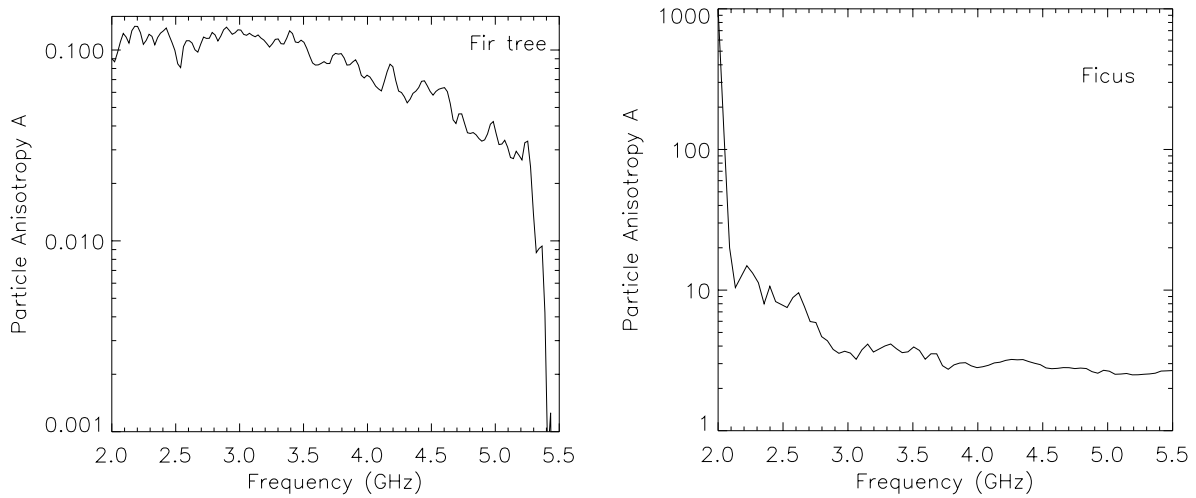
**Fig. 5.6.** Inversion results for the trees data: mean particle shape $A$. Fir tree (left) and ficus (right). Incidence angles $= 39° - 51°$. Frequency range $= 2 - 5.5$ GHz

span in elevation ($39° - 51°$). The frequency span is $2 - 5.5$ GHz. These are the same data used for computing the left plot of Fig. 4.13. Note that both fir tree and ficus were isolated (from the scattering viewpoint) and, therefore, the effect of the ground and the ground/tree interactions is not present in these results.

Regarding the ambiguity cited on Section 5.1, we have selected the prolate parameters ($A < 1$) for the fir tree and the oblate parameters ($A > 1$) for the ficus tree. This is also based on the loci occupied by the points in the $H - \alpha$ plane for both cases ($H > 0.62$ for the fir tree and $H < 0.62$ for the ficus) and on the *a priori* knowledge about the physical characteristics of the trees. In any case, even if we did not know whether it was oblate or prolate, the shape parameters obtained for the two trees would be very different because they are well separated in $H - \overline{\alpha}$. Hence we have a good discrimination in any case and have a two-valued shape parameter only for low entropy ($H < 0.62$) vegetation.

The next step is the physical interpretation of the results from Figs. 5.6 and 5.7. Note the following comments on the results from the fir tree:

- For frequencies below 3.5 GHz the backscatter appears to be dominated by particles of fixed anisotropy (around $A = 0.12$). This fact gives rise to a lower entropy than at higher frequencies, reflecting the fact that scattering here is dominated by larger scale branch and trunk structures.

- For frequencies above 3.5 GHz the backscatter mechanism changes and becomes dominated by scatterers of different shape at different wavelength scales. In this transition region the particles become more and more anisotropic (more like needles) and the width of the angular distribution increases. This is consistent with scattering from smaller scale branches and needles.
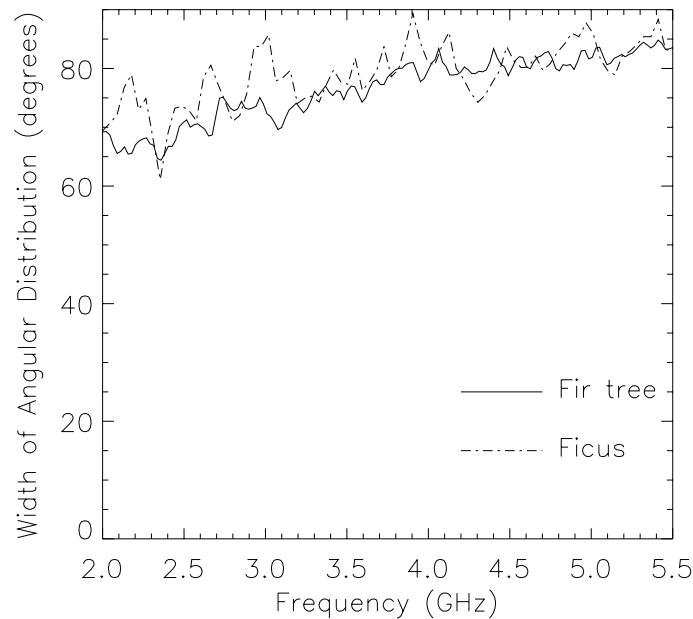
**Fig. 5.7.** Inversion results for the trees data: spread of orientation angles $\Theta$. Incidence angles $= 39° - 51°$. Frequency range $= 2 - 5.5$ GHz

- At the shortest wavelength the scattering is dominated by the smallest scale needle like structures on the tree, which have essentially a random distribution (a random cloud of dipoles) and highest entropy (0.95).

As expected, the results from the fir tree are consistent with the particle model employed in the inversion, since the structure of the tree (trunk-branches-leaves) is regularly scaled as a function of the frequency. Consequently, different parts of the trunk have been identified in the model at different frequencies, following a continuous change. However, this is not the case for the ficus tree. This kind of tree has two completely different components in its morphology: leaves and branches. As was stated previously, leaves are fairly elliptical disks and branches are cylindrical. We can see in Fig. 5.6 that for lower frequencies (less than 2.5 GHz) the particles present high values of $A$, corresponding to clouds of disks, which are the dominant mechanism in this case. At higher frequencies, the disks are more directive and only some of them are pointing to the receiver due to their random orientation. Thus, their response is averaged with the response from branches. Consequently, the $A$ values shown in the results are not directly related to any single scattering mechanism from the ficus. In addition, the constituent particles of the ficus are not electrically small at the working frequencies (for instance, the wavelength at 5 GHz is 6 cm whereas the leaves are more than 20 cm long), thus making difficult the applicability of this technique to such a vegetation type.

The width of angular distribution behaves for both trees in a similar way. This can be explained by looking at the $H - \overline{\alpha}$ loci in Fig. 4.13. The data are close to curve I at the border of the feasible region, and this curve corresponds to azimuthal symmetry, so
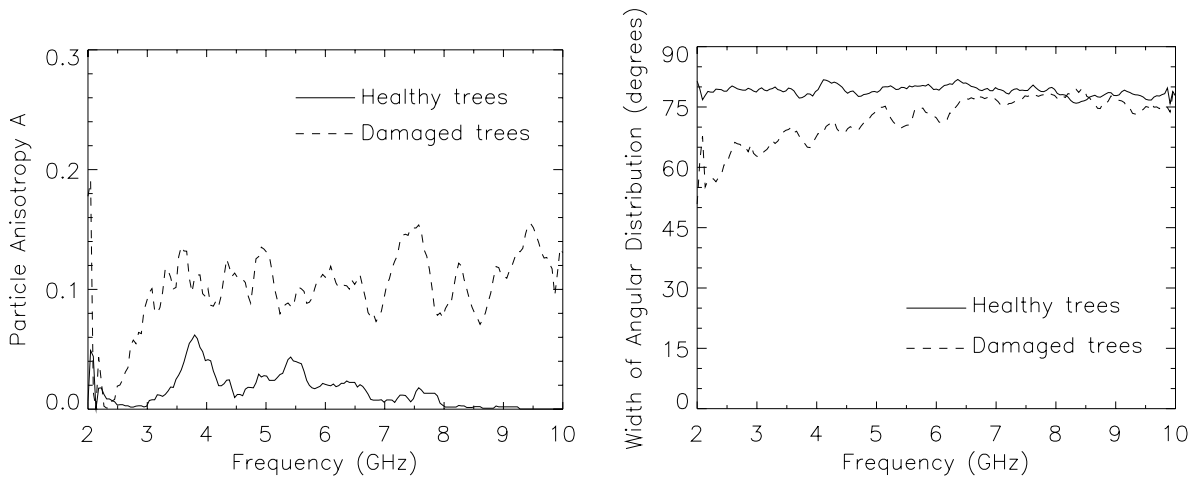
**Fig. 5.8.** Inversion results for the cluster of small fir trees in healthy and damaged status: mean particle shape $A$ (left) and spread of orientation angles $\Theta$ (right). Incidence angle $= 50°$. Frequency range $= 2 - 10$ GHz

there is no dependence on orientation at all and both distributions are very wide. It is the $H - \overline{\alpha}$ values which provide the discrimination between these data sets, not the width of the orientation distribution.

According to the variability present in Fig. 5.7, it is important to state that it is due to the randomness of the input data, but not to any potential sensitivity of the inversion to small errors in the input data. The fairly wide separation between loci in Fig. 5.4 indicates that this technique is basically robust because small changes in the input data will give small changes in the inverted parameters. However, for our data the entropy is high and so their statistical variability is high, requiring a large number of looks for good estimates of the eigenvalues and hence the $H - \overline{\alpha}$. Details of the variance of the estimates vs number of looks can be obtained by assuming Gaussian statistics and employing the complex Wishart distribution [152].

The second experimental result corresponds to the cluster of small fir trees. Fig. 5.8 illustrates the estimates of $A$ and $\Theta$ in the frequency range $2 - 10$ GHz for both states of the trees: healthy and damaged. In this case the sample was not isolated from the ground, so the ground-trunk interaction may influence the results since the incidence angle was $50°$.

The first interesting feature of the inverted particle anisotropy $A$ is the clear distinction between the healthy and the damaged situation at all frequencies. The healthy trees show a very low value of $A$ at all frequencies, thus revealing that the target is quite homogeneous and that its scattering is always dominated by the green needles. On the other hand, the damaged case exhibits a mainly uniform value about 0.1, which is nearly the same as the solitary fir tree at low frequencies. This phenomenon can be justified by the influence of the dead trees with no green needles, whose scattering is produced by the branches and trunks. The superposition of responses by dead and living trees is somewhat equivalent to the sum

of responses by the needles and branches in the solitary fir tree.

Another conclusion can be stated from the plots of the width of angular distribution for both cases. The healthy sample, as could be expected from the dominance of the needles as scatterers at all frequencies, shows a very high value of $\Theta$. This value is close to $90°$, which correspond to a fully random cloud of particles. In contrast, the damaged sample only exhibits the same high value of $\Theta$ from 6 GHz. Therefore, for lower frequencies the orientation distribution is not fully random. Anyway, this apparent lack of randomness must be analyzed by taking into account which are the effective scatterers at those frequencies, since we can expect to have a mixed response by living and dead trees as stated before.

So far, a comparison of the estimated particle anisotropy with the actual anisotropy (ground truth data) has not been tried. This exercise will be carried out in the future as part of an ongoing detailed morphological structure analysis of the vegetation samples, that was initiated with the fir tree [153, 154].

## 5.3   Conclusions

In this chapter it has been shown how an eigenvalue analysis of the average backscatter coherency matrix may be employed with a simple model of particle scattering to understand the physical basis of the radar observables in a clearer way than is obtained by looking at a simple polarimetric ratios such a HH/VV. In particular, it has been demonstrated that the $H - \alpha$ plane is a useful representation of the average properties of the data. On this plane, effects due to particle shape and orientation distributions are well separated, and hence one can employ this method in a robust inversion procedure to estimate the physical parameters of a cloud from experimental radar data.

The application of the algorithm has been validated with data collected at the EMSL from a fir tree, a ficus tree and a cluster of small fir trees. The results show a wavelength scale dependence of the shape and distribution of scatterers which reflects the complex volume scattering nature of such targets. These results indicate that such an inverse model can be usefully employed for the study of canopy scattering effects and for the inversion of radar data for vegetation and forestry classification problems. Although such shape and angle distributions are built into forward scattering models like vector radiative transfer [98], this is the first attempt known to the author to extract these parameters from radar data in an inversion process.

On the other hand, the mean orientation has already been applied to the extraction of surface slopes of non vegetated terrains in [66, 155, 156] (based on the polarization signature) and in [157] (based on the TD theory used in this thesis). In the experimental examples presented in this chapter the entropy is so high that the orientation distributions are wide and, therefore, the mean orientation is not a useful parameter. This is because we have carried out extensive averaging over azimuth to produce the estimates.

# Polarimetric SAR Interferometry: Retrieval of Vegetation Height

THE technique proposed in this chapter for the extraction of vegetation height estimates from SAR data consists basically in generating simultaneously various interferograms of the same scene. It has been demonstrated so far in this thesis that parts of trees or plants with different morphological characteristics exhibit different scattering behaviors. If those parts are physically located at different heights inside the vegetation volume or are characterized by dissimilar vertical distributions, their effective phase centers should be placed also at different heights. Since we have shown that polarimetry can distinguish between scattering behaviors, it can be applied to this problem in order to form interferograms associated with particular scattering mechanisms.

SAR Interferometry (InSAR) is a technique based on combining two SAR images of the same scene acquired from different positions and/or at different times. So far, InSAR has been widely used for topographic mapping (DEM generation) and detection of small coherent movements (differential interferometry) [158]-[160]. Moreover, in the last years InSAR has been also applied as an important tool to retrieve physical parameters of terrestrial surfaces. Whatever the final application is, accurate interferograms are required. The quality of the interferograms is closely related to the degree of correlation between the two complex SAR images, which is formally defined as *interferometric coherence*. The interferogram, or equivalently the *interferometric phase*, is a measure of the path length difference between the target and the two sensor positions. It can be used to derive the 3-D position of the image resolution element, allowing the generation of height maps. The interferometric correlation, or coherence, is a measure for the variance of the interferometric phase. It depends on two kinds of parameters: characteristics of the radar system (and data processing), and physical properties of the imaged scene. In this chapter, some basic definitions about InSAR will be cited for completeness, but the emphasis will be placed only on the aspects directly related with the extraction of vegetation height by means of polarimetric SAR interferometry. An exhaustive review of InSAR, including a complete bibliography, can be consulted in [161].

In order to establish an unified framework for studying polarimetric InSAR, a gener-

alization of the interferogram generation to the vector case is presented in this chapter. This generalization enables the use of all the polarimetric information of both images to form interferograms, and was originally proposed in [69].

It will be shown that the choice of the scattering mechanisms employed for constructing the interferograms relies on two general approaches. The first consists in a selection based on an *a priori* knowledge of the distribution of scattering mechanisms present in the scene. For example, if one knows that the two main contributions to backscatter are the direct scatter by the crown of the trees and the ground-trunk interaction, one can decide to form an interferogram with surface scattering type (i.e. $\alpha = 0°$ or using $S_{vv} + S_{hh}$) and another with dihedral type (i.e. $\alpha = 90°$ or using $S_{vv} - S_{hh}$). The second approach is not based on an *a priori* decision but on the solution of a fundamental issue in InSAR: the maximization of the interferometric coherence. It has been shown that the application of polarimetry to this issue leads to a new kind of decomposition of the scene scattering properties, which in turn enables the extraction of vegetation height [69]. Both approaches are analyzed in this chapter and compared with experimental data.

This chapter is organized in two main sections and a third with concluding remarks. Section 6.1 describes the theory necessary to understand the proposed method, while the experimental results are presented and discussed in Section 6.2.

# 6.1 Theory

The basic definitions concerning InSAR, with special mention of the interferometric coherence, are stated in the first section. Secondly, the generalization to vector interferometry is presented, and the coherence optimization by using polarimetry is detailed. This optimization also implies a new type of target decomposition that is explained in the text. Finally, the application of polarimetric radar interferometry to the retrieval of vegetation height is justified. Special emphasis is also placed on the comparison between the height retrieval by using the coherence optimization and that obtained by *a priori* assumptions about the scattering mechanisms.

Most of the formulation presented in this chapter has been replicated from [69]. However, all aspects that are considered to have important consequences on the estimation of vegetation height are intended to be explained more thoroughly in this thesis.

## 6.1.1 Interferometric Coherence

There exist various InSAR configurations depending on the system parameter that changes between the acquisitions of the two images employed to create the interferogram. The actual configuration defined by the EMSL geometry is equivalent to conventional *across-track* interferometry, i.e. the images are measured from two slightly different incidence angles.

Therefore, the following formulation will be presented on the general basis of an across-track InSAR system. The particular geometry of the EMSL will be described in the experimental results (Section 6.2).

An interferogram is the cross correlation between two complex signals $s_1$ and $s_2$ which correspond to the same physical cell, but are acquired from two spatially separate antennas. In our case, $s_1$ and $s_2$ denote the complex reflectivity values at two incidence angles, $\theta_1$ and $\theta_2$. The physical separation between the two antenna positions is called *baseline*. The interferometric phase $\phi$ is expressed as:

$$\phi = \arg\left(s_1 s_2^*\right), \tag{6.1}$$

where $^*$ means complex conjugation.

The interferometric coherence can be defined as the absolute value of the normalized complex cross correlation between both signals:

$$\gamma = \frac{|\langle s_1 s_2^* \rangle|}{\sqrt{\langle s_1 s_1^* \rangle \langle s_2 s_2^* \rangle}}, \tag{6.2}$$

where $\langle . \rangle$ indicates the expectation value. By definition, the coherence ranges in the interval $0 \leqslant \gamma \leqslant 1$.

Coherence is an essential parameter in interferometric applications, because the accuracy of the estimated interferometric phase is degraded by any loss of coherence. Following the explanations given in [69], the interferometric coherence can be modeled as a product of different contributions:

$$\gamma = \gamma_{SNR} \cdot \gamma_{Temporal} \cdot \gamma_{Baseline}. \tag{6.3}$$

The first term, $\gamma_{SNR}$, represents the decorrelation caused by additive noise. A simple formula can be derived for this term if the same signal-to-noise ratio ($SNR$) is assumed in both images, yielding [162]:

$$\gamma_{SNR} = \frac{1}{1 + 1/SNR}. \tag{6.4}$$

The dependence in (6.4) means that the influence of $\gamma_{SNR}$ is restricted to areas in the scene that exhibit low backscattering.

The second contribution, $\gamma_{Temporal}$, is the temporal coherence of the scene. In this case, decorrelation can be originated by changes in the scene occurring during the time interval between the two acquisitions. These changes may be due to alterations in the geometry and/or the scattering behavior of the scatterers inside the resolution cell.

Finally, the third source of decorrelation is the separation between the two antenna positions (baseline decorrelation). $\gamma_{Baseline}$ characterizes the loss of coherence due to the

difference in perspective from the two positions, since the same scene is viewed from a different look angle in each image. This contribution has been well analyzed by employing the Fourier domain. The difference between the two viewing angles produces a shift and a stretch of the two imaged terrain spectra [163]. In the case of pure surface scattering, this decorrelation can be compensated by shifting the transmitted central frequency during the second measurement or by removing the disjoint parts of both spectra by a common band filtering [163]. However, any distribution in height of the scatterers inside the resolution cell produces a spectral decorrelation (a change in the shape of the spectra) that cannot be compensated by spectral filtering [164]. A possible way to reduce this volume decorrelation is to exploit multiple baseline takes [165], which implies collecting data from multiple surveys.

A close inspection of these sources of decorrelation reveals that the last two, namely $\gamma_{Temporal}$ and $\gamma_{Baseline}$, must be strongly influenced by the wave polarization used in the images generation. This influence derives from the origin of these two decorrelation sources: the change (due to perspective or time) in the scattering behavior of the scene between both images. As demonstrated in previous chapters of this thesis, polarimetry deals with the vector nature of the electromagnetic waves and enables the identification and characterization of the scattering mechanisms present in a natural scene. Next sections illustrate how polarimetry can be applied to reduce the decorrelation between the two images that form the interferogram, thus improving the final accuracy of the interferometric phase.

## 6.1.2   Coherence Optimization by Polarimetry

We have seen in Section 6.1.1 that both temporal and baseline decorrelations are produced by a different scattering behavior of the scene in the two images. The general idea of applying polarimetry to optimize the interferometric coherence consists in selecting arbitrary scattering mechanisms in the SAR images, and hence choosing those scattering mechanisms that maximize the interferometric coherence. The polarimetric optimization of the interferometric coherence has an exact formal solution which has been formulated in [69].

### 6.1.2.1   Vector Interferometry

The derivation of this formulation is based on an extension of the interferogram formation, described above, to the vector case. This extension is also needed for incorporating all polarimetric information into the coherence problem.

The generalization of the interferometric phase and coherence to the vector case makes use of the target vectors defined in Chapter 3. Those target vectors are simply a vectorization of the scattering matrix that contains the full polarimetric information associated with each pixel of the SAR images. For convenience, the vectorization selected in this section is based on the Pauli spin matrices. Its application to the case of backscattering from

a reciprocal medium yields the following target vector:

$$\mathbf{k} = \frac{1}{\sqrt{2}} \begin{bmatrix} S_{vv} + S_{hh} \\ S_{vv} - S_{hh} \\ 2S_{vh} \end{bmatrix}, \tag{6.5}$$

which corresponds to $\mathbf{k}_{3P}$ in (3.88). Note that this formulation can be also derived on the basis of the $\mathbf{k}_{3L}$ vectors (see Chapter 3).

In interferometric measurements, the polarimetric information of both SAR images will be contained in two different scattering vectors, $\mathbf{k}_1$ and $\mathbf{k}_2$, for image 1 and image 2, respectively. Using the outer products formed by combinations of both scattering vectors, it is also possible to define the following $3 \times 3$ matrices:

$$[T_{11}] = \langle \mathbf{k}_1 \mathbf{k}_1^{*T} \rangle \tag{6.6}$$

$$[T_{22}] = \langle \mathbf{k}_2 \mathbf{k}_2^{*T} \rangle \tag{6.7}$$

$$[\Omega_{12}] = \langle \mathbf{k}_1 \mathbf{k}_2^{*T} \rangle, \tag{6.8}$$

where $[T_{11}]$ and $[T_{22}]$ are the standard coherency matrices containing the full polarimetric information for each separate image as defined in Chapter 3, and $[\Omega_{12}]$ is a new $3 \times 3$ complex matrix that contains not only polarimetric information, but also the interferometric phase relations of the different polarization channels between both images[1].

Since the interferogram is, by definition, the complex cross correlation of two scalar complex numbers, we need to convert the polarimetric information contained in $\mathbf{k}_1$ and $\mathbf{k}_2$ into scalar numbers. In order to perform that conversion, two normalized complex vectors $\mathbf{w}_1$ and $\mathbf{w}_2$ are introduced. Then, the scattering coefficients $\mu_1$ and $\mu_2$ are defined as the projection of the target vectors $\mathbf{k}_1$ and $\mathbf{k}_2$ onto the vectors $\mathbf{w}_1$ and $\mathbf{w}_2$, respectively:

$$\mu_1 = \mathbf{w}_1^{*T} \mathbf{k}_1 \tag{6.9}$$

$$\mu_2 = \mathbf{w}_2^{*T} \mathbf{k}_2. \tag{6.10}$$

The scalar values $\mu_1$ and $\mu_2$ are linear combinations of the elements of the vectors $\mathbf{k}_1$ and $\mathbf{k}_2$. The coefficients of these linear combinations are the entries of the vectors $\mathbf{w}_1$ and $\mathbf{w}_2$. Using the scalar values in (6.9)-(6.10), one can obtain a new expression for the vector interferogram formation as:

$$\mu_1 \mu_2^* = \left( \mathbf{w}_1^{*T} \mathbf{k}_1 \right) \left( \mathbf{w}_2^{*T} \mathbf{k}_2 \right)^* = \mathbf{w}_1^{*T} [\Omega_{12}] \mathbf{w}_2, \tag{6.11}$$

from which the interferometric phase is:

$$\phi = \arg \left( \mu_1 \mu_2^* \right) = \arg \left( \mathbf{w}_1^{*T} [\Omega_{12}] \mathbf{w}_2 \right). \tag{6.12}$$

---

[1]The expectation value symbols $\langle . \rangle$ have been omitted in the notation of the matrices for simplifying the formulation. In the following, a matrix denoted by $[T]$ corresponds to an average matrix (denoted as $\langle [T] \rangle$ in other chapters).

Moreover, the interferometric coherence can be generalized to the vector case, yielding:

$$\gamma = \frac{|\langle \mu_1 \mu_2^* \rangle|}{\sqrt{\langle \mu_1 \mu_1^* \rangle \langle \mu_2 \mu_2^* \rangle}} = \frac{\left|\langle \mathbf{w}_1^{*T}[\Omega_{12}]\mathbf{w}_2 \rangle\right|}{\sqrt{\langle \mathbf{w}_1^{*T}[T_{11}]\mathbf{w}_1 \rangle \langle \mathbf{w}_2^{*T}[T_{22}]\mathbf{w}_2 \rangle}} \tag{6.13}$$

As explained in Chapter 3, the normalized vectors $\mathbf{w}_1$ and $\mathbf{w}_2$ can be interpreted as two scattering mechanisms, since the *Point Target Reduction Theorem* is totally applicable to these vectors. Consequently, the calculus consisting in the projection of the measured data $\mathbf{k}_1$ and $\mathbf{k}_2$ onto these vectors is equivalent to the selection of arbitrary scattering mechanisms in both scenes.

Another comment should be made about the generalized expression of coherence in (6.13). It is important to realize that if $\mathbf{w}_1 \neq \mathbf{w}_2$, we are affected by two different correlations: the already explained interferometric contribution, and a polarimetric correlation between the two scattering mechanisms corresponding to $\mathbf{w}_1$ and $\mathbf{w}_2$. As a result, the total coherence can be described as the following product:

$$\gamma = \gamma_{Int} \cdot \gamma_{Pol}, \tag{6.14}$$

where $\gamma_{Int}$ corresponds to the original interferometric coherence shown in (6.3). Only in the case of $\mathbf{w}_1 = \mathbf{w}_2$ does $\gamma_{Pol}$ become one and $\gamma = \gamma_{Int}$.

### 6.1.2.2  Coherence Optimization

The idea of the polarimetric optimization of the interferometric coherence, presented in (6.13), consists in choosing the linear combinations of polarization channels that yield the highest coherence. In other words, we can optimize the coherence by properly selecting $\mathbf{w}_1$ and $\mathbf{w}_2$.

This optimization problem has been solved in [69] by maximizing the complex Lagrangian $L$ defined as:

$$L = \mathbf{w}_1^{*T}[\Omega_{12}]\mathbf{w}_2 + \lambda_1 \left(\mathbf{w}_1^{*T}[T_{11}]\mathbf{w}_1 - C_1\right) + \lambda_2 \left(\mathbf{w}_2^{*T}[T_{22}]\mathbf{w}_2 - C_2\right), \tag{6.15}$$

where $\lambda_1$ and $\lambda_2$ are Lagrange multipliers introduced for maximizing the numerator of (6.13) while keeping the denominator constant. $C_1$ and $C_2$ are constants. By setting the partial derivatives to zero, we arrive at the following pair of $3 \times 3$ complex eigenvalue problems:

$$\begin{aligned}
[T_{11}]^{-1}[\Omega_{12}][T_{22}]^{-1}[\Omega_{12}]^{*T}\mathbf{w}_1 &= \nu\mathbf{w}_1 \\
[T_{22}]^{-1}[\Omega_{12}]^{*T}[T_{11}]^{-1}[\Omega_{12}]\mathbf{w}_2 &= \nu\mathbf{w}_2,
\end{aligned} \tag{6.16}$$

where $\nu = \lambda_1\lambda_2^*$.

Both equations in (6.16) share the same eigenvalues $\nu$. It is possible to demonstrate that the three eigenvalues are real and non-negative, i.e. $\nu_1 \geqslant \nu_2 \geqslant \nu_3 \geqslant 0$. Each eigenvalue

is related to a pair of eigenvectors ($\mathbf{w}_{1_j}$ and $\mathbf{w}_{2_j}$, with $j = 1, 2, 3$), one for each image. The maximum coherence is given by the square root of the maximum eigenvalue:

$$\gamma_{opt} = \sqrt{\nu_1}, \tag{6.17}$$

while its corresponding eigenvectors are denoted as the *optimum* ones: $\mathbf{w}_{1_{opt}}$ and $\mathbf{w}_{2_{opt}}$. Therefore, to find the interferogram with the highest possible coherence, we project the target vectors $\mathbf{k}_1$ and $\mathbf{k}_2$ onto $\mathbf{w}_{1_{opt}}$ and $\mathbf{w}_{2_{opt}}$, yielding the two optimized scalar complex values $\mu_{1_{opt}}$ and $\mu_{2_{opt}}$. The resulting interferometric phase takes the form:

$$\phi = \arg\left(\mu_{1_{opt}}\mu_{2_{opt}}^*\right) = \arg\left(\mathbf{w}_{1_{opt}}^{*T}\mathbf{k}_1\mathbf{k}_2^{*T}\mathbf{w}_{2_{opt}}\right) = \arg\left(\mathbf{w}_{1_{opt}}^{*T}[\Omega_{12}]\mathbf{w}_{2_{opt}}\right). \tag{6.18}$$

Since the absolute phase of the eigenvectors is not uniquely defined by (6.16), it is necessary to use an additional condition which establishes the phase difference between them. One way to solve the problem is based on the fact that all the interferometric phase information must be contained only in the complex scattering vectors $\mathbf{k}_1$ and $\mathbf{k}_2$, so we can use the following condition:

$$\arg(\mathbf{w}_{1_{opt}}^{*T}\mathbf{w}_{2_{opt}}) = 0. \tag{6.19}$$

Regarding the existence of solutions in (6.16), it depends on the availability of the inverse matrices $[T_{11}]^{-1}$ and $[T_{22}]^{-1}$. In practice, image coherency matrices are of full rank 3, thus enabling this computation. Otherwise, the formulation can be rewritten for the special case of rank 2 or less [69].

The interferometric coherence optimization by means of polarimetry has been formally stated by proposing a generalized definition of coherence in (6.13). The solution presented in [69] makes use of a Lagrange function to find the optimum vectors $\mathbf{w}_{1_{opt}}$ and $\mathbf{w}_{2_{opt}}$. An alternative solution has been recently published in [166]. This new approach avoids the presence of the Lagrangian by introducing the concept of matrix *contraction*. This new analytical scheme seems to be more compact. Furthermore, it enables a new interpretation of the results. For example, the particular case of no backscattering in the cross-polar channel, which leads to sub-optimum results, has been treated and successfully derived. The mathematical derivations of this alternative procedure are out of the scope of the present thesis, since its application to the vegetation height estimation is totally equivalent to the former method.

A possible physical interpretation of the optimization procedure was also explained in [69]. It has already been shown that the proposed algorithm deals mainly with two sources of decorrelation: $\gamma_{Temporal}$ and $\gamma_{Baseline}$. The choice of the optimum vectors $\mathbf{w}$ can be understood as the extraction from the data of a deterministic scattering mechanism that has the closest possible relation to a *point scatterer*, in order to reduce the height distribution of the scattering centers inside the resolution cell to a point. In this way, the volume decorrelation is removed from $\gamma_{Baseline}$ and the coherence is improved. However, in the case of important temporal changes in the scene between both images, the optimization will lead to $\mathbf{w}_1 \neq \mathbf{w}_2$ (a loss in the polarimetric correlation $\gamma_{Pol}$), and therefore the algorithm cannot provide any improvement as the coherence will remain low, independently of the choice of polarization.

### 6.1.2.3  A New Target Decomposition

We have seen that the solution of the coherence optimization has the form of a pair of eigenvalue problems. Consequently, the obtained solutions should exhibit all the intrinsic characteristics of any eigenvector problem. This is illustrated in the following.

We have denoted the pairs of eigenvectors as $\{\mathbf{w}_{1_j}, \mathbf{w}_{2_j}\}$, with $j = 1, 2, 3$. The first vector pair $\{\mathbf{w}_{1_1}, \mathbf{w}_{2_1}\}$ is related to the highest eigenvalue, and represents the pair of optimum scattering mechanisms. These optimum scattering mechanisms have been found in the complete 3-D complex space of the target vectors $\mathbf{k}_1$ and $\mathbf{k}_2$. The second pair $\{\mathbf{w}_{1_2}, \mathbf{w}_{2_2}\}$, corresponding to the second highest eigenvalue, is contained in the 2-D subspace orthogonal to the first pair of eigenvectors. Within this subspace, they can be interpreted as the optimum scattering mechanisms. Finally, there remains a 1-D subspace orthogonal to the 2-D subspace generated by the first two pairs of eigenvectors. The third pair of eigenvectors, $\{\mathbf{w}_{1_3}, \mathbf{w}_{2_3}\}$, related to the lowest eigenvalue, represents the optimum scattering mechanisms within this 1-D subspace.

In a way similar to the target decompositions (TD) described in Chapter 3, the $3 \times 3$ matrices appearing in (6.16) can be expressed as a linear combination of three matrices that correspond to the outer products of the eigenvectors:

$$
\begin{aligned}
[T_{11}]^{-1}[\Omega_{12}][T_{22}]^{-1}[\Omega_{12}]^{*T} &= \nu_1(\mathbf{w}_{1_1}\mathbf{w}_{1_1}^{*T}) + \nu_2(\mathbf{w}_{1_2}\mathbf{w}_{1_2}^{*T}) + \nu_3(\mathbf{w}_{1_3}\mathbf{w}_{1_3}^{*T}) \\
[T_{22}]^{-1}[\Omega_{12}]^{*T}[T_{11}]^{-1}[\Omega_{12}] &= \nu_1(\mathbf{w}_{2_1}\mathbf{w}_{2_1}^{*T}) + \nu_2(\mathbf{w}_{2_2}\mathbf{w}_{2_2}^{*T}) + \nu_3(\mathbf{w}_{2_3}\mathbf{w}_{2_3}^{*T}).
\end{aligned}
\tag{6.20}
$$

Physically, the orthogonality exhibited by the eigenvectors can be interpreted as statistical independence between the scattering mechanisms they represent. Therefore, one can now form three different interferograms, each one related to a scattering mechanism independent from the others:

$$
\mu_{1_j}\mu_{2_j}^* = \left(\mathbf{w}_{1_j}^{*T}\mathbf{k}_1\right)\left(\mathbf{w}_{2_j}^{*T}\mathbf{k}_2\right)^* = \mathbf{w}_{1_j}^{*T}[\Omega_{12}]\mathbf{w}_{2_j}.
\tag{6.21}
$$

The construction of these three interferograms from the same scene enables the calculation of the relative phase differences between them, which in turn represent the topographic difference between the effective phase centers of the corresponding scattering mechanisms. The phase difference between two mechanisms $i$ and $j$ is given by:

$$
\Delta\phi_{ij} = \arg(\mu_{1_i}\mu_{2_i}^*) - \arg(\mu_{1_j}\mu_{2_j}^*).
\tag{6.22}
$$

The main difference between the new target decomposition formulated in (6.20) and other proposed decompositions (see Chapter 3) is that the selection of the scattering mechanisms $\mathbf{w}$ is performed on the basis of an optimization of the interferometric coherence. As a result, the interferogram generated by using the optimum scattering mechanisms has the highest possible coherence, thus permitting the most accurate estimation of the interferometric phase. This optimum accuracy would not be achieved if one construct an interferogram by employing an arbitrary scattering mechanism such as a linear polarization (HH, VV or HV) or a Pauli matrix (surface, dihedral, etc.).

### 6.1.3   Vegetation Height Retrieval: Approaches

The simultaneous construction of various interferograms from the same scene, corresponding to different scattering mechanisms, constitutes the basis of the application of polarimetric radar interferometry to vegetation height estimation. In general, vegetation volume is a very complex and heterogeneous medium. This physical complexity or lack of homogeneity can be considered, from the point of view of the radar, as an advantage for solving the problem of extracting the height of plants or trees. The reason is that the parts of the plants with different morphology exhibit different scattering properties. For instance, a forest scene can be regarded as a multilayer structure (e.g. crown-branches-trunks-ground) with different scattering behaviors along the vertical direction (e.g. dipoles-surfaces-double bounces). The phase differences between interferograms represent the topographic difference between the effective phase centers of the corresponding scattering mechanisms. Then, the height differences are directly related with the absolute vegetation height. The exact relationship between them depends on the particular parameters of the vegetation target (dielectric geometry) and on the radar system parameters (frequency, incidence angle, baseline, etc.).

In Section 6.1.2.3 the choice of the scattering mechanisms $\mathbf{w}$ to form the interferograms is based on the optimization of the interferometric coherence. In this way, three pairs of scattering mechanisms are selected. The first produces the highest coherence, whereas the other two yield lower coherences. In case of a non vegetated surface, all three pairs of scattering mechanisms produce interferograms centered at the surface topography. The interferogram with best quality is that generated with the optimum pair because its coherence is the highest. When we are interested in computing the height of a vegetation volume present in the scene (or an estimate related to the absolute height), we have to calculate the phase difference between first and second, or second and third, or first and third. A first problem arises at this stage on the real interpretation of those scattering mechanisms. Vectors $\mathbf{w}$ are selected to maximize the coherence, but no information is provided about their relative position inside the vegetation volume. In other words, it is possible to find the optimum scattering mechanisms located at the top of the plants, or at the ground level, or somewhere in between. Therefore, we cannot infer which mechanisms should be used for calculating the best parameter related to the actual height of the plants. In second place, although the first scattering mechanism produces a high coherence, nothing is said about the other two. As a result, the height differences between them may also exhibit a non-negligible variance.

In contrast with this choice resulting from the coherence optimization, a selection based on the knowledge of the scattering properties of the imaged scene can be employed. It consists in deciding *a priori* which scattering mechanisms should be used for generating the interferograms. For example, if one knows that the cross-polar return is mostly produced by the crown of the trees, and that the horizontal polarization backscatter comes from the ground-trunk interaction, two interferograms at HH and HV should be computed. Evidently, the advantage is the easier interpretation of the scattering mechanisms we are dealing with. The drawback is that it requires a previous knowledge of the scene.

As far as the phase accuracy is concerned, it will be shown in the next section that the

variance of the relative height differences is quite similar in both approaches, because most of the times the selected scattering mechanisms in the second approach exhibit coherences of the same order as those of the optimization.

Both approaches have been compared in this chapter. In the second method, two simple selections have been proposed. The first corresponds to interferograms with the three elements of the scattering matrices in the $v$–$h$ basis, i.e. HH, HV and VV. The second choice consists of the Pauli matrices, i.e. HH+VV, HH–VV and HV. It will be demonstrated that both cover most cases of scattering from vegetation, and present clear physical interpretations, thus being well adapted to this problem.

According to the generalization of the interferogram formation to the vector case, the same formulation holds for the alternative approach by using the following pairs of scattering mechanisms (with the same **w** in both images):

$$v\text{--}h \text{ Basis:} \qquad \mathbf{w}_1 = \frac{1}{\sqrt{2}} \begin{bmatrix} 1 \\ 1 \\ 0 \end{bmatrix} \quad \mathbf{w}_2 = \frac{1}{\sqrt{2}} \begin{bmatrix} 1 \\ -1 \\ 0 \end{bmatrix} \quad \mathbf{w}_3 = \begin{bmatrix} 0 \\ 0 \\ 1 \end{bmatrix}$$

$$\text{Pauli Matrices:} \quad \mathbf{w}_1 = \begin{bmatrix} 1 \\ 0 \\ 0 \end{bmatrix} \qquad \mathbf{w}_2 = \begin{bmatrix} 0 \\ 1 \\ 0 \end{bmatrix} \qquad \mathbf{w}_3 = \begin{bmatrix} 0 \\ 0 \\ 1 \end{bmatrix}$$

Note that the order is arbitrary in these cases, since it is not related to the coherence provided by each scattering mechanism.

The first work about a method based on an *a priori* selection of the scattering mechanisms has appeared recently in [167]. That study deals with the extraction of height of forests stands. For the choice of polarizations the authors analyzed the components of backscattering for such forest stands at L band. At this frequency, they demonstrated that the phase center for HH polarization tends to be close to the ground, while that for HV polarization is located somewhere up in the canopy [168]. This behavior is due to the main contributions to each polarization. The scattering for HH is predominantly created by the trunk-ground interaction, whereas for HV the direct backscatter from branches is dominant. The authors computed the height difference between the interferograms for HH and HV polarizations and later, by using a coherent scattering model for the trees, converted this value into an estimate of the height of the entire trees. The comparison with ground truth data was quite satisfactory, and a sensitivity analysis of the system parameters was also presented. The interferograms at HH, HV and VV have been also applied in the experimental results presented in the next section. However, in this thesis, no coherent scattering model has been employed for relating the height differences with the total physical height.

From the reasons explained above about the selection of polarization for each interferogram, it follows that perhaps better estimates would be achieved by employing the

scattering mechanisms corresponding to the Pauli matrices. For example, the trunk-ground interaction is a clear dihedral behavior whose return is mainly present in the subtraction of copolar responses, HH–VV. Furthermore, the direct scattering from the canopy could be better modeled by the odd scatterer polarization, i.e. HH+VV. This decomposition has been also applied in the experimental results of Section 6.2.

With regard to the interferograms generated by employing the scattering mechanisms resulting from the coherence optimization, to date two test sites have been presented in the literature: 1) an area with corn fields in Switzerland, measured at L band by E-SAR [169, 170], and 2) a mixed forestry/agricultural area close to Lake Baikal, measured at L band by SIR-C [69]. In the first case an approximate height of about 2.2 m was estimated for corn fields, but no ground truth data were available. In the second, a comparison with the actual ground truth was recently published in [171]. These references introduce an important point that is carefully considered in the following.

Since the original publication of the coherence optimization by polarimetry in [69], no details have been provided by the authors about the practical implementation of the vegetation height retrieval algorithm. In all results it has been stated that the final height is retrieved by using the optimum scattering mechanisms. However, it is not said whether they use the two mechanisms associated with the first and second eigenvalues, or just the two most separate inside the vegetation volume. As will be shown in the next section, this criterion has important implications in the final estimated height. Moreover, a comparison between the results obtained by the optimum polarizations, and those provided by using HH and HV, or HH+VV and HH–VV, was also presented in [171]. The comparison fails to state the criterion for the optimum mechanisms, but in the discussion it is said that the results provided by them are well adjusted to the true height of the trees, whereas the other choices of polarizations underestimate the height. It seems that the comparison in [171] is not consistent since in one case they use the two most separate centers in a group of three, whereas in the other they only look at two centers. In the next section, it will be demonstrated for different vegetation samples that all three choices provide similar estimates if the most separate mechanisms are employed. Moreover, the authors of [171] expected to retrieve the total height of the trees directly from the interferogram differences. This is not totally correct, because the scattering centers can be located anywhere inside the volume, and not necessarily at the top and bottom extremes of the trees.

## 6.2  Experimental Results

The geometry employed at EMSL for the interferometric experiments is depicted in Fig. 6.1. Since the range from the antennas to the focus is constant and known, $R_0$, the interferometric phase can be studied in terms of the path difference between the ranges to a target point located at coordinates $(Y, H)$. The phase can be expressed as:

$$\phi = 2k(R_2 - R_1) \simeq 2k\left[Y(\sin\theta_1 - \sin\theta_2) + H(\cos\theta_1 - \cos\theta_2)\right], \qquad (6.23)$$

where $k = 2\pi f/c$ is the wavenumber at the central frequency, and the transmission-reception procedure is repeated for each antenna position.

The expression in (6.23) presents a dependence of the interferometric phase on both spatial coordinates $Y$ and $H$. It is known that the dependence on the ground-range variable $Y$ can be canceled by applying a so-called *wavenumber shift* [164]. It consists in changing the transmitted frequencies in both measurements. Note that when this frequency shift cannot be implemented at the measurement time, it can be applied later as a spectral filtering which eliminates the non-coincident bands in both images. In fact, the wavenumber shift is applied for improving the coherence, since it reduces the baseline decorrelation as was commented in Section 6.1.1. In the case of the experiments at EMSL the wavenumber shift can be readily applied by selecting different frequency bands for the images, because the data are always acquired over a large bandwidth with a small step between frequencies [137].

The introduction of a change in the transmitted frequency affects the phase formula in (6.23), yielding:

$$\phi = 2(k_2 R_2 - k_1 R_1) \simeq 2[Y(k_1 \sin\theta_1 - k_2 \sin\theta_2) + H(k_1 \cos\theta_1 - k_2 \cos\theta_2)] \qquad (6.24)$$

The spectral shift between the two images is intended to remove the dependence on $Y$. Therefore, it must satisfy:

$$k_1 \sin\theta_1 = k_2 \sin\theta_2, \qquad (6.25)$$
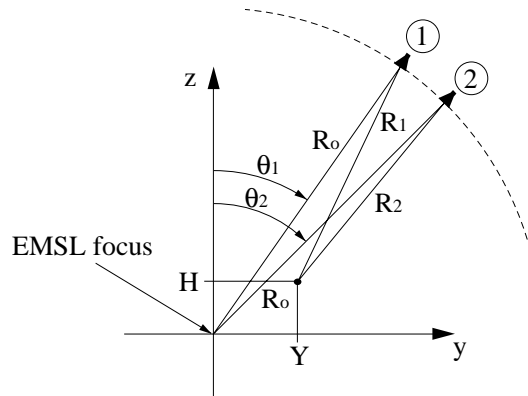


**Fig. 6.1.** Geometry of the interferometric experiments at EMSL

that substituted in (6.24) yields

$$\phi = 2k_1 H \left( \cos\theta_1 - \frac{\sin\theta_1}{\sin\theta_2} \cos\theta_2 \right). \tag{6.26}$$

In order to achieve a more compact notation, the following variables are introduced:

$$\theta_c = \frac{\theta_1 + \theta_2}{2} \tag{6.27}$$

$$\Delta\theta = \theta_2 - \theta_1. \tag{6.28}$$

If we assume that $\Delta\theta$ is very small, we can apply the following approximations:

$$\sin\theta_1 = \sin(\theta_2 - \Delta\theta) \simeq \sin\theta_2 - \Delta\theta \cos\theta_2 \tag{6.29}$$

$$\cos\theta_1 = \cos(\theta_2 - \Delta\theta) \simeq \cos\theta_2 + \Delta\theta \sin\theta_2, \tag{6.30}$$

that substituted into (6.26) yield:

$$\phi \simeq 2k_1 H \frac{\Delta\theta}{\sin\theta_2}. \tag{6.31}$$

Finally, from (6.31) we can express the interferometric phase as produced by the variation along the vertical coordinate $z$:

$$\phi = k_z H, \tag{6.32}$$

with the following effective propagation constant $k_z$:

$$k_z = \frac{2k\Delta\theta}{\sin\theta_c}. \tag{6.33}$$

The set-up employed at EMSL is different from that used in conventional SAR interferometry since the whole vegetation sample must be confined inside a single resolution cell in order to apply the algorithm and, as a result, there is only one pixel in each image. Consequently, spatial averaging cannot be performed. Instead, two alternative averaging techniques have been used. The first consists in rotating the target in azimuth in order to obtain independent samples. The minimum angular step that provides statistical independence between samples depends on the target size in terms of the wavelength. The second approach is known as frequency averaging or frequency agility, and is based on collecting the radar returns from non-overlapping frequency bands. Both techniques are equivalent to some extent, as explained in [172]. In most cases both methods have been combined for achieving a large number of samples and reducing the final variance of the estimates.

Two kinds of scanning geometries have been employed. The first consists in measuring the backscattering at a few closely-spaced incidence angles, and rotating the sample in

azimuth over $360°$ in order to obtain as many independent samples as possible. The second type of measurements was originally planned for three-dimensional inverse SAR (ISAR) imaging. Its particular characteristic is that the target is rotated only about a narrow angular span (typically $10°$ to $20°$), and it employs a very small step as is usually needed in radar imaging. Consequently, the number of independent samples in azimuth is low for our purposes, and additional frequency averaging must be applied to reduce the variability of the results.

In order to minimize the phase noise and hence to improve the accuracy of the height estimates, the interferograms for each scattering mechanism were multi-looked over the entire set of independent samples. The importance of this multi-look procedure is justified below with experimental results. The number of samples, which can be regarded as pixels of a conventional image, changed between experiments as was explained above. Note that we are not affected by the loss of resolution that the multi-look procedure entails because our scene is completely homogeneous (in fact we are always looking at the same target). The conversion from interferometric phase to height is calculated by using (6.32). It is also important to emphasize that the estimates presented in the next results are not affected by phase ambiguities because the maximum height of the plants (plus the standard deviation) does not exceed the ambiguity height [161].

The application of polarimetric radar interferometry to the estimation of vegetation height has been tested with three different samples: the maize sample C, the cluster of small fir trees and the rice sample (see photographs and physical descriptions in Chapter 4). The experiments on the maize sample were carried out over the whole azimuth range, whereas the other two correspond to imaging configurations. The results for the maize will be more extensively analyzed than the other two because they are less exposed to biases and inaccuracies thanks to the larger number of independent samples.

Two experiments were carried out on the maize sample. In both of them the incidence angle ranged from $44°$ to $45°$ with a step of $0.25°$, and the target was rotated in azimuth with a step of $5°$, thus obtaining 72 independent samples. The frequency span was 0.3 to 4.3 GHz in the first case and 1.5 to 9.5 GHz in the second. The reflectivity images were computed with a narrow bandwidth (40 MHz) in order to enclose the whole target inside the resolution cell. In the next figures, the displayed frequency range is limited to L, S and C band because at shorter wavelengths some ambiguities arise in the results due to the large baselines that have been employed.

The first results are shown in Fig. 6.2 for both frequency bands. The baseline is $0.25°$ and the averaging is performed over 72 azimuth positions and 9 frequencies, thus yielding 648 independent samples. These figures illustrate the height estimates for different polarizations as a function of frequency.

Many comments can be derived from these plots. For example, it is interesting to compare the optimum scattering mechanisms with those represented by the Pauli matrices. Up to 2 GHz there is an equivalence between the positions of the scattering mechanisms of the Pauli matrices and those obtained by the coherence optimization. The mechanism
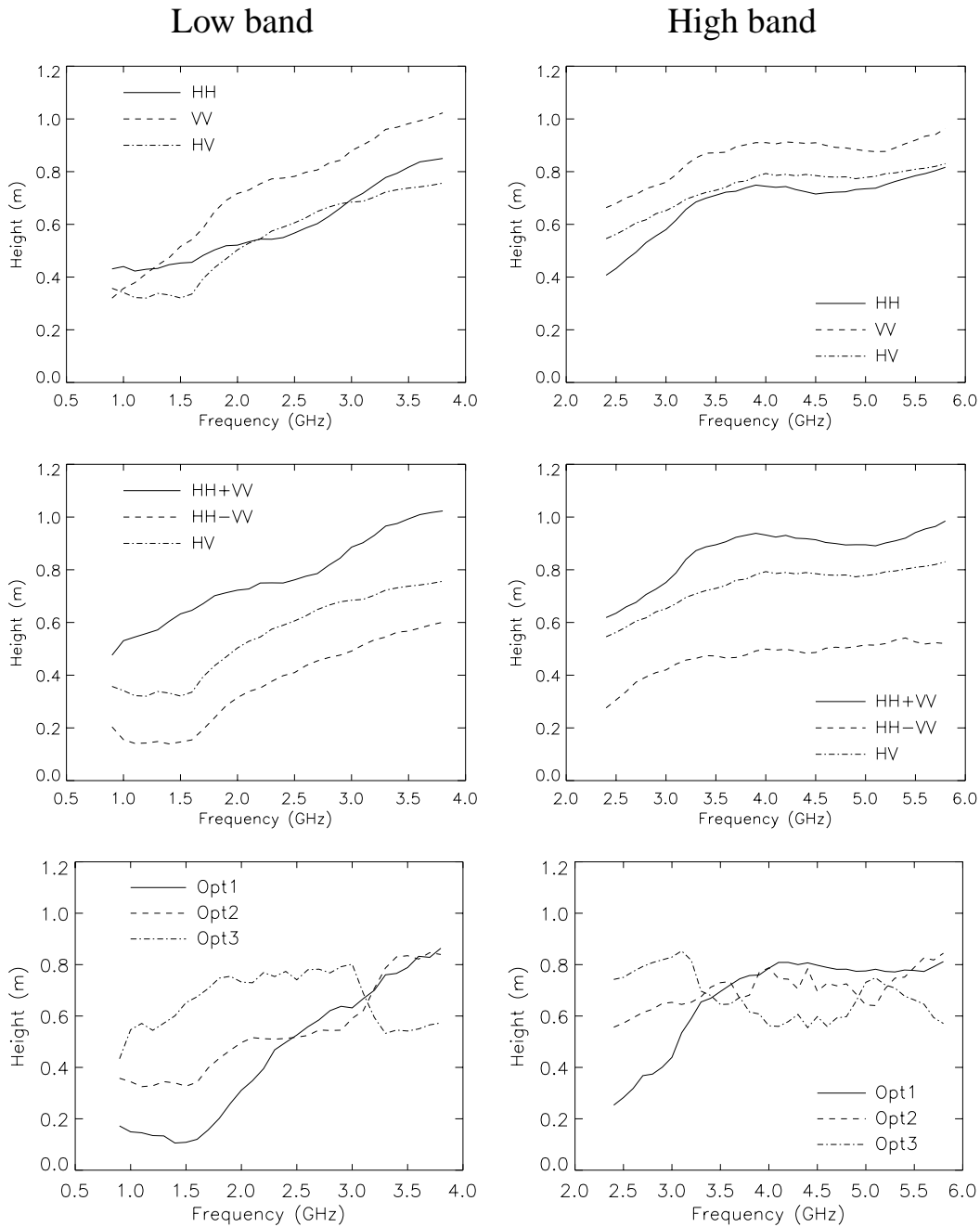
**Fig. 6.2.** Maize sample. Height of the scattering centers vs frequency. Parameters: $B = 0.25°$, $\theta_c = 45°$, Samples = 72 angles $\times$ 9 frequencies. Top: $v$–$h$ basis. Center: Pauli matrices. Bottom: optimum scattering mechanisms

with the highest coherence is equivalent to the dihedral type (HH–VV), which is located close to the ground. Physically, it is produced by the stem-ground interaction which clearly dominates for this target at low frequencies and with the current incidence angle. The second optimum mechanism (related to the middle coherence) is located at almost the same

height as the cross-polar scattering. Finally the optimum mechanism with lower coherence is associated with the direct return (HH+VV) from the scatterers.

For frequencies higher than 3 GHz the optimum scattering mechanisms change their relative positions. For example, from 3 to 3.5 GHz the second and third mechanisms swap (the third goes to the lowest position, and the second to the highest). Moreover, from 3.5 GHz the first and second mechanisms are almost coincident in height, while the third remains under both of them. These changes in the optimum scattering mechanisms will be present in the rest of results too. This phenomenon constitutes a drawback of the mechanisms provided by the coherence optimization method. This is not observed for the mechanisms derived on the basis of their physical position in the sample.

It is important to highlight that for this sample the HH–VV response comes from the lowest point for all frequencies, while HH+VV is always located at the highest position. The separation between them is about 0.4 m. As was stated in the previous section, this estimate can be converted to an absolute height by analyzing the position of the scattering centers as a function of the physical dimensions and characteristics of the target, but this conversion is out of the scope of this thesis.

With regard to the phase centers for the $v$–$h$ basis, they are closer together than those extracted from the Pauli matrices for all frequencies. This is because they are physically not well separate in the vegetation volume of maize. For example, the HH return comes not only from the ground-stem interaction, but also from all the parts of the stems. Consequently, this choice of basis does not seem optimum for maize crops monitoring.

According to the obtained results, a hypothetical system for remotely controlling the growth of maize crops may be designed. The working frequency can be L, S or C band, since the estimates behave equally for all this range. The incidence angle is preferred around $45°$ because (although not demonstrated in these indoor experiments) at steeper angles the direct return from the ground may dominate and mask the other backscattered fields, and from gentler angles all scattering centers would approach one to each other because the return is mostly dominated by the direct response of the above-ground volume. Finally, the best processing should be based on the retrieval of the height centers of the HH+VV and HH–VV channels.

Note that the results shown in the left and right columns in Fig. 6.2 present some discrepancies in their common band (2.4–3.8 GHz). They may be due to the change in the measurement system between both experiments, since the antennas are different as was explained in Chapter 4. Nevertheless, the conclusions about the behavior of the estimates are perfectly valid for both cases, as well as the best performance of the choice of HH+VV and HH–VV as the ideal channels for an inversion algorithm. The system performance only should be taken into account when converting those estimates into absolute heights (by means of scattering models).

The uncertainty of the estimates is also analyzed here. Any interferometric phase can be studied as a random variable. The first-order statistics of the interferometric phase has
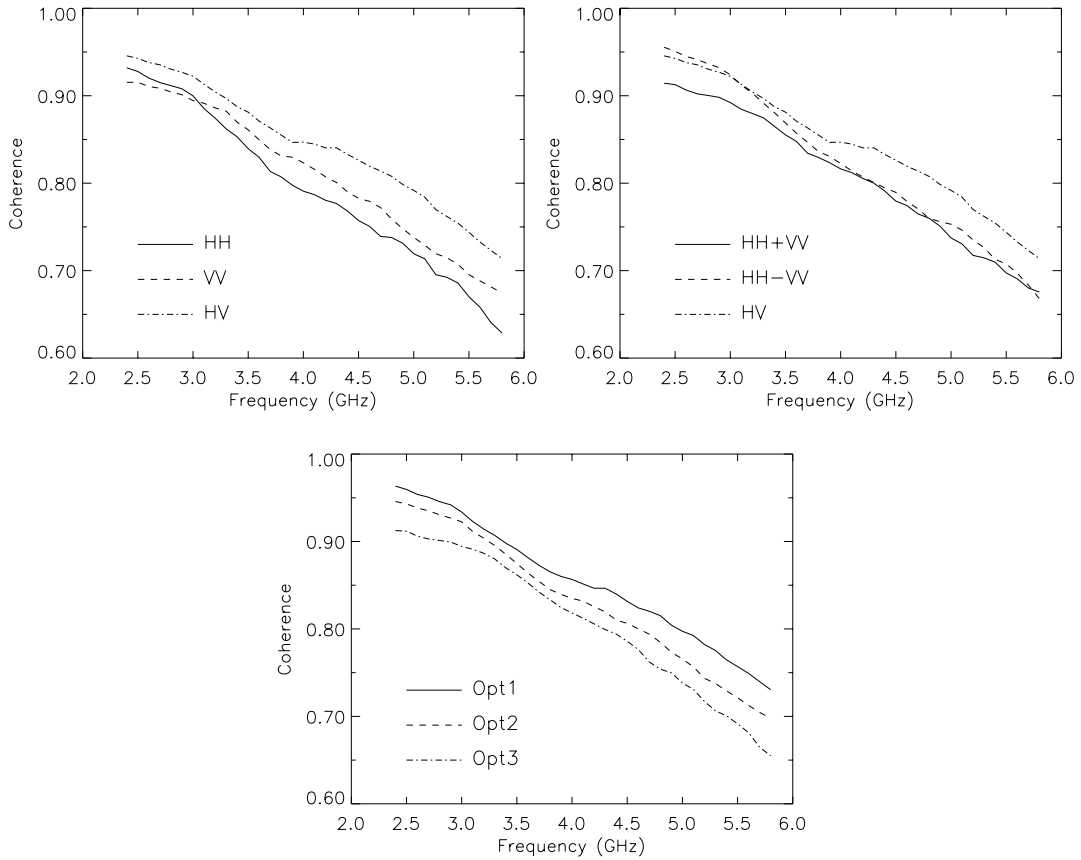
**Fig. 6.3.** Maize sample. Mean coherence for the scattering mechanisms vs frequency (high band). Parameters: $B = 0.25°$, $\theta_c = 45°$, Samples = 72 angles $\times$ 9 frequencies. Top left: $v$–$h$ basis. Top right: Pauli matrices. Bottom: optimum scattering mechanisms

been widely described in the literature, and an explicit expression for its probability density function (PDF) has been also provided [173, 162, 152]. The standard deviation of the phase decreases as the coherence increases, but even for high coherences the standard deviation is rather large. For example, for $\gamma = 0.9$, the standard deviation is $\sigma_\phi \approx 40°$. Since our height estimates are based on the interferometric phase, the phase estimation process is an important issue. It has been demonstrated that the standard deviation of the phase estimation can be drastically reduced by introducing a *multi-look* procedure. This method consists in averaging the final interferogram over a number of independent interferograms of the same scene. In practice, it can be performed by averaging over some pixels of the scene if it is homogeneous or if a loss of spatial resolution is not a constraint. In the EMSL configuration it is possible to average the interferogram over independent samples. An expression of the resulting interferometric phase is:

$$\phi = \arg\left(\sum_{i=1}^{L} s_1^i s_2^{i*}\right), \tag{6.34}$$

where $L$ is the number of samples used in the multi-look estimate.
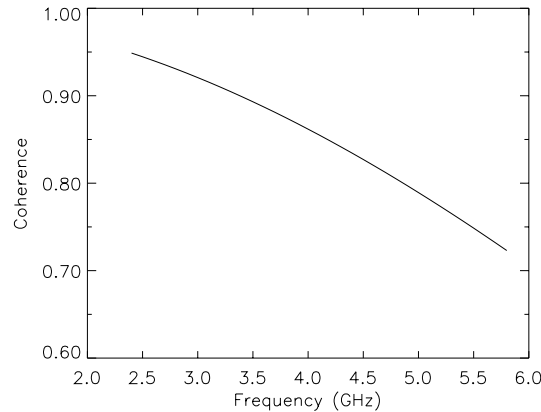
**Fig. 6.4.** Mean coherence vs frequency according to (6.35). Parameters: $B = 0.25°$, $\theta_c = 45°$, $\Delta z = 1.8$ m

**Table 6.1.** Mean coherences of the interferograms at 5 GHz and $B = 0.25°$

| | | | |
|---|---|---|---|
| Optimum | $\gamma_1 = 0.7974$ | $\gamma_2 = 0.7657$ | $\gamma_3 = 0.7384$ |
| $v$–$h$ basis | $\gamma_{hh} = 0.7193$ | $\gamma_{vv} = 0.7380$ | $\gamma_{hv} = 0.7918$ |
| Pauli matrices | $\gamma_{hh+vv} = 0.7374$ | $\gamma_{hh-vv} = 0.7531$ | $\gamma_{hv} = 0.7918$ |

With this technique, the PDF of the phase estimate changes, and the standard deviation decreases drastically [174, 152, 161]. For example, a coherence of 0.9 now yields a standard deviation of $10°$ with only $L = 8$, and even less for higher values of $L$.

The influence of this uncertainty in our height estimates is illustrated in the following. First of all, the mean coherence for each scattering mechanism is plotted as a function of the frequency in Fig. 6.3. The coherence follow a decreasing trend when the frequency increases. This function has been studied in different references by varying the frequency, the baseline or the total height of the target. In our case, a suitable expression is [137, 175, 176]:

$$\gamma = \text{sinc}\left(2\frac{f}{c} \cdot \frac{\Delta\theta}{\sin\theta_c}\Delta z\right), \tag{6.35}$$

where $\text{sinc}(x) = \sin(\pi x)/(\pi x)$ and $\Delta z$ is the total height of the scattering volume. For the current parameters the resulting coherence is plotted in Fig. 6.4, where $\Delta z$ corresponds to the total maize height: 1.8 m. There is a full agreement with the results of Fig. 6.3.

A study of the estimate variance follows for a single frequency. The numerical values of the mean coherences at 5 GHz are displayed in Table 6.1. With those coherence values, the first-order standard deviation of the individual phase estimates of each interferogram is worse than $50°$. The translation of this deviation into height values for this baseline is about 70–80 cm, which is of the same order of the expected height. Therefore, a multi-look procedure must be carried out to improve the estimation process. The standard deviations (in height units) for the above cases are shown in Table 6.2 for $L = 1$ (single-look), $L = 4$

**Table 6.2.** Standard deviations of the individual height estimates (in meters) for various values of $L$. Parameters: $f = 5$ GHz, $B = 0.25°$

L=1 (single-look)

| | | | |
|---|---|---|---|
| Optimum | $\sigma_1 = 0.73$ | $\sigma_2 = 0.79$ | $\sigma_3 = 0.81$ |
| $v$–$h$ basis | $\sigma_{hh} = 0.80$ | $\sigma_{vv} = 0.79$ | $\sigma_{hv} = 0.75$ |
| Pauli matrices | $\sigma_{hh+vv} = 0.81$ | $\sigma_{hh-vv} = 0.84$ | $\sigma_{hv} = 0.75$ |

L=4

| | | | |
|---|---|---|---|
| Optimum | $\sigma_1 = 0.24$ | $\sigma_2 = 0.30$ | $\sigma_3 = 0.40$ |
| $v$–$h$ basis | $\sigma_{hh} = 0.37$ | $\sigma_{vv} = 0.42$ | $\sigma_{hv} = 0.25$ |
| Pauli matrices | $\sigma_{hh+vv} = 0.40$ | $\sigma_{hh-vv} = 0.41$ | $\sigma_{hv} = 0.25$ |

L=24

| | | | |
|---|---|---|---|
| Optimum | $\sigma_1 = 0.08$ | $\sigma_2 = 0.09$ | $\sigma_3 = 0.12$ |
| $v$–$h$ basis | $\sigma_{hh} = 0.12$ | $\sigma_{vv} = 0.11$ | $\sigma_{hv} = 0.10$ |
| Pauli matrices | $\sigma_{hh+vv} = 0.12$ | $\sigma_{hh-vv} = 0.11$ | $\sigma_{hv} = 0.10$ |

and $L = 24$. The improvement obtained by the multi-look technique in the final estimates is quite evident.

We are interested not only in the accuracy of the height estimates for each interferogram. Since the retrieval algorithm estimates the height as the relative difference between interferograms, it is important to analyze the variance of the height differences. In first approximation the *error propagation formula* can be applied to this study. The height estimate $h$ is the difference between two random variables $h_x$ and $h_y$ that correspond to the heights derived from the interferograms computed for two different scattering mechanisms, $x$ and $y$. Both random variables are characterized by a mean and a standard deviation:

$$h_x = \overline{h}_x \pm \Delta h_x \tag{6.36}$$

$$h_y = \overline{h}_y \pm \Delta h_y. \tag{6.37}$$

The final estimate is a function of two variables, $h_x$ and $h_y$, that can be written as:

$$h = f(h_x, h_y) = h_x - h_y. \tag{6.38}$$

The *error propagation formula* states that the error of the estimate must satisfy the following expression:

$$\Delta h \leqslant \sqrt{\left(\frac{\partial f}{\partial h_x}\right)^2 \Delta h_x^2 + \left(\frac{\partial f}{\partial h_y}\right)^2 \Delta h_y^2} = \sqrt{\Delta h_x^2 + \Delta h_y^2}. \tag{6.39}$$

**Table 6.3.** Standard deviations of the final height estimates (in meters). Parameters: $f = 5$ GHz, $B = 0.25°$, $L = 24$

| | | | |
|---|---|---|---|
| Optimum | $\sigma_{1,2} = 0.12$ | $\sigma_{1,3} = 0.13$ | $\sigma_{2,3} = 0.16$ |
| $v$–$h$ basis | $\sigma_{hh,vv} = 0.15$ | $\sigma_{hh,hv} = 0.12$ | $\sigma_{vv,hv} = 0.12$ |
| Pauli matrices | $\sigma_{hh+vv,hh-vv} = 0.14$ | $\sigma_{hh+vv,hv} = 0.12$ | $\sigma_{hh-vv,hv} = 0.17$ |

The standard deviations of the final height estimates for $L = 24$ are shown in Table 6.3. Leaving apart the small inaccuracies of these numerical estimates due to the small number of samples, the agreement with expectations is evident. Note that a theoretical derivation of the PDF of these final estimates is out of the scope of the present thesis.

The main conclusion that can be drawn from this analysis is that the choice of the optimum scattering mechanisms yielded by the coherence optimization does not improve significantly the quality of the height estimations with respect to the other mechanisms selected on the basis of an *a priori* knowledge. The similarity of the coherences in all three cases is evident. As a result, as far as the height estimation is concerned, there is no degradation in the results obtained by using Pauli matrices or $v$–$h$ basis when compared to the optimum scattering mechanisms.

The dependence on the baseline has not been widely analyzed in this thesis due to the limited number of experiments. However, the same computations of Fig. 6.2 have been repeated in Fig. 6.5 for a baseline of $B = 0.5°$. In general, the estimates have the same behavior and the final results are almost the same. There are only some significant changes for frequencies greater than 4.5 GHz. Therefore, in principle the baseline is not a critical parameter for this application. This conclusion should be confirmed by a further and deeper analysis of all the parameters involved in the procedure.

We have explained above that the final height estimates are obtained as the maximum differences between interferograms. These final results as a function of frequency are plotted in Fig. 6.6. The estimates of the optimum scattering mechanisms present a quite complicated dependence on the working frequency. An inspection of the estimation procedure explains the reasons for these varying estimates. Any change in the estimates is produced by: 1) a displacement (absolute or relative to the other mechanisms) of the phase center of a mechanism when the frequency changes, and/or 2) an interchange in the physical meaning of the scattering mechanism that can produce a swap in their relative order. For example, there is a band around 3–4 GHz where the estimates change their trend for both baselines. This phenomenon is caused by a change in the order of the optimum scattering mechanisms, whereas the rest of fluctuations are due to variations in the height level of the individual mechanisms. Again, this figure is a confirmation that the estimates obtained with the Pauli spin matrices are more stable than those retrieved with the coherence optimization.

The second target to be measured was the rice sample. The number of independent samples obtained by azimuth rotation is low (in this case, there are only three samples). Nine frequency sub-bands were used in the averaging, thus leading to a total of 27 independent

## Low band                                            ## High band
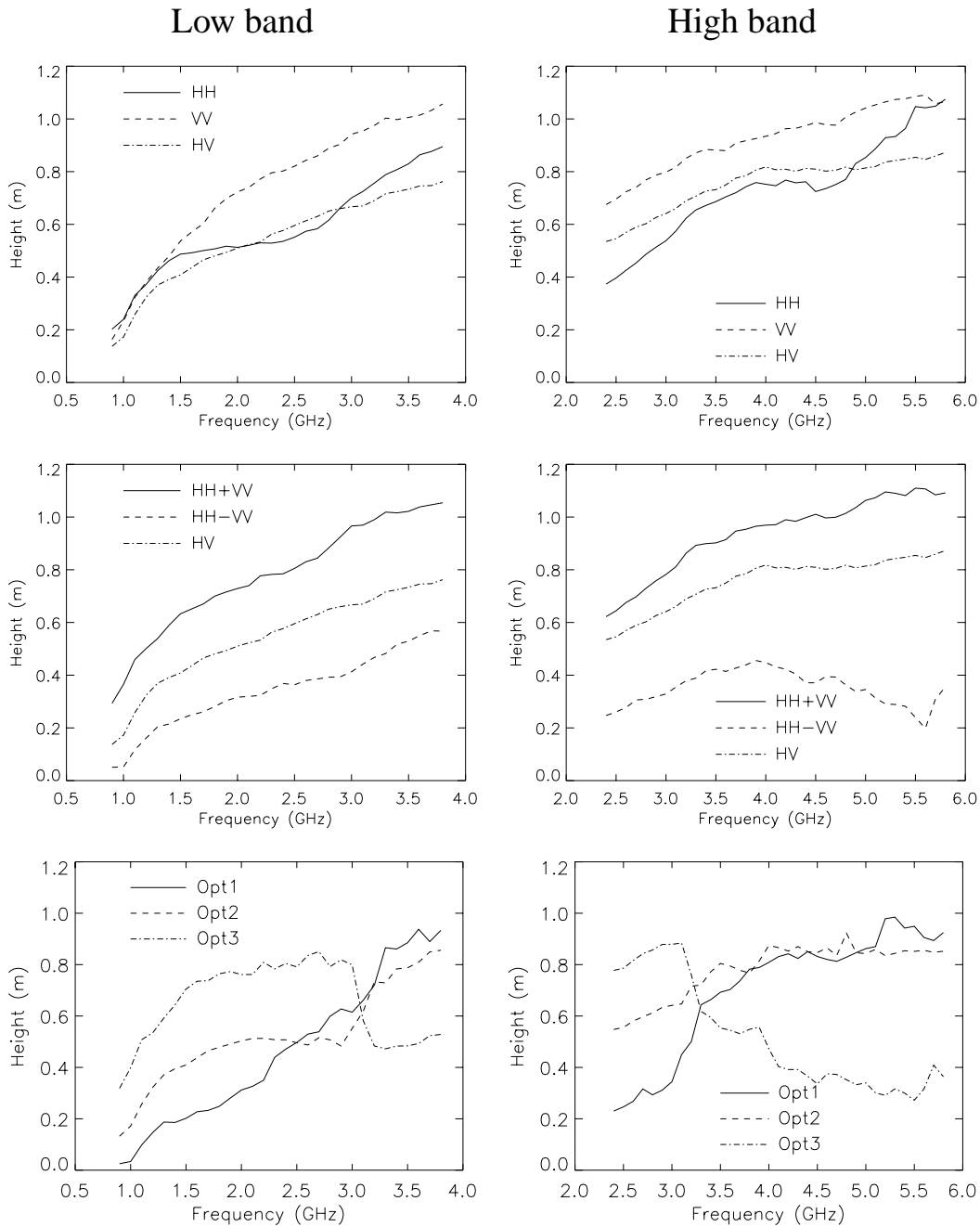


**Fig. 6.5.** Maize sample. Height of the scattering centers vs frequency. Parameters: $B = 0.5°$, $\theta_c = 45°$, Samples = 72 angles × 9 frequencies. Top: $v$–$h$ basis. Center: Pauli matrices. Bottom: optimum scattering mechanisms

samples for each estimate. Again, two frequency bands were used in the experiment: 0.3 to 4.3 GHz and 1.5 to 9.5 GHz, the baselines being $1°$ in the first case and $0.5°$ in the second. The bandwidth employed in the image reconstruction was 80 MHz. This sample is shorter than the maize (only 60 cm high), so it is not expected to present ambiguities at high

**Fig. 6.6.** Maize sample. Maximum height difference between scattering centers vs frequency. Parameters: $\theta_c = 45°$, Samples = 72 angles $\times$ 9 frequencies.

frequencies. Fig. 6.7 shows the estimates for L, S, C and X band.

At first sight, the estimates behave more irregularly than for the maize sample. In fact, only for frequencies higher than 4 GHz the separation between scattering mechanisms follow the expected distribution (i.e. HH–VV at the bottom and HH+VV at the top). At low frequencies there exist many fluctuations on the estimates. This phenomenon may be produced by different causes. For example, at low frequencies all the backscatter return is dominated by the ground-stem interaction, which is many dB's above the scattering by the rest of the plant components. Moreover, the physical structure of the plants is more random than the maize. Finally, an additional source of variance in all estimates (not only at low frequencies) is the low number of independent samples used in the averaging.

As in the maize experiment, the optimum scattering mechanisms vary significantly their relative position inside the volume when the frequency changes. For instance, from 4 to 5 GHz the first is at the bottom and the third at the top, whereas from 6.5 to 7.5 GHz they are swapped. There are also bands with all three optimum mechanisms centered at the same

Low band, $B = 1°$                          High band, $B = 0.5°$
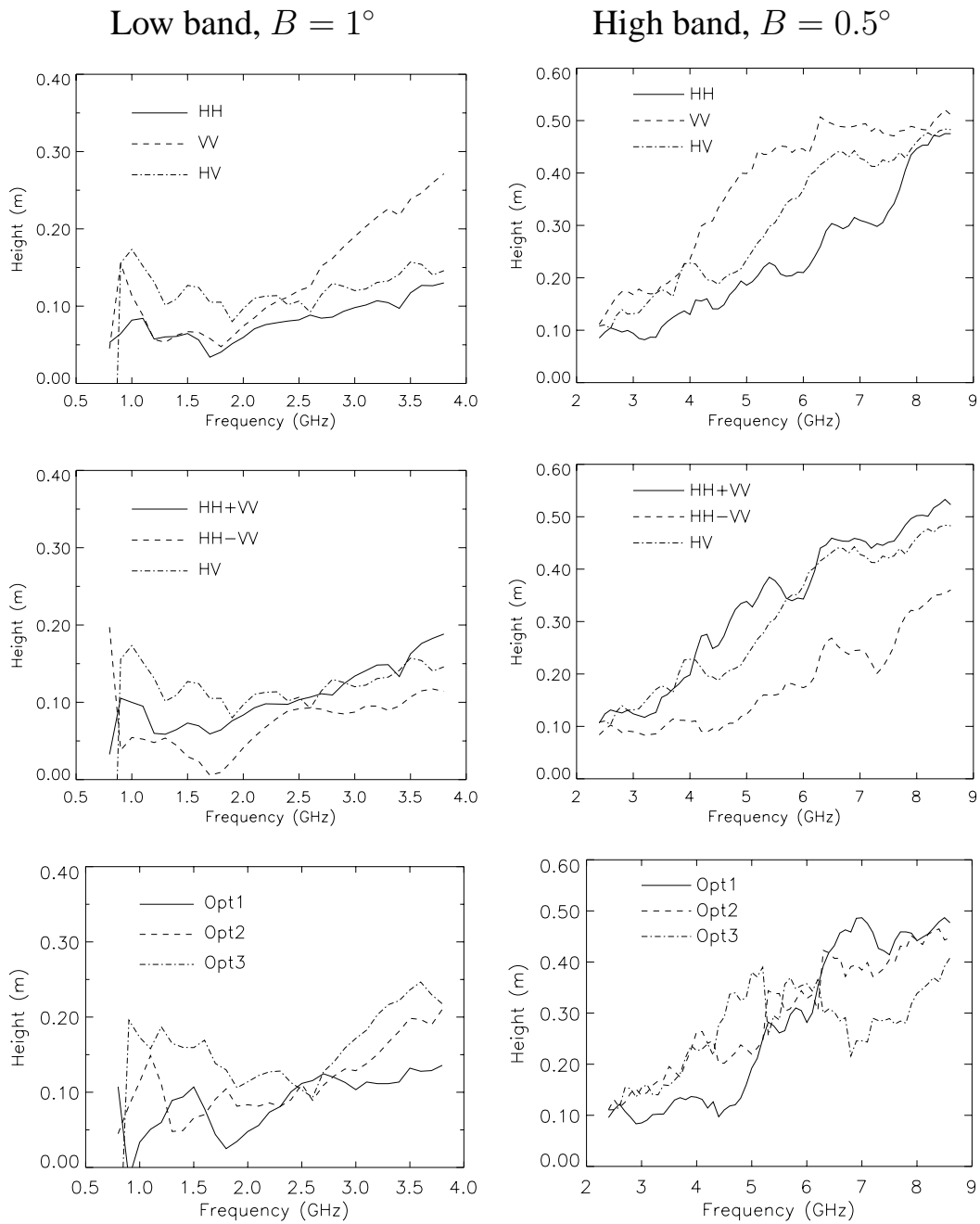


**Fig. 6.7.** Rice sample. Height of the scattering centers vs frequency. Parameters: $\theta_c = 45°$, Samples = 3 angles × 9 frequencies. Top: $v$–$h$ basis. Center: Pauli matrices. Bottom: optimum scattering mechanisms. Left: Low band with $B = 1°$. Right: High band with $B = 0.5°$

height. Therefore, their choice is not a good starting point for the height estimation. In contrast, the mechanisms associated with the Pauli matrices exhibit a fairly uniform separation of about 20 cm independently from the frequency. Regarding the $v$–$h$ basis, the estimates are not as clearly separate as the Pauli matrices ones. These phenomena are also evident in
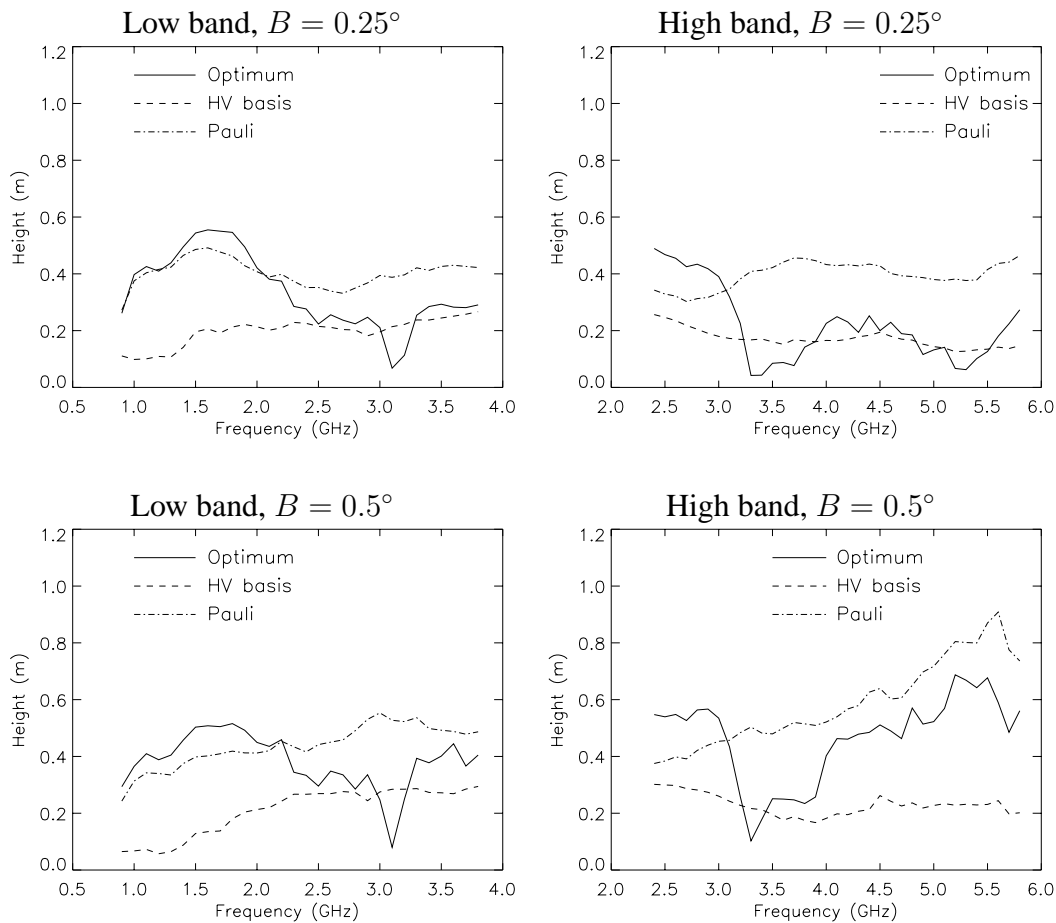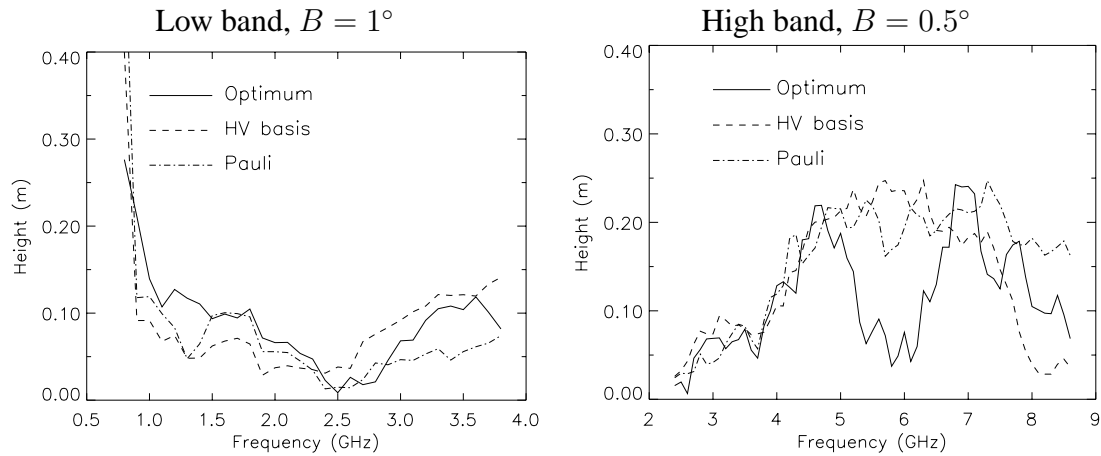
**Fig. 6.8.** Rice sample. Maximum height difference between scattering centers vs frequency. Parameters: $\theta_c = 45°$, Samples = 3 angles $\times$ 9 frequencies. Left: Low band with $B = 1°$. Right: High band with $B = 0.5°$

Fig. 6.8, where the maximum differences between mechanisms are depicted.

As a conclusion, a monitoring system may be designed for remote control of rice crops as well. In this case, however, the working frequency should be at C or X band, since the backscatter from the upper part of the plants is masked by the ground-stem interaction at lower frequencies. The same criteria as the maize can be stated for the incidence angle.

The last measurements were performed on the cluster of small fir trees for 1 to 10 GHz, with an incidence angle of $45°$. The baseline in this case is $0.5°$. A total of 54 independent samples were used for each estimate, obtained from 6 samples in azimuth and 9 sub-bands. The bandwidth employed in the images generation was 40 MHz. The resulting estimates are shown in Fig. 6.9 as a function of the frequency for L, S and C band.

For this target the phase centers corresponding to all scattering mechanisms are always very close together. A justification to this behavior can be found in the physical structure of the target. As was explained in previous chapters, this is a very random volume with no dominant orientation of its components. Moreover, it exhibits similar scattering properties for all microwave frequencies due to its architecture, which is formed by particles with the same shape and different sizes, thus producing the same dominating scattering at different wavelengths. Finally, this homogeneity is observed over the whole target, thus not presenting a clear distribution of different behaviors as a function of height. As a result, all polarization channels (HH, VV and HV) behave in similar manner and it is impossible to find different phase centers for each of them consistently. The maximum height differences are also shown in Fig. 6.9. There is only a meaningful estimate for low frequencies as a result of the difference between HH and VV or HV.

This lack of applicability of polarimetry is expected wherever there is not a significant orientation of the particles in a target, because, by definition, polarimetry deals with
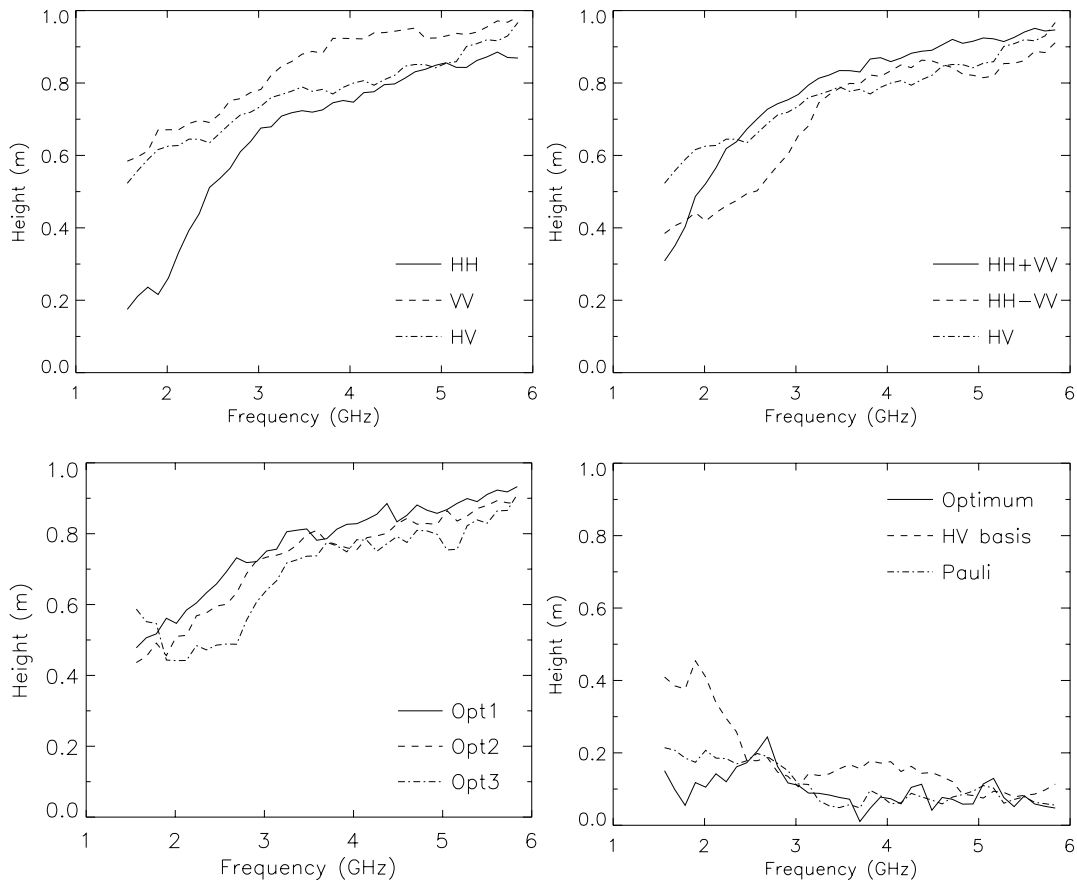
**Fig. 6.9.** Cluster of fir trees. Height of the scattering centers vs frequency. Parameters: $\theta_c = 45°$, $B = 0.5°$, Samples = 6 angles × 9 frequencies. Top left: $v$–$h$ basis. Top right: Pauli matrices. Bottom left: optimum scattering mechanisms. Bottom right: Maximum height differences

rotations, angles or orientations. In previous examples, with the maize and rice samples, the ground was a key feature, since it changes importantly the polarization of the wave, thus introducing orientation information in the scattered field. In our sample with fir trees there is almost no return from the ground or the ground-trunk interaction (see Chapter 4). However, in natural forests this return is commonly present at low frequencies (L band), and the height can be retrieved by means of polarimetric interferometry [167].

Finally, as suggested in a recent publication [177], for volumes with a random distribution of particles (without any preferred orientation) polarimetry has little contribution in this estimation method. This is also true because of the low return from the ground. Instead, for a very oriented volume as maize this method is expected to work better. Note that a first estimation of a parameter related to the differential extinction coefficient between orthogonal polarizations (which is fundamental for the success of this technique [177]) was presented in Chapter 4.

# 6.3   Conclusions

Some comments about the performance of this method as experimented at EMSL are discussed here. In the first place, various approaches for making use of polarimetry from computing simultaneous interferograms have been presented. All of them consist in projecting the polarimetric information of both images onto scattering mechanisms, thus retrieving the phase center associated with each mechanism. In order to perform this projection, a vector formulation of the interferogram formation is adopted [69]. The selection of the scattering mechanisms may be based on two different criteria. The first option assumes an *a priori* knowledge of the scene for choosing those scattering mechanisms that correspond to different vegetation components. The second option derives from the optimization of the interferometric coherence, which can be accomplished by properly choosing scattering mechanisms in both images. The formalization of that optimization leads to an eigenvalue problem which in turn yields a target decomposition into three pairs of scattering mechanisms. The scattering mechanisms associated with the higher eigenvalue produce the highest coherence, and the three pairs exhibit statistical independence between them. Both choices have been compared in this chapter.

In general, the approach based on the coherence optimization presents an important drawback: there is not information about the location of the scattering mechanisms inside the vegetation volume. It is possible to find all three mechanisms on the same position or, when they are physically separate, they can interchange their relative positions when the frequency varies. Instead, the approach based on a previous decision about the scattering mechanisms is better justified from the physical point of view and, moreover, leads to better results. According to the experiments presented in this chapter, the best choice consists of the first two Pauli spin matrices, which represent surface or direct scattering and dihedral scattering. The implementation is performed by calculating the interferograms of the HH+VV and HH–VV polarizations, and the height estimate is the difference between them. The HH+VV interferogram represents the effective phase center of the direct scattering from the above-ground volume, whereas the HH–VV interferogram corresponds to the ground-trunk interaction. Finally, although not presented here, a conversion of the retrieved height to an absolute value may be carried out on the basis of a scattering model of the vegetation target.

Measurements were performed for a maize sample, a rice sample and a cluster of small fir trees. For both crop samples the estimates behave regularly with frequency. The maize sample yielded consistent estimates from L to C band, whereas the results for the rice were only valid for C and X band. On the other hand, the algorithm failed for the cluster of trees. This is due to the random structure of the sample, without any preferred orientation and without any backscatter return from the ground at the chosen incidence angles. As a result, the method cannot distinguish between different heights (phase centers) as a function of the polarization.

The experiments conducted so far at EMSL about the application of polarimetric interferometry to the extraction of vegetation height lead to an important conclusion: in laboratory conditions, the inversion of a parameter directly related to the absolute vegeta-

tion height is possible by simultaneously computing interferograms for several polarization states. The generalization of this approach to conventional air- or spaceborne InSAR systems is discussed in the global conclusions of the thesis (Chapter 8).

# 3-D Radar Imaging by Using Range Migration Techniques

T HE identification of scattering centers inside vegetation volume and the quantification of their polarimetric contribution by means of decomposition techniques constitute a new analysis method presented in Chapter 4. The application of this technique requires the formation of high resolution radar images of the vegetation samples. These images can be generated by a variety of focusing algorithms, as was explained in Section 2.5. A 2-D reflectivity image can be formed by synthesizing an 1-D aperture with a wide-band radar. Accordingly, a 3-D reflectivity image is formed by synthesizing a 2-D aperture. For example, in an anechoic chamber the typical geometries of the 2-D apertures that can be synthesized are planar, spherical and cylindrical.

However, not all focusing algorithms match the specific configuration of the EMSL. The most restricting property of the radar measurements at EMSL is the near-field situation of the antennas with respect to the target. When the radar is in the far-field zone of the target, the illuminating wavefront can be considered to be plane and, hence, the focusing procedure reduces to an interpolation plus a 3-D inverse discrete Fourier transform [131]. Instead, if the radar is located in the near-field region, the planar wavefront assumption is no longer valid, and a straightforward fast Fourier processing cannot be used in the image reconstruction. Near-field ISAR imaging by a direct Fourier inversion yields images which are progressively unfocused at points with increasing distances from the center of rotation [128], or even images with misplaced scattering centers.

Three types of conventional imaging algorithms, commonly used in the SAR community, were cited in Section 2.5: Polar Format Algorithm (PFA), Range Migration Algorithm (RMA) and Chirp Scaling Algorithm (CSA). These methods include additional operations in the focusing procedure, like complex products and interpolations, but all three are still quite efficient because their implementation is mostly based on FFT's, thus speeding up the computation time. Nevertheless, their applicability to near-field ISAR configurations is limited by the correction of the wavefront curvature, that is accounted for in a exact manner only by the RMA. Consequently, the RMA has been chosen for the construction of an efficient

near-field 3-D ISAR algorithm adapted to the EMSL.

A 3-D version of the RMA algorithm is formulated for the first time in this thesis. Its derivation is described in two steps. Firstly, the 2-D synthetic aperture is assumed to be planar. As an input, the algorithm requires frequency domain backscatter data which can be acquired using a stepped frequency radar. Thus, resolution in the vertical and horizontal cross-range directions is given by the dimensions of the synthetic aperture, whereas resolution in range is provided by the synthesized frequency bandwidth. Frequency domain data are preferred because the RMA algorithm works in the frequency-wavenumber domain. Note that the focusing of time domain data acquired with a pulsed system would become straightforward by simply applying a Fourier transform. Secondly, an extension of the algorithm to cylindrical and spherical scanning geometries (the usual ones at EMSL) will be formulated and implemented by means of spectral translations to reduce the problem to the planar aperture case. Note again that the measurements are supposed to be fully controlled, and therefore factors such as irregular sample spacing, platform position errors and mitigation of RFI have not been investigated.

This chapter is organized as follows. Section 7.1 presents the formulation of the 3-D RMA, which has been derived by using the method of stationary phase (MSP) [178] as suggested in [129] for the 2-D RMA. Two alternative interpretations of the algorithm are shown to facilitate its understanding. The implementation of the method, divided into different data processing steps, is described in Section 7.2. Some practical aspects on the performance of the algorithm, the required sampling criteria and the resulting resolutions, are also explained in this section. Section 7.3 illustrates numerical simulations that have been carried out for testing the algorithm with the assumption of a planar synthetic aperture. Experimental results showing the validity of this imaging method are provided in Section 7.3. Next, Section 7.4 deals with the extension of the 3-D RMA to cylindrical and spherical scanning geometries. This extension is also illustrated with numerical simulations and experimental results. Finally, some conclusions are summarized in Section 7.5.

## 7.1   Formulation of the 3-D RMA

Let us consider the measurement set-up shown in Fig. 7.1. A stepped frequency radar illuminates a target with a CW of frequency $f$. The antenna positions are $(x_a, y_a, z_a)$, which synthesize a rectangular aperture on a plane parallel to the $XZ$ at a distance $y = y_a$. The measurement points form a rectangular grid with spacings $\Delta x_a$ and $\Delta z_a$ along the horizontal and vertical cross-range directions, respectively. At each antenna position the synthesized frequency bandwidth is $B$. Thus, the acquired backscatter data $d(x_a, f, z_a)$ are function of two spatial coordinates and the working frequency. The frequency variable is directly related with the wavenumber, that for radar data is defined as $k_r = 4\pi f/c$. Consequently, the measurement data can also be denoted as $d(x_a, k_r, z_a)$.

Assuming that there is a point scatterer located at $(x, y, z)$ with reflectivity $s(x, y, z)$,
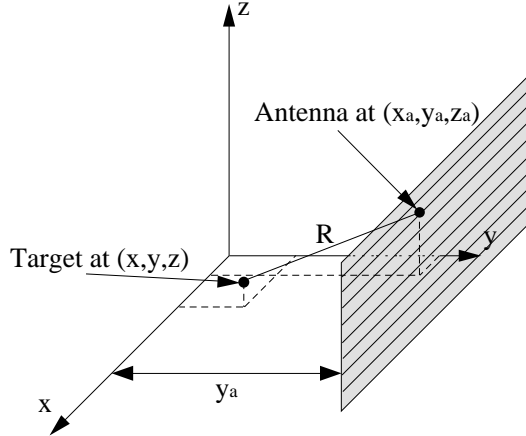
**Fig. 7.1.** Measurement and imaging geometry

then the measured backscatter is:

$$d(x_a, k_r, z_a) = s(x, y, z) \ \exp\left[jk_r y_a\right] \ \exp\left[-jk_r R\right], \tag{7.1}$$

where $R$ is the range to the point scatterer, i.e.

$$R = \sqrt{(x - x_a)^2 + (y - y_a)^2 + (z - z_a)^2}. \tag{7.2}$$

The first exponential[1] in (7.1) establishes a reference plane at the center of the scene which is $y_a$ away from the aperture. In the 2-D RMA this reference was a line parallel to the linear aperture. The second exponential simply accounts for the phase history associated with the point scatterer. Note that, for the sake of simplicity, the losses due to the free-space propagation and the antenna pattern are not considered here.

If the target is distributed, the acquired backscattered can be regarded as the integration of all contributions from the target volume:

$$d(x_a, k_r, z_a) = \iiint\limits_V s(x, y, z) \ \exp\left[jk_r y_a\right] \ \exp\left[-jk_r R\right] \ dx \ dy \ dz, \tag{7.3}$$

where $V$ denotes the volume occupied by the target, and linearity has been assumed as usual.

A focused image can be reconstructed by performing a convolution of the data with a focusing function, which in turn is the complex conjugate of the exponential terms. The 3-D radar reflectivity map associated with a distributed target can be expressed as:

$$s(x, y, z) = \iiint\limits_{A, k_r} d(x_a, k_r, z_a) \ \exp\left[-jk_r y_a\right] \ \times$$

$$\exp\left[jk_r \sqrt{(x - x_a)^2 + (y - y_a)^2 + (z - z_a)^2}\right] \ dx_a \ dz_a \ dk_r, \tag{7.4}$$

---

[1] The exponential function is denoted as $\exp[x]$, instead of $e^x$, in some equations of this chapter. This notation has been employed to make the argument more readable

where $A$ denotes the surface of the synthesized aperture. Equation (7.4) can be reformulated in order to show that the focusing algorithm can be simply described by means of a 2-D convolution and a frequency integration:

$$s(x, y, z) = \int_{k_r} \exp\left[-jk_r y_a\right] \left\{ \iint_A d(x_a, k_r, z_a) \times \right.$$

$$\left. \exp\left[jk_r \sqrt{(x - x_a)^2 + (y - y_a)^2 + (z - z_a)^2}\right] \, dx_a \, dz_a \right\} dk_r. \quad (7.5)$$

The 2-D convolution (in braces) on the aperture coordinates $(x_a, z_a)$ could be computed in the Fourier domain as a complex product. This alternative calculus is denoted as:

$$\iint D(k_x, k_r, k_z) \, E(k_x, y_a, k_z) \, \exp\left[jk_x x + jk_z z\right] \, dk_x \, dk_z, \quad (7.6)$$

where $D(k_x, k_r, k_z)$ is the 2-D horizontal/vertical cross-range Fourier transform (FT) of the frequency domain backscatter data, and $E(k_x, y_a, k_z)$ is the following 2-D FT:

$$E(k_x, y_a, k_z) = \iint \exp\left[jk_r \sqrt{x^2 + (y - y_a)^2 + z^2}\right] \exp\left[-jk_x x - jk_z z\right] \, dx \, dz. \quad (7.7)$$

In order to apply (7.6), the FT described in (7.7) must be known. This kind of integrals, under certain conditions, can be evaluated analytically by using the Method of Stationary Phase (MSP) [178]. The MSP states that the main contribution to the integral comes from points with stationary phase (nulls of the phase derivative), and gives an asymptotic expansion for the integral. The evaluation of the 2-D integral in (7.7) by means of the MSP results in (see Section 7.1.2):

$$E(k_x, y_a, k_z) \simeq \frac{j2\pi k_r}{k_y^2} \, \exp\left[jk_y(y_a - y)\right], \quad (7.8)$$

where $k_y^2 = k_r^2 - k_x^2 - k_z^2$. Replacing the 2-D FT by its asymptotic expansion in (7.5), the 3-D reflectivity image is given by:

$$s(x, y, z) \simeq \iiint_K D(k_x, k_r, k_z) \frac{j2\pi k_r}{k_y^2} \, \exp\left[-jk_r y_a\right] \times$$

$$\exp\left[jk_x x + jk_z z + jk_y(y_a - y)\right] \, dk_x \, dk_r \, dk_z. \quad (7.9)$$

Note that the last exponential term has the form of the Fourier kernel in a 3-D Inverse FFT (IFFT). However, prior to this 3-D IFFT, the wavenumber domain backscatter data need to be resampled uniformly in $k_y$ (i.e., a 1-D interpolation known as Stolt interpolation [133]). Then, by substituting the frequency wavenumber variable $k_r$ by $k_y$, the reflectivity image takes the form:

$$s(x, y', z) \simeq \iiint_K D(k_x, k_y, k_z) \frac{j2\pi}{k_y} \, \exp\left[-jk_r y_a\right] \times$$

$$\exp\left[jk_y y_a\right] \exp\left[jk_x x + jk_z z + jk_y y'\right] \, dk_x \, dk_y \, dk_z, \quad (7.10)$$

where the ground-range variable has been reversed and $y' = -y$. The amplitude term has been modified due to the change of variables ($k_r \rightarrow k_y$). Eq. (7.10) indicates that the reflectivity image can be simply obtained through a 3-D IFFT of the product of the resampled wavenumber domain backscatter data by a complex exponential (also known as matched filter).

## 7.1.1   An Alternative Interpretation of the RMA

The starting point of the previous derivation of the 3-D RMA was the focusing function that is needed for reconstructing the image, as it is shown in (7.4). However, there is an alternative viewpoint for justifying this method. The idea is that if we had the reflectivity image in the Fourier domain, we could reduce the whole processing to a simple 3-D IFFT:

$$s(x, y, z) = \iiint_K S(k_x, k_y, k_z) \, \exp\left[jk_x x + jk_y y + jk_z z\right] \, dk_x \, dk_y \, dk_z. \tag{7.11}$$

Consequently, the objective is to reconstruct the reflectivity image by using a 3-D IFFT in the last step. This is equivalent to finding the relationship between $S(k_x, k_y, k_z)$ and $D(k_x, k_y, k_z)$.

Firstly, we know that $s(x, y, z)$ and $S(k_x, k_y, k_z)$ must form a Fourier transform pair, thus:

$$S(k_x, k_y, k_z) = \iiint_V s(x, y, z) \, \exp\left[-jk_x x - jk_y y - jk_z z\right] \, dx \, dy \, dz, \tag{7.12}$$

where $V$ denotes the volume occupied by the target.

The frequency domain backscatter data $d(x_a, k_r, z_a)$ can be regarded as the integral of the spatial distribution of reflectivity $s(x, y, z)$, weighted by an exponential phase term:

$$d(x_a, k_r, z_a) = \iiint_V s(x, y, z) \, \exp\left[-jk_r R\right] \, dx \, dy \, dz, \tag{7.13}$$

where $R$ is the range to the point at $(x, y, z)$, i.e.

$$R = \sqrt{(x - x_a)^2 + (y - y_a)^2 + (z - z_a)^2}. \tag{7.14}$$

If one performs performs a cross-range 2-D FT on the acquired data over the aperture $A$, the result can be expressed as:

$$D(k_x, k_r, k_z) = \iint_A d(x_a, k_r, z_a) \, \exp\left[-jk_x x - jk_z z\right] \, dx_a \, dz_a. \tag{7.15}$$

By substituting (7.13) into (7.15) and evaluating the resulting surface integral by means of the MSP, the final result[2] is:

$$D(k_x, k_r, k_z) = \iiint_V s(x, y, z) \, \exp\left[-jk_x x - jk_y y - jk_z z\right] \, dx \, dy \, dz, \qquad (7.16)$$

which has the same form as (7.12). This shows that the 3-D FFT of the reflectivity image, $S(k_x, k_y, k_z)$, is directly related to the 2-D FFT of the measured data, $D(k_x, k_r, k_z)$. A total identity between both is achieved by including the matched filter and the Stolt transformation $(k_r \to k_y)$.

## 7.1.2 Application of the Stationary Phase Method to the RMA Derivation

The 2-D Fourier Transform in (7.7) can be evaluated asymptotically by using the Method of Stationary Phase (MSP) [178]. This method provides an analytical solution to integrals of the form

$$N(k) = \iint_R f(x, y) \, \exp\left[jk\mu(x, y)\right] \, dx \, dy, \qquad (7.17)$$

where $R$ is a region in the $XY$ plane, and $\mu(x, y)$ is a function assumed to be twice-continuously differentiable in $R$. The asymptotic evaluation of $N(k)$ for large $k$ can be obtained by looking for the zeros of the first derivative of the argument of the exponential term. The major contribution to the integral in (7.17) comes from a small neighborhood near the points where the two first derivatives of $\mu(x, y)$ vanish. These points are known as points of stationary phase.

In the RMA, the objective is to evaluate the integral

$$E(k_x, k_z) = \iint \exp\left[jk_r \sqrt{x^2 + (y - y_a)^2 + z^2}\right] \, \exp\left[-jk_x x - jk_z z\right] \, dx \, dz. \qquad (7.18)$$

The phase of the exponential term is given by

$$\Phi(x, z) = k\mu(x, z) = k_r R - k_x x - k_z z \qquad (7.19)$$

$$R = \sqrt{x^2 + (y - y_a)^2 + z^2}. \qquad (7.20)$$

If there is only one point of stationary phase, the resulting asymptotic expansion of $E(k_x, k_z)$ is

$$E(k_x, k_z) \simeq \frac{j2\pi}{\sqrt{\Phi_{xx}\Phi_{zz} - \Phi_{xz}^2}} \exp\left[j\Phi(x_0, z_0)\right], \qquad (7.21)$$

---

[2]The matched filter term has been omitted in the final expression

where $\Phi_{xx}$, $\Phi_{zz}$ and $\Phi_{xz}$ denote the second partial derivatives of $\Phi(x, z)$ evaluated at the stationary point. The stationary point $(x_0, z_0)$ is the point where the phase $\Phi(x, z)$ takes an extreme value, i.e.,

$$\frac{\partial \Phi}{\partial x}\bigg|_{(x_0, z_0)} = 0 \qquad (7.22)$$

$$\frac{\partial \Phi}{\partial z}\bigg|_{(x_0, z_0)} = 0 \qquad (7.23)$$

and, at the same time, it is assumed that

$$\Phi_{xx}\Phi_{zz} - \Phi_{xz}^2 \neq 0 \qquad \Phi_{zz} \neq 0. \qquad (7.24)$$

The first derivatives of the phase function are:

$$\Phi_x(x, z) = \frac{\partial \Phi}{\partial x} = -k_x + \frac{k_r x}{R} \qquad (7.25)$$

$$\Phi_z(x, z) = \frac{\partial \Phi}{\partial z} = -k_z + \frac{k_r z}{R}. \qquad (7.26)$$

There is only one point were both first derivatives vanish simultaneously:

$$x_0 = \frac{k_x(y_a - y)}{\sqrt{k_r^2 - k_x^2 - k_z^2}} \qquad (7.27)$$

$$z_0 = \frac{k_z(y_a - y)}{\sqrt{k_r^2 - k_x^2 - k_z^2}}. \qquad (7.28)$$

The second partial derivatives are:

$$\Phi_{xx}(x, z) = \frac{\partial^2 \Phi}{\partial x^2} = \frac{k_r \left[z^2 + (y - y_a)^2\right]}{R^3} \qquad (7.29)$$

$$\Phi_{zz}(x, z) = \frac{\partial^2 \Phi}{\partial z^2} = \frac{k_r \left[x^2 + (y - y_a)^2\right]}{R^3} \qquad (7.30)$$

$$\Phi_{xz}(x, z) = \frac{\partial^2 \Phi}{\partial x \partial z} = -\frac{k_r x z}{R^3}, \qquad (7.31)$$

which evaluated at the stationary point $(x_0, z_0)$ yield,

$$\Phi_{xx}(x_0, z_0) = \frac{(k_x^2 - k_r^2)\sqrt{k_r^2 - k_x^2 - k_z^2}}{k_r^2 (y - y_a)} \qquad (7.32)$$

$$\Phi_{zz}(x_0, z_0) = \frac{(k_z^2 - k_r^2)\sqrt{k_r^2 - k_x^2 - k_z^2}}{k_r^2 (y - y_a)} \qquad (7.33)$$

$$\Phi_{xz}(x_0, z_0) = \frac{k_x k_z \sqrt{k_r^2 - k_x^2 - k_z^2}}{k_r^2 (y - y_a)}. \qquad (7.34)$$

Moreover, the function $\Phi(x, y)$ evaluated at the stationary point is:

$$\Phi(x_0, z_0) = \sqrt{k_r^2 - k_x^2 - k_z^2} \, (y_a - y).$$ (7.35)

Finally, substituting (7.32-7.35) into (7.21), the resulting expression for the 2-D Fourier transform of (7.18) is

$$E(k_x, k_z) \simeq \frac{j2\pi(y - y_a)k_r}{k_y^2} \, \exp\left[jk_y(y_a - y)\right],$$ (7.36)

where $k_y = \sqrt{k_r^2 - k_x^2 - k_z^2}$.

Note that the factor $(y - y_a)$ in (7.36) cannot be applied in practice because the ground-range variable $y$ is not defined in the wavenumber domain. This is an amplitude factor and as such has a negligible effect on the quality of the final image. Thus, the asymptotic expansion to be used in the RMA becomes:

$$E(k_x, k_z) \simeq \frac{j2\pi k_r}{k_y^2} \, \exp\left[jk_y(y_a - y)\right].$$ (7.37)

## 7.2 Description of the Algorithm

### 7.2.1 Practical Implementation

This section deals with the practical implementation of the 3-D RMA. From (7.10), the image reconstruction process can be naturally split into four sequential steps (see Fig. 7.2), namely: a 2-D cross-range FFT, matched filtering, Stolt interpolation, and a 3-D IFFT. The first and the last steps are obvious and will not be discussed here. However, the matched filter and the Stolt interpolation deserve special treatment.

The matched filter is necessary to introduce a motion compensation to the wavenumber domain backscatter data. This motion compensation corrects the wavefront curvature of all scatterers at the same ground range as the scene center (i.e., the origin of the coordinates system). In the successive step, the residual range curvature of all scatterers will be removed. The phase associated with the matched filter is space-invariant and depends only on the range to the scene center $y_a$, the frequency and the cross-range wavenumbers. It is given by

$$\Phi_{\mathrm{MF}}(k_x, k_r, k_z) = -k_r \, y_a + k_y \, y_a = -k_r \, y_a + \sqrt{k_r^2 - k_x^2 - k_z^2} \, y_a,$$ (7.38)

where the identity

$$k_y = \sqrt{k_r^2 - k_x^2 - k_z^2}$$ (7.39)

is known as the Stolt transformation.
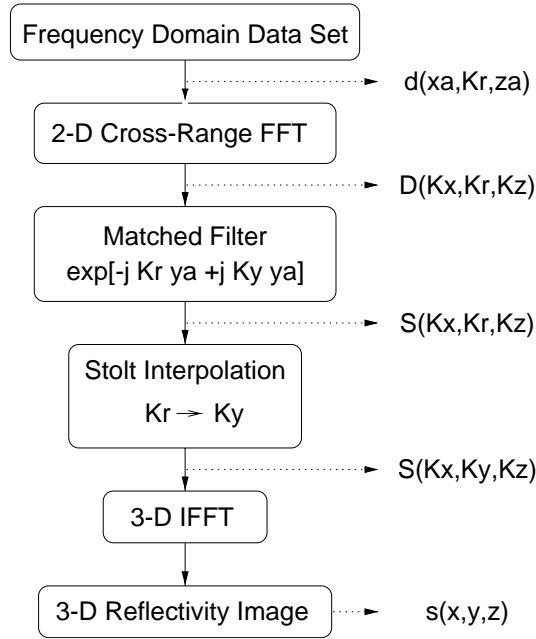
**Fig. 7.2.** Block diagram of the 3-D RMA

The third step in the 3-D RMA is the Stolt interpolation. This interpolation compensates the range curvature of all scatterers by an appropriate warping of the wavenumber domain backscatter data. After the matched filter, the transformed data continue being equally spaced in frequency, and hence in the $k_r$ variable. In order to prepare the data for the last 3-D Inverse FT, the next step consists of a change of variables defined by the Stolt transformation, which can be implemented as a 1-D interpolation. As a result, the wavenumber domain backscatter data will be uniformly sampled in the $k_y$ domain. In the present implementation of the algorithm, the sampling frequency is increased to be highly above the Nyquist limit, then a Lagrange interpolation preceded by a frequency downconversion is applied.

Note that, in (7.39), $k_y$ must be real and therefore the region in the wavenumber domain where the asymptotic expansion of the MSP is valid reduces to,

$$k_r^2 \geqslant k_x^2 + k_z^2 \tag{7.40}$$

The field modes which satisfy this inequality are the so-called propagating modes, whereas those which do not propagate are the evanescent modes. The amplitude of the evanescent modes is affected by an exponential factor which rapidly vanishes with an increasing distance to the aperture $(y_a - y)$. In the formulation presented here, it is assumed that (7.40) is satisfied. In practice, the data points in the wavenumber domain outside the region defined by (7.40) will be discarded by applying a mask prior to the matched filter.

Once the Stolt interpolation is performed, the wavenumber domain backscatter data have to be multiplied by the amplitude terms due to change of variable and the asymptotic expansion of (7.10). Then, the 3-D reflectivity image is obtained by simply applying a 3-D IFFT.

## 7.2.2   Resolutions

The resolutions in the resulting 3-D reflectivity image depend on the frequency bandwidth, the center frequency and the dimensions of the synthetic aperture. The ground-range resolution is usually expressed as,

$$\delta_y \simeq \frac{c}{2B}, \tag{7.41}$$

where $B$ is the frequency bandwidth. The horizontal and vertical cross-range resolutions are,

$$\delta_x \simeq \frac{\lambda_c y_a}{2L_x} = \frac{cy_a}{2f_c L_x} \tag{7.42}$$

$$\delta_z \simeq \frac{\lambda_c y_a}{2L_z} = \frac{cy_a}{2f_c L_z}, \tag{7.43}$$

where $L_x$ and $L_z$ are the lengths of the 2-D synthetic aperture, and $\lambda_c$ is the wavelength at the center frequency $f_c$.

In practice, the frequency domain backscatter data are windowed to lower the side-lobes in the imagery, and as a result, the final resolutions become slightly poorer than those given by the above formulas.

## 7.2.3   Sampling Criteria

Assuming that the target is confined within a rectangular box of dimensions $D_x \times D_y \times D_z$ centered at the origin of the coordinates, the required sampling steps in the measurement to satisfy the Nyquist criterion are given by

$$\Delta_f \leqslant \frac{c}{2D_y} \tag{7.44}$$

$$\Delta_{x_a} \leqslant \frac{\lambda_{min}}{2} \frac{\sqrt{(L_x + D_x)^2/4 + y_a^2}}{L_x + D_x} \tag{7.45}$$

$$\Delta_{z_a} \leqslant \frac{\lambda_{min}}{2} \frac{\sqrt{(L_z + D_z)^2/4 + y_a^2}}{L_z + D_z}, \tag{7.46}$$

where $\lambda_{\min}$ is the wavelength at the maximum working frequency.

The sampling intervals given by (7.45) and (7.46) are the usual ones in strip map SAR. The measurement points on the aperture require certain spacing in order to sample adequately the phase history associated with all the scatterers after the matched filter. The sampling frequencies in a strip map SAR are much higher than those in a spotlight configuration. Note that in a spotlight SAR the maximum cross-range spacing only depends on the target size and the distance to the aperture, but not on the aperture size as in a strip map SAR. Consequently strip map SAR measurements have associated larger data volumes and longer measurement times.
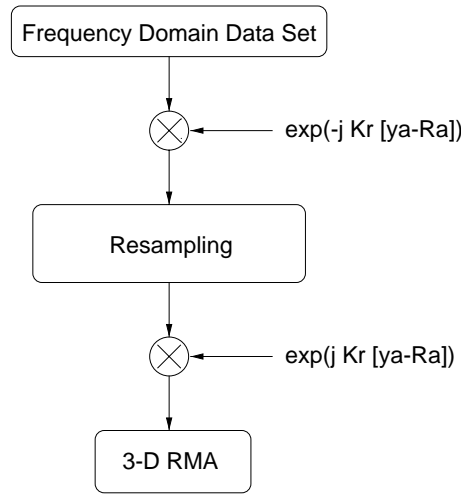
**Fig. 7.3.** Pre-processing of data sampled at spotlight rate

Running a strip map SAR measurement at spotlight SAR sampling frequency introduces aliasing in the acquired data set. However, the origin of the aliasing is known and can be eliminated by establishing a deterministic phase correction term. This correction term can be expressed as:

$$\text{HF}(x_a, k_r, z_a) = \exp\left[jk_r(y_a - \sqrt{x_a^2 + y_a^2 + z_a^2})\right].$$ (7.47)

After applying the correction, the aliasing has been eliminated, and the sampling rate can be increased in order to satisfy (7.45) and (7.46). Finally, a second phase correction, complex conjugate of the first, is applied to restore the original phase reference in the data. The main advantage of this procedure is the reduction of both data volume and measurement time. From the viewpoint of the RMA, this pre-processing is completely transparent and does not introduce any side effect. Note that the 3-D RMA maintains the same requirements in terms of internal memory and computational load. The flowchart associated with this pre-processing is shown in Fig. 7.3. The resulting cross-range sampling intervals (i.e., those used in a spotlight SAR) are:

$$\Delta_{x_a} \leqslant \frac{\lambda_{min}y_a}{2\sqrt{D_x^2 + D_y^2}}$$ (7.48)

$$\Delta_{z_a} \leqslant \frac{\lambda_{min}y_a}{2\sqrt{D_z^2 + D_y^2}}.$$ (7.49)

In [135, 136] an alternative technique to process strip map data at spotlight sampling frequency is presented. This method, named Frequency domain Replication and Downsampling (RMA-FReD) in [136], has been used with airborne data for 2-D images. With this approach the blurred replicas due to the aliasing fall ideally out of the scene, and the final image presents a slightly lower signal-to-background-ratio and a wider impulse response. If
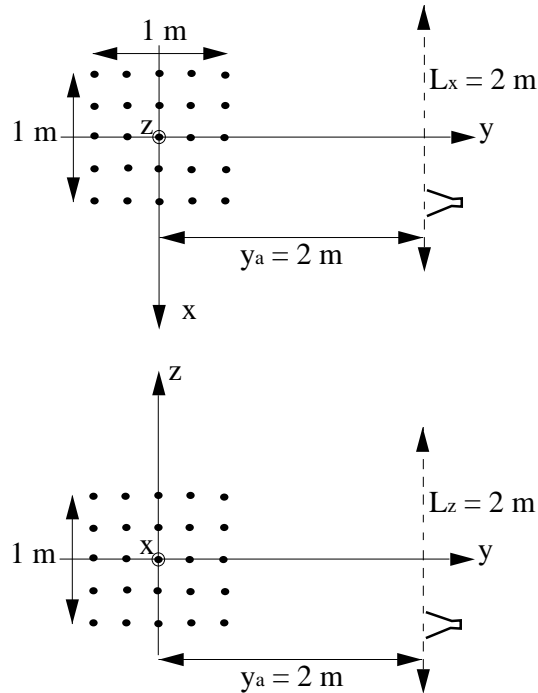
**Fig. 7.4.** Measurement set-up used in the numerical simulation with the 3-D array of 125 point scatterers

this minor degradation in the image quality is accepted, one can use the RMA-FReD as a quick-look processor. Note that, with the RMA-FReD, the data volume to be processed is by far smaller than that in the conventional RMA. In the next section, the results obtained with these two processors are compared.

# 7.3   Results

The high computational efficiency and accurate image reconstruction of the algorithm are demonstrated both with numerical simulations and measurements using an outdoor linear SAR system. The code of the algorithm has been implemented in C programming language. The computer used to focus the data is a high performance Sun Ultra-Sparc workstation, equipped with a 64 bit CPU and 128 MByte of RAM. What follows is the description of the measurement set-ups and the results on simulated and real data sets.

## 7.3.1   Numerical Simulations

Fig. 7.4 shows a sketch of the target used in the first numerical simulation. The target consists of a 3-D array of $5 \times 5 \times 5$ point scatterers uniformly distributed within a box of side 1 m.

(a)



(b)
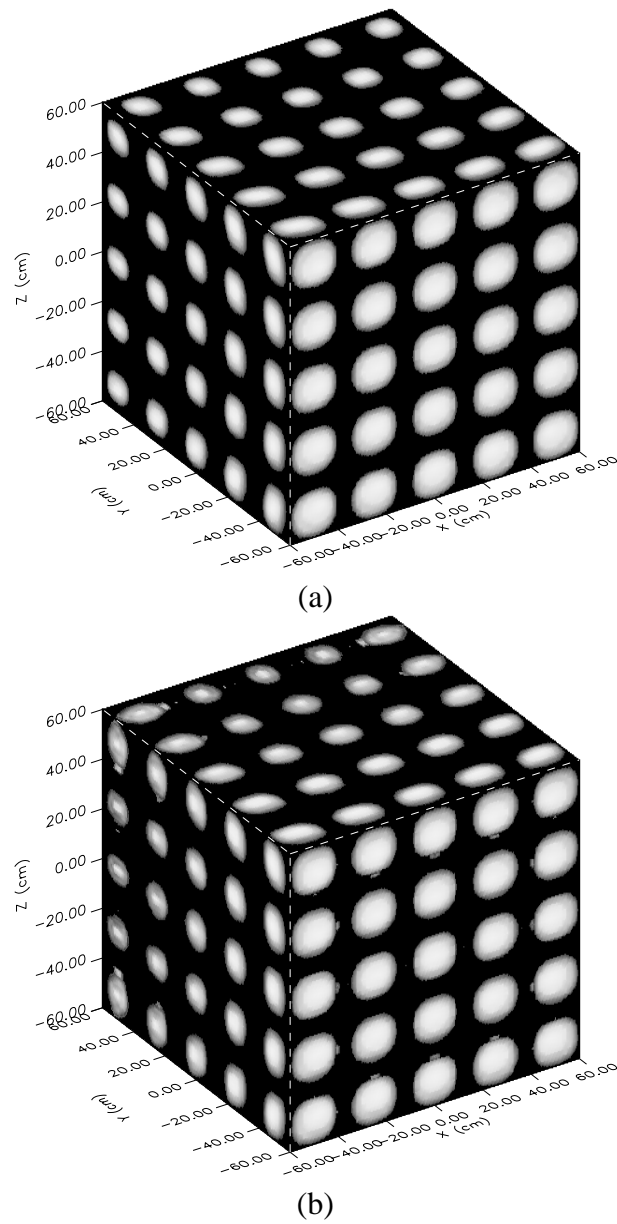
**Fig. 7.5.** Projections of the 3-D SAR image onto the XY, XZ and YZ planes. Simulation of 125 point scatterers. Parameters: $y_a = L_x = L_z = 2$ m, $f = 2$–$6$ GHz, $\delta_x = \delta_y = \delta_z = 3.75$ cm, $\Delta_f = 100$ MHz, $\Delta_{x_a} = \Delta_{x_a} = 4$ cm, Displayed dynamic range is 50 dB. (a) Original RMA (b) RMA-FReD

All scatterers have the same RCS: 0 dBsm. A TX/RX antenna synthesizes a planar aperture of 2 m $\times$ 2 m located at $y_a = 2$ m from the target center. The number of measurement points is 51, spaced 4 cm apart, both in the horizontal and vertical cross-range directions. These sampling intervals have been selected according to the spotlight criterion. The resulting sampling intervals without the proposed pre-processing would be 2 cm. The frequency ranges from 2 to 6 GHz, sampling a total of 41 points with a step of 100 MHz. According to these parameters the theoretical resolution is 3.75 cm along the three main axes.

Two 3-D reflectivity images have been reconstructed using the RMA and the RMA-FReD, respectively. The reflectivity images have been reconstructed in a cube of side 1.2 m, with a total of 61 boxel in each dimension. Fig. 7.5 shows the projection of the images onto the three main planes. A Kaiser-Bessel ($\alpha = 2$) window has been applied along all dimensions of the frequency domain data set [179]. The dynamic range displayed in the image is 50 dB. Both results show a slight dependence on the ground-range coordinate ($y$). This effect is common in near-field measurements since the algorithm does not focus with the same resolution close and distant points. For close points the effective aperture angle is larger than for distant ones, thus providing better resolutions in the near range area of the target. Anyway, the quality of the whole reconstructed image is quite satisfactory and, moreover, the computation time is short. In the RMA case the processing time was 3 min and 40 secs, requiring about 13 MB of RAM. The image obtained with the RMA-FReD processor exhibits some inaccuracies with reflectivity values below $-30$ dBsm. These imperfections are present in the near range zone because this area introduces the highest spatial frequencies, which in turn were degraded by aliasing. However, with this processor, the processing time was only 1 min, requiring 3 MB of RAM.

The second simulation is intended to estimate the dynamic range of the 3-D RMA processor. The target is similar to that used in the previous simulation. It consists of three parallel planes spaced 40 cm apart, where 9 scatterers have been uniformly distributed as shown in Fig. 7.6a. The reflectivities of the point scatterers range from 0 to -80 dBsm. The measurement set-up is identical to that of the first simulation. The reflectivity image has been reconstructed using the 3-D RMA. Fig. 7.6b shows the slice corresponding to a vertical plane parallel to the aperture at $y = 0$. The dynamic range of this image is 100 dB. As in the previous results, a Kaiser-Bessel ($\alpha = 2$) window has been applied. It is seen that the dynamic range of the imaging algorithm is better that 80 dB. In practice, the dynamic range will be limited by the presence of noise in the system. Table 7.1 compares the values of reconstructed and actual reflectivities. The maximum error is in the order of 1.5 dB.

**Table 7.1.** Reflectivity values for the target in Fig. 7.6

| Nominal (dBsm) | y=-0.4 | y=0 | y=0.4 |
|:---:|:---:|:---:|:---:|
| 0 | -0.08 | -0.10 | -0.12 |
| -10 | -10.39 | -10.53 | -10.71 |
| -20 | -20.71 | -20.95 | -21.30 |
| -40 | -40.69 | -40.94 | -41.30 |
| -60 | -60.75 | -60.99 | -61.31 |
| -80 | -79.82 | -80.45 | -81.07 |

(a)



(b)
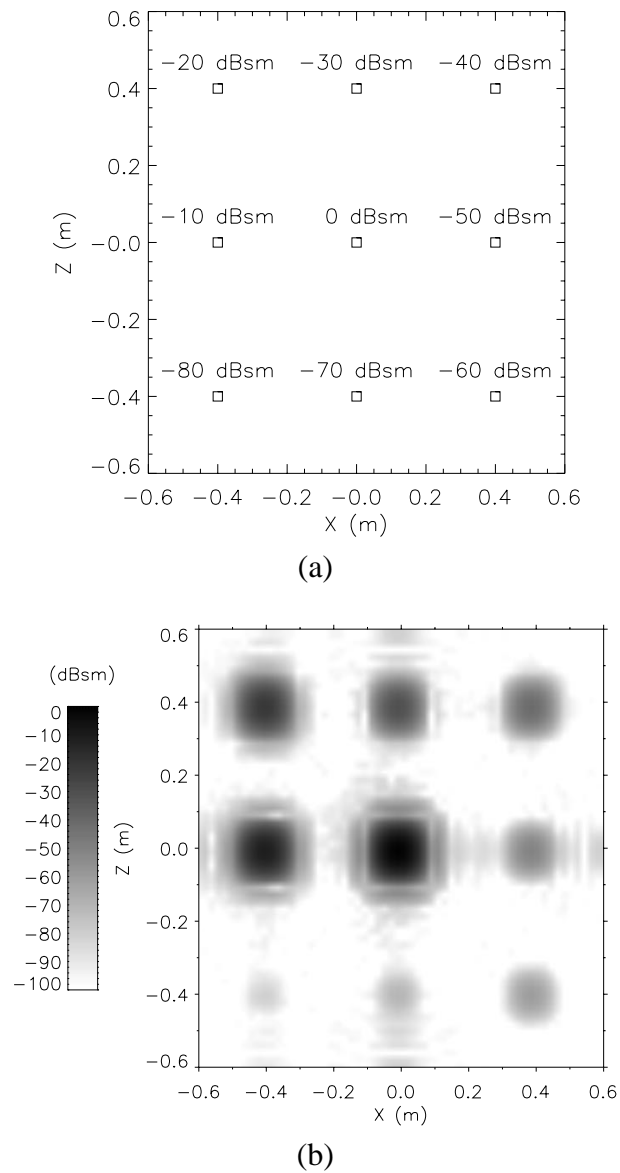
**Fig. 7.6.** Target modeled to evaluate the dynamic range. (a) Sketch of the target. (b) Slice of the reflectivity image.

## 7.3.2 Experimental Results

The proposed 3-D imaging algorithm has been validated experimentally by using an outdoor linear SAR system developed at JRC which is known as LISA. This system is based on a stepped frequency radar equipped with a 2-D positioning system. The maximum aperture dimensions are limited to 5 m and 1 m in the horizontal and vertical cross-range directions, respectively. The positioning accuracy is better than 0.1 mm. The frequency range is basically limited by the type of antennas being used. The system performs quasi-monostatic measurements using two closely spaced horn antennas.

Fig. 7.7 shows a scheme and photographs of the measurement set-up used in the experimental validation. The target consists of a 3-D arrangement of eight metallic spheres of diameter 7.62 cm. The dimensions of the 2-D synthetic aperture are 1 m × 1 m, with a total of 41 measurement points equally spaced along the horizontal and vertical directions. The backscattered fields in HH polarization were acquired at 401 frequency points spaced 5 MHz within the frequency range 15.5 to 17.5 GHz. The range, from the center of the aperture, to the center of the target was 2.3 m. The plane of the aperture was tilted 14 degrees from the vertical. The expected resolutions are 2 cm in the horizontal ($X$) and vertical ($Z$) cross-range directions, and 7.5 cm in the ground-range ($Y$) direction.

The measurement time required in this experiment is approximately 2 hours. A 3-D reflectivity image confined in a box of side 60 cm with 61 boxel in each dimension has been reconstructed. The processing time was 1 min and 43 secs. Fig. 7.8 shows some slices out of the reconstructed 3-D image: three slices at different ground-range ($y = -16, 0, +16$ cm) and cross-range ($x = -16, 0, +16$ cm) positions. The displayed dynamic range is 20 dB. As expected, the reflectivity at the positions of the spheres is about -23.4 dBsm, corresponding to RCS given by the physical optics approximation. The measured spatial resolutions are in agreement with the expected ones. Note that the reflectivity peaks of the spheres closer to the antennas are narrower because the effective synthetic aperture is larger in the near range. On the other hand, the spheres have a diameter of about four wavelengths and therefore they are not ideal point scatterers. As a result, a minor degradation or defocusing must be expected.
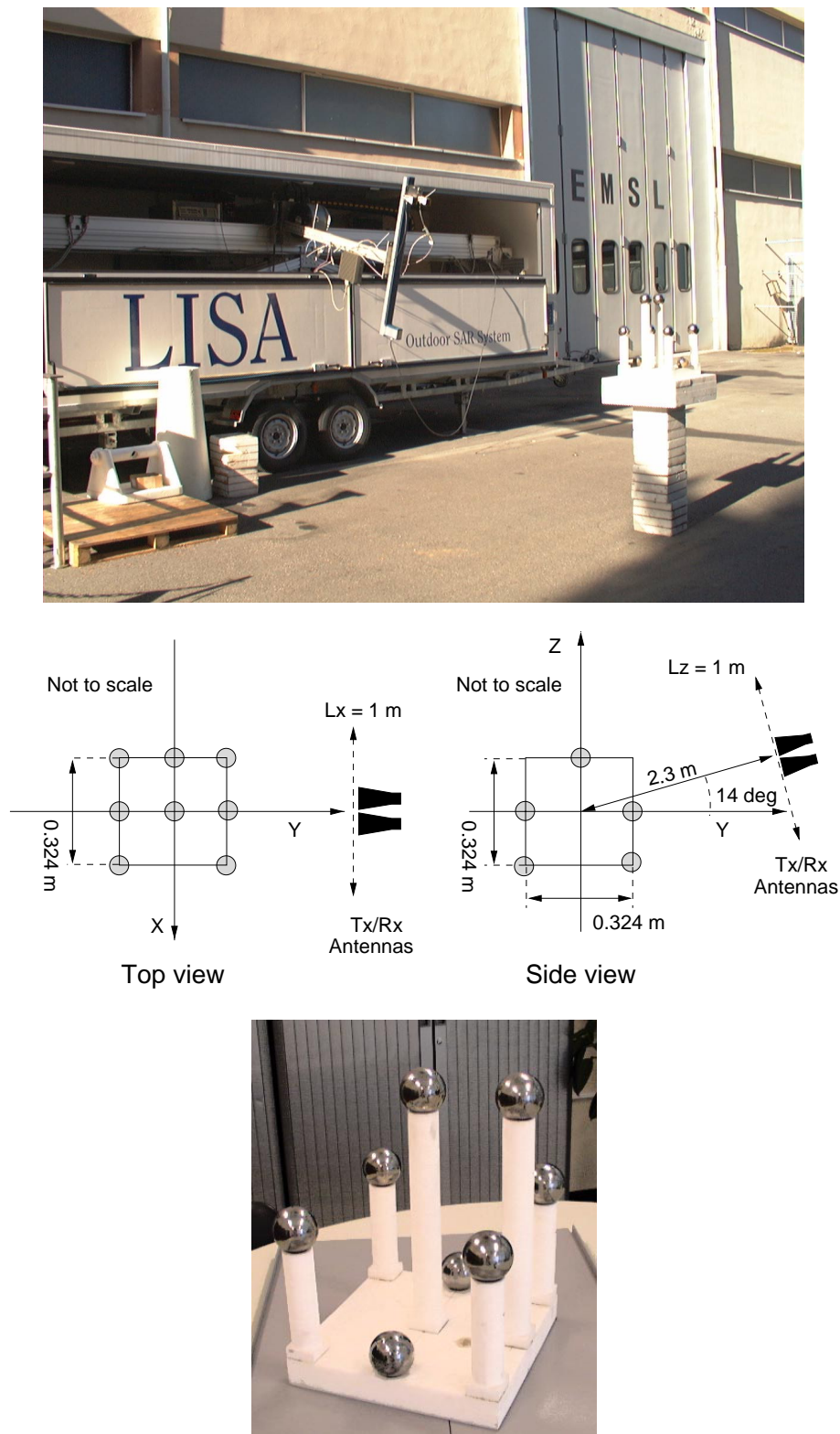
**Fig. 7.7.** Photographs and scheme of the experiment with LISA
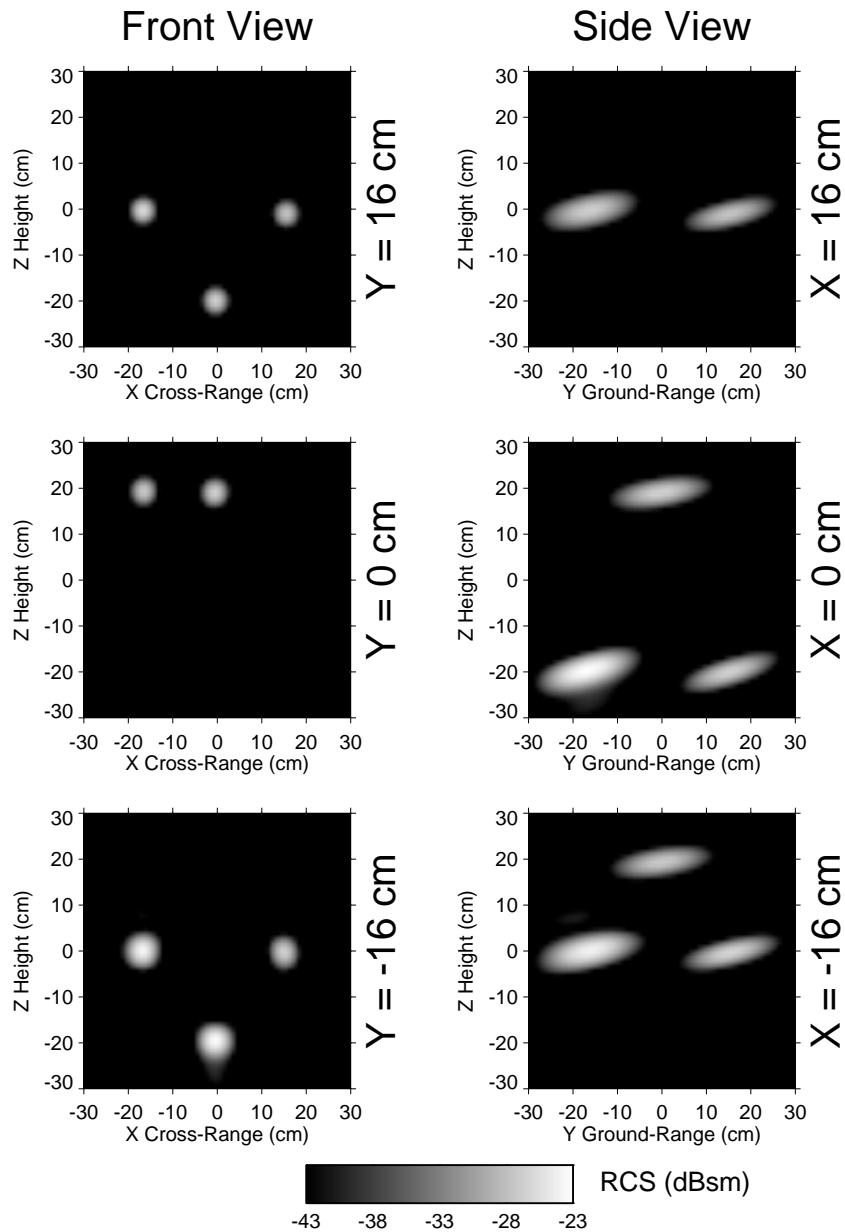
**Fig. 7.8.** Slices of the reconstructed 3-D image with the eight spheres measured by LISA

# 7.4    Extension of RMA to Cylindrical and Spherical Scanning Geometries

We have seen that the main advantage of the RMA is the simultaneous accuracy and efficiency demonstrated when applied to near-field configurations. The accuracy is excellent thanks to the totally exact compensation of the wavefront curvature, which is exclusive of this technique. The algorithm is also very efficient from the computational point of view because it can be readily implemented with only FFT's and an 1-D interpolation. Since

the RMA enables the production of highly accurate images, even in near-field conditions, it constitutes an ideal approach for experiments in anechoic chambers.

As was described in previous sections, this algorithm reaches the maximum efficiency when the synthetic aperture is planar. In that case, the method can be applied directly in the cartesian coordinate system, and hence the data processing along all directions can be performed by using only FFT's. Unfortunately, there is a considerable number of anechoic chambers or indoor facilities that do not offer the possibility of carrying out such SAR experiments by synthesizing a planar aperture. Two common cases are cited here. The first is an inverse SAR set-up, whose aperture is generated in one dimension by a rotation of the target about azimuth and in the other by changing the position of the antennas over a vertical circular rail (i.e. modifying the incidence angle). Consequently, the synthetic aperture becomes a portion of a spherical surface. The second common configuration is that of a linear SAR with an additional varying incidence angle produced as in the former case. The resulting aperture conforms a part of a cylindrical surface. Both configurations can be applied at the EMSL.

It would be desirable to develop new versions of the 3-D RMA adapted to these scanning geometries. However, as was stated before, the advantage of the cartesian coordinate system (i.e. the massive computation by FFT's) would be lost if the cylindrical or spherical coordinate systems were considered. The best solution, hence, is performing a transformation from the original data, acquired on non-planar apertures, into equivalent data on a planar aperture, before the RMA is applied. In that way, the computational cost of the RMA is maintained, and only a moderate additional load must be considered as a result of the transformation.

The proposed transformation has been carried out by employing field translations in a similar way to those used in antenna measurements. These types of translations are accomplished by accounting for the field nature of the data in order to preserve all information. The working principle is the following: since the target is confined by the surface on which the data are measured (a cylinder or a sphere), it is possible to find the field in any other point in space by only knowing the field on the surface. The aim of this translation is to find the field that *would have been measured* on a planar aperture by knowing the field that *was really measured* on a cylindrical or spherical surface.

The first step of the method is the calculation of the modal coefficients of the harmonics into which the measured field can be decomposed. This modal expansion is the solution of the wave equation. The modal coefficients are determined by matching the fields on the surface on which the fields are known. Once those coefficients are found, the mode summation is used for retrieving the field at a planar surface close to the original aperture. At that stage, the RMA can be applied to the translated fields as it was originally formulated. This procedure is summarized in the scheme depicted in Fig. 7.9. Note that, in general, the original aperture does not cover the whole cylindrical or spherical surface, but the field can be assumed to be zero on the non-covered part of the surface. It will be demonstrated in the text that this assumption does not introduce an important error if the region in which the translated field is computed is close enough to the surface with the original data.
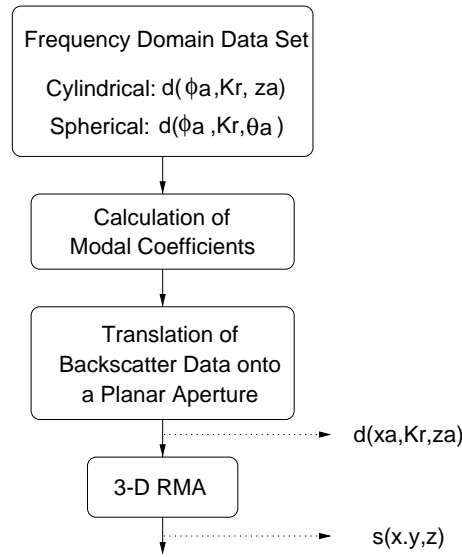
**Fig. 7.9.** Scheme of the data processing for non-planar scanning geometries

The text is organized as follows. Section 7.4.1 describes briefly the formulation of the data translation as a previous stage of the RMA processing. Details of the practical implementation of the translation are provided in Appendices C and D for the cylindrical and spherical case, respectively. Some numerical simulations are analyzed in Section 7.4.2, and Section 7.4.3 shows experimental results obtained by applying this technique.

## 7.4.1  Data Translation to a Planar Aperture

### 7.4.1.1  Cylindrical Aperture

Let us consider the geometry depicted in Fig. 7.10a. For convenience, the axis of the linear displacement is associated with the cylindrical $Z$ axis. The angular position of the antennas can be denoted by the standard azimuth angle $\phi$. By using the cylindrical coordinate system, the wave equation can be easily formulated and solved (see details in Appendix C).

For each frequency, the acquired field must satisfy the wave equation. The general solution of that equation is a modal expansion with the following form:

$$\psi(A, \phi, z) = \sum_{n=-N}^{N} \sum_{k_z=-K_{Zmax}}^{K_{Zmax}} c_{n,k_z} H_n^{(2)}(k_\rho A) \, e^{jn\phi} \, e^{jk_z z}, \qquad (7.50)$$

where $A$ denotes the radius of the cylindrical surface.

The translation procedure starts by computing the coefficients of this modal expansion. This calculus is carried out in a efficient way by means of FFT's. Once the coefficients

(a) Cylindrical to planar        (b) Spherical to planar
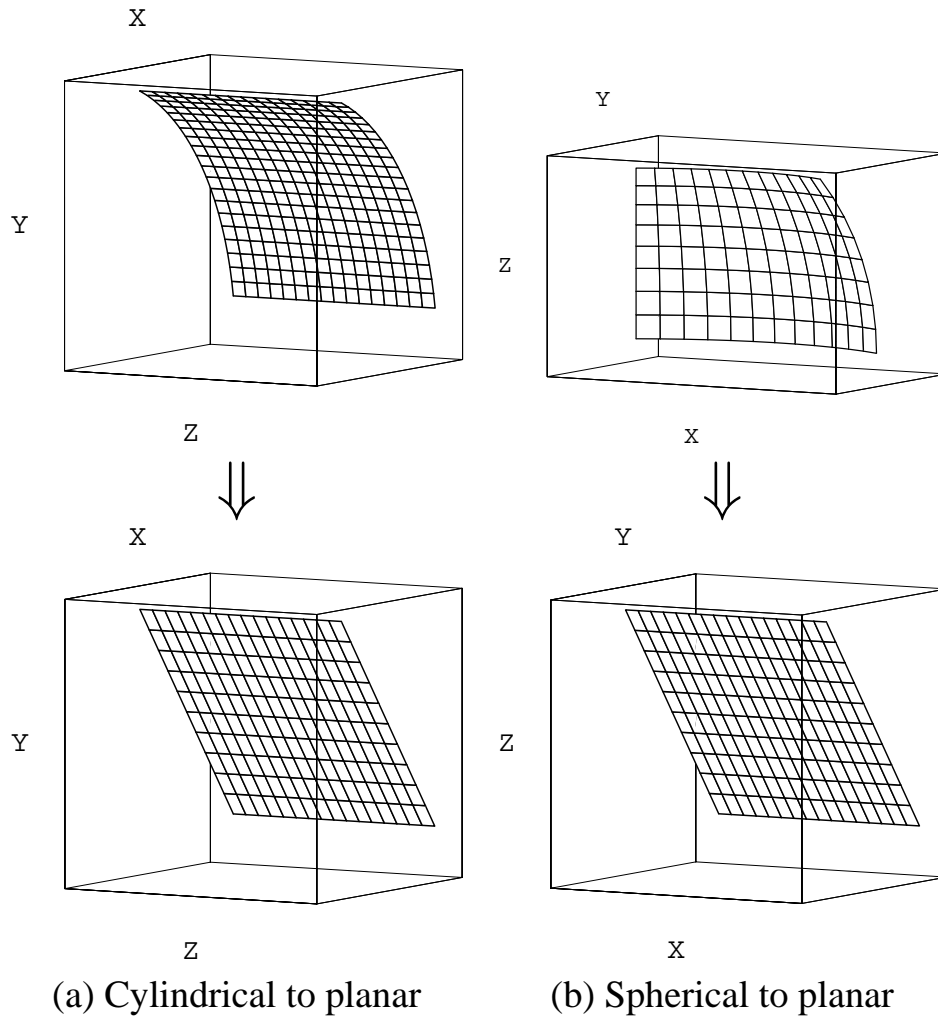
**Fig. 7.10.** Geometry of the original cylindrical and spherical apertures and the final planar aperture

are obtained, the summation of harmonics can be used to retrieve the field values at every point on the planar aperture. The retrieved values have the appropriate form to be applied as an input to the original 3-D RMA.

### 7.4.1.2   Spherical Aperture

The spherical-to-planar configuration is depicted in Fig. 7.10b. In this case the standard spherical coordinate system matches this geometry. The solution of the wave equation is an expansion in series of spherical harmonics (see Appendix D):

$$\psi(A, \phi, \theta) = \sum_{n=0}^{N} \sum_{m=-n}^{n} c_{m,n}\, e^{jm\phi} \left( \frac{m}{|m|} \right)^m \overline{P}_n^m(\cos\theta)\, h_n^{(2)}(kA). \qquad (7.51)$$
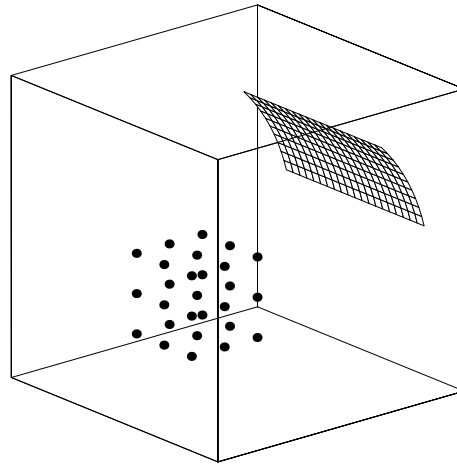
**Fig. 7.11.** Measurement set-up used in the numerical simulation with a 3-D array of 27 point scatterers and a cylindrical synthetic aperture

The calculation of the expansion coefficients is similar in formulation to the method described in [180, Chapter 4]. Only a few modifications have been introduced in order to apply this technique to the scalar wave equation instead of the vector one used in that book. The procedure is based on the exploitation of orthogonality properties of both the exponential functions and the associate Legendre functions. The computation can be efficiently implemented by FFT's as in the cylindrical case. However, the relations between the orthogonality of the associate Legendre functions and the FFT's are not as straightforward as before, thus increasing the computational complexity. See Appendix D for details.

There is an important point to clarify. In antenna measurements the acquired fields on the aperture only travel the path from the antenna under test (the source) to the probe antennas, whereas in a radar configuration the field travels from the antenna to the target and from the target back to the antenna. Consequently, the wave equations to be solved must take it into account. A simple way to incorporate this into the formulation is to consider *twice* the wavenumber in the wave equation. In other words, the wavenumber $k$ at this stage is redefined as $4\pi f/c$ instead of $2\pi f/c$, where $f$ in the working frequency and $c$ is the velocity of light. This modification holds for both cylindrical and spherical cases.

## 7.4.2 Numerical Simulations

Fig. 7.11 shows a sketch of the geometry used in the first numerical simulation. The target consists of a 3-D array of $3 \times 3 \times 3$ point scatterers uniformly distributed within a box of side 0.8 m, i.e. the scatterers form a mesh with a spacing of 40 cm. All scatterers have the same RCS: 0 dBsm. A TX/RX antenna synthesizes a cylindrical aperture in the angular range $20° \leqslant \phi \leqslant 40°$ with a radius of 2 m, centered at the target center. The linear dimension of the aperture is $L_z = 2$ m, and the frequency ranges from 2 to 6 GHz.
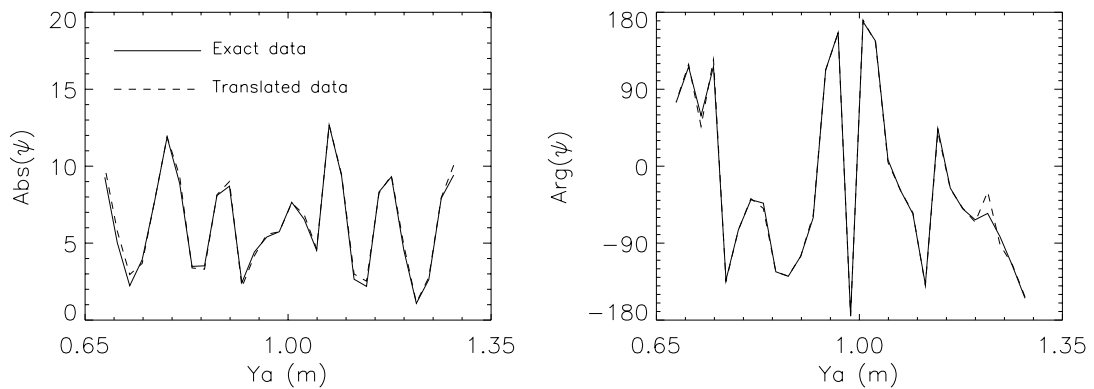
(a) Z = 0 m (center)
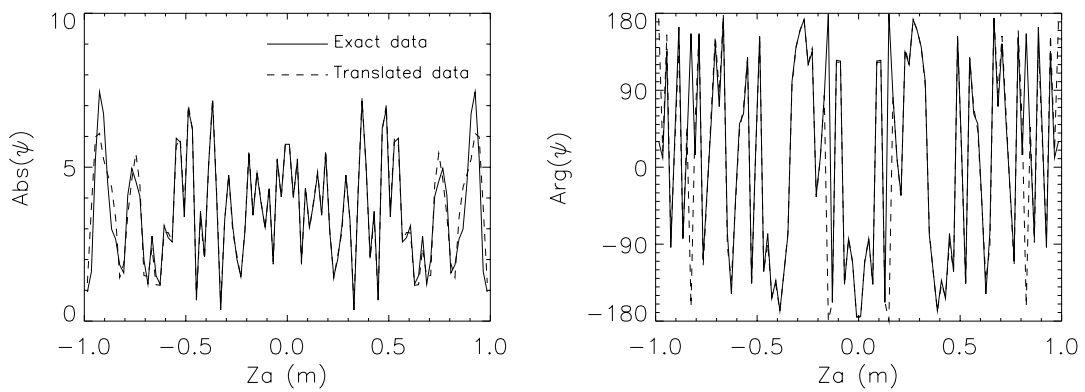


(b) Y = 0.985 m (center)
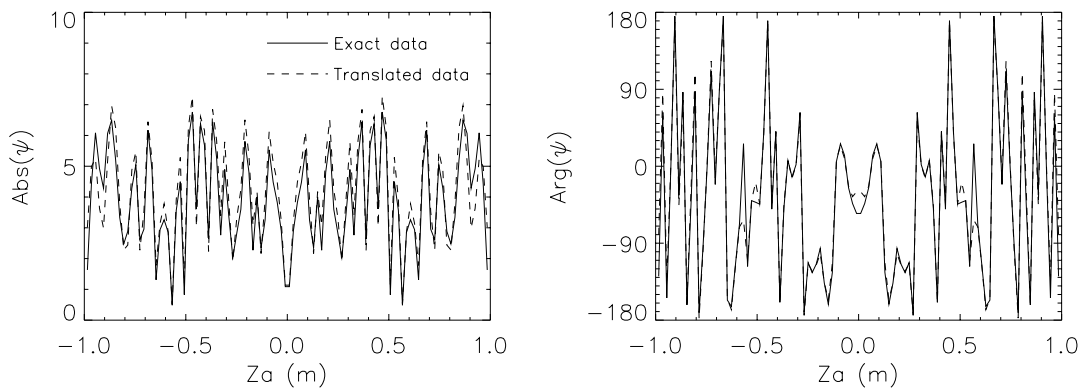


(c) Y = 0.748 m

**Fig. 7.12.** Comparison between translated and exact fields on the planar aperture. (a) Line at Z=0. (b) Line at Y=0.985. (c) Line at Y=0.748

In order to illustrate the performance of the translation from the cylindrical aperture to the planar one, some intermediate results are shown in Fig. 7.12. These plots correspond to a comparison between the translated fields (obtained by applying the translation discussed in previous sections to the original data acquired on the cylindrical aperture) and the fields
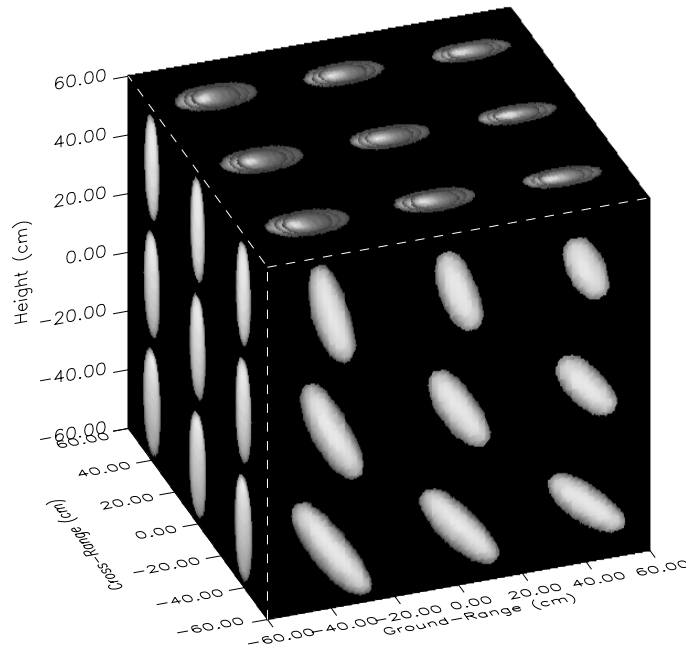
**Fig. 7.13.** Projections of the 3-D SAR image onto the three main planes. Simulation of 27 point scatterers with a cylindrical aperture. Parameters: $R = 2$ m, $f = 2$–6 GHz, $\Delta_f = 100$ MHz, $20° \leqslant \phi \leqslant 40°$, $\Delta_\phi = 1°$, $L_z = 2$ m, $\Delta_{z_a} = 4$ cm. Displayed dynamic range = 30 dB

that would be measured on the planar aperture if it were employed instead of the cylindrical one. Fig. 7.12 presents the modulus and phase of the scattered fields along three linear subapertures: the first consists of a line at constant $z$ at the center of the aperture; the second corresponds to a line at constant $y$ at the center of the aperture; and the third is a line at constant $y$ but close to the bottom extreme of the aperture.

Some conclusions can be drawn from the behavior of the translated fields. Firstly, it is evident that a quite good agreement has been found between translated and exact fields, thus fully validating this technique. In general, the phase is more accurate than the modulus. This is a good characteristic when working with radar imaging because the information is mainly contained in the phase. As expected, there are small discrepancies in the phase when the corresponding modulus is low. The error is higher at the extremes of the aperture, but this will not cause problems on the imaging reconstruction because a windowing is normally applied for reducing the secondary lobes. Therefore, the extremes of the aperture are mostly masked by the window weights. Note that there exist some peaks in the phase which could be considered as errors but are only skips of $2\pi$ due to the cyclic nature of the phase. Finally, note that the curves at constant $y$ are symmetric with respect to the center, whereas the curves at constant $z$ are not. This is due to the symmetry of the aperture and the target along the $z$ axis, which is not present on the aperture over $\phi$ because of the employed angular range. Similar curves have been obtained in the spherical case.

Once the translation previous to the RMA processing has been validated, results of the complete image generation are presented in the next figures. The first result corresponds

**Table 7.2.** Computational performance

| Step | Time (s) |
|---|---|
| Freq-Domain Data Load | 0.36 |
| Equalization (Optional) | 54.31 |
| Translation to a Planar Aperture | 46.63 |
| 2-D Along-Track FFT | 14.76 |
| Matched Filter and Stolt Interpolation | 53.53 |
| 3-D Final IFFT | 60.09 |
| Coordinates Transformation (Optional) | 3.51 |
| Total Elapsed Time | 233.19 |

to the image generated from the data used in the former simulation. Fig. 7.13 shows a 3-D image obtained from the array of 27 point scatterers. The image consists of a cube of side 1.2 m with a total of 61 boxel along every direction. A Kaiser-Bessel ($\alpha = 2$) window has been applied along all dimensions of the frequency domain data set [179]. The displayed dynamic range is 30 dB. The image exhibits a different focusing for points at near and far range due to the near field situation, but the reconstructed scatterers are located at their actual positions, and their reflectivity agrees with the simulated RCS.

Table 7.2 presents the computation time of the algorithm in order to gain an insight into the complexity of each part. Both equalization and coordinates transformation are optional steps, so they are not considered in the total computation time. Note that the translation to the planar aperture entails less than 1/3 of the total elapsed time. The required memory in this simulation was about 11 MB.

**Table 7.3.** Reflectivity values for the target in Fig. 7.14

| Nominal (dBsm) | x=-0.5 | x=0 | x=0.5 |
|---|---|---|---|
| 0 | 0.03 | -0.09 | -0.16 |
| -10 | -10.49 | -10.92 | -11.70 |
| -20 | -21.05 | -21.72 | -21.93 |
| -30 | -30.54 | -30.89 | -31.46 |
| -40 | -41.10 | -41.81 | -42.09 |
| -50 | -52.05 | -50.23 | -50.66 |
| -60 | -60.82 | -61.88 | -61.95 |
| -70 | -68.48 | -69.38 | -71.18 |
| -80 | -77.63 | -79.48 | -82.36 |

It is worthwhile studying the effect of the translation on the dynamic range of the final image. It was demonstrated in Section 7.3.2 that the imaging algorithm exhibits a dynamic range better than 80 dB, which in practice means that the actual dynamic range will be limited

(a)



(b)
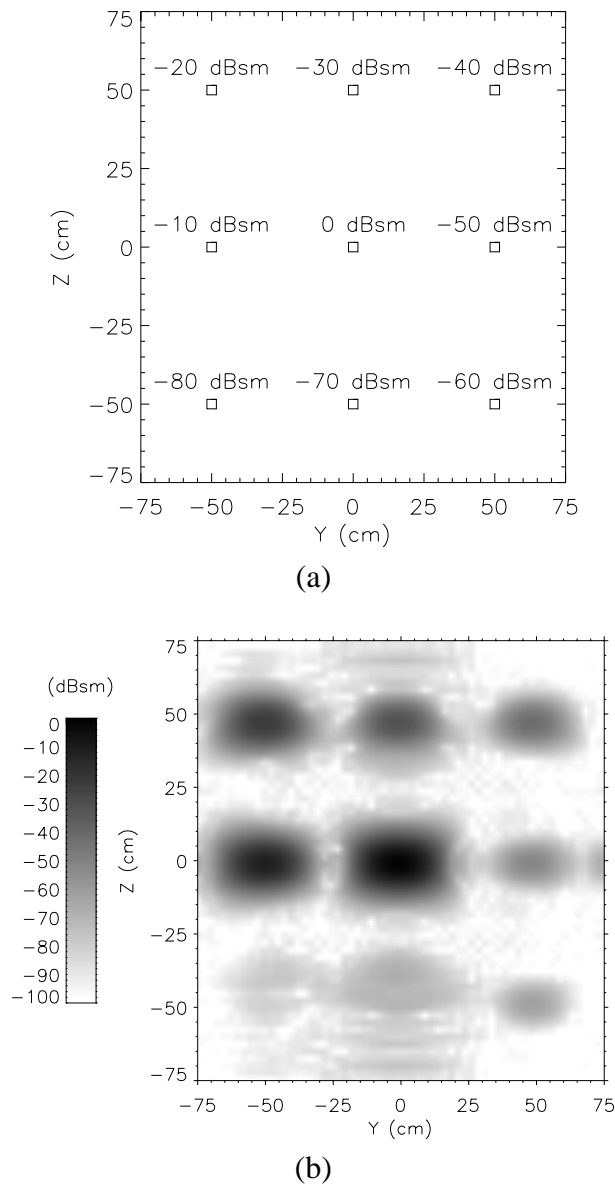
**Fig. 7.14.** Target modeled to evaluate the dynamic range. (a) Sketch of the target. (b) Slice of the reflectivity image

by system noise. However, in the cylindrical and spherical cases, the translation introduces small inaccuracies in the signal as was previously shown. These imperfections should have an effect on the quality of the final image. This influence has been analyzed by using a target with a high dynamic range. The target consists of three parallel planes as that displayed in Fig. 7.14a, separated 50 cm one from each other along the ground-range direction. Each plane presents 9 point targets with reflectivities ranging from 0 to -80 dBsm. The synthetic aperture is identical to that employed in the former example, but now the angle range is $-15° \leqslant \phi \leqslant 15°$. Fig. 7.14b shows a slice corresponding to the central plane. The displayed dynamic range is 100 dB. The effective dynamic range free of noise is approximately around 70 dB, thus being slightly poorer than in the planar aperture case. Table 7.3 compares the
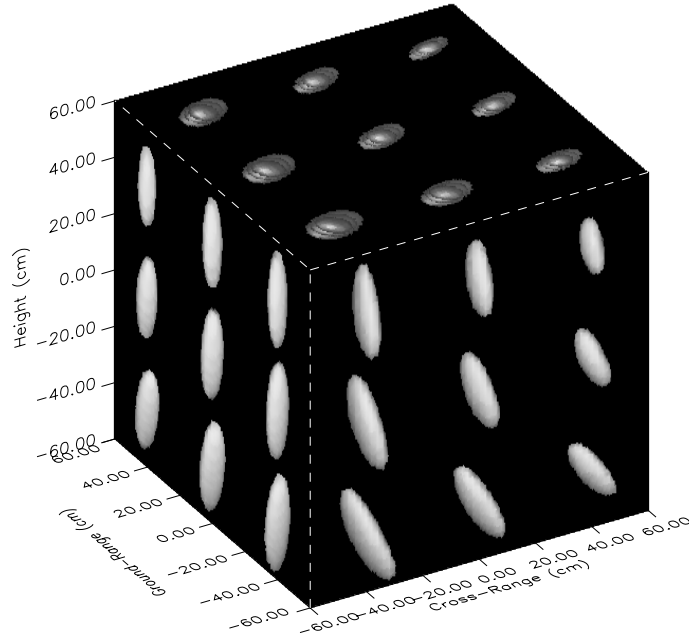
**Fig. 7.15.** Projections of the 3-D SAR image onto the three main planes. Simulation of 27 point scatterers with a spherical aperture. Parameters: $R = 2$ m, $f = 2$–6 GHz, $\Delta_f = 100$ MHz, $0° \leqslant \phi \leqslant 45°$, $60° \leqslant \theta \leqslant 75°$, $\Delta_\phi = \Delta_\theta = 1°$. Displayed dynamic range = 30 dB

values of retrieved and nominal reflectivities. The maximum error is around 2.5 dB.

It is important to mention that the situation analyzed for illustrating the data translation and the influence on the final dynamic range is very severe, due to a extreme near-field condition. It is possible to demonstrate that when the antenna and the target are more separated (even without approaching a far-field situation) the translation performs better and the final dynamic range is not as degraded as before. An example will be presented in the next section.

The illustration of the spherical case is introduced in Fig. 7.15. The target is the same as Fig. 7.13, but now the antenna synthesizes an aperture with the shape of a portion of a sphere with a radius of 2 m. The angular ranges are $0° \leqslant \phi \leqslant 45°$ and $60° \leqslant \theta \leqslant 75°$. Again, the quality of the final image is quite high, thus demonstrating the utility of the present method. In the spherical case the translation is more time consuming than before, and yields a computation time of the same order as the rest of the focusing algorithm. This increase of time is due to the coefficients computation, described in Appendix D, which is more complicated than the cylindrical case.
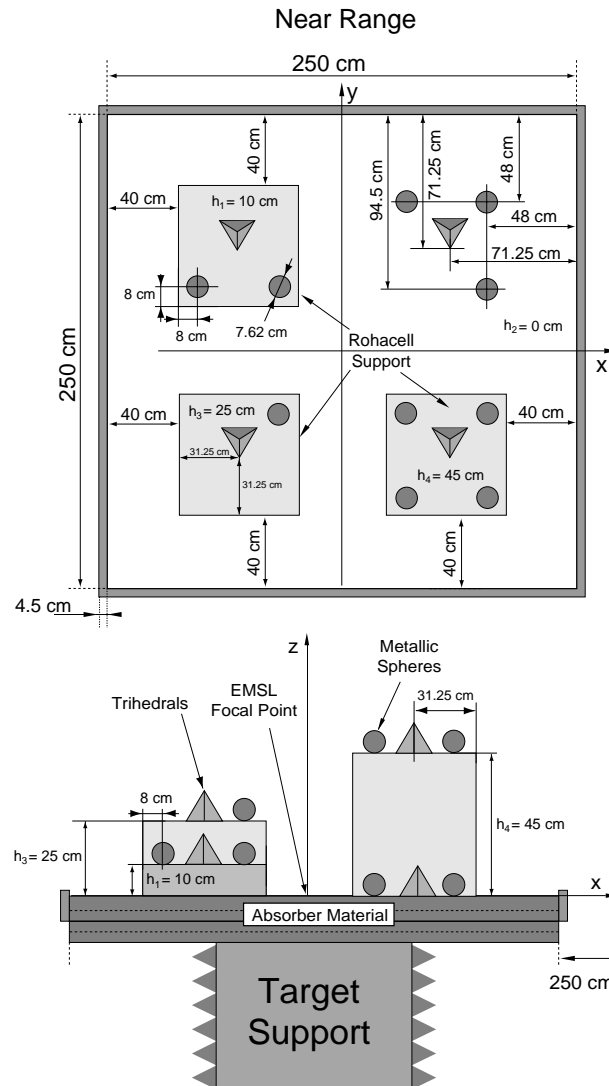
**Fig. 7.16.** Top view and side view of a scheme of the target used in the experimental validation of the cylindrical aperture

## 7.4.3 Experimental Results

A scheme of the target used in the first experiment is depicted in Fig. 7.16, and a photograph is also shown in Fig. 7.17. The target consists of an arrangement of metallic spheres and trihedrals. The spheres have a diameter of 7.62 cm. There are two pairs of trihedrals with different side lengths: 28 cm and 19.5 cm. The spheres and trihedrals are distributed on four planes at different heights, and are fixed by supports of rohacell. More geometrical details are described in Fig. 7.16.

The measurement was carried out in the frequency range 6–10 GHz. The target positioner was moved along a segment of 4 m, and the antennas covered the angular range $35° \leqslant \phi \leqslant 55°$. With these parameters the approximate theoretical resolutions to be ob-
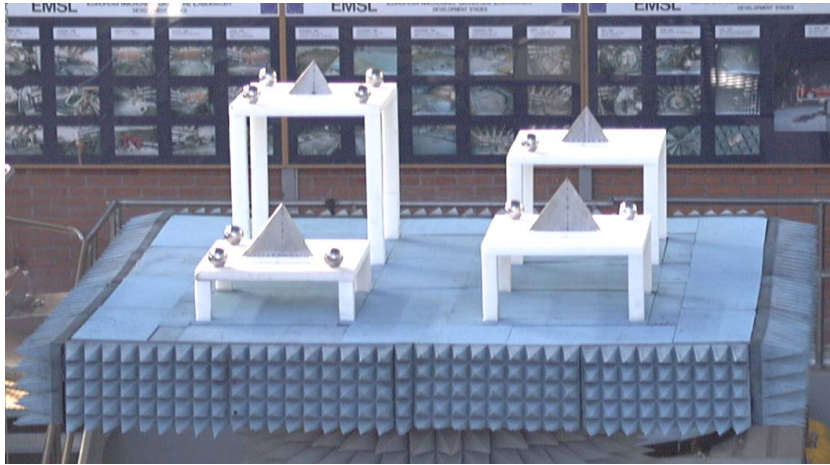
**Fig. 7.17.** Photograph of the target used in the experimental validation of the cylindrical aperture

tained are 3.75 cm in ground-range, 4.4 cm in cross-range and 5.4 cm in height, respectively. Radar backscatter data were acquired at two polarizations: HH and VV. Fig. 7.18 shows the images obtained at both polarizations. The reflectivity was reconstructed in a box of 2 m $\times$ 2 m $\times$ 0.8 m, with 201 $\times$ 201 $\times$ 41 boxels. The displayed dynamic range is 60 dB.

The quality of images presented in Fig. 7.18 confirm the accuracy of the image generation algorithm under a cylindrical scanning geometry. It is important to observe how the spheres are well distinguished along the three main directions, yielding resolutions in agreement with the expectations. On the other hand, the trihedrals exhibit a composite response: a high peak centered at the trihedral phase center and a $\Lambda$ shape due to the diffraction on the front edges. The peak at the phase center is independent from the polarization, showing the same form in both images at HH and VV. Instead, the reflectivity at the edges changes with the polarization due to their orientations. For example, the HH images show horizontal segments with high reflectivity at all four trihedrals, whereas the other two edges of the front triangle do not appear. Moreover, the upper peak of the two large trihedrals is also present in the HH images. On the other hand, the horizontal edges have disappeared in the VV images, but the other edges are present. Note that both edges of the large trihedrals can be distinguished, but only the external one is evident in the small trihedrals. This phenomenon is caused by the asymmetry of the aperture with respect to those edges.

The image is also accurate from the quantitative point of view. The expected RCS at the central frequency (8 GHz) coincide with the retrieved RCS. The spheres show an RCS of about -23 dBsm, the large trihedrals 6.6 dBsm and the small trihedrals 0.3 dBsm. The theoretical reflectivity values can be calculated following the formulas in [181].

Finally, note that the total computation time was only 1 hour and 1 minute. The part corresponding to the field translation entailed 41 minutes, and the RMA processing the remaining 20 minutes.

An experimental test of the spherical case has been also carried out at the EMSL. The
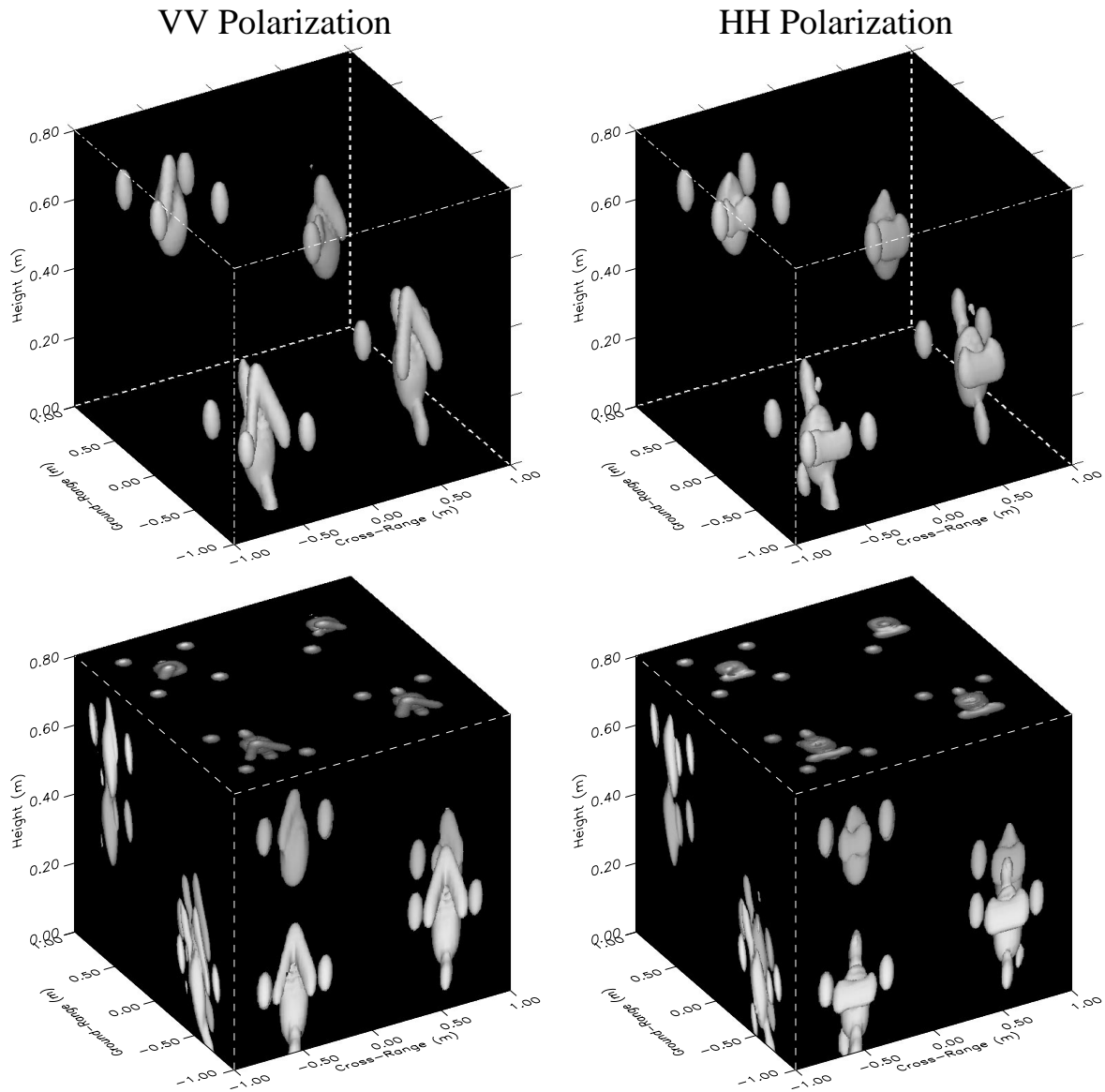
**Fig. 7.18.** Isosurfaces and projections of the 3-D SAR image obtained in the experiment with a cylindrical aperture. Parameters: $R = 9.56$ m, $f = 6$–$10$ GHz, $\Delta_f = 40$ MHz, $35° \leqslant \phi \leqslant 55°$, $\Delta_\phi = 0.5°$, $L_z = 4$ m, $\Delta_{z_a} = 2.5$ cm. Displayed dynamic range = 60 dB

target used in this measurement is the 3-D arrangement of eight metallic spheres that was already used in Section 7.3.2 (see photograph at the bottom of Fig. 7.7). The measurement has been conducted with the same angular span in azimuth and elevation ($45°$), sampling at 61 equally spaced points. The backscattered fields were acquired in HH polarization at 801 frequency points spaced 5 MHz within the frequency range 8–12 GHz. The number of frequency points has been reduced by a factor of 20 after calibration. The range to the center of the coordinates system is $R = 9.56$ m. The measurement time required in this experiment is approximately 50 h. Note that there are 3600 antenna positions on the 2-D synthetic aperture.
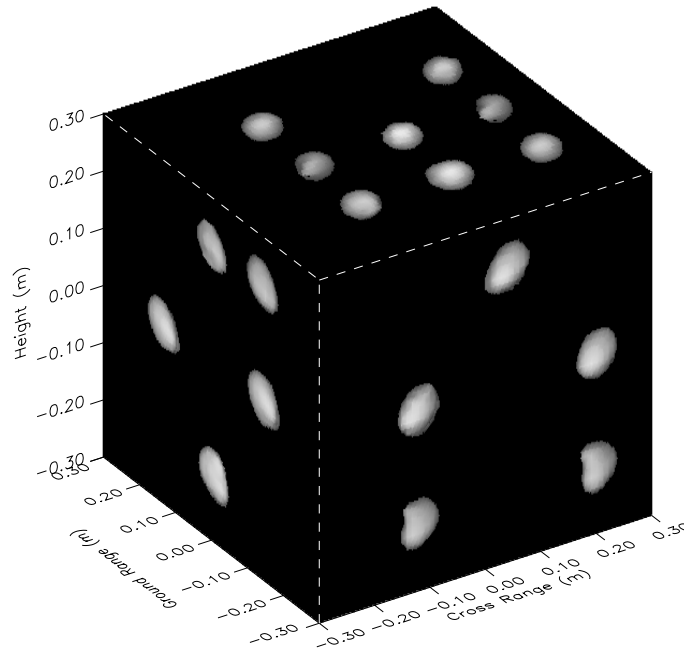
**Fig. 7.19.** Projections of the 3-D SAR image onto the three main planes. Experiment with a spherical aperture. Parameters: $R = 9.56$ m, $f = 8$–$12$ GHz, $0° \leqslant \phi \leqslant 45°$, $45° \leqslant \theta \leqslant 90°$. Displayed dynamic range = 20 dB

A 3-D ISAR image consisting of a cube of side 60 cm with a total of 61 boxel along every direction was reconstructed and is shown in Fig. 7.19. The achieved resolutions, as expected, are about 2 cm along the cross-range and height directions, and 4 cm along the ground-range direction.

The total processing time was 2 h 5 min. The most consuming step was the translation to a planar aperture, which entailed 1 h 42 min. This experiment has been compared with a result presented in [143]. In that paper the author employed the same data set for the experimental validation of a different imaging algorithm. The processing time with that method was 3 h 27 min. Therefore, the 3-D RMA has demonstrated its efficiency even with the use of a spherical geometry. Note that a direct comparison is appropriate in this case because both implementations were programmed in the same language, and compiled and executed on the same platform.

## 7.5   Conclusions

A new near-field 3-D radar imaging algorithm has been presented. It is an extension of the 2-D range migration algorithm. The formulation has been justified by using the method of stationary phase. Implementation aspects including sampling criteria, resolutions and computational complexity have been assessed. Numerical simulations have demonstrated

the efficiency of the algorithm. The quality of the focused images is also very high, and dynamic ranges better than 80 dB have been reached in numerical simulations.

The developed algorithm exhibits maximum efficiency when the synthetic aperture is planar. In that case the method can be applied directly in the cartesian coordinate system, and can be implemented by using FFT codes and an 1-D Lagrange interpolator. Moreover, an extension of the 3-D RMA to the case of synthetic apertures with cylindrical and spherical shapes has been introduced. Data acquired on those non-planar geometries are accurately translated onto a planar aperture by using field translations in a way similar to antenna measurement techniques. Once this translation is accomplished, the original 3-D RMA can be applied. The computational efficiency of the method is maintained, since the translation only entails a moderate increase of the total computation time.

The algorithm has been also validated experimentally using a vehicle-mounted SAR system and the EMSL. All results have manifested the high performance of the algorithm when it is applied to experimental data sets.

A complementary extension of the 3-D RMA is currently being investigated. It consists in incorporating a superresolution code (e.g. MUSIC, linear prediction, etc.) after the Stolt interpolation, instead of the final inverse Fourier transform. This substitution should fit well because the data are uniformly spaced in the Fourier domain at that stage, which is the starting point of those superresolution algorithms.

CHAPTER 8

# Conclusions

The main objectives of this thesis have been accomplished. A review of the results is presented in the following. This chapter also illustrates the possible application of the main results of the thesis to real air- or spaceborne systems, paying special attention to the general design parameters and requirements to operate these techniques. Some fields of research are also proposed as future extensions of the work developed here.

In first place, a polarimetric analysis of the radar backscatter response from vegetation has been completed successfully. Decomposition techniques have been applied in various domains, providing a wealth of useful information about how vegetation is seen by a radar. This decomposition was performed in three domains: 1) frequency domain data, 2) time domain profiles, and 3) high resolution radar images. All three cases have yielded complementary information because depending on the domain the signal is sensible to different target characteristics.

The results in the frequency domain have shown the scattering properties of the samples as a whole. In general, the structure of an entire vegetation volume is so random that the polarimetric entropy reaches its highest level for every scattering mechanism, and the targets can be analyzed only in terms of backscattered power and depolarization. However, both frequency and incidence angle have revealed that the backscatter return is very influenced by the measurement geometry and band. The exact relationship between observations and frequency band and incidence angle depends on the physical structure of the target. Therefore, the variation of these parameters change from a vegetation kind to other, and also between different samples of the same kind when they have dissimilar morphologies. For all samples the dominant scattering mechanism at steep angles is close to surface type due to the reflection on the ground.

The frequency domain results have been justified by transforming the measured data into time domain and thus identifying the position of the sample parts that contribute to the scattering mechanisms. The time domain decomposition helps to understand the scattering processes present in the samples and their dependence on the frequency and incidence angle, leading to some interesting findings. For example, at X band the penetration into the maize

samples is quite high and, at the same time, there is a strong response from the leaves. Moreover, maize samples with young and mature plants have shown a different scattering behavior as the wave penetrates into the sample. A differential extinction coefficient between orthogonal polarizations has been estimated in both cases. This differential extinction coefficient is a key parameter for future polarimetric and interferometric studies on wave propagation through vegetation. Concerning the measurements on the cluster of small fir trees, the high dependence on the working band observed in the frequency domain has been associated with the varying penetration depth observed in the time domain results. Plots of entropy and average alpha as a function of range also confirm that this target can be simply modeled as a random volume over a half-space interface (the ground). The multi-layer vertical distribution of scattering mechanisms inside the vegetation volume has been demonstrated, so this work validates experimentally the foundations of polarimetric interferometry for vegetation height retrieval.

Some 3-D reflectivity images obtained by ISAR experiments have been employed, together with decomposition techniques, for identifying the position and characteristics of the scattering mechanisms in the target volume. These results have demonstrated the complex nature of the interaction of the electromagnetic waves and the vegetation structure. Different types of scattering mechanisms have been successfully located inside the samples. For example, the fir tree exhibits a wide variety of scattering mechanisms: the trunk interacts with the ground and with some branches in a clear dihedral fashion, some external branches exhibit a planar arrangement that creates a surface type scattering, and the rest of the tree is mainly dominated by the random dipole return from needles and branches. The ficus is more heterogeneous and, as a result, the reflectivity images can be described as a distribution of well-defined spots corresponding to leaves and branches. The spatial distribution of alpha and entropy values shows a cluster of leaves in the near-range area that produces a clear surface-like response. This response may be originated by leaves which are oriented normally to the line of sight, thus pointing to the antenna. The other parts of the image show a dipole-like behavior that may be due to the scattering produced by the cylindrical branches on which no leaves are pointing to the antennas. For this target the entropy is very low everywhere, as can be expected for a sample with its physical characteristics, i.e. it is a plant with big and regular components (leaves and branches) in contrast with the fir tree. Additional results were obtained for a cluster of small fir trees in healthy and damaged conditions, and for a sample of rice crop.

Once all vegetation samples have been carefully examined and characterized with fully polarimetric measurements and an ensuing target decomposition study, two inversion methods have been presented and tested.

The first is a novel retrieval algorithm that shows the potentials of radar polarimetry. This method enables the extraction of the particle shape and orientation distribution (average value and width of the distribution) from radar backscatter data. In its development, the target is assumed to be homogeneous and composed of electrically small particles. It has been shown how an eigenvalue analysis of the average backscatter coherency matrix may be employed with a simple model of particle scattering to understand the physical basis of the radar observables in a clearer way than is obtained by looking at simple polarimetric ratios

such a HH/VV. In particular, it has been demonstrated that the $H-\alpha$ plane is a useful representation of the average properties of the data. On this plane, effects due to particle shape and orientation distributions are well separated, and hence one can employ this method in a robust inversion procedure to estimate the physical parameters of a cloud from experimental radar data.

This technique has been tested with samples of different morphologies to illustrate its discrimination capabilities. For example, the physical components of a fir tree and a ficus plant have been extracted from the data. In this thesis this inversion technique has been tested only with frequency domain data (i.e. purely scatterometric). As a result, the estimation of the particle shape behaves better than that of the angular distribution of orientations, because the latter is influenced by the randomness of the target and an extensive azimuth averaging. In the future, an extension to time domain data and high resolution images is planned. It is expected to recover the shape and orientation of the components that are present in every part of the vegetation structure, and hence the assumption of a homogeneous volume is no longer necessary.

The results show a wavelength scale dependence of the shape and distribution of scatterers which reflects the complex volume scattering nature of such targets. These results indicate that such an inverse model can be usefully employed for the study of canopy scattering effects and for the inversion of radar data for vegetation and forestry classification problems. Although such shape and angle distributions are built into forward scattering models like vector radiative transfer [98], this is the first attempt known to the author to extract these parameters from radar data in an inversion process.

It is important to emphasize that the estimation results provided by this method are quite satisfactory despite the simplicity of the particle model and the inversion procedure. These encouraging results enable us to predict that an improvement of the method could be affordable. The logical extension of the algorithm is the inclusion of more sophisticated particle models which would allow the use of larger and complex particles. Moreover, it would be important to study the effect of multiple scattering and interaction between particles.

The second retrieval technique that has been examined in this thesis is the estimation of height of vegetation covers by polarimetric SAR interferometry. This method consists in combining interferometry and polarimetry in order to generate simultaneous interferograms of the same scene. Each interferogram is associated with a different scattering mechanism. In this way, since vegetation usually exhibits dissimilar scattering properties at different height levels (as previously demonstrated with decomposition results), the relative difference between those interferograms has a direct relation with the height of the vegetation cover present in the scene. This method has been validated for different frequencies and samples, yielding important conclusions about its applicability in real scenarios.

Some ideas can be anticipated about the use of this technique in real air- or space-borne systems. If the application is control or monitoring of crops (e.g. corn and rice) the use of C band is preferred to lower bands because it is important to measure a non negligible return from the above-ground volume. At L band the backscatter is strongly dominated by

the stem-ground interaction in such a way that the other scatter components become masked. Moreover, since agricultural covers presents moderate heights (not more than 4 m), C band provides better sensitivity to small height changes than L band for the same baseline. A crucial point for the feasibility of this technique is the wave penetration into the vegetation volume. In general, for agricultural layers C band provides enough penetration depth to reach the ground. On the other hand, on forest applications, where the vegetation volume is usually larger (some tens of meters) L band is better suited. This has been confirmed by some recent outdoor experiments [167, 171]. The bandwidth employed in the measurements is not a constraint, since the resolution in slant range must be poorer than the vegetation depth for enclosing the whole vegetation cover within a vertical resolution cell. If a large bandwidth is available, it can be used in a multi-look processing for improving the estimates accuracy.

An issue that has not been studied at EMSL is the spatial averaging needed in real situations. This aspect must be considered when working on natural scenarios and using air- or spaceborne systems. Some indications about the complete procedure that should be employed in those cases are presented in [171]. In general, a multi-look scheme is useful to reduce the variance of the estimates of the individual interferograms, and consequently of the interferogram difference.

With regard to the incidence angle of the InSAR system, no special requirements are necessary, since the ideal angle is around $45°$. This incidence is also recommended in any interferometric system for balancing the probabilities of lay-over and shadow, and to move the so-called *blind angle region* towards less critical terrain slopes [161]. As far as our application is concerned, this angle is optimum because it allows a balance between the backscatter returns from the ground-trunk (or ground-stem) interaction and from the above-ground volume. Steeper angles would produce a larger direct response from the ground, while gentler ones yield longer paths of the waves into the vegetation volume (thus making difficult the penetration down to the ground) and a larger direct response from the above-ground volume than the ground-trunk interaction. The baseline, which is another important parameter in InSAR, can be selected or designed on the same basis as conventional (non polarimetric) interferometry.

It is implicit in these comments that an InSAR system capable of providing useful data to this retrieval algorithm should be fully polarimetric. From the examples presented in the previous section, the best combinations of polarizations for estimating the height are HH+VV and HH-VV, which are physically associated with the direct backscatter from the above-ground particles and the ground-trunk interaction, respectively. A simpler InSAR system might be designed without fully polarimetric properties, but providing only the two copolar responses (HH and VV), because the crosspolar return is not used in that case. Anyway, if the system is designed as a multipurpose device, the entire scattering matrix should be measured in order to perform an interferometric coherence optimization, which provides a remarkable improvement in DEM generation. The calibration procedure for a polarimetric-interferometric airborne system has been deeply detailed in [170, 182]. These references provide the main requirements of hardware and processing for this application as well.

Since vegetation is a target with large temporal decorrelation properties, a single-pass

interferometric system is preferred to a repeat-pass one. However, if for a specific application the temporal decorrelation is not extreme, the algorithm can be still applied with guarantees of success. The only price to be paid is a lower accuracy in the height estimates due to a lower coherence.

It is also very important to note that the application of polarimetric interferometry to vegetation height retrieval has the unique characteristic of being exempt of the problems associated with absolute phase measurements with respect to a reference. Since the retrieved height results from a relative difference between two simultaneous interferograms, the estimates are immune to errors caused by phase unwrapping [167]. The only condition is, of course, that the difference between the two phase centers associated with both scattering mechanisms has to be smaller than $2\pi$. This requirement is easily satisfied for any operating InSAR system.

Currently there is no operational spaceborne fully polarimetric interferometric SAR system. Only a few airborne systems, like E-SAR from DLR, have introduced this polarimetric capabilities. So far, the only fully polarimetric InSAR data available from a spaceborne platform correspond to two missions of the Shuttle Imaging Radar SIR-C/X-SAR conducted in 1994, on a repeat-pass mode, at L and C band. A new mission of the space shuttle, called Shuttle Radar Topographic Mission (SRTM), is about to be launched. This constitutes the first spaceborne single-pass/dual-antenna across-track interferometer to be operated, and reuses the capabilities at C and X band of previous missions. The interferometric data will not be fully polarimetric, but only HH and VV at C band. However they will be available in single-pass mode and will provide a good field to test polarimetric SAR interferometry for the retrieval of vegetation height. The lack of crosspolar data may not influence in the success of this technique because, as illustrated in this thesis, the choice of the combined channels HH+VV and HH–VV leads to excellent results. A review of other past, current and future interferometric SAR systems can be consulted in [161].

Some theoretical studies of the potentials of polarimetric SAR interferometry for retrieval of vegetation height have been carried out lately [177, 183]. The main conclusion of these analyses is that single-baseline polarimetric interferometry can be used to estimate the heights of oriented volumes and underlying topography, whereas if vegetation shows no preferred orientation (random oriented volume) polarimetry gives less information and two baselines should be employed. These papers emphasize the importance of the differential extinction coefficient between orthogonal polarizations, which was firstly introduced as a crucial parameter (and also quantified) in this thesis. These ideas agree totally with the results described in this thesis, since the best estimates were obtained for the maize (a vertically oriented volume) and the worst ones for the cluster of fir trees (a random oriented volume).

There is also an active line of research about modeling of vegetation covers for studying the behavior of polarimetric SAR interferometry with respect to the retrieval of biophysical parameters. The main characteristic of these models is that they must be coherent in order to provide an absolute phase, which is necessary in interferometry. Some ideas derived in this thesis should be incorporated in these models.

With regard to the generation of 3-D radar images at EMSL, a new and efficient algorithm has been formulated, implemented and successfully tested. This proposed algorithm is based on range migration techniques, and exhibits maximum efficiency when the synthetic aperture is planar. It is an extension of the 2-D range migration algorithm. The formulation has been justified by using the method of stationary phase. Implementation aspects including sampling criteria, resolutions and computational complexity have been assessed. In the planar case the method can be applied directly in the cartesian coordinate system, and can be implemented by using FFT codes and an 1-D Lagrange interpolator. Moreover, an extension of the 3-D RMA to the case of synthetic apertures with cylindrical and spherical shapes has been introduced. Data acquired on those non-planar geometries are accurately translated onto a planar aperture by using field translations in a way similar to antenna measurement techniques. Once this translation is accomplished, the original 3-D RMA can be applied. The computational efficiency of the method is maintained, since the translation only entails a moderate increase of the total computation time. This procedure corrects exactly the wavefront curvature effect. As a result, it constitutes an ideal approach for producing images in the EMSL, in which a near-field situation is usually present. Numerical simulations have demonstrated the efficiency of the algorithm. The quality of the focused images is also very high, and dynamic ranges better than 80 dB have been reached in numerical simulations. The algorithm has been also validated experimentally using a vehicle-mounted SAR system and the EMSL. All results have manifested the high performance of the algorithm when it is applied to experimental data sets.

A complementary extension of the 3-D RMA is currently being investigated. It consists in incorporating a superresolution code (e.g. MUSIC, linear prediction, etc.) after the Stolt interpolation, instead of the final inverse Fourier transform. This substitution should fit well because the data are uniformly spaced in the Fourier domain at that stage, which is the starting point of those superresolution algorithms.

In summary, the main goal of this thesis has been achieved, i.e. a demonstration of the remarkable contribution that polarimetry can offer in quantitative remote sensing of vegetation. These methods have been successfully tested in laboratory conditions. The methods presented here are expected to be applied in real scenarios under natural conditions. The results of this thesis should lead to a better deployment of the information provided by radar polarimetry in remote sensing. Finally, note that the work conducted in this thesis has produced a great interest in the scientific community. This interest is endorsed by the publication of this research in several papers in international journals and the discussion of its results in various conferences. A list with all publications is shown in the next pages.

# Publications

## Papers in Journals

[1] J. M. Lopez-Sanchez, J. Fortuny, "Polarimetric studies of different types of vegetation," *European Microwave Signature Laboratory Newsletter.*, no. 13, pp. 8–9, Aug. 1998.

[2] J. M. Lopez-Sanchez, H. Esteban-Gonzalez, M. Baquero-Escudero, and J. Fortuny, "An electromagnetic scattering model for multiple tree trunks above a tilted rough ground plane," *IEEE Trans. Geosci. Remote Sensing*, vol. 37, pp. 659–667, Mar. 1999.

[3] S. R. Cloude, J. Fortuny, J. M. Lopez-Sanchez, and A. J. Sieber, "Wide-band polarimetric radar inversion studies for vegetation layers," *IEEE Trans. Geosci. Remote Sensing*, vol. 37, pp. 2430–2441, Sept. 1999.

[4] J. M. Lopez-Sanchez, J. Fortuny, S. R. Cloude, and A. J. Sieber, "Indoor polarimetric radar measurements on vegetation samples at L, S, C and X band," *J. Electromag. Waves Appl.* Accepted for publication in April 1999. Scheduled date not avalilable.

[5] J. M. Lopez-Sanchez and J. Fortuny, "3-D radar imaging using range migration techniques," *IEEE Trans. Antennas Propagat.* Submitted for publication in January 1999.

[6] L. Sagués, J. M. Lopez-Sanchez, J. Fortuny, X. Fàbregas, A. Broquetas, and A. J. Sieber, "Indoor experiments on polarimetric SAR interferometry," *IEEE Trans. Geosci. Remote Sensing*. Submitted for publication in April 1999.

## Papers in Conferences

[1] G. Nesti, R. Estevan de Quesada, J. M. Lopez-Sanchez, and A. J. Sieber, "Implementation of the integral equation model for rough surfaces with generic isotropic autocorrelation functions," in *Proceedings of the IEEE International Geoscience and Remote Sensing Symposium (IGARSS)*, vol. 3, Singapore, pp. 1361–1364, Aug. 1997.

[2] H. Esteban, J. M. Lopez-Sanchez, M. Baquero, J. Fortuny, G. Nesti, and A. J. Sieber, "An electromagnetic scattering model for tree trunks over a tilted rough ground plane," in *Proceedings of the IEEE International Geoscience and Remote Sensing Symposium (IGARSS)*, vol. 4, Singapore, pp. 1871–1873, Aug. 1997.

[3] J. M. Lopez-Sanchez, J. Fortuny, and A. J. Sieber, "Experimental validation of an entropy-based classification scheme using a wide-band polarimetric radar," in *Proceedings of the IEEE International Geoscience and Remote Sensing Symposium (IGARSS)*, vol. 5, Seattle, WA, USA, pp. 2381–2383, July 1998.

[4] J. M. Lopez-Sanchez, J. Fortuny, A. J. Sieber, and K. Sarabandi, "Validation of the backscattered frequency correlation function for the inversion of biophysical parameters from natural targets," in *Proceedings of the IEEE International Geoscience and Remote Sensing Symposium (IGARSS)*, vol. 5, Seattle, WA, USA, pp. 2390–2392, July 1998.

[5] J. M. Lopez-Sanchez, J. Fortuny, A. J. Sieber, and S. R. Cloude, "Experimental validation of an entropy-based classification scheme using a wide-band polarimetric radar," in *Proceedings of the PIERS - Workshop on Advances in Radar Methods*, Baveno, Italy, pp. 208–210, July 1998.

[6] J. M. Lopez-Sanchez, J. Fortuny, and A. J. Sieber, "3-D Radar imaging using range migration techniques," in *Proceedings of the 20th Annual Meeting & Symposium, Antenna Measurement Techniques Association (AMTA'98)*, Montreal, Canada, pp. 30–35, Oct. 1998.

[7] J. Fortuny, J. M. Lopez-Sanchez, G. Nesti, and A. J. Sieber, "Inversion of biophysical parameters from natural targets using a wide-band polarimetric system," in *Proceedings of the 2nd International Symposium on Retrieval of Bio- and Geo-physical Parameters from SAR Data for Land Applications*, Noordwijk, The Netherlands, pp. 61–64, ESTEC, Oct. 1998.

[8] J. M. Lopez-Sanchez, L. Sagués, J. Fortuny, X. Fàbregas, A. Broquetas, A. J. Sieber, and S. R. Cloude, "Laboratory experiments of polarimetric radar interferometry: DEM generation and vegetation height estimation," in *Proceedings of the IEEE International Geoscience and Remote Sensing Symposium (IGARSS)*, vol. 4, Hamburg, Germany, pp. 2206–2208, June 1999.

[9] J. Fortuny, J. M. Lopez-Sanchez, G. Nesti, and A. J. Sieber, "Experimental validation of polarimetric interferometry in the EMSL," in *Proceedings of the XXVIth General Assembly of the International Union of Radio Science (URSI)*, Toronto, Canada, pp. 881, Aug. 1999.

[10] J. Fortuny, J. M. Lopez-Sanchez, L. Sagués, S. R. Cloude, K. P. Papathanassiou, and W. Keydel, "Wide band polarimetric interferometry for DEM improvement and retrieval of vegetation height," in *Proceedings of the 29th European Microwave Conference, (EMC'99)*, Munich, Germany, vol. 3, pp. 315–318, Oct. 1999.

# Abbreviations and Band Designations

## Abbreviations

| | |
|---|---|
| BSA | Backward Scattering Alignment |
| CSA | Chirp Scaling Algorithm |
| CW | Continuous Wave |
| DEM | Digital Elevation Model |
| DFT | Discrete Fourier Transform |
| FFT | Fast Fourier Transform |
| FReD | Frequency domain Replication and Downsampling |
| FSA | Forward Scattering Alignment |
| FT | Fourier Transfrom |
| IFFT | Inverse Fast Fourier Transform |
| InSAR | SAR Interferometry |
| ISAR | Inverse SAR |
| MSP | Method of Stationary Phase |
| PFA | Polar Format Algorithm |
| PDF | Probability Density Function |
| RCS | Radar Cross Section |
| RFI | Radio Frequency Interference |
| RMA | Range Migration Algorithm |
| SAR | Synthetic Aperture Radar |
| TD | Target Decomposition |

**Table A.1.** Band Designations

| Band Designation | Frequency (GHz) | Wavelength (cm) |
|:---:|:---:|:---:|
| P | 0.225 – 0.39 | 77.9 – 133.3 |
| L | 0.39 – 1.55 | 19.3 – 77.9 |
| S | 1.55 – 4.20 | 7.1 – 19.3 |
| C | 4.20 – 5.75 | 5.2 – 7.1 |
| X | 5.75 – 10.9 | 2.7 – 5.2 |
| K | 10.9 – 36.0 | 0.83 – 2.7 |
| Q | 36.0 – 46.0 | 0.65 – 0.83 |
| V | 46.0 – 56.0 | 0.53 – 0.65 |
| W | 56.0 – 100.0 | 0.30 – 0.53 |

# Scattering by a Random Cloud of Ellipsoids

CHAPTER 5 was devoted to explain a method for retrieving the shape and the orientation distribution of elementary particles that constitute a random medium. This random medium is a quite usual model for vegetation volumes. The inversion method was based on a scattering model for the constituent particles, which are regarded as ellipsoids of small electrical size. Although the scattering theory for this type of particles can be found in [11], it is important to derive and present the formulation for the polarimetric analysis used in this thesis, i.e. on the basis of the coherency matrix. Moreover, a notation coherent with the rest of the text is also necessary to avoid misleading formulas. Therefore, for the sake of completeness and clarity, this appendix illustrates the details of the scattering model for a random cloud of ellipsoids and presents the particular case employed in Chapter 5.

The material is organized as follows. Section B.1 gives the explicit expressions of the scattering matrix of one individual particle. The entries of the scattering matrix are functions of the shape ratio of the particle and its orientation in the global reference system. An averaging over the distributions of orientation angles yields the coherency matrices corresponding to a set of particles, as is described in Section B.2. In that section, the loci of $H$ and $\overline{\alpha}$ are studied as a function of the particle shape ratio and the width of the orientation distribution. That study constitutes the foundations of the inversion algorithm presented in Chapter 5. However, it will be shown that the loci of $H$ and $\overline{\alpha}$ also depend on the specific definition of the orientation angles, in such a way that if the particles are initially rotated, the final loci are different. Therefore, a new formulation for a rotated case is presented in Section B.3. In fact, this final formulation was that actually applied in the development of the inversion technique, as will be justified in the text.

# B.1    Scattering Matrix for One Particle

In the following it is assumed that the particle analyzed in this section is small compared to the wavelength, both outside and inside the particle. The scattering by such a small particle can be studied in terms of a concept known as *polarizability $\rho$*. The simplification introduced by the small size is that the particle may be considered to be placed in a homogeneous incident field $\mathbf{E}^i$. This incident field creates an induced dipole moment for which the following electrostatic formula is applicable:

$$\mathbf{p} = \rho \mathbf{E}^i. \tag{B.1}$$

In general, $\rho$ is a tensor, so the directions of $\mathbf{p}$ and $\mathbf{E}^i$ coincide only if the field is applied in one of the three main directions of the particle. Let the orientation of the particle in space be characterized by three perpendicular unit vectors $\mathbf{n}_1$, $\mathbf{n}_2$ and $\mathbf{n}_3$ (see Fig. B.1). The particle is then characterized by the three tensor components $\rho_1$, $\rho_2$ and $\rho_3$, also called *polarizabilities*, in such a way that any incident field

$$\mathbf{E}^i = E_1 \mathbf{n}_1 + E_2 \mathbf{n}_2 + E_3 \mathbf{n}_3 \tag{B.2}$$

gives the dipole moment:

$$\mathbf{p} = \rho_1 E_1 \mathbf{n}_1 + \rho_2 E_2 \mathbf{n}_2 + \rho_3 E_3 \mathbf{n}_3. \tag{B.3}$$
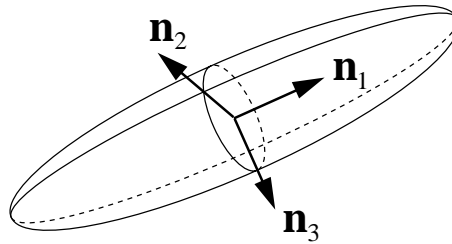


**Fig. B.1.** Generic particle oriented according to its three unit vectors

In the case we are analyzing, the incident field is a time-harmonic plane wave with an arbitrary polarization, and the dipole (which now is an oscillating dipole) radiates in all directions. This type of scattering is called *Rayleigh scattering*. For a point at a distance $r \gg \lambda$ from the particle and in a direction that makes an angle $\gamma$ with $\mathbf{p}$, the magnitude of the scattered field is proportional to $|\mathbf{p}| \sin \gamma$. The unit vector of the scattered field is directed as the component of $\mathbf{p}$ normal to the vector that joins the particle with the field point[1].

Due to its flexibility for modeling many possible particles shapes by only working with the axes lengths (spheres, needles, disks, etc.), an ellipsoid was the particle shape cho-

---

[1]The basic physics underlying this formulation are explained elsewhere [11, Chapter 6]
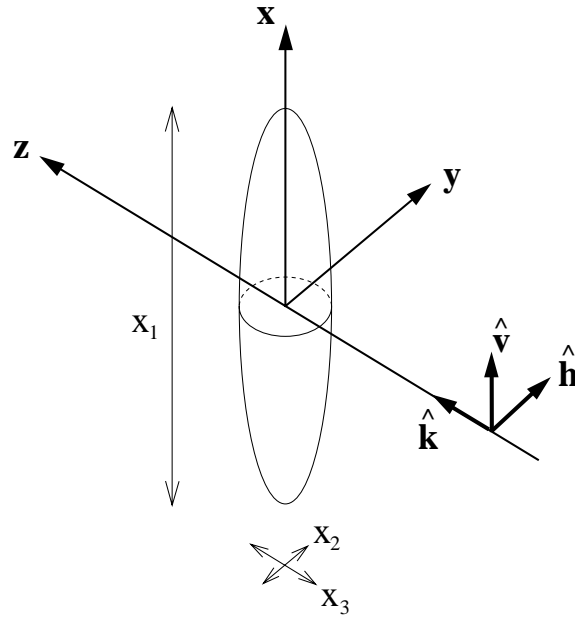
**Fig. B.2.** Scattering geometry by an ellipsoid in the canonical (non-rotated) position

sen for the polarimetric inversion method presented in Chapter 5. For an ellipsoid, the polarizabilities have the expression:

$$\rho_i = \frac{V}{4\pi \left( L_i + \frac{1}{\epsilon_r - 1} \right)} \qquad i = 1, 2, 3, \tag{B.4}$$

where $V$ is the total volume of the ellipsoid, $\epsilon_r$ is the relative dielectric constant of the particle, and $L_i$ are three factors depending on the ratios of the axes.

The values of $L_i$ can be accurately described by the following relationships:

$$L_1 + L_2 + L_3 = 1 \tag{B.5}$$

$$L_1 : L_2 : L_3 = \frac{1}{x_1} : \frac{1}{x_2} : \frac{1}{x_3}, \tag{B.6}$$

where $x_i$ are the lengths of the three main axes of the ellipsoid. Note that (B.5) always holds, and (B.6) is an approximate rule with enough accuracy for our purposes [11, pp. 70–73].

In order to compute the entries of the scattering matrix for an arbitrary ellipsoid, let us assume the geometry depicted in Fig. B.2. For simplicity the incidence direction has been selected as the positive **z** axis, and only the backscattering case will be considered in the following. Fig. B.2 shows the ellipsoid in the canonical position, i.e. with its three axes ($\mathbf{n}_1$, $\mathbf{n}_2$ and $\mathbf{n}_3$) parallel to the cartesian unit vectors $\hat{\mathbf{x}}$, $\hat{\mathbf{y}}$ and $\hat{\mathbf{z}}$, respectively.

The induced dipole moment presents the following three components:

$$p_x = E_v^i P_{11} + E_h^i P_{12} \tag{B.7}$$

$$p_y = E_v^i P_{21} + E_h^i P_{22} \tag{B.8}$$

$$p_z = E_v^i P_{31} + E_h^i P_{32}, \tag{B.9}$$

where the incident field is decomposed into vertical and horizontal components.

The constants $P_{ik}$ stand for

$$P_{ik} = P_{ki} = c_{i1}c_{k1}\rho_1 + c_{i2}c_{k2}\rho_2 + c_{i3}c_{k3}\rho_3, \tag{B.10}$$

where $c_{ij}$ are the coefficients of the following linear relations:

$$\mathbf{x} = c_{11}\mathbf{n}_1 + c_{12}\mathbf{n}_2 + c_{13}\mathbf{n}_3 \tag{B.11}$$

$$\mathbf{y} = c_{21}\mathbf{n}_1 + c_{22}\mathbf{n}_2 + c_{23}\mathbf{n}_3 \tag{B.12}$$

$$\mathbf{z} = c_{31}\mathbf{n}_1 + c_{32}\mathbf{n}_2 + c_{33}\mathbf{n}_3. \tag{B.13}$$

These linear combinations provide the relationship between the particle orientation and the coordinate system. The standard procedure for obtaining an explicit formula for the coefficients $c_{ij}$ is the application of the Euler angles. The displacement of a body due to a rotation about a fixed point can be modeled by performing three Euler rotations about two of three mutually perpendicular axes fixed in the body. By assuming a right-handed frame of axes, the rotations are illustrated in Fig. B.3, where the original axes are named $(x, y, z)$. The typical rotations about Euler angles are defined in the following order:

1. Rotation of $\phi$ about $z \rightarrow (x', y', z')$, with $0 \leqslant \phi < 2\pi$

2. Rotation of $\tau$ about $y' \rightarrow (x'', y'', z'')$, with $0 \leqslant \tau < \pi$

3. Rotation of $\theta$ about $z'' \rightarrow (x''', y''', z''')$, with $0 \leqslant \theta < 2\pi$

In this thesis, these three angles are called: spin angle $\phi$, tilt angle $\tau$, and canting or rotation angle $\theta$. For each rotation, the original axes can be expressed in terms of the new axes by using a rotation matrix. The expression of the three rotation matrices is[2]:

$$[C_\phi] = \begin{bmatrix} \cos\phi & -\sin\phi & 0 \\ \sin\phi & \cos\phi & 0 \\ 0 & 0 & 1 \end{bmatrix} \tag{B.14}$$

$$[C_\tau] = \begin{bmatrix} \cos\tau & 0 & \sin\tau \\ 0 & 1 & 0 \\ -\sin\tau & 0 & \cos\tau \end{bmatrix} \tag{B.15}$$

$$[C_\theta] = \begin{bmatrix} \cos\theta & -\sin\theta & 0 \\ \sin\theta & \cos\theta & 0 \\ 0 & 0 & 1 \end{bmatrix}, \tag{B.16}$$

---

[2]Note that if one wants to express the new axes in terms of the original axes all the matrices should be transposed
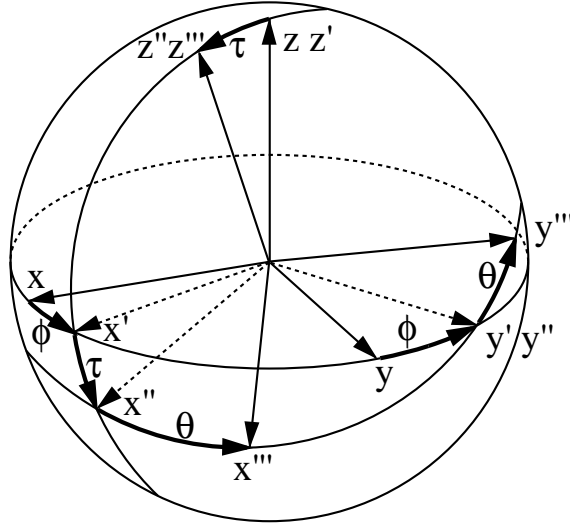
**Fig. B.3.** Illustration of the Euler angles and the three rotations

and the chain of rotations is denoted by a matrix product:

$$[C] = [C_\theta][C_\tau][C_\phi], \tag{B.17}$$

where the order has been reversed in order to apply the rotation about the canting angle $\theta$ in the last step as required in the model used in Chapter 5. The entries of $[C]$ are directly the $c_{ij}$ coefficients needed above.

As was explained before, the backscattered field can be obtained as the component of $\mathbf{p}$ that is perpendicular to the propagation direction. By expressing the measured field in terms of the vertical and horizontal polarizations of the BSA convention, it yields:

$$E_v^s = p_x \quad \text{and} \quad E_h^s = p_y. \tag{B.18}$$

Finally, by substituting (B.7)-(B.9) into (B.18), the scattering matrix of an ellipsoid in the backscattering direction can be expressed as:

$$[S] = \begin{bmatrix} P_{11} & P_{12} \\ P_{21} & P_{22} \end{bmatrix}, \tag{B.19}$$

where the elements $P_{ij}$ were defined in (B.10). To turn back to the notation used throughout the thesis, the scattering matrix of an ellipsoid, oriented according to the Euler angles, can be written in the following form:

$$[S] = \begin{bmatrix} a & c \\ c & d \end{bmatrix}, \tag{B.20}$$

where

$$
\begin{aligned}
a =\,&\rho_1(\cos\theta\cos\tau\cos\phi - \sin\theta\sin\phi)^2 \\
&+ \rho_2(\sin\theta\cos\phi + \cos\theta\cos\tau\sin\phi)^2 \\
&+ \rho_3\cos^2\theta\sin^2\tau
\end{aligned}
\tag{B.21}
$$

$$
\begin{aligned}
d =\,&\rho_1(\sin\theta\cos\tau\cos\phi + \cos\theta\sin\phi)^2 \\
&+ \rho_2(\cos\theta\cos\phi - \sin\theta\cos\tau\sin\phi)^2 \\
&+ \rho_3\sin^2\theta\sin^2\tau
\end{aligned}
\tag{B.22}
$$

$$
\begin{aligned}
c =\,&\rho_1(\sin\theta\cos\tau\cos\phi + \cos\theta\sin\phi)(\cos\theta\cos\tau\cos\phi - \sin\theta\sin\phi) \\
&- \rho_2(\sin\theta\cos\phi + \cos\theta\cos\tau\sin\phi)(\cos\theta\cos\phi - \sin\theta\cos\tau\sin\phi) \\
&+ \rho_3\cos\theta\sin\theta\sin^2\tau.
\end{aligned}
\tag{B.23}
$$

## B.1.1   The Spheroid Case

In order to reduce the number of parameters or degrees of freedom of the model, the case of an spheroid is analyzed in the rest of the text. For such an spheroid there are two equal axes that, for convenience, are selected $x_2 = x_3$, so the rotation about the spin Euler angle $\phi$ is not longer meaningful. Therefore it is possible simplifying the elements of the scattering matrix defined in (B.21)-(B.23) by taking $\phi = 0$. The resulting scattering amplitudes are:

$$
a = \rho_1\cos^2\theta\cos^2\tau + \rho_2\sin^2\theta + \rho_3\cos^2\theta\sin^2\tau
\tag{B.24}
$$

$$
d = \rho_1\sin^2\theta\cos^2\tau + \rho_2\cos^2\theta + \rho_3\sin^2\theta\sin^2\tau
\tag{B.25}
$$

$$
c = (\rho_1\cos^2\tau - \rho_2 + \rho_3\sin^2\tau)\cos\theta\sin\theta,
\tag{B.26}
$$

where a further simplification ($\rho_2 = \rho_3$) has not been included.

Moreover, of particular importance is the *anisotropy* $A$ defined as the ratio of eigenvalues of $[S]$ when $\tau = 0$. In that case, the scattering amplitudes are:

$$
a = \rho_1\cos^2\theta + \rho_2\sin^2\theta
\tag{B.27}
$$

$$
d = \rho_1\sin^2\theta + \rho_2\cos^2\theta
\tag{B.28}
$$

$$
c = \rho_1\cos\theta\sin\theta - \rho_2\cos\theta\sin\theta,
\tag{B.29}
$$

and the eigenvalues for this particular case are $\rho_2$ and $\rho_1$. Then, their ratio yields:

$$
A = \frac{\rho_2}{\rho_1} = \frac{L_1(\epsilon_r - 1) + 1}{L_2(\epsilon_r - 1) + 1}.
\tag{B.30}
$$

Since we have assumed spheroidal shapes ($x_2 = x_3$) the anisotropy $A$ can be expressed in terms of the particle shape ratio $m = x_2/x_1$. In the spheroidal case, the relations between $L_1$ and $L_2$, firstly shown in (B.5)-(B.6), yield:

$$
L_1 + 2L_2 = 1 \quad \text{and} \quad \frac{L_1}{L_2} = \frac{x_2}{x_1} = m.
\tag{B.31}
$$

Both can be substituted into (B.30), and the resulting expression is:

$$A = \frac{m\epsilon_r + 2}{m + \epsilon_r + 1},$$ (B.32)

where $m$ is defined in the range $0 < m < \infty$ and corresponds to:

$$\begin{cases} m < 1 & \text{Prolate spheroids} \\ m > 1 & \text{Oblate spheroids} \end{cases}$$ (B.33)

As was already explained in Chapter 5, the constituent particles of a vegetation target usually exhibit a high dielectric constant at microwave frequencies. As a result (B.32) can be reduced to $A \simeq m$ and, consequently, $A$ can be regarded as the particle shape ratio. This will be used in next section to simplify the mathematical derivations.

## B.2 Coherency Matrices for a Cloud of Particles

This section is dedicated to the analysis of the scattering by a cloud of ellipsoids by using target decomposition techniques. The analysis is specifically performed by plotting the pairs of entropy $H$ and dominant scattering mechanism $\overline{\alpha}$ on the $H - \alpha$ plane. This study concentrates on two main parameters of the cloud of particles: the shape of the particles and the orientation distribution. It is assumed that only single scattering is significant, and that each particle in the cloud acts independently of its neighbors. We also assume that the particles in the cloud are identical in size but have a distribution of orientation angles around zero. Therefore, the ensemble averaging of the coherency matrix is calculated by integration over the angular spans of interest.

The expression of the coherency matrix, in terms of the scattering amplitudes, is:

$$\langle [T] \rangle = \frac{1}{2} \langle \begin{bmatrix} (a+d)^2 & a^2 - d^2 & 2(a+d)c \\ a^2 - d^2 & (a-d)^2 & 2(a-d)c \\ 2(a+d)c & 2(a-d)c & 4c^2 \end{bmatrix} \rangle,$$ (B.34)

where, for the sake of simplicity, the polarizabilities are considered to be real. Note that the results are easily generalized to the complex case.

Let $t_{ij}(\theta, \tau, \phi)$ be the elements of the coherency matrix corresponding to a single particle oriented according to the three angles $(\theta, \tau, \phi)$. Then, the resulting element of the average coherency matrix, $\langle t_{ij} \rangle$, is computed by integrating over the angular ranges in which each angle is defined. This can be expressed as:

$$\langle t_{ij} \rangle = \int_\theta \int_\tau \int_\phi t_{ij}(\theta, \tau, \phi) \sin\tau \, d\phi \, d\tau \, d\theta,$$ (B.35)

where the factor $\sin \tau$ comes from the size of the differential on the unit sphere (or differential solid angle).

Some cases with different degrees of randomness are presented in the next sections in order to illustrate the behavior of the $H - \overline{\alpha}$ loci as a function of the parameters of interest in the inversion algorithm.

Furthermore, since we are interested in the shape of the particles, and not in their absolute size, the polarizabilities have been normalized. As a result, the following formulation is derived by taking $\rho_1 = 1$ and $\rho_2 = \rho_3 = A$. This expression comes from the definition of the particle anisotropy $A$ in (B.30).

## B.2.1   A totally random cloud of ellipsoids

The first situation to be analyzed is a totally random cloud of ellipsoids. This case was also studied in [11] by using the Mueller matrix. By applying the relations between the entries of the Mueller matrix $\langle [M] \rangle$ and the coherency matrix $\langle [T] \rangle$, described in Chapter 3, it is possible to demonstrate that the results presented in the following are in total agreement with the derivations shown in [11] for a random cloud of ellipsoids.

The averaging is computed over the whole range of every Euler angle, thus performing the following integration:

$$\langle t_{ij} \rangle = \frac{1}{8\pi^2} \int_0^{2\pi} \int_0^{\pi} \int_0^{2\pi} t_{ij}(\theta, \tau, \phi) \, \sin \tau \, d\phi \, d\tau \, d\theta, \tag{B.36}$$

where the normalization factor has been introduced for convenience.

The resulting coherency matrix is diagonal:

$$\langle [T] \rangle = \begin{bmatrix} t_{11} & 0 & 0 \\ 0 & t_{22} & 0 \\ 0 & 0 & t_{33} \end{bmatrix} \tag{B.37}$$

and the normalized entries are:

$$t_{11} = (2 + 6A + 7A^2) \tag{B.38}$$
$$t_{22} = (A - 1)^2 \tag{B.39}$$
$$t_{33} = (A - 1)^2. \tag{B.40}$$

The values of $H$ and $\overline{\alpha}$ as a function of $A$ are plotted in Fig. B.4. As might be expected from the full randomness of the cloud, all the points corresponding to this coherency matrix lie along the border of the feasible region on the $H - \alpha$ plane. For spherical particles, with $A = 1$ ($\log_{10} A = 0$), the orientation does not change their aspect, so the entropy is always zero and the dominant scattering mechanism $\overline{\alpha} = 0$ corresponds to scattering from surfaces or spheres. The limit cases when $A \to 0$ (dipoles or needles) and $A \to \infty$ (disks) yield the following extreme values:
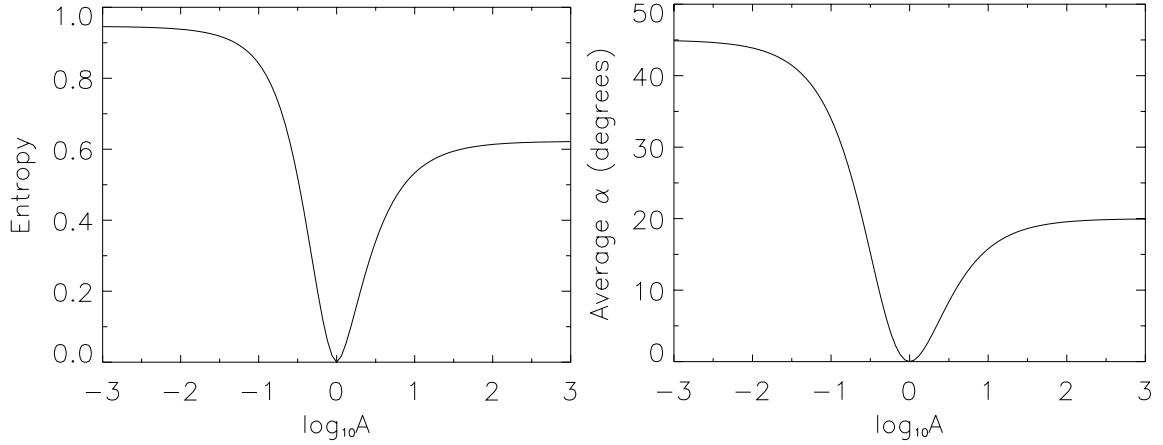
**Fig. B.4.** $H$ and $\overline{\alpha}$ plots as a function of the particle anisotropy $A$ for a fully random cloud of particles

$$
\begin{array}{llll}
\text{Prolate} & A \to 0 & \overline{\alpha} \to 45° & H \to 0.95 \\
\text{Oblate} & A \to \infty & \overline{\alpha} \to 20° & H \to 0.62
\end{array}
$$

The inversion method proposed in this thesis has profited from the different absolute maxima of $H$ and $\overline{\alpha}$ for prolate and oblate cases, thus yielding unambiguous the ranges $0.62 < H < 0.95$ or $20° < \overline{\alpha} < 45°$.

## B.2.2 Random cloud in $\tau$ and $\phi$. Finite span in $\theta$

A second important case consists of a cloud of ellipsoids with fully random distributions over $\tau$ and $\phi$, but with a distribution over a finite span in $\theta$. The distribution in $\theta$ is chosen to be uniform and ranging from $-\Theta$ to $\Theta$.

Now the integrals are:

$$
\langle t_{ij} \rangle = \frac{1}{4\pi} \frac{1}{2\Theta} \int_{\theta=-\Theta}^{\theta=\Theta} \int_0^{\pi} \int_0^{2\pi} t_{ij}(\theta, \tau, \phi) \, \sin\tau \, d\phi \, d\tau \, d\theta, \tag{B.41}
$$

and the resulting coherency matrix is:

$$
\langle [T] \rangle = \begin{bmatrix} t_{11} & t_{12} & 0 \\ t_{12} & t_{22} & 0 \\ 0 & 0 & t_{33} \end{bmatrix}, \tag{B.42}
$$

Prolate: $0 < A < 1$                    Oblate: $1 < A < \infty$
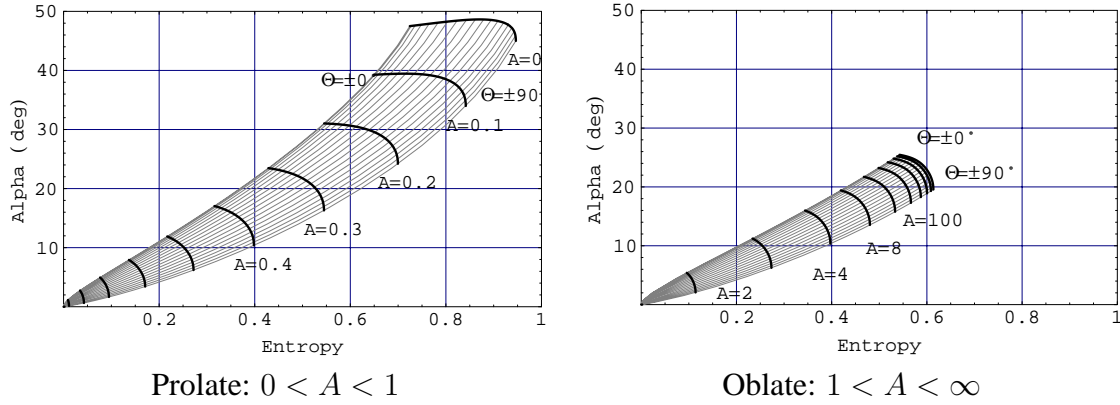
**Fig. B.5.** $H - \overline{\alpha}$ plots for a cloud with a finite span in $\theta$: $0 < \Theta < \pi/2$, and totally random in $\tau$ and $\phi$

where

$$t_{11} = \frac{2}{15}(2 + 6A + 7A^2) \tag{B.43}$$

$$t_{12} = \frac{(11A^2 - 2A - 9)\sin 2\Theta}{120\Theta} \tag{B.44}$$

$$t_{22} = \frac{(A-1)^2(32\Theta + 3\sin 4\Theta)}{240\Theta} \tag{B.45}$$

$$t_{33} = \frac{(A-1)^2(32\Theta - 3\sin 4\Theta)}{240\Theta}. \tag{B.46}$$

From this coherency matrix one can compute the plots for prolate and oblate cases shown in Fig. B.5. These are parametric curves with two varying parameters: $A$ and $\Theta$, and their principles were explained in Chapter 5. We can see that the loci are always close to the curve of maximum entropy for every scattering mechanism. In fact, even for no variation in $\theta$ ($\Theta = 0$) the loci do not exhibit zero entropy, neither for the prolate nor the oblate case. This is logical because the angle $\phi$ is defined in the same way as $\theta$, so a range of $2\pi$ in $\phi$ produce some amount of entropy. In the extreme situation of maximum $\Theta$, the loci of both entropy and dominant scattering mechanism coincide with the results of the previous case: full randomness about all angles.

Note that for natural targets with high entropy, as those modeled by this particle distribution, the spacing between lines in Fig. B.5 already predicts that the inversion of the shape parameter $A$ is better than the inversion of the width of distribution, since the isolines in the first case are more distant than in the latter.
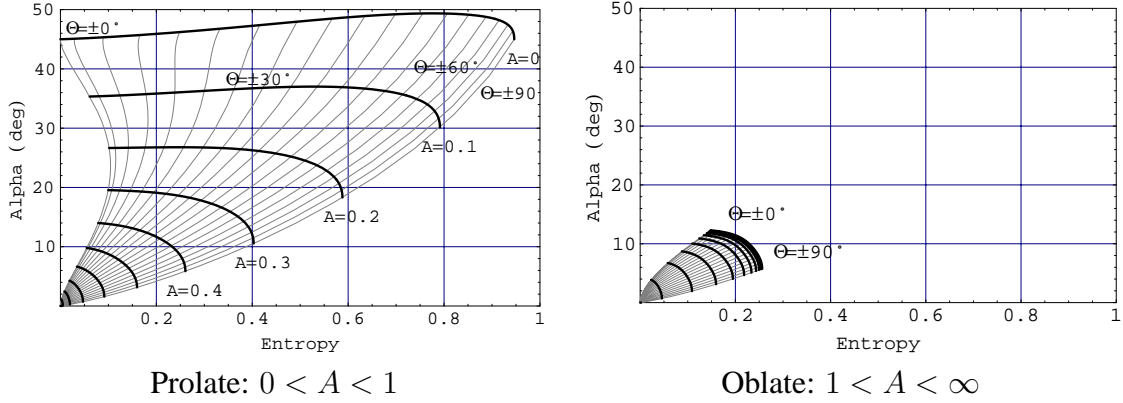
**Fig. B.6.** $H - \overline{\alpha}$ plots for a cloud random in $\tau$ with a finite span in $\theta$: $0 < \Theta < \pi/2$, and $\phi = 0$

## B.2.3 Constant $\phi = 0$, random cloud in $\tau$, and finite span in $\theta$

The third case consists in fixing $\phi = 0$, while keeping a full randomness in $\tau$ and a finite span in $\theta$. The elements of the scattering matrix when $\phi = 0$ were already presented in (B.24)-(B.26).

With this configuration, the integration for the coherency matrix is:

$$\langle t_{ij} \rangle = \frac{1}{2\Theta} \int_{\theta=-\Theta}^{\theta=\Theta} \int_0^\pi t_{ij}(\theta, \tau) \, \sin \tau \, d\tau \, d\theta, \tag{B.47}$$

resulting in the following non-zero terms:

$$t_{11} = \frac{(3 + 14A + 43A^2)}{15} \tag{B.48}$$

$$t_{12} = \frac{(3 + 4A - 7A^2) \sin 2\Theta}{30\Theta} \tag{B.49}$$

$$t_{22} = \frac{(A - 1)^2 (4\Theta + \sin 4\Theta)}{40\Theta} \tag{B.50}$$

$$t_{33} = \frac{(A - 1)^2 (4\Theta - \sin 4\Theta)}{40\Theta}. \tag{B.51}$$

The loci of $H$ and $\overline{\alpha}$ are plotted in Fig. B.6. Note that there exist considerable changes from the previous case. For example, the oblate case does not reach the maximum entropy of 0.62 as before. This lower entropy is caused by the aspect of the particles from the antenna position. Due to the fixed $\phi = 0$, the effect of the tilt angle $\tau$ is to rotate directly the particle from its initial position. When $\phi \neq 0$ the particle was already rotated on the plane normal to the line of sight, thus introducing more randomness in the scattering process. Moreover, the weighting function $\sin \tau$ in the integration penalizes the positions where $\tau$ is close to $0°$

and $180°$ (for which the particle is like a dipole as seen from the radar), whereas gives more importance to positions close to $\tau = 90°$ (for which it is like a sphere). These ideas are described in a graphical way in Fig. B.7.



Particle oriented at $\tau = 0°$     Particle oriented at $\tau = 90°$
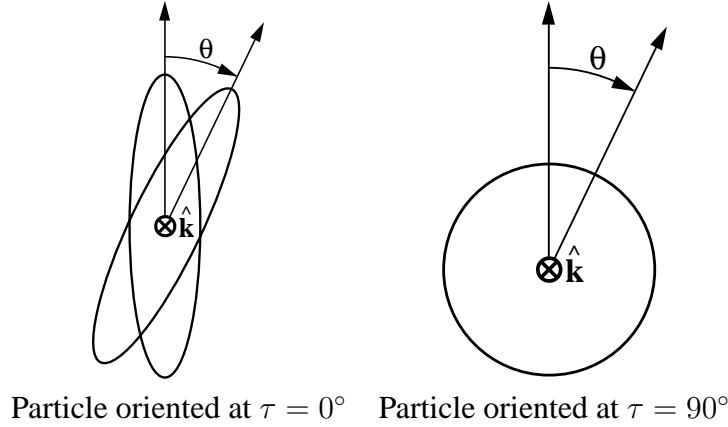
**Fig. B.7.**  Aspect of the particles from the radar viewpoint when $\phi = 0$ for two different values of $\tau$

On the other hand, the prolate particles have now an entropy span from 0 to 0.95, thus covering mostly the region on the plane with $\overline{\alpha} \leqslant 45°$. Prolate particles, hence, can still provide low entropy if they are not very randomly oriented.

## B.2.4   Constant $\phi = 0$ and $\tau = 0$, and finite span in $\theta$

The final case treated in this section corresponds to a distribution of particles lying on a plane normal to the line of sight. For such a geometry, it is necessary to fix $\tau = 0$. Moreover, when $\tau = 0$ the other two angles $\phi$ and $\theta$ are equivalent. As a result, it is enough to provide freedom to $\theta$ by fixing $\phi = 0$ as well. The entries of the scattering matrix for $\phi = \tau = 0$ were shown in (B.27)-(B.29), and the coherency matrix is obtained by the following integration:

$$\langle t_{ij} \rangle = \frac{1}{2\Theta} \int_{\theta=-\Theta}^{\theta=\Theta} t_{ij}(\theta) \, d\theta. \tag{B.52}$$

The resulting non-zero terms are:

$$t_{11} = (1 + A)^2 \tag{B.53}$$

$$t_{12} = \frac{(1 - A^2)\sin 2\Theta}{2\Theta} \tag{B.54}$$

$$t_{22} = \frac{(A - 1)^2(4\Theta + \sin 4\Theta)}{8\Theta} \tag{B.55}$$

$$t_{33} = \frac{(A - 1)^2(4\Theta - \sin 4\Theta)}{8\Theta}. \tag{B.56}$$

In this configuration, the plots are similar for oblate and prolate cases since, from the radar position, a particle with $A$ close to 0 is viewed equivalently to a particle with very high $A$ (see Fig. B.9 for demonstration).



Prolate: $0 < A < 1$                                   Oblate: $1 < A < \infty$

**Fig. B.8.** $H - \overline{\alpha}$ plots for a cloud random with a finite span in $\theta$: $0 < \Theta < \pi/2$, and $\tau = \phi = 0$
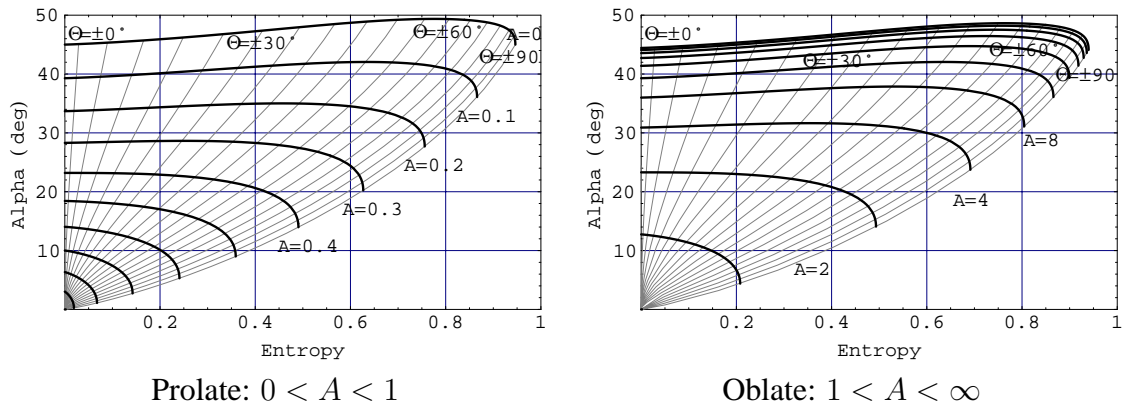


Prolate: $A < 1$                  Oblate: $A > 1$
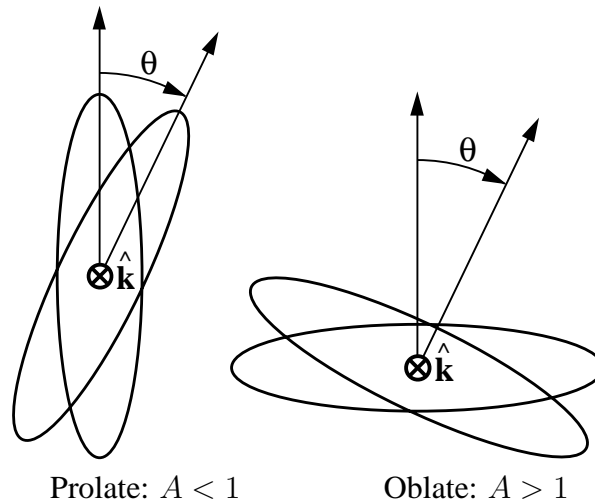
**Fig. B.9.** Aspect of the particles from the radar viewpoint when $\phi = \tau = 0$ for prolate and oblate cases

# B.3   Coherency Matrices for a Cloud of Particles: Different Initial Position

The variety of the results presented in Section B.2, as a function of the angles that can be fixed for each plot, suggests that new results could be obtained if the spheroid were defined in a different manner. This phenomenon is illustrated in this section.

The study case is a spheroid like that displayed in Fig. B.10. This corresponds to the same as before but rotated $90°$ in tilt. Equivalently, the formulation can be easily derived by interchanging or swapping the first and third polarizabilities, $\rho_1$ and $\rho_3$. This interchange means that the two equal axes lengths would be $x_1 = x_2$, instead of $x_2 = x_3$. Therefore, by simply swapping $\rho_1$ and $\rho_3$ the new formulation can be obtained in a simple way.
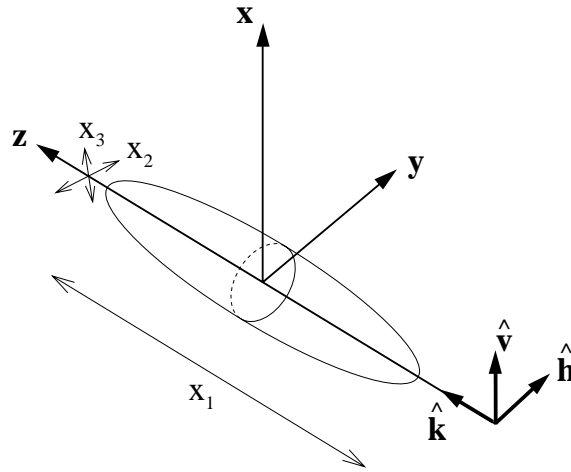


**Fig. B.10.** Scattering geometry by an ellipsoid for the new initial position. Displayed according to $\tau = 0°$

By introducing this change in the scattering matrix, its entries yield:

$$
\begin{aligned}
a =\ & \rho_1 \cos^2 \theta \sin^2 \tau \\
& + \rho_2 (\sin \theta \cos \phi + \cos \theta \cos \tau \sin \phi)^2 \\
& + \rho_3 (\cos \theta \cos \tau \cos \phi - \sin \theta \sin \phi)^2
\end{aligned}
\tag{B.57}
$$

$$
\begin{aligned}
d =\ & \rho_1 \sin^2 \theta \sin^2 \tau \\
& + \rho_2 (\cos \theta \cos \phi - \sin \theta \cos \tau \sin \phi)^2 \\
& + \rho_3 (\sin \theta \cos \tau \cos \phi + \cos \theta \sin \phi)^2
\end{aligned}
\tag{B.58}
$$

$$
\begin{aligned}
c =\ & \rho_1 \cos \theta \sin \theta \sin^2 \tau \\
& - \rho_2 (\sin \theta \cos \phi + \cos \theta \cos \tau \sin \phi)(\cos \theta \cos \phi - \sin \theta \cos \tau \sin \phi) \\
& + \rho_3 (\sin \theta \cos \tau \cos \phi + \cos \theta \sin \phi)(\cos \theta \cos \tau \cos \phi - \sin \theta \sin \phi).
\end{aligned}
\tag{B.59}
$$

The same particular cases of previous sections are revisited in the next sections with

the new formulation.

## B.3.1 Random cloud in $\tau$ and $\phi$. Finite span in $\theta$

The case of full randomness in $\tau$ and $\phi$, and a finite span in $\theta$, results in the following non-zero elements of the coherency matrix:

$$t_{11} = \frac{2}{15}(2 + 6A + 7A^2) \tag{B.60}$$

$$t_{12} = \frac{(2 + A - 3A^2)\sin 2\Theta}{15\Theta} \tag{B.61}$$

$$t_{22} = \frac{(A - 1)^2(4\Theta + \sin 4\Theta)}{30\Theta} \tag{B.62}$$

$$t_{33} = \frac{(A - 1)^2(4\Theta - \sin 4\Theta)}{30\Theta}. \tag{B.63}$$

The loci of entropy and dominant scattering mechanism on the $H-\alpha$ plane are shown in Fig. B.11. Note that for low spans in $\theta$ the resulting entropy is lower than in Fig. B.5. This phenomenon is caused by the new geometry because the aspect of the particle does not change with the initial rotation about $\phi$, thus leaving the entropy to be produced only by the rotations about $\tau$ and $\theta$.
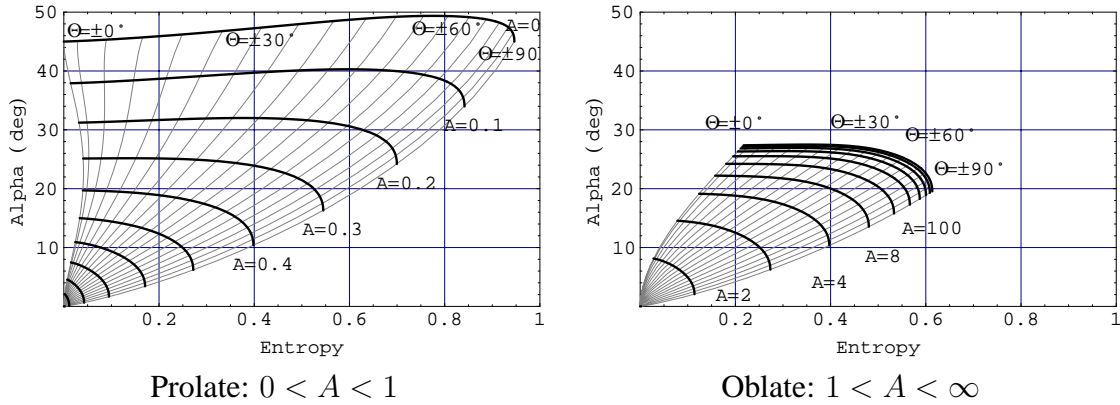


Fig. B.11. $H - \overline{\alpha}$ plots for a cloud with a finite span in $\theta$: $0 < \Theta < \pi/2$, and totally random in $\tau$ and $\phi$

## B.3.2 Constant $\phi = 0$, random cloud in $\tau$, and finite span in $\theta$

From the previous explanation of Fig. B.11, it follows that the $\phi$ angle has lost its effect on the polarimetric behavior of the cloud of particles. This effect has been further demonstrated

Rotation about $\phi$         Rotation about $\theta$
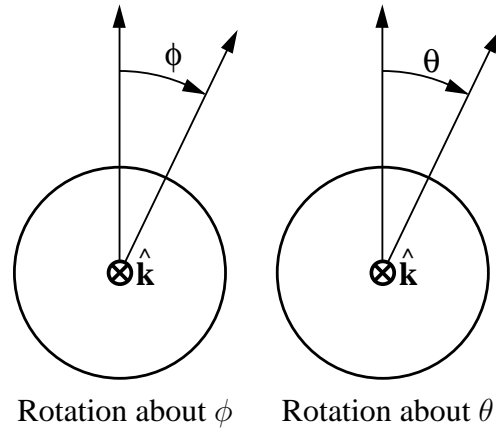
**Fig. B.12.** Aspect of the particle from the radar viewpoint when it is rotated about $\phi$ and $\theta$ when $\tau = 0$

by substituting $\phi = 0$ into the scattering amplitudes, yielding:

$$a = \rho_1 \cos^2 \theta \sin^2 \tau + \rho_2 \sin^2 \theta + \rho_3 \cos^2 \theta \cos^2 \tau \tag{B.64}$$

$$d = \rho_1 \sin^2 \theta \sin^2 \tau + \rho_2 \cos^2 \theta + \rho_3 \sin^2 \theta \cos^2 \tau \tag{B.65}$$

$$c = (\rho_1 \sin^2 \tau - \rho_2 + \rho_3 \cos^2 \tau) \cos \theta \sin \theta. \tag{B.66}$$

When the coherency matrices are computed, the resulting entries are exactly the same as those presented in (B.60)-(B.63), thus confirming the expectations.

This independence with respect to $\phi$ is the reason of the choice of this configuration for the development of the inversion algorithm described in Chapter 5.

## B.3.3 Constant $\phi = 0$ and $\tau = 0$, and finite span in $\theta$

Finally, let us study the particular case of no tilt angle variation, i.e. $\tau = 0$. In this situation the only varying angle is $\theta$, but from the antenna position the particle does not change with this angle. This effect is shown in Fig. B.12.

This is also obvious in the entries of the scattering matrix:

$$a = \rho_2 \sin^2 \theta + \rho_3 \cos^2 \theta \tag{B.67}$$

$$d = \rho_2 \cos^2 \theta + \rho_3 \sin^2 \theta \tag{B.68}$$

$$c = (\rho_3 - \rho_2) \cos \theta \sin \theta. \tag{B.69}$$

If we substitute the spheroid condition $x_2 = x_3$, the scattering matrix becomes proportional to the identity matrix. The only present scattering mechanism is, hence, surface (or sphere) type. Moreover, the coherency matrix presents only $t_{11} \neq 0$.

# Cylindrical Wave Formulation

THE conjunction of the linear movement of the target positioner with the circular movement of the antennas sled produces a synthetic aperture with cylindrical shape. Backscatter data acquired under this geometry at EMSL can be used as an input to the 3-D RMA by first translating them to a planar aperture. This translation must be performed by accounting for their field nature in order to preserve all information.

The translation is based on the following known principle. In a source-free region, specifying the tangential electric field everywhere on a closed surface is sufficient to determine the total field elsewhere, if certain additional conditions hold. In our case, this closed surface is the indefinite cylinder on which the measurements are acquired. The transformation of field data from a cylindrical surface to another place is accomplished by representing the field as a summation of free-space modes. The mode coefficients are determined by matching the fields on the surface with the modal expansion solution of the wave equation. Once these coefficients are found, the field can be computed everywhere by using the mode summation. Note that, although the field is only known on a portion of the cylinder, if the points where the field has to be translated are close to this portion, a negligible error is obtained by assuming the field to be zero on the rest of the cylinder.

The formulation and actual implementation of this field translation under cylindrical coordinates are shown in this appendix. The translation is repeated for every frequency in the synthesized bandwidth. Section C.1 presents the formal solution of the scalar wave equation in cylindrical coordinates. The practical procedure that has been implemented, emphasizing the use of Fourier Transforms to accelerate the computations, is described in Section C.2.

# C.1 Solution to the Scalar Wave Equation in Cylindrical Coordinates

The solution of the wave equation in cylindrical coordinates has been widely detailed in literature [184, 185]. In this study we are mainly interested in the scalar wave equation, since we assume the measured values to be purely scalar data. It is known that some non-zero radial component exists in near-field situations, but if we consider it negligible the results are accurate enough for our purposes.

By using the conventional cylindrical coordinate system, the scalar Helmholtz equation can be written as [185]:

$$\frac{1}{\rho}\frac{\partial}{\partial \rho}\left(\rho\frac{\partial \psi}{\partial \rho}\right) + \frac{1}{\rho^2}\frac{\partial^2 \psi}{\partial^2 \phi} + \frac{\partial^2 \psi}{\partial^2 z} + k^2\psi = 0, \tag{C.1}$$

where the scalar field is denoted as $\psi$.

This equation can be solved by the method of separation of variables, yielding the following elementary wave functions:

$$\psi_{k_\rho,n,k_z} = B_n(k_\rho\rho)h(n\phi)h(k_z z), \tag{C.2}$$

where $h(x)$ are solutions of the *harmonic* equation, and $B_n(k_\rho\rho)$ are solutions of the *Bessel equation* of order $n$. The wavenumbers along $\rho$ and $z$, i.e. $k_\rho$ and $k_z$, are interrelated by:

$$k_\rho^2 + k_z^2 = k^2. \tag{C.3}$$

A general solution for (C.1) can be constructed as a linear combination of the elementary wave functions. This linear combination is formed by sums over $n$ and $k_z$, or $n$ and $k_\rho$ (but not over $k_z$ and $k_\rho$ since they are not independent). For convenience, we will construct the general solutions as:

$$\psi = \sum_n \sum_{k_z} c_{n,k_z} \psi_{k_\rho,n,k_z}. \tag{C.4}$$

The *harmonic function* can be chosen as a linear combination of $\sin(x)$ and $\cos(x)$, or $e^{jx}$ and $e^{-jx}$. The complex exponentials have been chosen because they are more suited for a direct use of Fourier transforms. For the azimuthal variable $\phi$ the function must be periodic (with a period of $2\pi$), so $n$ must be an integer. For the cartesian variable $z$, its wavenumber does not present this restriction and can be a real number. On the other hand, the *Hankel function of second kind* $H_n^{(2)}(k_\rho\rho)$ has been selected for the solution of the *Bessel equation*. This choice is based upon the signal to be modeled, which is a field reflected from the target and, hence, can be regarded as an outward-traveling wave. In summary, the elementary wave functions take the form:

$$\psi_{k_\rho,n,k_z} = H_n^{(2)}(k_\rho\rho)\,e^{jn\phi}\,e^{jk_z z}, \tag{C.5}$$

with $n$ integer.

The summation in (C.4) is understood in this way:

$$\sum_n \sum_{k_z} = \sum_{n=-\infty}^{\infty} \sum_{k_z=-\infty}^{\infty} . \tag{C.6}$$

In practice, the summations will be always truncated at values $n = \pm N$ and $k_z = \pm K_{Z_{max}}$. The maximum value of $n$ depends on the radius of the minimum cylinder, centered at the same point of the measurement cylinder, that contains all the scattering points of the target. If the radius of the minimum cylinder is named $\rho_0$, the following empirical rule gives an estimate for $N$:

$$N = [k_\rho \rho_0] + n_1, \tag{C.7}$$

where the square brackets denote the *integer part*, and the integer $n_1$ depends on the accuracy required. The maximum value of $k_z$ depends on the maximum degree of variation of the signal in the $z$ direction, which in turn is usually fixed by the $z$ dimension of the target.

Note that, as was justified in Chapter 7, $k$ must be *twice* the wavenumber, i.e. $k = 4\pi f/c$. This modification is introduced in the formulation in order to take into account the round-trip path followed by the radar signal, instead of the one-way situation present in antenna measurements.

## C.2   Practical Implementation

In next sections, the analytical method for solving the coefficients of the cylindrical modes summation is formulated, and the application of this method to the practical case of sampled data is presented.

### C.2.1   Analytical Computation of the Coefficients $c_{n,k_z}$

From the previous equations we can conclude that the field measured at a single frequency on a cylinder of radius $\rho = A$ can be expressed as a linear combination of the elementary wave functions in the following way:

$$\psi(A, \phi, z) = \sum_{n=-N}^{N} \sum_{k_z=-K_{Z_{max}}}^{K_{Z_{max}}} c_{n,k_z} \, H_n^{(2)}(k_\rho A) \, e^{jn\phi} \, e^{jk_z z}. \tag{C.8}$$

To begin with, it is useful to rewrite (C.8) in the following way:

$$\psi(A, \phi, z) = \sum_{k_z=-K_{Z_{max}}}^{K_{Z_{max}}} c_{k_z}(\phi, A) \, e^{jk_z z},$$  (C.9)

where

$$c_{k_z}(\phi, A) = \sum_{n=-N}^{N} c_{n,k_z} H_n^{(2)}(k_\rho A) \, e^{jn\phi}.$$  (C.10)

As is evident from (C.9), $c_{k_z}(\phi, A)$ is a coefficient in the expansion of $\psi$ into a finite Fourier series in $z$. We can solve (C.9) for $c_{k_z}(\phi, A)$ by multiplying both sides by $e^{-jk_z' z}$ and integrating with respect to $z$ from $z_{min}$ to $z_{max}$:

$$\int_{z_{min}}^{z_{max}} \psi(A, \phi, z) \, e^{-jk_z' z} dz =$$

$$\int_{z_{min}}^{z_{max}} \left[ \sum_{k_z=-K_{Z_{max}}}^{K_{Z_{max}}} c_{k_z}(\phi, A) \, e^{jk_z z} \right] e^{-jk_z' z} dz = (z_{max} - z_{min}) \, c_{k_z}(\phi, A).$$  (C.11)

Therefore, the coefficients $c_{k_z}(\phi, A)$ are the Fourier transform of the data along $z$, i.e.:

$$c_{k_z}(\phi, A) = \frac{1}{z_{max} - z_{min}} \int_{z_{min}}^{z_{max}} \psi(A, \phi, z) \, e^{-jk_z z} dz.$$  (C.12)

The next step consists in rewriting the $z$-transformed formula (C.10) in this way:

$$c_{k_z}(\phi, A) = \sum_{n=-N}^{N} c_{n,k_z}(A) \, e^{jn\phi},$$  (C.13)

where

$$c_{n,k_z}(A) = c_{n,k_z} H_n^{(2)}(k_\rho A).$$  (C.14)

The application of the Fourier transform to the $\phi$ variable, in an analogous way as before with $z$, yields the analytical solution for the coefficients $c_{n,k_z}(A)$:

$$c_{n,k_z}(A) = \frac{1}{2\pi} \int_0^{2\pi} c_{k_z}(\phi, A) \, e^{-jn\phi} d\phi.$$  (C.15)

Finally, the radial dependence can be removed from the coefficients $c_{n,k_z}$ by dividing by the Hankel functions:

$$c_{n,k_z} = \frac{c_{n,k_z}(A)}{H_n^{(2)}(k_\rho A)}.$$  (C.16)

## C.2.2 Discrete Computation of the Coefficients $c_{n,k_z}$

In the former section we have derived the analytical expressions for the determination of the coefficients of the summation of wave functions or harmonics. They have the form of two Fourier transforms. Consequently, the most efficient way to compute them is by using FFT's.

In order to do that, the samples must be taken (as it is always the case) with constant sampling. For example, for the integral over $\phi$, the samples are taken with a constant angular separation $\Delta\phi$. This angular step depends on the number of harmonics, $N$, that must be considered. The relation is:

$$\Delta\phi \leqslant \frac{2\pi}{2N + 1}. \tag{C.17}$$

In case of having $2N + 1$ samples over the whole rotation, we can employ the Fast Fourier Transform to obtain $c_{n,k_z}(A)$:

$$c_{n,k_z}(A) = \text{FFT}(c_{k_z}(i\Delta\phi, A)), \tag{C.18}$$

where $i = 0, 1, \ldots, 2N$ denote the samples.

In practice we only have samples over a portion of the azimuth rotation. As stated in Chapter 7, this is not a problem for the final result because the place into which the field will be translated is close to the original cylindrical portion. The data can be completed with zeros in the region with unknown field and then it is possible to employ the FFT as before. A similar method could be employed for the Fourier transform along $z$.

Note that a technique based on the chirp $z$-transform [186, 187] has been used in both cases on the actual implementation. This type of transform is more flexible and enables the use of arbitrary ranges and sampling steps in both the original and the transformed domains.

Finally, a flow chart of the procedure that has been implemented is depicted in Fig. C.1. The algorithm is constituted by some nested loops. Note that both direct and inverse transformations from $z$ to $k_z$ are performed by FFT's because both origin and destination domains are equally spaced in those variables. Instead, the conversion from $n$ to $y$ is carried out by means of a summation because an uniform sampling in $y$ corresponds to an unequal spacing in $\phi$.
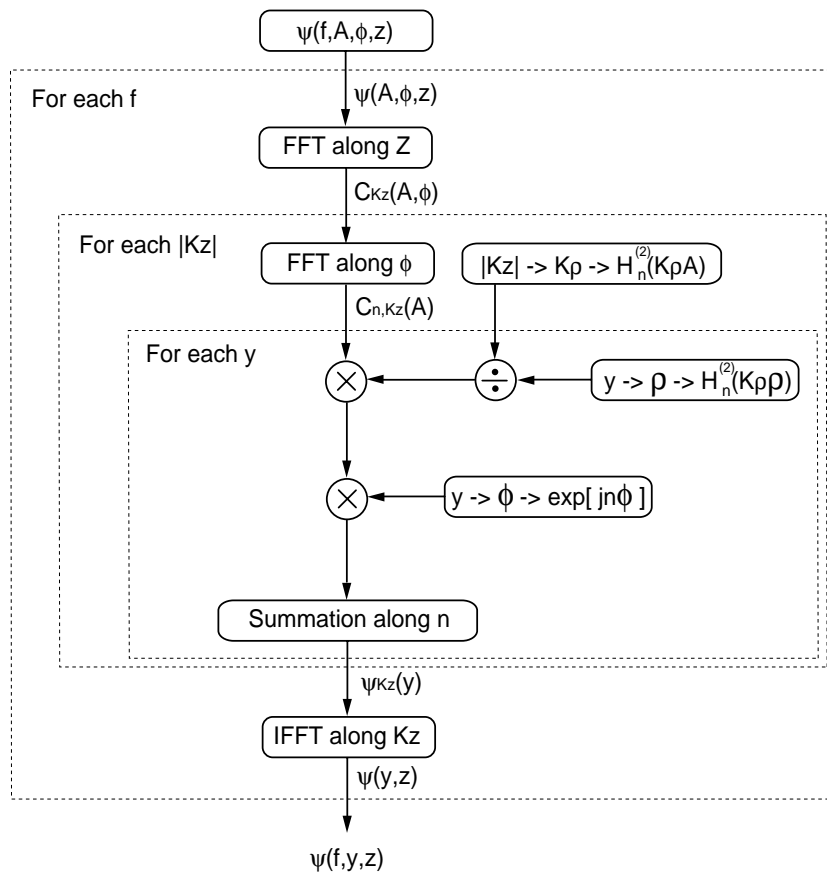
**Fig. C.1.** Block diagram of the field translation from a cylindrical to a planar aperture

# Spherical Wave Formulation

INVERSE SAR (ISAR) is a common configuration at the EMSL for radar imaging measurements. The data are collected for some elevation incidence angles while the target is rotated in azimuth. Therefore, the synthetic aperture is a portion of a sphere. As in the cylindrical case described in Appendix C, these data can still be used by the 3-D RMA as input backscattered fields by first translating them to a planar aperture.

Following the same procedure as in the cylindrical case, the transformation of the field data from a spherical surface to other positions is accomplished by representing the field as a summation of free-space modes, and the mode coefficients are determined by matching the fields on the surface on which the fields are known. Once these coefficients are found, the field can be computed elsewhere by using the modes summation.

In the following, Section D.1 presents the formal solution of the scalar wave equation in spherical coordinates. Section D.2 describes the steps of the coefficients computation from the analytical view point, and also the practical implementation of this procedure, which is based on Fourier techniques.

## D.1 Solution to the Scalar Wave Equation in Spherical Coordinates

By using the conventional spherical coordinate system, the scalar Helmholtz equation can be written as [185]:

$$\frac{1}{r^2}\frac{\partial}{\partial r}\left(r^2\frac{\partial\psi}{\partial r}\right) + \frac{1}{r^2\sin\theta}\frac{\partial}{\partial\theta}\left(\sin\theta\frac{\partial\psi}{\partial\theta}\right) + \frac{1}{r^2\sin^2\theta}\frac{\partial^2\psi}{\partial^2\phi} + k^2\psi = 0. \qquad \text{(D.1)}$$

Again, this wave equation can be solved by the method of separation of variables,

yielding the following elementary wave functions:

$$\psi_{m,n} = b_n(kr)L_n^m(\cos\theta)h(m\phi), \tag{D.2}$$

where $h(m\phi)$ are solutions of the *harmonic* equation, $L_n^m(\cos\theta)$ are the *associate Legendre functions* and $b_n(kr)$ are the *spherical Bessel functions*. A general solution of (D.1) can be constructed as a linear combination of the elementary wave functions:

$$\psi = \sum_m \sum_n c_{m,n}\psi_{m,n}. \tag{D.3}$$

The *harmonic function* can be chosen as a linear combination of $\sin(m\phi)$ and $\cos(m\phi)$, or $e^{jm\phi}$ and $e^{-jm\phi}$, with $m$ an integer. The complex exponentials have been preferred because they are more suited for a direct use of Fourier transforms. A study of the solutions of the Legendre equation shows that if $\psi$ is finite in the range 0 to $\pi$, then $n$ must also be an integer, and $L_n^m(\cos\theta)$ must be the *associate Legendre function* of first kind $P_n^m(\cos\theta)$. Finally, the *spherical Bessel function* can be selected depending on the behavior of the wave that it is representing. In our case, the radar signal is reflected from the target, so it can be modeled as an outward-traveling wave. Therefore, $b_n(kr)$ corresponds to the *spherical Hankel function* of second kind $h_n^{(2)}(kr)$. In conclusion, the elementary wave functions take the form:

$$\psi_{m,n} = h_n^{(2)}(kr)\,P_n^m(\cos\theta)\,e^{jm\phi}, \tag{D.4}$$

with $m$ and $n$ integers.

The summation in (D.3) is understood in this way:

$$\sum_m \sum_n = \sum_{n=0}^{\infty} \sum_{m=-n}^{n}, \tag{D.5}$$

since $P_n^m(\cos\theta)$ vanishes for $|m| > n$. In practice, the summations will be always truncated at a value $n = N$ which depends on the radius of the minimum sphere, centered at the same point of the measurement sphere, that contains all the scattering points of the target [180]. If the radius of the minimum sphere is named $r_0$, the following empirical rule gives an estimate for $N$:

$$N = [kr_0] + n_1, \tag{D.6}$$

where the square brackets denote the *integer part*, and the integer $n_1$ depends on the accuracy required. Note that $k$ is defined as $4\pi f/c$, according to the justification stated in Chapter 7.

## D.2 Practical Implementation

Some definitions about the associate Legendre functions, that will be needed in successive derivations, are presented in first place. The analytical method for solving the coefficients of the spherical modes summation is described later. Finally, the application of this method to the practical case of sampled data is explained.

## D.2.1   Associate Legendre Functions

The associate Legendre functions have been defined in a few different ways in the literature, thus becoming necessary to state here which definition we are using. The definition employed in the present work is the same as [185] and [188]:

$$P_n^m(\cos\theta) = (-1)^m \sin^m\theta \, \frac{d^m P_n(\cos\theta)}{d(\cos\theta)^m}, \tag{D.7}$$

where

$$P_n(\cos\theta) = \frac{1}{2^n n!} \frac{d^n}{d(\cos\theta)^n} (\cos^2\theta - 1)^n \tag{D.8}$$

is the Legendre polynomial. Another expression without the $(-1)^m$ factor is given in [184] and [180].

Since the values of the associate Legendre functions grow significantly with their order, they cannot be represented with double precision numbers when their order is high. To prevent this constraint the normalized associate Legendre functions must be employed:

$$\overline{P}_n^m(\cos\theta) = \sqrt{\frac{2n+1}{2} \frac{(n-m)!}{(n+m)!}} \, P_n^m(\cos\theta). \tag{D.9}$$

Therefore, we will employ the normalized associate Legendre functions in all derivations. Two properties of these functions that will be required later are:

**Orthogonality**   The normalized associate Legendre functions satisfy:

$$\int_{-1}^{1} \overline{P}_n^m(\cos\theta) \, \overline{P}_k^m(\cos\theta) \, d(\cos\theta) = \delta_{nk}, \tag{D.10}$$

where $\delta_{nk}$ is Kronecker's delta ($\delta_{nk} = 1$ for $n = k$ and $\delta_{nk} = 0$ for $n \neq k$).

**Fourier expansion**   The normalized associate Legendre functions can be Fourier expanded in this way:

$$\overline{P}_n^m(\cos\theta) = j^m \sum_{p=-n}^{n} d_{m,p} \, e^{jp\theta} = j^{-m} \sum_{p=-n}^{n} d_{m,p} \, e^{-jp\theta}. \tag{D.11}$$

The coefficients vanish for $(p+n)$ odd, and they satisfy the recurrence relation:

$$(n+p+2)(n-p-1) \, d_{m,p+2} - 2(n^2 - p^2 + n - 2m^2) \, d_{m,p} + $$
$$(n+p-1)(n-p+2) \, d_{m,p-2} = 0, \quad \text{(D.12)}$$

with the initial values

$$d_{m,n} = \frac{1}{2^{2n}} \frac{(2n)!}{n!} \sqrt{\frac{2n+1}{2}} \sqrt{\frac{1}{(n+m)!(n-m)!}} \tag{D.13}$$

$$d_{m,n-2} = \frac{n-2m^2}{2n-1} d_{m,n}. \tag{D.14}$$

For $m = 0$, the recurrence in (D.12) takes the form:

$$(n+p)(n-p+1)\, d_{0,p} - (n+p-1)(n-p+2)\, d_{0,p-2} = 0. \tag{D.15}$$

## D.2.2   Analytical Computation of the Coefficients $c_{m,n}$

The following derivations are mainly based on the method presented in [180, Chapter 4], but many particular considerations have been done in order to apply this technique to the scalar wave equation instead of the vector one used in that book. From the previous sections we can conclude that the field measured at a single frequency on a sphere of radius $r = A$ can be expressed as a linear combination of the elementary wave functions in the following way:

$$\psi(A,\phi,\theta) = \sum_{n=0}^{N} \sum_{m=-n}^{n} c_{m,n}\, e^{jm\phi}\, \overline{P}_n^m(\cos\theta)\, h_n^{(2)}(kA). \tag{D.16}$$

Since the associate Legendre functions satisfy that $\overline{P}_n^m(\cos\theta) = \overline{P}_n^{(-m)}(\cos\theta)$ we only will employ $m$ positive for computing these functions. Moreover, we have extracted a factor $(m/|m|)^m$ from the coefficients in order to simplify their calculus as in [180], yielding:

$$\psi(A,\phi,\theta) = \sum_{n=0}^{N} \sum_{m=-n}^{n} c_{m,n}\, e^{jm\phi} \left(\frac{m}{|m|}\right)^m \overline{P}_n^m(\cos\theta)\, h_n^{(2)}(kA), \tag{D.17}$$

where $(m/|m|)^m = 1$ for $m = 0$. In this section we will show the analytical solution of (D.17) for the unknowns, i.e. the coefficients $c_{m,n}$, by assuming that the field $\psi$ is known on a sphere of radius $A$.

In the first step we exploit the orthogonality of the exponential function:

$$\int_0^{2\pi} e^{j(m-p)\phi} d\phi = 2\pi\delta_{mp}. \tag{D.18}$$

Let us rewrite (D.17) as

$$\psi(A,\phi,\theta) = \sum_{m=-N}^{N} c_m(A,\theta)\, e^{jm\phi}, \tag{D.19}$$

where

$$c_m(A, \theta) = \sum_{n=|m|}^{N} c_{m,n} \left( \frac{m}{|m|} \right)^m \overline{P}_n^m(\cos \theta) \, h_n^{(2)}(kA). \tag{D.20}$$

As is evident from (D.19), $c_m(A, \theta)$ is a coefficient in the expansion of $\psi$ into a finite Fourier series in $\phi$. One can solve (D.19) for $c_m(A, \theta)$ by multiplying both sides by $e^{-jp\phi}$ and integrating with respect to $\phi$ from 0 to $2\pi$ :

$$\int_0^{2\pi} \psi(A, \phi, \theta) \, e^{-jp\phi} d\phi = \int_0^{2\pi} \left[ \sum_{m=-N}^{N} c_m(A, \theta) \, e^{jm\phi} \right] e^{-jp\phi} d\phi = 2\pi c_p(A, \theta). \tag{D.21}$$

Substituting for convenience $p$ by $m$, and rearranging, gives the transformed data:

$$c_m(A, \theta) = \frac{1}{2\pi} \int_0^{2\pi} \psi(A, \phi, \theta) e^{-jm\phi} d\phi. \tag{D.22}$$

Therefore, $c_m(A, \theta)$ is the Fourier transform along azimuth of the measured data $\psi(A, \phi, \theta)$.

The next step consists in rewriting the $\phi$-transformed formula (D.20) in this way:

$$c_m(A, \theta) = \sum_{n=|m|}^{N} c_{m,n}(A) \left( \frac{m}{|m|} \right)^m \overline{P}_n^m(\cos \theta), \tag{D.23}$$

where

$$c_{m,n}(A) = c_{m,n} \, h_n^{(2)}(kA). \tag{D.24}$$

Equation (D.23) can be solved by applying the orthogonality of the normalized associate Legendre functions (D.10), yielding:

$$c_{m,n}(A) = \left( \frac{m}{|m|} \right)^m \int_0^{\pi} c_m(A, \theta) \, \overline{P}_n^m(\cos \theta) \sin \theta d\theta. \tag{D.25}$$

Finally, the radial dependence can be removed from the coefficients by dividing by the Hankel functions:

$$c_{m,n} = \frac{c_{m,n}(A)}{h_n^{(2)}(kA)}. \tag{D.26}$$

## D.2.3 Discrete Computation of the Coefficients $c_{m,n}$

In the former section we have derived the analytical expressions for the determination of the coefficients of the summation of wave functions or harmonics. They have the form of two integrals and a simple division. Here we will consider the question of calculating those integrals by numerical methods. In fact, both of them are particularly simple, since they can be evaluated by Fourier techniques.

### D.2.3.1 Integral in $\phi$

The $\phi$-integral was presented in (D.22), being $c_m(A, \theta) = 0$ for $|m| > N$. We now have to determine $c_m(A, \theta)$ by evaluating the integral from samples of $\psi(A, \phi, \theta)$.

The samples are taken with a constant angular separation $\Delta\phi$. This angular step depends on the number of harmonics, $N$, that must be considered [180]. The relation is:

$$\Delta\phi \leqslant \frac{2\pi}{2N+1}. \tag{D.27}$$

When we have $2N + 1$ samples over the whole rotation, we can employ the Fast Fourier Transform to obtain $c_m(A, \theta)$:

$$c_m(A, \theta) = \text{FFT}(\psi(A, i\Delta\phi, \theta)), \tag{D.28}$$

where $i = 0, 1, \ldots, 2N$ denote the samples.

In practice, we only have samples over a portion of the azimuth rotation. In order to calculate $c_m(A, \theta)$, the data can be completed with zeros in the region with unknown field and then it is possible to employ the FFT as before. This assumption does not introduce any significant error if the region into which the fields are translated is close to the original aperture.

### D.2.3.2 Integral in $\theta$

The $\theta$-integral is shown in (D.25), where $c_{m,n}(A) = 0$ for $n > N$. We now have to determine $c_{m,n}(A)$ by evaluating the integral from samples of $c_m(A, \theta)$. Here, again, the samples are taken with a constant angular separation $\Delta\theta$. This angular step depends on the number of harmonics, $N$, that must be considered [180]. The relation is:

$$\Delta\theta \leqslant \frac{2\pi}{2N+1}. \tag{D.29}$$

Now the integral is not a simple Fourier Transform, but we can employ the Fourier expansion of the associate Legendre functions (D.11) to exploit the efficiency of the computations with FFT's.

There is a second aspect to consider: the domain of the $\theta$ angle is only $0 \leqslant \theta \leqslant \pi$, instead of the $2\pi$ complete rotation. However, by knowing that $(m/|m|)^m \overline{P}_n^m(\cos\theta)$ is periodic in $\theta$ with period $2\pi$, and that its parity about $\theta = \pi$ is the same as $m$ (odd if $m$ is odd, and even if $m$ is even), we can extend the data in the following way:

$$\hat{c}_m(A, \theta) = \begin{cases} c_m(A, \theta), & 0 \leqslant \theta \leqslant \pi \\ c_m(A, 2\pi - \theta), & \pi < \theta < 2\pi, \quad m \text{ even} \\ -c_m(A, 2\pi - \theta), & \pi < \theta < 2\pi, \quad m \text{ odd} \end{cases} \tag{D.30}$$

The extended data $\hat{c}_m(A, \theta)$ can be expanded into a finite Fourier series as,

$$\hat{c}_m(A, \theta) = \sum_{l=-N}^{N} b_{m,l} \, e^{jl\theta}. \tag{D.31}$$

By substituting (D.11) and (D.31) in (D.25) it gives,

$$c_{m,n}(A) = \int_{\theta=0}^{\pi} \sum_{l=-N}^{N} b_{m,l} \, e^{jl\theta} \, j^{-m} \sum_{p=-n}^{n} d_{m,p} \, e^{-jp\theta} \sin\theta d\theta \tag{D.32}$$

$$= j^{-m} \sum_{l=-N}^{N} b_{m,l} \sum_{p=-n}^{n} d_{m,p} \int_{\theta=0}^{\pi} e^{j(l-p)\theta} \sin\theta d\theta. \tag{D.33}$$

The integral in (D.33) can be denoted as $G(l-p)$, and has an analytical solution:

$$G(l-p) = \begin{cases} \pm j\frac{\pi}{2}, & (l-p) = \pm 1 \\ 0, & |l-p| = 3, 5, 7, \ldots \\ \frac{2}{1-(l-p)^2}, & |l-p| = 0, 2, 4, \ldots \end{cases} \tag{D.34}$$

Hence we arrive to the following expression:

$$c_{m,n}(A) = j^{-m} \sum_{l=-N}^{N} b_{m,l} \sum_{p=-n}^{n} d_{m,p} G(l-p), \tag{D.35}$$

where the only unknowns on the right-hand side are now the Fourier coefficients $b_{m,l}$.

A further study of the elements in (D.35) yields an additional simplification. From their definition, it is observed that:

$$b_{m,l} = (-1)^m b_{m,-l} \tag{D.36}$$
$$d_{m,p} = (-1)^m d_{m,-p}, \tag{D.37}$$

and therefore,

$$b_{m,l} \, d_{m,p} = b_{m,-l} \, d_{m,-p}. \tag{D.38}$$

Since

$$G(l-p) = -G(p-l), \quad (l-p) = \pm 1, \tag{D.39}$$

the terms with $(l-p) = \pm 1$ cancel, and we can rewrite:

$$c_{m,n}(A) = j^{-m} \sum_{p=-n}^{n} d_{m,p} \sum_{l=-N}^{N} \prod (l-p) b_{m,l}, \tag{D.40}$$

where

$$\prod(l-p) = \begin{cases} 0, & (l-p) \text{ odd} \\ \frac{2}{1-(l-p)^2}, & (l-p) \text{ even} \end{cases} \tag{D.41}$$

and $\prod(l-p) = \prod(p-l)$.

The $l$-summation in (D.40) resembles, for each value of $p$, a convolution between two sequences. Hence, it can be evaluated efficiently by means of FFT's. If the result is named $K_m(p)$, the final expression of the coefficients is:

$$c_{m,n}(A) = j^{-m} \sum_{p=-n}^{n} d_{m,p} K_m(p). \tag{D.42}$$

The complete procedure of the coefficients computation is described in the flow chart drawn in Fig. D.1. The rectangles with dashed lines correspond to loops. Note that the coefficients are explicitly available at the end of this process. This was not the case in the translation from cylindrical to planar aperture because they were reused for each $n$ immediately after their calculus. The retrieval of the field from the obtained spherical coefficients is illustrated in Fig. D.2.
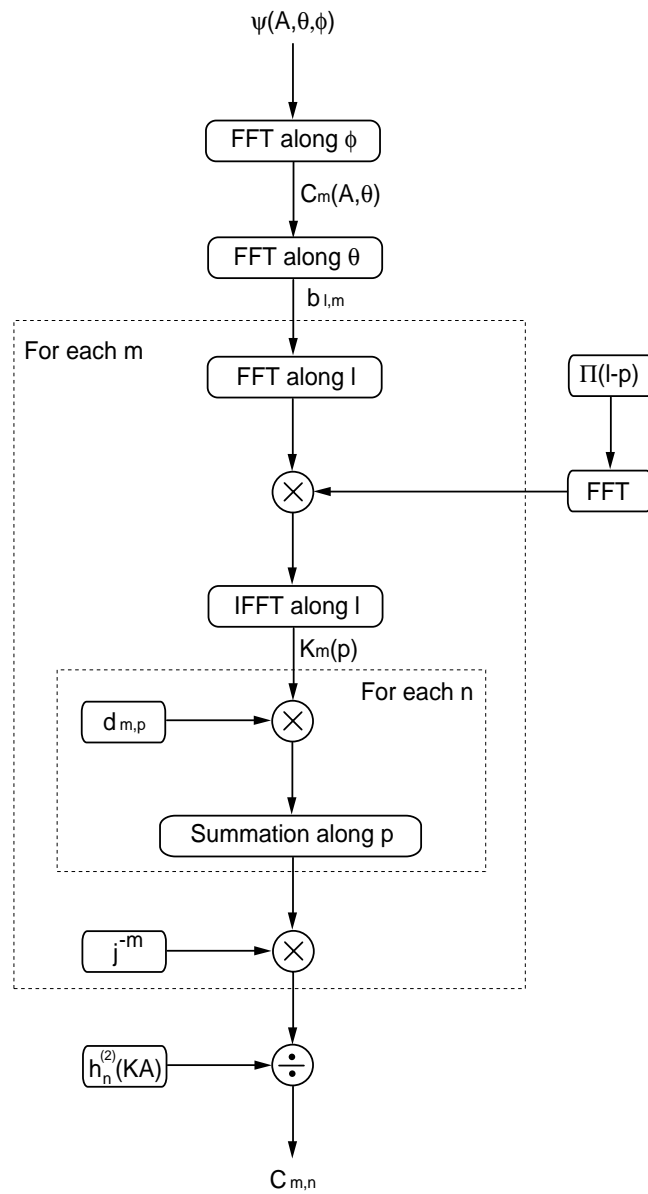
**Fig. D.1.** Block diagram of the coefficients computation from the field measured on a spherical aperture
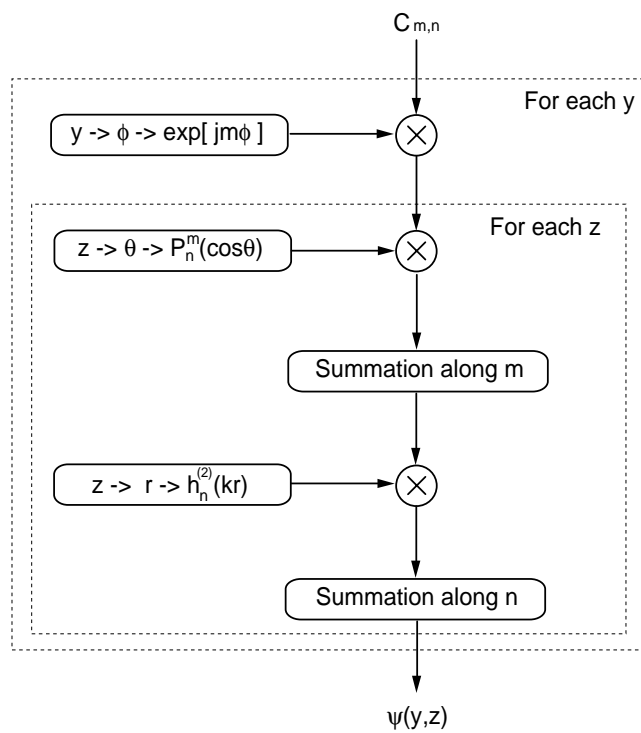
**Fig. D.2.** Block diagram of field extraction from the previously computed coefficients in the spherical case

# Bibliography

[1] F. T. Ulaby, R. K. Moore, and A. K. Fung, *Microwave Remote Sensing: Fundamentals and Radiometry*, vol. I. Artech House, 1981.

[2] F. T. Ulaby, R. K. Moore, and A. K. Fung, *Microwave Remote Sensing: Radar Remote Sensing and Surface Scattering and Emission Theory*, vol. II. Artech House, 1982.

[3] F. T. Ulaby, R. K. Moore, and A. K. Fung, *Microwave Remote Sensing: From Theory to Applications*, vol. III. Artech House, 1986.

[4] J. R. Huynen, *Phenomenological Theory of Radar Targets*. PhD thesis, Technical University, Delft, The Netherlands, 1970.

[5] W.-M. Boerner, "Historical development of radar polarimetry, incentives for this workshop, and overview of contributions to these proceedings," in *Direct and Inverse Methods in Radar Polarimetry, Part I, NATO-ARW* (W.-M. Boerner *et al.*, eds.), pp. 1–32, Kluwer Academic Publishers, 1992.

[6] E. Krogager, *Aspects of Polarimetric Radar Imaging*. PhD thesis, Technical University of Denmark, Copenhagen, Denmark, 1993.

[7] W.-M. Boerner *et al.*, "Polarimetry in radar remote sensing. Basic and applied concepts," in *Manual of Remote Sensing: Principles and Applications of Imaging Radar* (F. M. Henderson and A. J. Lewis, eds.), vol. 8, ch. 5, Wiley, 3 ed., 1998.

[8] G. Sinclair, "The transmission and reception of elliptically polarized waves," *Proc. IRE*, vol. 38, pp. 148–151, Feb. 1950.

[9] R. C. Jones, "A new calculus for the treatment of optical systems–Part I. Description and discussion of the calculus," *J. Opt. Soc. Am.*, vol. 31, pp. 488–493, 1941.

[10] M. Born and E. Wolf, *Principles of Optics*. Pergamon, 1980.

[11] H. C. van de Hulst, *Light Scattering by Small Particles*. Dover, 1981.

[12] E. M. Kennaugh, "Polarization properties of radar reflection," Master's thesis, Dept. of Electrical Engineering, The Ohio State University, Columbus, OH, USA, 1952.

[13] V. H. Rumsey, "Part I: Transmission between elliptically polarized antennas," *Proc. IRE*, vol. 39, pp. 535–540, May 1951.

[14] G. A. Deschamps, "Part II: Geometrical representation of the polarization of a plane electromagnetic wave," *Proc. IRE*, vol. 39, pp. 540–544, May 1951.

[15] G. A. Deschamps and P. E. Mast, "Poincaré sphere representation of partially polarized fields," *IEEE Trans. Antennas Propagat.*, vol. 21, pp. 474–478, July 1973.

[16] M. L. Kales, "Part III: Elliptically polarized waves and antennas," *Proc. IRE*, vol. 39, pp. 544–549, May 1951.

[17] J. I. Bohnert, "Part IV: Measurements on elliptically polarized antennas," *Proc. IRE*, vol. 39, pp. 549–552, May 1951.

[18] C. D. Graves, "Radar polarization power scattering matrix," *Proc. IRE*, vol. 44, pp. 248–252, Feb. 1956.

[19] S. H. Bickel, "Some invariant properties of the polarization scattering matrix," *Proc. IEEE*, vol. 53, pp. 1070–1072, Aug. 1965.

[20] S. H. Bickel and J. F. A. Ormsby, "Error analysis, calibration, and the polarization scattering matrix," *Proc. IEEE*, vol. 53, pp. 1087–1089, Aug. 1965.

[21] S. H. Bickel and R. H. T. Bates, "Effects of magneto-ionic propagation on the polarization scattering matrix," *Proc. IEEE*, vol. 53, pp. 1087–1089, Aug. 1965.

[22] J. R. Copeland, "Radar target classification by polarization properties," *Proc. IRE*, vol. 48, pp. 1290–1296, July 1960.

[23] O. Lowenschuss, "Scattering matrix application," *Proc. IEEE*, vol. 53, pp. 988–992, Aug. 1965.

[24] G. A. Ioannidis and D. E. Hammers, "Optimum antenna polarizations for target discrimination in clutter," *IEEE Trans. Antennas Propagat.*, vol. 27, pp. 357–363, May 1979.

[25] W.-M. Boerner, M. B. El-Arini, C.-Y. Chan, and P. M. Mastoris, "Polarization dependence in electromagnetic inverse problems," *IEEE Trans. Antennas Propagat.*, vol. 29, pp. 262–271, Mar. 1981.

[26] K. R. Carver, C. Elachi, and F. T. Ulaby, "Microwave remote sensing from space," *Proc. IEEE*, vol. 73, pp. 970–996, 1985.

[27] D. Giuli, "Polarization diversity in radars," *Proc. IEEE*, vol. 74, no. 2, pp. 245–269, 1986.

[28] J. J. van Zyl, H. A. Zebker, and C. Elachi, "Imaging radar polarization signatures," *Radio Science*, vol. 22, pp. 529–543, July 1987.

[29] W.-M. Boerner *et al.*, eds., *Direct and Inverse Methods in Radar Polarimetry, NATO-ARW*, Kluwer Academic Publishers, 1992.

[30] IRESTE, University of Nantes, *Proceedings of First International Workshop on Radar Polarimetry (JIPR'90)*, Atlanpole, La Chantrerie, Nantes, France, Mar. 1990.

[31] IRESTE, University of Nantes, *Proceedings of Second International Workshop on Radar Polarimetry (JIPR'92)*, France, Sept. 1992.

[32] IRESTE, University of Nantes, *Proceedings of Third International Workshop on Radar Polarimetry (JIPR'95)*, France, Mar. 1995.

[33] F. T. Ulaby and C. Elachi, eds., *Radar Polarimetry for Geoscience Applications*. Artech House, 1990.

[34] J. A. Kong, ed., *Polarimetric Remote Sensing*, vol. 3 of *PIER*. Elsevier, 1990.

[35] W. Wiesbeck and D. Kähny, "Single reference, three target calibration and error correction for monostatic, polarimetric free space measurements," *Proc. IEEE*, vol. 79, pp. 1551–1558, Oct. 1991.

[36] A. Freeman, Y. Shen, and C. L. Werner, "Polarimetric SAR calibration experiment using active radar calibrators," *IEEE Trans. Geosci. Remote Sensing*, vol. 28, pp. 224–240, Mar. 1990.

[37] J. D. Klein and A. Freeman, "Quadpolarization SAR calibration using target reciprocity," *J. Electromag. Waves Appl.*, vol. 5, no. 7, pp. 735–751, 1991.

[38] A. Freeman, Y. Shen, and C. L. Werner, "Calibration of Stokes and scattering matrix format polarimetric SAR data," *IEEE Trans. Geosci. Remote Sensing*, vol. 30, pp. 531–539, May 1992.

[39] J. J. van Zyl, "Calibration of polarimetric radar images using only image parameters and trihedral corner reflector responses," *IEEE Trans. Geosci. Remote Sensing*, vol. 28, pp. 337–348, May 1990.

[40] K. Sarabandi and F. T. Ulaby, "A convenient technique for polarimetric calibration of single-antenna radar systems," *IEEE Trans. Geosci. Remote Sensing*, vol. 28, pp. 1022–1033, Nov. 1990.

[41] K. Sarabandi, L. E. Pierce, and F. T. Ulaby, "Calibration of a polarimetric imaging SAR," *IEEE Trans. Geosci. Remote Sensing*, vol. 30, pp. 540–549, May 1992.

[42] K. Sarabandi, Y. Oh, and F. T. Ulaby, "Measurement and calibration of differential Mueller matrix of distributed targets," *IEEE Trans. Antennas Propagat.*, vol. 40, pp. 1524–1532, Dec. 1992.

[43] K. Sarabandi, "Calibration of a polarimetric synthetic aperture radar using a known distributed target," *IEEE Trans. Geosci. Remote Sensing*, vol. 32, pp. 575–582, May 1994.

[44] S. Chandrasekhar, *Radiative Transfer*. Dover, 1960.

[45] S. R. Cloude and E. Pottier, "A review of target decomposition theorems in radar polarimetry," *IEEE Trans. Geosci. Remote Sensing*, vol. 34, pp. 498–518, Mar. 1996.

[46] E. Krogager, "Coherent integration of scattering matrices," in *Proceedings of Third International Workshop on Radar Polarimetry (JIPR'95)*, Univ. Nantes, France, IRESTE, pp. 708–719, Mar. 1995.

[47] E. Krogager and Z. H. Czyz, "Properties of the sphere, diplahe, helix decomposition," in *Proceedings of Third International Workshop on Radar Polarimetry (JIPR'95)*, Univ. Nantes, France, IRESTE, pp. 106–114, Mar. 1995.

[48] J. W. Goodman, "Some fundamental properties of speckle," *J. Opt. Soc. Am.*, vol. 66, pp. 1145–1150, Nov. 1976.

[49] J.-S. Lee, I. Jurkevich, P. Dewaele, P. Wambacq, and A. Oosterlinck, "Speckle filtering of synthetic aperture radar images: A review," *Remote Sensing Reviews*, vol. 8, pp. 313–340, 1994.

[50] L. M. Novak and M. C. Burl, "Optimal speckle reduction in polarimetric SAR imagery," *IEEE Trans. Aerospace Electronic Syst.*, vol. 26, pp. 293–305, Mar. 1990.

[51] A. Lopes and F. Sery, "Optimal speckle reduction for the product model on multilook polarimetric SAR imagery and the Wishart distribution," *IEEE Trans. Geosci. Remote Sensing*, vol. 35, pp. 632–647, May 1997.

[52] S. R. Cloude, "Group theory and polarisation algebra," *Optik*, vol. 75, no. 1, pp. 26–36, 1986.

[53] S. R. Cloude, "Lie groups in electromagnetic wave propagation and scattering," *J. Electromag. Waves Appl.*, vol. 6, no. 8, pp. 947–974, 1992.

[54] S. R. Cloude, "Lie groups in electromagnetic wave propagation and scattering," in *Electromagnetic Symmetry* (C. E. Baum, ed.), ch. 2, Taylor & Francis, 1995.

[55] S. R. Cloude, "Uniqueness of target decomposition theorems in radar polarimetry," in *Direct and Inverse Methods in Radar Polarimetry, Part I, NATO-ARW* (W.-M. Boerner *et al.*, eds.), pp. 267–296, Kluwer Academic Publishers, 1992.

[56] J. J. van Zyl, "Application of Cloude's target decomposition theorem to polarimetric imaging radar data," in *SPIE, Radar Polarimetry*, vol. 1748, pp. 184–191, 1992.

[57] S. R. Cloude and E. Pottier, "Concept of polarization entropy in optical scattering," *Optical Engineering*, vol. 34, pp. 1599–1610, June 1995.

[58] M. I. Mishchenko, "Enhanced backscattering of polarized light from discrete random media: Calculations in exactly the backscattering direction," *J. Opt. Soc. Am. A*, vol. 9, pp. 978–982, June 1992.

[59] A. Freeman and S. L. Durden, "A three component scattering model to describe polarimetric SAR data," in *SPIE, Radar Polarimetry*, vol. 1748, pp. 213–224, 1992.

[60] A. Freeman, S. L. Durden, and R. Zimmerman, "Mapping sub-tropical vegetation using multi-frequency, multi-polarization SAR data," in *Proceedings of the IEEE International Geoscience and Remote Sensing Symposium (IGARSS)*, Houston, TX, USA, vol. 2, pp. 1686–1689, May 1992.

[61] A. Freeman and S. L. Durden, "A three-component scattering model for polarimetric SAR data," *IEEE Trans. Geosci. Remote Sensing*, vol. 36, pp. 963–973, May 1998.

[62] S. R. Cloude and E. Pottier, "An entropy based classification scheme for land applications of polarimetric SAR," *IEEE Trans. Geosci. Remote Sensing*, vol. 35, pp. 68–78, Jan. 1997.

[63] E. Pottier, "The "$H/A/\alpha$" polarimetric decomposition approach applied to POLSAR data processing," in *Proceedings of the PIERS - Workshop on Advances in Radar Methods*, Baveno, Italy, pp. 120–122, July 1998.

[64] M. Hellman and E. Krätzschmar, "A new approach for interpretation of full-polarimetric SAR-Data," in *Proceedings of the PIERS - Workshop on Advances in Radar Methods*, Baveno, Italy, pp. 204–207, July 1998.

[65] J. J. van Zyl, "Unsupervised classification of scattering behavior using radar polarimetry data," *IEEE Trans. Geosci. Remote Sensing*, vol. 27, pp. 36–45, Jan. 1989.

[66] D. L. Schuler, J.-S. Lee, and G. De Grandi, "Measurement of topography using polarimetric SAR images," *IEEE Trans. Geosci. Remote Sensing*, vol. 34, pp. 1266–1276, Sept. 1996.

[67] S. R. Cloude and K. P. Papathanassiou, "Coherence optimisation in polarimetric SAR interferometry," in *Proceedings of the IEEE International Geoscience and Remote Sensing Symposium (IGARSS)*, Singapore, vol. 4, pp. 1932–1934, Aug. 1997.

[68] S. R. Cloude and K. P. Papathanassiou, "Polarimetric radar interferometry," in *SPIE, Wideband Interferometric Sensing and Imaging Polarimetry*, San Diego, CA, USA, vol. 3120, 1997.

[69] S. R. Cloude and K. P. Papathanassiou, "Polarimetric SAR interferometry," *IEEE Trans. Geosci. Remote Sensing*, vol. 36, pp. 1551–1565, Sept. 1998.

[70] G. Graf and B. Röde, "Radar scattering from a solitary fir tree," in *Proceedings of the IEEE International Geoscience and Remote Sensing Symposium (IGARSS)*, Munich, Germany, vol. 2, pp. 8.1–8.6, June 1982.

[71] F. T. Ulaby, C. T. Allen, G. Eger III, and E. Kanemasu, "Relating the microwave backscattering coefficient to leaf area index," *Remote Sensing of Environment*, vol. 14, pp. 113–133, 1984.

[72] D. R. Brunfeldt and F. T. Ulaby, "Measured microwave emission and scattering in vegetation canopies," *IEEE Trans. Geosci. Remote Sensing*, vol. 22, pp. 520–524, Nov. 1984.

[73] L. K. Wu, R. K. Moore, R. Zoughi, A. Afifi, and F. T. Ulaby, "Preliminary results on the determination of the sources of scattering from vegetation canopies at 10 GHz," *Int. J. Remote Sensing*, vol. 6, no. 2, pp. 299–313, 1985.

[74] F. T. Ulaby, A. Tavakoli, and T. B. A. Senior, "Microwave propagation constant for a vegetation canopy with vertical stalks," *IEEE Trans. Geosci. Remote Sensing*, vol. 25, pp. 714–725, Nov. 1987.

[75] A. J. Sieber, "Forest signatures in imaging and non-imaging microwave scatterometer data," *ESA Journal*, vol. 9, pp. 431–448, 1985.

[76] R. Zoughi, L. K. Wu, and R. K. Moore, "Identification of major backscattering sources in trees and shrubs at 10 GHz," *Remote Sensing of Environment*, vol. 19, pp. 269–290, 1986.

[77] D. E. Pitts, G. D. Badhwar, E. Reyna, R. Zoughi, L.-K. Wu, and R. K. Moore, "Estimation of X-band scattering properties of tree component," *IEEE Trans. Geosci. Remote Sensing*, vol. 26, pp. 612–616, Sept. 1988.

[78] R. Zoughi, J. Bredow, S. Osman, and R. K. Moore, "Fine resolution signatures of coniferous and deciduous trees at C band," *Int. J. Remote Sensing*, vol. 10, no. 1, pp. 147–169, 1989.

[79] H. Hirosawa, Y. Matsuzaka, M. Daito, and H. Nakamura, "Measurement of backscatter from conifers in the C and X bands," *Int. J. Remote Sensing*, vol. 8, no. 11, pp. 1687–1694, 1987.

[80] H. Hirosawa, Y. Matsuzaka, and O. Kobayashi, "Measurement of microwave backscatter from a cypress with and without leaves," *IEEE Trans. Geosci. Remote Sensing*, vol. 27, pp. 698–701, Nov. 1989.

[81] J. F. Paris, "Probing thick vegetation canopies with a field microwave scatterometer," *IEEE Trans. Geosci. Remote Sensing*, vol. 24, pp. 886–893, Nov. 1986.

[82] W. E. Westman and J. F. Paris, "Detecting forest structure and biomass with C band multipolarization radar: Physical model and field tests," *Remote Sensing of Environment*, vol. 22, pp. 249–269, 1987.

[83] R. K. Moore, S. Osman, R. Zoughi, and J. Bredow, "Measurements of radar backscatter from an artificial tree: An indication of azimuthal variations and polarization sensitivity of trees," *Int. J. Remote Sensing*, vol. 12, no. 3, pp. 401–417, 1991.

[84] D. H. Hoekman, "Measurements of the backscatter and attenuation properties of forest stands at X, C and L band," *Remote Sensing of Environment*, vol. 23, pp. 397–416, 1987.

[85] F. T. Ulaby, D. N. Held, M. C. Dobson, K. C. McDonald, and T. B. A. Senior, "Relating polarization phase difference of SAR signals to scene properties," *IEEE Trans. Geosci. Remote Sensing*, vol. 25, pp. 83–92, Jan. 1987.

[86] D. E. Pitts, G. D. Badhwar, and E. Reyna, "The use of a helicopter mounted ranging scatterometer for estimation of extinction and scattering properties of forest canopies. Part II: Experimental results for high density aspen," *IEEE Trans. Geosci. Remote Sensing*, vol. 26, pp. 144–151, Mar. 1988.

[87] F. T. Ulaby, M. W. Whitt, and M. C. Dobson, "Measuring the propagation properties of a forest canopy using a polarimetric scatterometer," *IEEE Trans. Antennas Propagat.*, vol. 38, pp. 251–258, Feb. 1990.

[88] T. B. A. Senior, K. Sarabandi, and F. T. Ulaby, "Measuring and modelling the backscattering cross section of a leaf," *Radio Science*, vol. 22, pp. 1109–1116, 1987.

[89] K. Sarabandi, T. B. A. Senior, and F. T. Ulaby, "Effect of curvature on the backscattering from a leaf," *J. Electromag. Waves Appl.*, vol. 2, no. 7, pp. 653–670, 1988.

[90] M. A. Karam, A. K. Fung, and Y. M. M. Antar, "Electromagnetic wave scattering from some vegetation samples," *IEEE Trans. Geosci. Remote Sensing*, vol. 26, pp. 799–808, Nov. 1988.

[91] E. Mougin, A. Lopes, and T. Le Toan, "Microwave propagation at X band in cylindrical-shaped forest components: Attenuation observations," *IEEE Trans. Geosci. Remote Sensing*, vol. 28, pp. 60–69, Jan. 1990.

[92] A. Lopes and E. Mougin, "Microwave coherent propagation in cylindrical-shaped forest components: Interpretation of attenuation observations," *IEEE Trans. Geosci. Remote Sensing*, vol. 28, pp. 315–324, May 1990.

[93] K. J. Ranson and S. S. Saatchi, "C-band microwave scattering from small balsam fir," *IEEE Trans. Geosci. Remote Sensing*, vol. 30, pp. 924–932, Sept. 1992.

[94] E. Mougin, A. Lopes, M. A. Karam, and A. K. Fung, "Effect of tree structure on X-band microwave signature of conifers," *IEEE Trans. Geosci. Remote Sensing*, vol. 31, pp. 655–667, May 1993.

[95] S. M. C. Brown and J. C. Bennett, "High-resolution microwave polarimetric imaging of small trees," *IEEE Trans. Geosci. Remote Sensing*, vol. 37, pp. 48–53, Jan. 1999.

[96] J. Fortuny and A. J. Sieber, "Three-dimensional synthetic aperture radar imaging of a fir tree: First results," *IEEE Trans. Geosci. Remote Sensing*, vol. 37, pp. 1006–1014, Mar. 1999.

[97] F. T. Ulaby, "SAR biophysical retrievals: Lessons learned and challenges to overcome," in *Proceedings of the 2nd International Symposium on Retrieval of Bio- and Geo-physical Parameters from SAR Data for Land Applications*, Noordwijk, The Netherlands, ESTEC, pp. 19–25, Oct. 1998.

[98] L. Tsang, J. A. Kong, and R. T. Shin, *Theory of Microwave Remote Sensing*. Wiley Interscience, 1985.

[99] F. T. Ulaby, K. Sarabandi, K. C. McDonald, M. W. Whitt, and M. C. Dobson, "Michigan microwave canopy scattering model," *Int. J. Remote Sensing*, vol. 11, no. 7, pp. 1223–1253, 1990.

[100] N. S. Chauhan, R. H. Lang, and K. J. Ranson, "Radar modeling of a boreal forest," *IEEE Trans. Geosci. Remote Sensing*, vol. 29, pp. 627–638, July 1991.

[101] S. H. Yueh, J. A. Kong, J. K. Jao, R. T. Shin, and T. Le Toan, "Branching model for vegetation," *IEEE Trans. Geosci. Remote Sensing*, vol. 30, pp. 390–402, Mar. 1992.

[102] J. M. Stiles and K. Sarabandi, "Scattering from cultural grass canopies: A phase coherent model," in *Proceedings of the IEEE International Geoscience and Remote Sensing Symposium (IGARSS)*, Lincoln, NE, USA, vol. 1, pp. 720–722, 1996.

[103] R. H. Lang, R. Landry, O. Kavakhioglu, and J. C. Deguise, "Simulation of microwave backscatter from a red pine stand," in *SPIE, Multispectral Microw. Sensing Forestry, Hydrol. Natural Resour.*, Rome, Italy, vol. 2314, pp. 538–548, 1994.

[104] Y.-C. Lin and K. Sarabandi, "A Monte Carlo coherent scattering model for forest canopies using fractal-generated trees," *IEEE Trans. Geosci. Remote Sensing*, vol. 37, pp. 440–451, Jan. 1999.

[105] L. E. Pierce, K. Sarabandi, and F. T. Ulaby, "Application of an artificial neural network in canopy scattering inversion," in *Proceedings of the IEEE International Geoscience and Remote Sensing Symposium (IGARSS)*, Houston, TX, USA, vol. 2, pp. 1067–1069, May 1992.

[106] L. E. Pierce, K. Sarabandi, and F. T. Ulaby, "Application of an artificial neural network in canopy scattering inversion," *Int. J. Remote Sensing*, vol. 15, no. 16, pp. 3263–3270, 1994.

[107] P. F. Polatin, K. Sarabandi, and F. T. Ulaby, "An iterative inversion algorithm with application to the polarimetric radar response of vegetation canopies," *IEEE Trans. Geosci. Remote Sensing*, vol. 32, pp. 62–71, Jan. 1994.

[108] Y.-C. Lin and K. Sarabandi, "Retrieval of forest parameters using a fractal-based coherent scattering model and a genetic algorithm," *IEEE Trans. Geosci. Remote Sensing*, vol. 37, pp. 1415–1424, May 1999.

[109] T. Kurosu, M. Fujita, and K. Chiba, "Monitoring of rice crop growth from space using the ERS-1 C-band SAR," *IEEE Trans. Geosci. Remote Sensing*, vol. 33, pp. 1092–1096, July 1995.

[110] T. Le Toan, F. Ribbes, L.-F. Wang, N. Floury, K.-H. Ding, J. A. Kong, M. Fujita, and T. Kurosu, "Rice crop mapping and monitoring using ERS-1 data based on experiment and modeling results," *IEEE Trans. Geosci. Remote Sensing*, vol. 35, pp. 41–56, Jan. 1997.

[111] M. T. Svendsen and K. Sarabandi, "Retrieval of vegetation parameters from SAR data using a coherent scattering model of grassland," in *Proceedings of the 2nd International Symposium on Retrieval of Bio- and Geo-physical Parameters from SAR Data for Land Applications*, Noordwijk, The Netherlands, ESTEC, pp. 115–121, Oct. 1998.

[112] T. Le Toan, A. Beaudoin, J. Riom, and D. Guyon, "Relating forest biomass to SAR data," *IEEE Trans. Geosci. Remote Sensing*, vol. 30, pp. 403–411, Mar. 1992.

[113] M. C. Dobson, F. T. Ulaby, T. Le Toan, A. Beaudoin, E. S. Kasischke, and N. Christensen, "Dependence of radar backscatter on coniferous forest biomass," *IEEE Trans. Geosci. Remote Sensing*, vol. 30, pp. 412–415, Mar. 1992.

[114] M. L. Imhoff, "A theoretical analysis of the effect of forest structure on synthetic aperture radar backscatter and the remote sensing of biomass," *IEEE Trans. Geosci. Remote Sensing*, vol. 33, pp. 341–352, Mar. 1995.

[115] M. L. Imhoff, "Radar backscatter and biomass saturation: Ramifications for global biomass inventory," *IEEE Trans. Geosci. Remote Sensing*, vol. 33, pp. 511–518, Mar. 1995.

[116] H. Israelson, L. M. H. Ulander, J. I. H. Askne, J. E. S. Fransson, P.-O. Frölind, A. Gustavsson, and H. Hellsten, "Retrieval of forest stem volume using VHF SAR," *IEEE Trans. Geosci. Remote Sensing*, vol. 33, pp. 331–340, Mar. 1995.

[117] T. Le Toan and N. Floury, "On the retrieval of forest biomass from SAR data," in *Proceedings of the 2nd International Symposium on Retrieval of Bio- and Geo-physical Parameters from SAR Data for Land Applications*, Noordwijk, The Netherlands, ESTEC, pp. 595–600, Oct. 1998.

[118] K. Sarabandi, "$\Delta$k-radar equivalent to interferometric SAR's: A theoretical study for determination of vegetation height," *IEEE Trans. Geosci. Remote Sensing*, vol. 35, pp. 1267–1276, Sept. 1997.

[119] K. Sarabandi and A. Nashashibi, "Analysis and application of backscattered frequency correlation function," *IEEE Trans. Geosci. Remote Sensing*, vol. 37, pp. 1895–1906, July 1999.

[120] K. Sarabandi, S. R. Legault, A. Nashashibi, A. J. Sieber, and J. Fortuny, "Applications of the frequency covariance function in remote sensing of environment," in *Proceedings of the PIERS - Workshop on Advances in Radar Methods*, Baveno, Italy, pp. 73–75, July 1998.

[121] H. A. Zebker and J. Villasenor, "Decorrelation in interferometric radar echoes," *IEEE Trans. Geosci. Remote Sensing*, vol. 30, pp. 950–959, Sept. 1992.

[122] U. Wegmüller and C. L. Werner, "SAR interferometric signatures of forest," *IEEE Trans. Geosci. Remote Sensing*, vol. 33, pp. 1153–1161, Sept. 1995.

[123] U. Wegmüller and C. L. Werner, "Retrieval of vegetation parameters with SAR interferometry," *IEEE Trans. Geosci. Remote Sensing*, vol. 35, pp. 18–24, Jan. 1997.

[124] M. Engdahl and M. Borgeaud, "ERS-1/2 Tandem interferometric coherence and agricultural crop height," in *Proceedings of the 2nd International Symposium on Retrieval of Bio- and Geo-physical Parameters from SAR Data for Land Applications*, Noordwijk, The Netherlands, ESTEC, pp. 121–127, Oct. 1998.

[125] J. O. Hagberg, L. M. H. Ulander, and J. I. H. Askne, "Repeat-pass SAR interferometry over forested terrain," *IEEE Trans. Geosci. Remote Sensing*, vol. 33, pp. 331–340, Mar. 1995.

[126] J. I. H. Askne, P. B. G. Dammert, L. M. H. Ulander, and G. Smith, "C-band repeat-pass interferometric SAR observations of the forest," *IEEE Trans. Geosci. Remote Sensing*, vol. 35, pp. 25–35, Jan. 1997.

[127] R. N. Treuhaft, S. N. Madsen, M. Moghaddam, and J. J. van Zyl, "Vegetation characteristics and underlying topography from interferometric radar," *Radio Science*, vol. 31, pp. 1449–1485, Nov. 1996.

[128] D. L. Mensa, *High Resolution Radar Cross Section Imaging*. Artech House, 2nd ed., 1991.

[129] W. G. Carrara, R. S. Goodman, and R. M. Majewski, *Spotlight Synthetic Aperture Radar. Signal Processing Algorithms*. Artech House, 1995.

[130] D. A. Ausherman, A. Kozma, J. L. Walker, H. M. Jones, and E. C. Poggio, "Developments in radar imaging," *IEEE Trans. Aerospace Electronic Syst.*, vol. 20, pp. 363–400, July 1984.

[131] D. L. Mensa, G. Heidbreder, and G. Wade, "Aperture synthesis by object rotation in coherent imaging," *IEEE Trans. Nuclear Science*, vol. 27, pp. 989–998, Apr. 1980.

[132] C. Cafforio, C. Prati, and E. Rocca, "SAR data focusing using seismic migration techniques," *IEEE Trans. Aerospace Electronic Syst.*, vol. 27, pp. 194–207, Mar. 1991.

[133] R. Stolt, "Migration by Fourier transform techniques," *Geophysics*, no. 43, pp. 49–76, 1978.

[134] C. Prati, A. Monti Guarnieri, and F. Rocca, "Spot mode SAR focusing with the $\omega - k$ technique," in *Proceedings of the IEEE International Geoscience and Remote Sensing Symposium (IGARSS)*, Helsinki, Finland, pp. 631–634, 1991.

[135] C. Prati and F. Rocca, "Focusing SAR data with time-varying Doppler centroid," *IEEE Trans. Geosci. Remote Sensing*, vol. 30, pp. 550–559, May 1992.

[136] A. Golden Jr., S. C. Wei, K. K. Ellis, and S. Tummala, "Migration processing of spotlight SAR data," in *SPIE, Algorithms for Synthetic Aperture Radar Imagery*, Orlando, FL, USA, vol. 2230, pp. 25–35, 1994.

[137] J. Fortuny, E. Ohlmer, A. J. Sieber, P. Pasquali, C. Prati, and F. Rocca, "Validating SAR interferometry applications by using EMSL," in *Proceedings of the IEEE International Geoscience and Remote Sensing Symposium (IGARSS)*, Pasadena, CA, USA, vol. 2, pp. 736–738, Aug. 1994.

[138] C. Yerkes and E. Webster, "Implementation of $\omega - k$ synthetic aperture radar imaging algorithm on a massively parallel supercomputer," in *SPIE, Algorithms for Synthetic Aperture Radar Imagery*, Orlando, FL, USA, vol. 2230, pp. 171–178, 1994.

[139] R. K. Raney, H. Runge, R. Bamler, I. G. Cumming, and F. H. Wong, "Precision SAR processing using chirp scaling," *IEEE Trans. Geosci. Remote Sensing*, vol. 32, pp. 786–799, July 1994.

[140] A. Broquetas, L. Jofre, and A. Cardama, "A near field spherical wave inverse synthetic aperture radar technique," in *Proceedings of the IEEE Antennas and Propagation Society International Symposium*, Chicago, IL, USA, vol. 2, pp. 114–117, July 1992.

[141] J. Fortuny, A. J. Sieber, J. Palau, and A. Broquetas, "QUICKSAR: A near field linear/inverse synthetic aperture radar processor," in *Proceedings of Progress in Electromagnetic Research Symposium (PIERS)*, Nordwijk, The Netherlands, 1994.

[142] A. Broquetas, J. Palau, L. Jofre, and A. Cardama, "Spherical wave near-field imaging and radar cross-section measurement," *IEEE Trans. Antennas Propagat.*, vol. 46, pp. 730–735, May 1998.

[143] J. Fortuny, "An efficient three dimensional near field ISAR algorithm using the method of stationary phase," *IEEE Trans. Aerospace Electronic Syst.*, vol. 34, pp. 1261–1270, Oct. 1998.

[144] C. A. Balanis, *Advanced Engineering Electromagnetics*. Wiley, 1989.

[145] A. Guissard, "Mueller and Kennaugh matrices in radar polarimetry," *IEEE Trans. Geosci. Remote Sensing*, vol. 32, pp. 590–597, May 1994.

[146] D. G. M. Anderson and R. Barakat, "Necessary and sufficient conditions for a Mueller matrix to be derivable from a Jones matrix," *J. Opt. Soc. Am. A*, vol. 11, pp. 2305–2319, Aug. 1994.

[147] M. Borgeaud, R. T. Shin, and J. A. Kong, "Theoretical models for polarimetric radar clutter," *J. Electromag. Waves Appl.*, vol. 1, no. 1, pp. 73–89, 1987.

[148] S. R. Cloude, "An entropy based classification scheme for polarimetric SAR data," in *Proceedings of the IEEE International Geoscience and Remote Sensing Symposium (IGARSS)*, Florence, Italy, vol. 3, pp. 2000–2002, July 1995.

[149] A. J. Sieber, "The European Microwave Signature Laboratory," *EARSel Advances in Remote Sensing*, vol. 2, pp. 195–204, Jan. 1993.

[150] G. Nesti, A. J. Sieber, G. De Grandi, J. Fortuny, and E. Ohlmer, "Recent advances at the European Microwave Signature Laboratory," in *SPIE, Microwave Instrumentation and Satellite Photogrammetry for Remote Sensing of the Earth*, Rome, Italy, vol. 2313, pp. 56–63, 1994.

[151] G. Nesti, P. Pampaloni, M. Hallikainen, M. Mancini, P. Troch, and M. von Shönermark, "Experimental research at the EMSL on scattering properties of non vegetated terrains," in *Proceedings of the IEEE International Geoscience and Remote Sensing Symposium (IGARSS)*, Florence, Italy, vol. 3, pp. 2020–2022, July 1995.

[152] J.-S. Lee, K. W. Hoppel, S. A. Mango, and A. R. Miller, "Intensity and phase statistics of multilook polarimeric and interferometric SAR imagery," *IEEE Trans. Geosci. Remote Sensing*, vol. 32, pp. 1017–1028, Sept. 1994.

[153] A. Franchois, Y. Piñeiro, and R. H. Lang, "Microwave permittivity measurements of two conifers," *IEEE Trans. Geosci. Remote Sensing*, vol. 36, pp. 1384–1395, Sept. 1998.

[154] R. H. Lang, R. Landry, A. Franchois, G. Nesti, and A. J. Sieber, "Microwave tree scattering experiment: Comparison of theory and experiment," in *Proceedings of the IEEE International Geoscience and Remote Sensing Symposium (IGARSS)*, Seattle, WA, USA, vol. 5, pp. 2384–2386, July 1998.

[155] D. L. Schuler, J.-S. Lee, and T. L. Ainsworth, "Compensation of terrain azimuthal slope effects in geophysical parameter studies using polarimetric SAR data," *Remote Sensing of Environment*, vol. 69, pp. 139–155, 1999.

[156] D. L. Schuler, J.-S. Lee, T. L. Ainsworth, E. Pottier, and W.-M. Boerner, "Terrain slope measurement accuracy using polarimetric SAR data," in *Proceedings of the IEEE International Geoscience and Remote Sensing Symposium (IGARSS)*, Hamburg, Germany, vol. 5, pp. 2652–2654, June 1999.

[157] E. Pottier, D. L. Schuler, J.-S. Lee, and T. L. Ainsworth, "Estimation of the terrain surface azimuthal/range slopes using polarimetric decomposition of POLSAR data," in *Proceedings of the IEEE International Geoscience and Remote Sensing Symposium (IGARSS)*, Hamburg, Germany, vol. 4, pp. 2212–2214, June 1999.

[158] A. K. Gabriel, R. M. Goldstein, and H. A. Zebker, "Mapping small elevation changes over large areas: Differential radar interferometry," *J. Geophys. Res.*, vol. 94, no. B7, pp. 9183–9191, 1989.

[159] D. Massonet and T. Rabaute, "Radar interferometry: Limits and potential," *IEEE Trans. Geosci. Remote Sensing*, vol. 31, pp. 455–464, Mar. 1993.

[160] H. A. Zebker, P. A. Rosen, R. M. Goldstein, A. K. Gabriel, and C. L. Werner, "On the derivation of coseismic displacement fields using differential radar interferometry: The Landers earthquake," *J. Geophys. Res.*, vol. 99, no. B10, pp. 19617–19634, 1994.

[161] R. Bamler and P. Hartl, "Synthetic aperture radar interferometry," *Inverse Problems*, vol. 14, pp. R1–R54, 1998.

[162] D. Just and R. Bamler, "Phase statistics of interferograms with applications to synthetic aperture radar," *Applied Optics*, vol. 33, pp. 4361–4368, July 1994.

[163] C. Prati and F. Rocca, "Improving slant-range resolution with multiple SAR surveys," *IEEE Trans. Aerospace Electronic Syst.*, vol. 29, pp. 135–143, June 1993.

[164] F. Gatelli, A. Monti Guarnieri, F. Parizzi, P. Pasquali, C. Prati, and F. Rocca, "The wavenumber shift in SAR interferometry," *IEEE Trans. Geosci. Remote Sensing*, vol. 32, pp. 855–864, July 1994.

[165] M. Cattabeni, A. Monti Guarnieri, and F. Rocca, "Estimation and improvement of coherence in SAR interferograms," in *Proceedings of the IEEE International Geoscience and Remote Sensing Symposium (IGARSS)*, Pasadena, CA, USA, vol. 2, pp. 720–722, Aug. 1994.

[166] E. Lüneburg and S. R. Cloude, "Contractions, Hadamard products and their application to polarimetric radar interferometry," in *Proceedings of the IEEE International Geoscience and Remote Sensing Symposium (IGARSS)*, Hamburg, Germany, vol. 4, pp. 2224–2226, June 1999.

[167] K. Sarabandi, C. G. Brown, and L. Pierce, "Tree height estimation from the polarimetric and interferometric radar response," in *Proceedings of the IEEE International Geoscience and Remote Sensing Symposium (IGARSS)*, Hamburg, Germany, vol. 4, pp. 1986–1988, June 1999.

[168] C. B. Wilsen, K. Sarabandi, and Y.-C. Lin, "The effect of tree architecture on the polarimetric and interferometric radar responses," in *Proceedings of the IEEE International Geoscience and Remote Sensing Symposium (IGARSS)*, Seattle, WA, USA, vol. 3, pp. 1499–1501, July 1998.

[169] K. P. Papathanassiou and S. R. Cloude, "Phase decomposition in polarimetric SAR interferometry," in *Proceedings of the IEEE International Geoscience and Remote Sensing Symposium (IGARSS)*, Seattle, WA, USA, vol. 4, pp. 2184–2186, July 1998.

[170] K. P. Papathanassiou, A. Reigber, R. Sheiber, R. Horn, A. Moreira, and S. R. Cloude, "Airborne polarimetric SAR interferometry," in *Proceedings of the IEEE International Geoscience and Remote Sensing Symposium (IGARSS)*, Seattle, WA, USA, vol. 4, pp. 1901–1903, July 1998.

[171] J. Gabriel, C. Schmullius, K. P. Papathanassiou, D. Darizhapov, G. Tathkov, T. Tsybjitov, and W.-M. Boerner, "Tree height extraction using polarimetric SAR interferometry," in *Proceedings of the IEEE International Geoscience and Remote Sensing Symposium (IGARSS)*, Hamburg, Germany, vol. 4, pp. 2131–2133, June 1999.

[172] A. A. Monakov, J. Vivekanandan, A. S. Stjernman, and A. K. Nyström, "Spatial and frequency averaging techniques for a polarimetric scatterometer system," *IEEE Trans. Geosci. Remote Sensing*, vol. 32, pp. 187–196, Jan. 1994.

[173] K. Sarabandi, "Derivation of phase statistics from the Mueller matrix," *Radio Science*, vol. 27, pp. 553–560, Sept. 1992.

[174] I. R. Joughin, D. P. Winebrenner, and D. B. Percival, "Probability density functions for multilook polarimetric signatures," *IEEE Trans. Geosci. Remote Sensing*, vol. 32, pp. 562–574, May 1994.

[175] L. Sagués, M. Bara, X. Fàbregas, and A. Broquetas, "A study of spectral decorrelation sources in wide band interferometry," in *Proceedings of the PIERS - Workshop on Advances in Radar Methods*, Baveno, Italy, pp. 64–66, July 1998.

[176] L. Sagués, J. M. Lopez-Sanchez, J. Fortuny, X. Fàbregas, A. Broquetas, and A. J. Sieber, "Indoor experiments on polarimetric SAR interferometry," *IEEE Trans. Geosci. Remote Sensing*, 2000. Accepted for publication.

[177] R. N. Treuhaft and S. R. Cloude, "The structure of oriented vegetation from polarimetric interferometry," *IEEE Trans. Geosci. Remote Sensing*, vol. 37, pp. 2620–2624, Sept. 1999.

[178] A. Papoulis, *Systems and Transforms with Applications in Optics*. McGraw-Hill, 1968.

[179] F. J. Harris, "On the use of windows for harmonic analysis with the Discrete Fourier Transform," *Proc. IEEE*, vol. 66, pp. 51–83, Jan. 1978.

[180] J. E. Hansen, *Spherical Near-Field Antenna Measurements*. Peter Peregrinus Ltd., 1988.

[181] G. T. Ruck *et al.*, *Radar Cross Section Handbook*, vol. 1. Plenum Press, 1970.

[182] K. P. Papathanassiou and M. Zink, "Polarimetric calibration of the airborne experimental SAR system of DLR," in *Proceedings of EUSAR*, Friedrichshafen, Germany, pp. 259–262, May 1998.

[183] R. N. Treuhaft and P. R. Siqueira, "The vertical structure of vegetated land surfaces from interferometric and polarimetric data," *Radio Science*, 1999. Accepted for publication.

[184] J. A. Stratton, *Electromagnetic Theory*. McGraw-Hill, 1941.

[185] R. F. Harrington, *Time-Harmonic Electromagnetic Fields*. McGraw-Hill, 1961.

[186] L. R. Rabiner, R. W. Schafer, and C. M. Rader, "The chirp $z$-transform algorithm," *IEEE. Trans. Audio Electroacust.*, vol. 17, pp. 86–92, June 1969.

[187] B. Ulriksson, "Conversion of frequency-domain data to the time domain," *Proc. IEEE*, vol. 74, pp. 74–77, Jan. 1986.

[188] M. Abramowitz and I. A. Stegun, *Handbook of Mathematical Functions*. Dover, 1970.